

# Refinement of 3D lung cancer models for automation and patient stratification with mode-of-action studies

Dissertation zur Erlangung des  
naturwissenschaftlichen Doktorgrades  
der Julius-Maximilians-Universität Würzburg



vorgelegt von

Matthias Peindl

geboren in Freyung

Würzburg, 2023

Eingereicht am: .....

**Mitglieder der Promotionskommission:**

Vorsitzender: .....

Gutachter:       **Dr. Gudrun Dandekar**  
Lehrstuhl für Tissue Engineering und Regenerative Medizin,  
Universitätsklinikum Würzburg

Gutachter:       **Prof. Dr. Thomas Dandekar**  
Lehrstuhl für Bioinformatik,  
Universität Würzburg

Tag des Promotionskolloquiums: .....

Doktorurkunde ausgehändigt am: .....

*Julius Maximilians University Würzburg*



## **Refinement of 3D lung cancer models for automation and patient stratification with mode-of-action studies**

Weiterentwicklung von 3D Lungentumormodellen zur Automatisierung und  
Patienten-Stratifizierung mit Untersuchungen zur Wirkungsweise

Dissertation for the attainment of the doctoral degree in natural sciences of the  
Julius-Maximilian-University Würzburg

Submitted by

**Matthias Peindl**

From

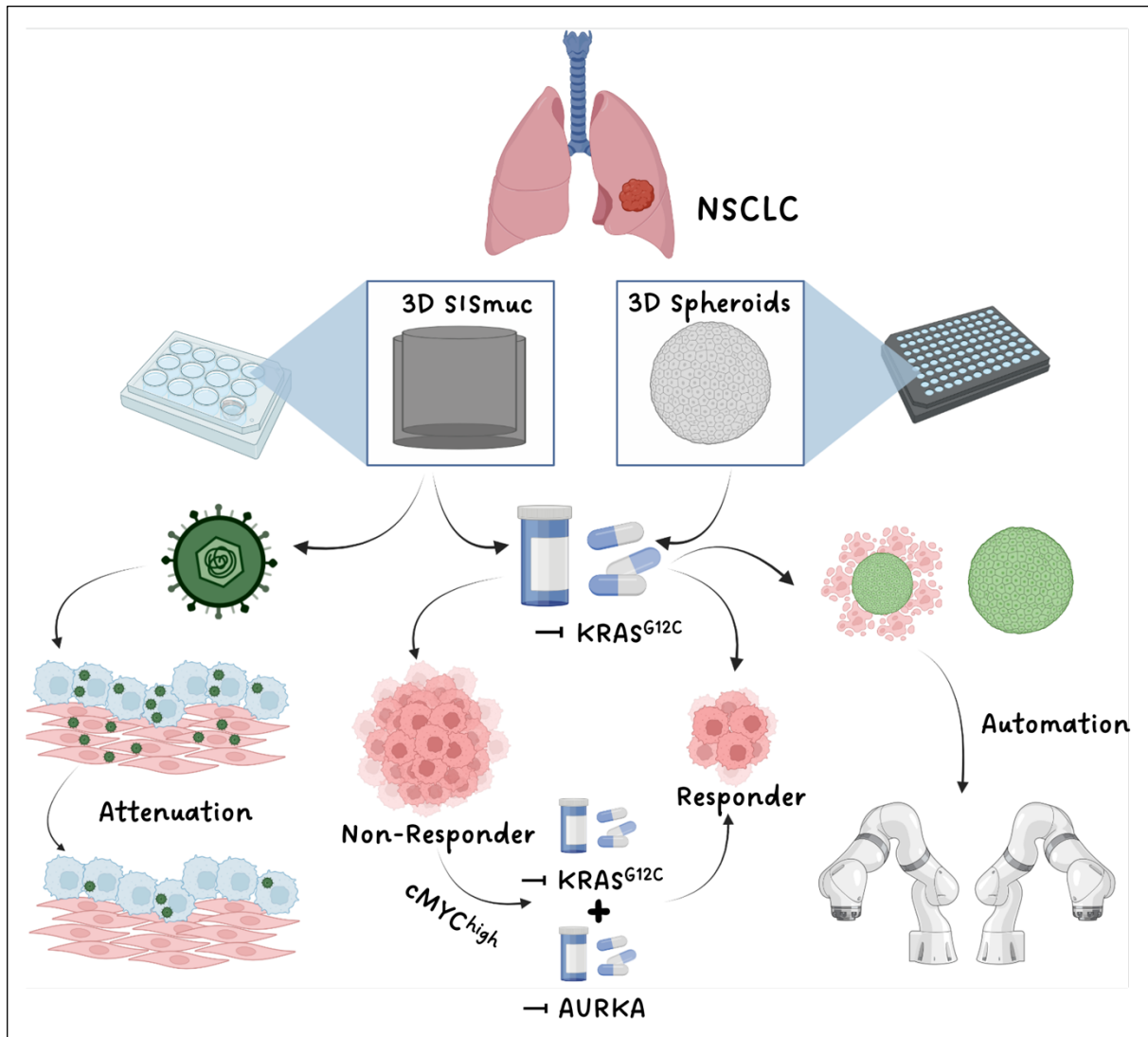
Freyung (Ndb., Germany)

Würzburg, 2023

*“A man is a success if he gets up in the morning and goes to bed at night,  
and in between does what he wants to do.”*

- Bob Dylan

Graphical Abstract



**Graphical Abstract:** Summary illustrating the three pillars of the doctoral thesis, including the patient stratification for *KRAS*<sup>G12C</sup>-mutated NSCLC, the efficacy and safety assessment of a novel HSV-1 based oncolytic virus on 3D SISmuc models and the establishment of a proof-of-concept process for automated drug testing on 3D spheroids. Figure was created with BioRender.

**Abstract**

Lung cancer is the main cause of cancer-related deaths worldwide. Despite the availability of several targeted therapies and immunotherapies in the clinics, the prognosis for lung cancer remains poor. A major problem for the low benefit of these therapies is intrinsic and acquired resistance, asking for pre-clinical models for closer investigation of predictive biomarkers for refined personalized medicine and testing of possible combination therapies as well as novel therapeutic approaches to break resistances.

One third of all lung adenocarcinoma harbor mutations in the *KRAS* gene, of which 39 % are transitions from glycine to cysteine in codon 12 (*KRAS*<sup>G12C</sup>). Being considered “undruggable” in previous decades, *KRAS*<sup>G12C</sup>-inhibitors now paved the way into the standard-of-care for lung adenocarcinoma treatment in the clinics. Still, the overall response rates as well as overall survival of patients treated with *KRAS*<sup>G12C</sup>-inhibitors are sobering. Therefore, 3D *KRAS*<sup>G12C</sup>-biomarker *in vitro* models were developed based on a decellularized porcine jejunum (SISmuc) using commercial and PDX-derived cell lines and characterized in regards of epithelial-mesenchymal-transition (EMT), stemness, proliferation, invasion and *c-MYC* expression as well as the sensitivity towards *KRAS*<sup>G12C</sup>-inhibitor. The phenotype of lung tumors harboring *KRAS* mutations together with a *c-MYC* overexpression described in the literature regarding invasion and proliferation for *in vivo* models was well represented in the SISmuc models. A higher resistance towards targeted therapies was validated in the 3D models compared to 2D cultures, while reduced viability after treatment with combination therapies were exclusively observed in the 3D models. In the test system neither EMT, stemness nor the *c-MYC* expression were directly predictive for drug sensitivity. Testing of a panel of combination therapies, a sensitizing effect of the aurora kinase A (AURKA) inhibitor alisertib for the *KRAS*<sup>G12C</sup>-inhibitor ARS-1620 directly correlating with the level of *c-MYC* expression in the corresponding 3D models was observed. Thereby, the capability of SISmuc tumor models as an *in vitro* test system for patient stratification was demonstrated, holding the possibility to reduce animal experiments.

Besides targeted therapies the treatment of NSCLC with oncolytic viruses (OVs) is a promising approach. However, a lack of *in vitro* models to test novel OVs limits the transfer from bench to bedside. In this study, 3D NSCLC models based on the SISmuc were evaluated for their capability to perform efficacy and risk assessment of oncolytic viruses (OVs) in a pre-clinical setting. Hereby, the infection of cocultures of tumor cells and fibroblasts on the SISmuc with provided viruses demonstrated that in contrast to a wildtype herpes simplex virus 1 (HSV-1) based OV, the attenuated version of the OV exhibited specificity for NSCLC cells with a more advanced and highly proliferative phenotype, while fibroblasts were no longer permissive for infection. This approach introduced SISmuc tumor models as novel test system for *in vitro* validation of OVs.

Finally, a workflow for validating the efficacy of anti-cancer therapies in 3D tumor spheroids was established for the transfer to an automated platform based on a two-arm-robot system. In a proof-of-concept process, H358 spheroids were characterized and treated with the *KRAS*<sup>G12C</sup>-inhibitor ARS-1620. A time- and dose-dependent reduction of the spheroid area after treatment was defined together with a live/dead-staining as easy-to-perform and cost-effective assays for automated drug testing that can be readily performed *in situ* in an automated system.

## **Zusammenfassung**

Lungentumoren sind die Hauptursache für krebsbedingte Todesfälle weltweit. Trotz der Verfügbarkeit diverser zielgerichteter Therapien und Immuntherapien im klinischen Alltag ist die Prognose für Lungenkrebs nach wie vor schlecht. Eine Hauptursache hierfür sind intrinsische und erworbene Resistenzen. Hieraus ergibt sich ein Bedarf für präklinische Modelle zur genaueren Untersuchung prädiktiver Biomarker für eine verbesserte personalisierte Medizin und zur Testung von Kombinationstherapien sowie neuartiger therapeutischer Ansätze, um bestehende Resistenzen zu brechen. Ein Drittel aller Lungen-Adenokarzinome weisen Mutationen im *KRAS*-Gen auf, von denen 39 % Transitionen von Glycin zu Cystein in Codon 12 (*KRAS*<sup>G12C</sup>) darstellen. Obwohl *KRAS* in den vergangenen Jahrzehnten als "unbehandelbar" galt, haben sich *KRAS*<sup>G12C</sup>-Inhibitoren nun den Weg in die klinische Standardbehandlung von Lungen-Adenokarzinomen gebahnt. Jedoch sind die Ansprech- und Überlebensraten von Patienten, die mit *KRAS*<sup>G12C</sup>-Inhibitoren behandelt werden, ernüchternd. Daher wurden in dieser Arbeit 3D *KRAS*<sup>G12C</sup>-Biomarker *in vitro* Modelle basierend auf dezellularisierten Schweinedünndarm (SISmuc) unter Verwendung kommerzieller und PDX-abgeleiteter Zelllinien aufgebaut und hinsichtlich der epithelial-mesenchymalen Transition (EMT), Stammzell-Eigenschaften, Proliferation, Invasion und *c-MYC*-Expression sowie der Sensitivität gegenüber *KRAS*<sup>G12C</sup>-Inhibitoren charakterisiert. Der in der Literatur für *in vivo* Modelle beschriebene Phänotyp von Lungentumoren mit *KRAS*-Mutationen und *c-MYC*-Überexpression in Bezug auf Invasion und Proliferation war in den SISmuc-Modellen reproduzierbar. Während in den 3D Modellen erhöhte Resistenz gegenüber zielgerichteten Therapien im Vergleich zu 2D beobachtet wurde, konnte eine verringerte Viabilität nach der Behandlung mit Kombinationstherapien ausschließlich in den 3D Modellen beobachtet werden. Im Test-System zeigten sich weder EMT noch die *c-MYC*-Expression als direkt prädiktiv für die Sensitivität gegenüber *KRAS*<sup>G12C</sup>-Inhibitoren. Bei der Prüfung von verschiedenen Kombinationstherapien, wurde eine sensibilisierende Wirkung des Aurora-Kinase A (AURKA)-Inhibitors Alisertib für den *KRAS*<sup>G12C</sup>-Inhibitor ARS-1620 beobachtet, welche direkt mit dem Grad der *c-MYC*-Expression in den entsprechenden 3D-Modellen korrelierte. Hierdurch konnte die Eignung von SISmuc Tumor Modellen als *in vitro* Test-System zur Patienten-Stratifizierung gezeigt werden, welches die Möglichkeit einer Reduktion von Tierversuchen birgt. Neben zielgerichteten Therapien ist die Behandlung von NSCLC mit onkolytischen Viren (OVs) ein vielversprechender Ansatz. Es mangelt jedoch an *in vitro* Modellen, um neue OVs in einer präklinischen Umgebung zu testen. Hierfür wurden 3D-NSCLC-Modelle auf der Grundlage der SISmuc bezüglich ihrer Eignung zur Durchführung von Wirksamkeits- und Risikobewertungen von OVs untersucht. Dabei zeigte die Infektion von Kokulturen aus Tumorzellen und Fibroblasten auf der SISmuc mit bereitgestellten Viren, dass die abgeschwächte Version des OV im Gegensatz zu einem auf dem Wildtyp des Herpes Simplex Virus 1 (HSV-1) basierenden OV eine Spezifität für NSCLC-Zellen mit einem fortgeschritteneren und stark proliferativen Phänotyp aufwies, während Fibroblasten sich für eine Infektion nicht länger permissiv zeigten. Dieser Ansatz stellt unter Beweis, dass SISmuc-Tumormodelle sich als neues Test-System zur *in vitro* Prüfung von OVs eignen. Schließlich wurde ein Arbeitsablauf zur Validierung der Wirksamkeit von Krebstherapien in 3D-Tumor-Sphäroiden für die Übertragung auf eine automatisierte Plattform auf der Grundlage eines zweiarmigen Robotersystems entwickelt. In einem Proof-of-Concept-Prozess wurden H358-Sphäroide charakterisiert und mit dem *KRAS*<sup>G12C</sup>-Inhibitor ARS-1620 behandelt. Eine zeit- und dosisabhängige Reduktion der Sphäroid-Fläche nach der Behandlung wurde zusammen mit einer Lebend/Tot-Färbung als einfach durchzuführender und kostengünstiger Assay für automatisierte Medikamententests definiert, welche *in situ* in einer automatisierten Umgebung durchgeführt werden können.

**Table of Contents**

**Graphical Abstract**..... I

**Abstract** ..... II

**Zusammenfassung** ..... III

**Table of Contents** ..... IV

**List of published content** ..... VI

**List of Figures** ..... VII

**List of Tables** ..... IX

**1 Introduction**..... 1

    1.1 *KRAS<sup>G12C</sup>-targeted therapies in non-small cell lung cancer* ..... 1

        1.1.1 Classification, prognosis, and diagnosis of lung cancer ..... 1

        1.1.2 Treatment of non-small cell lung cancer in the clinics ..... 2

        1.1.3 The biology of KRAS ..... 3

        1.1.4 KRAS mutations in lung cancer ..... 4

        1.1.5 Inhibition of KRAS<sup>G12C</sup> with covalent allele-specific inhibitors ..... 5

        1.1.6 Resistance mechanisms for KRAS<sup>G12C</sup>-inhibitors ..... 6

    1.2 *In vitro tumor models for automation and mode-of-action studies* ..... 11

        1.2.1 Spheroids as 3D tumor model for automated drug testing ..... 11

        1.2.2 Decellularized tissue as biological matrix for 3D tumor models ..... 13

    1.3 *Treatment of non-small cell lung cancer with oncolytic viruses* ..... 14

    1.4 *Genotype of lung cancer cell lines used in this study* ..... 15

    1.5 *Aims of the Thesis* ..... 17

**2 Material and Methods** ..... 18

    2.1 *Material* ..... 18

        2.1.1 Cells ..... 18

        2.1.2 Cell culture ..... 18

        2.1.3 Drugs and Growth Factors ..... 20

        2.1.4 Decellularization ..... 21

        2.1.5 Reagents for assays and commercial kits ..... 21

        2.1.6 RNA isolation and RT-qPCR ..... 22

        2.1.7 Primers ..... 22

        2.1.8 Protein isolation and Western Blot ..... 23

        2.1.9 Antibodies ..... 25

        2.1.10 Histology and staining ..... 26

        2.1.11 Plaque assays ..... 28

        2.1.12 General laboratory equipment ..... 28

        2.1.13 Software ..... 29

    2.2 *Methods* ..... 30

        2.2.1 Decellularization of porcine jejunum ..... 30

        2.2.2 Cell culture ..... 31

        2.2.3 Histology ..... 34

        2.2.4 *In vitro* assays for drug efficacy assessment ..... 36

        2.2.5 Expression analysis ..... 40

        2.2.6 Statistical analysis ..... 43



<b>3</b>	<b>Results</b>	<b>44</b>
3.1	<i>Patient stratification for KRAS<sup>G12C</sup>-mutated NSCLC</i>	44
3.1.1	Differential EMT-phenotype and ARS-1620 sensitivity in KRAS <sup>G12C</sup> -mutated cell lines in 2D	44
3.1.2	Advanced NSCLC phenotype in MYC-overexpressing KRAS <sup>G12C</sup> -mutated HCC44 cells in 3D	45
3.1.3	Resistance towards KRAS <sup>G12C</sup> -inhibition in HCC44 3D tumor models	51
3.1.4	TGF- $\beta$ induced EMT is insufficient to mediate drug resistance	56
3.1.5	No correlation between KRAS <sup>G12C</sup> -inhibitor sensitivity with EMT, MYC-expression or stemness in PDX-derived cells	59
3.1.6	Efficacy of combined AURKA and KRAS <sup>G12C</sup> -inhibition in MYC-overexpressing and KRAS-mutated cells in 3D tumor models	66
3.2	<i>SIS muc tumor models as a platform for safety and efficacy testing of a genetically modified HSV-1 for the treatment of NSCLC</i>	68
3.2.1	Infection of NSCLC cells with genetically modified HSV-1 in 3D tumor models	68
3.2.2	Co-cultures with fibroblasts for safety evaluation of oncolytic viruses	70
3.2.3	Infection of co-culture models with attenuated oncolytic viruses	73
3.2.4	Efficacy of attenuated oncolytic viruses on advanced stage NSCLC models	77
3.3	<i>Automation of 3D tumor models</i>	79
3.3.1	Inability of HCC827 cells for spheroid formation	79
3.3.2	Formation of compact spheroids in ULA-coated plates by H358 cells	81
3.3.3	Sensitivity of H358 spheroids towards KRAS <sup>G12C</sup> -inhibition	83
3.3.4	Transfer of methodology to other cell types	87
3.3.5	Translation of the manual process to automation in a robotic platform	88
<b>4</b>	<b>Discussion</b>	<b>92</b>
4.1	<i>Patient stratification for KRAS-mutated NSCLC based on SIS muc tumor models</i>	92
4.1.1	KRAS-biomarker models as representers for different phenotypes	92
4.1.2	HCC44 cells on the SIS muc as surrogate models for advanced stage NSCLC with MYC and KRAS cooperation	94
4.1.3	Differential sensitivity of H358 and HCC44 tumor models towards KRAS <sup>G12C</sup> -inhibition	96
4.1.4	Neither EMT nor c-MYC are exclusive predictive biomarkers for KRAS-targeted therapies	97
4.1.5	Sensitizing effect of AURKA inhibition for KRAS-inhibition in MYC-overexpressing tumor cells	99
4.2	<i>Efficacy and safety assessment of oncolytic viruses on SIS muc tumor models</i>	101
4.3	<i>Established proof-of-concept process for automated drug testing on tumor spheroids</i>	103
<b>5</b>	<b>Outlook</b>	<b>106</b>
	<b>Supplemental Information</b>	<b>107</b>
	<b>Bibliography</b>	<b>109</b>
	<b>List of Abbreviations</b>	<b>119</b>
	<b>Acknowledgments</b>	<b>122</b>
	<b>Appendix</b>	<b>124</b>
	<i>List of Publications</i>	124
	<i>Curriculum Vitae</i>	125
	<i>Eidesstattliche Erklärungen</i>	126

**List of published content**

Parts of this doctoral thesis were published in the following scientific article:

Peindl M\*, Göttlich C\*, Crouch S, Hoff N, Lüttgens T, Schmitt F, Pereira JGN, May C, Schliermann A, Kronenthaler C, Cheufou D, Reu-Hofer S, Rosenwald A, Weigl E, Walles T, Schüler J, Dandekar T, Nietzer S, Dandekar G. EMT, Stemness, and Drug Resistance in Biological Context: A 3D Tumor Tissue/In Silico Platform for Analysis of Combinatorial Treatment in NSCLC with Aggressive KRAS-Biomarker Signatures. *Cancers*. 2022; 14(9):2176. <https://doi.org/10.3390/cancers14092176> (\*shared first authorship)

As stated by the publisher, for articles published in this journal the copyright is retained by the authors [1]. A screenshot of the corresponding webpage can be found in the end of the bibliography (p. 118).

Parts of Chapter 3.1 contain rephrased parts and figures of the publication, accounting for Figures 1 – 4, 7, 8, 10, 12, 14 and 15.

The following publication was submitted to the journal *Molecular Therapy* (January 2023):

Christina Funk, Nadja Uhlig, Zsolt Ruzsics, Florentin Baur, Matthias Peindl, Sarah Nietzer, Gudrun Dandekar, Catherine Botteron, Christian Werno, Thomas Grunwald, Susanne M. Bailer: TheraVision - Platform Technology for the Development of Oncolytic Viruses based on Herpes Simplex Virus Type 1.

Parts of Chapter 3.2 may therefore contain rephrased parts and figures of the article in the case of publication.

**List of Figures**

Figure 1 Immunofluorescence staining of EMT-markers in H358 and HCC44 cells ..... 45

Figure 2 Drug testing of ARS-1620 in H358 and HCC44 cells in 2D ..... 46

Figure 3 H&E and collagen IV staining of H358 and HCC44 3D tumor models..... 47

Figure 4 Characterization of H358 and HCC44 SISmuc tumor models ..... 49

Figure 5 GSEA hallmark analysis of H358 versus HCC44 3D tumor models ..... 50

Figure 6 Tissue architecture of H358 and HCC44 tumor models after ARS-1620 treatment 51

Figure 7 Quantitative ARS-1620 drug testing of H358 and HCC44 tumor models ..... 53

Figure 8 Western blot of H358 and HCC44 tumor models after ARS-1620 treatment..... 54

Figure 9 RNAseq of H358 and HCC44 3D tumor models after ARS-1620 treatment..... 55

Figure 10 ARS-1620 sensitivity of TGF- $\beta$  stimulated H358 tumor models..... 58

Figure 11 Inhibition of the T $\beta$ RI in HCC44 cells with galunisertib ..... 59

Figure 12 Characterization and drug testing of KRAS<sup>G12C</sup>-mutated PDX-derived NSCLC cells  
..... 62

Figure 13 Candidates for resistance mechanisms in HCC44 tumor models..... 62

Figure 14 Testing of combination therapies in HCC44 cells in 2D ..... 64

Figure 15 Testing of combination therapies in HCC44 cells in 3D ..... 65

Figure 16 c-MYC expression after combined KRAS<sup>G12C</sup> and AURKA inhibition..... 66

Figure 17 Marker expression and drug sensitivity of KRAS<sup>G12C</sup>-biomarker models ..... 67

Figure 18 Infection of HCC827 and A549 monoculture models with oncolytic viruses ..... 69

Figure 19 Oncolytic effects of the P- and PZ-virus on NSCLC cells in 3D ..... 70

Figure 20 Cocultures of NSCLC cells with human fibroblasts for safety testing of oncolytic  
viruses ..... 71

Figure 21 Oncolytic effects of P- and PZ-virus on NSCLC cells in co-cultures ..... 72

Figure 22 Safety testing of P- and PZ-virus on coculture models ..... 73

Figure 23 Infection of HCC827 coculture models with attenuated oncolytic viruses..... 74

Figure 24 Increased MOI for infection of HCC827 co-cultures models with attenuated oncolytic  
viruses ..... 76

Figure 25 THP1 models after infection with attenuated oncolytic viruses ..... 77

Figure 26 Infection of HCC44 tumor models with attenuated oncolytic viruses ..... 78

Figure 27 HCC827 spheroid generation approach under different culture conditions ..... 80

Figure 28 H358 spheroids in ULA-coated 96-well plates ..... 81

Figure 29 H358 spheroids in ULA-coated 96-well plates ..... 82

Figure 30 Morphology of H358 spheroids after ARS-1620 treatment ..... 83

Figure 31 Morphological changes in H358 spheroids after ARS-1620 treatment ..... 84

Figure 32 Caspase-3 and -7 activation in ARS-1620 treated H358 spheroids ..... 85

Figure 33 Live-dead staining of H358 spheroids..... 86

---

Figure 34 MDA-MB231, ASC and co-culture spheroids.....	88
Figure 35 Schematic workflow of spheroid generation and drug testing.....	90
Figure 36 Detailed workflow for translation into the robotic platform .....	91
Figure S 1 Invasion of H358 cells in 3D after TGF- $\beta$ 1 stimulation .....	107
Figure S 2 Infection of fibroblasts on HCC827 coculture models.....	107
Figure S 3 Viral titers of attenuated oncolytic viruses in different models and MOIs .....	108

**List of Tables**

Table 1 Genotype of NSCLC cell lines used in this work .....	16
Table 2 List of cell lines and primary cells .....	18
Table 3 List of Media, Supplements and Materials for cell culture .....	18
Table 4 List of inhibitors, drugs, and growth factors for the treatment of cells .....	20
Table 5 List of chemicals for the decellularization of porcine jejunum .....	21
Table 6 List of reagents and kits for assays .....	21
Table 7 Chemicals and reagents for RT-qPCR.....	22
Table 8 List of primers used for qPCR .....	22
Table 9 Chemicals and reagents for protein biochemistry .....	23
Table 10 Primary and secondary antibodies for Immunofluorescence Staining and Western Blotting .....	25
Table 11 List of buffers, chemicals and material for histology and staining .....	26
Table 12 List of chemicals for plaque assays .....	28
Table 13 List of general laboratory equipment and devices.....	28
Table 14 Software for data analysis, figure design and citation .....	29
Table 15 Program or schedule for paraffin embedding as well as dehydration and rehydration of samples prior to H&E or immunofluorescence staining. ....	35
Table 16 Mix for qPCR per well.....	41
Table 17 Thermal cycling protocol for qPCR.....	41

## 1 Introduction

Three distinct research projects were addressed during this thesis. At first, during a BMBF-funded project aiming for the reduction of animal experiments (“Remis3R”), 3D KRAS<sup>G12C</sup>-biomarker models were established on a biological matrix based on decellularized porcine jejunum containing the former mucosa and submucosa of the tissue (SISmuc) for mode-of-action studies, investigation of predictive biomarkers as well as combination strategies to break resistances for KRAS<sup>G12C</sup>-targeted therapies in cooperation with the Chair of Bioinformatics in Würzburg. Secondly, the 3D SISmuc tumor models were further evaluated regarding their capability for pre-clinical *in vitro* efficacy and risk assessment of novel herpes simplex virus type-1 (HSV-1) based oncolytic viruses (OVs) in the course of the joint project TheraVision of the Fraunhofer IGB (Stuttgart), Fraunhofer IZI (Leipzig), Fraunhofer ITEM (Braunschweig, Regensburg) and Fraunhofer ISC (Würzburg). Finally, a proof-of-concept process should be established for the development and subsequent testing of targeted therapies on 3D lung cancer spheroids for the translation into a two-arm robotic system together with the Fraunhofer ISC (Würzburg), funded by the Bavarian Research Foundation in the project FORTiTher (“Forschungsverbund Tumordiagnostik für individualisierte Therapie”).

### 1.1 KRAS<sup>G12C</sup>-targeted therapies in non-small cell lung cancer

#### 1.1.1 Classification, prognosis, and diagnosis of lung cancer

Ranked as second most leading cause of death right behind heart diseases, cancer was causative for 602,350 deaths in the U.S. in 2020 [2]. Further considering worldwide cancer statistics for both sexes, which relativizes high numbers of gender specific tumor types like breast or prostate cancer, lung cancer was the second most common tumor type with 11.4 % after female breast cancer in 2020. Due to the poor prognosis of the disease, malignancies of the lung clearly lead the cancer mortality statistics [3]. The lifetime risk of being diagnosed with lung cancer is around 6 % depending on the current age [4].

In both the clinics but also in biomedical research however, lung cancer cannot be described as a single disease, as tumors in this organ highly differ regarding their histopathology, the cells of origin, treatment options and thereby in the subsequent prognosis. The group of highly malignant tumors developing from anaplastic cells with low levels of cytoplasm and neuroendocrine characteristics are referred to as small cell lung cancer (SCLC) [5]. While the overall 5-year survival rate for SCLC is 7 %, tumors that already spread to distant organs including the contralateral lung depict an even poorer prognosis for the 5-year survival of only 3 % [6]. This entity accounts for 12.6 % of all lung cancers whereas with 84.3 % the more common type is referred to as non-small cell lung cancer (NSCLC) [4]. NSCLC is further subdivided into three distinct subtypes: squamous cell carcinoma (SCC), large cell carcinoma and the most common subtype adenocarcinoma representing 59 % of all NSCLC [4, 5]. Compared to SCLC the prognosis regarding the 5-year survival rate is better in NSCLC but

nevertheless poor with 26 % in general and only 8 % whenever the tumor has metastasized to distant locations [6].

Unfortunately, NSCLC is in most cases diagnosed too late when the disease is in an advanced stage. Screening approaches like chest radiography or cytologic analysis of the sputum did not have a beneficial outcome for the patients in clinical trials and symptoms which can be a sign for NSCLC are often unspecific like cough, hemoptysis, chest pain and dyspnea [7]. Once lung cancer is considered in the differential diagnosis, x-ray, computer tomography (CT) or bronchoscopy can help to confirm the diagnosis while it is mandatory to assure the diagnosis with a biopsy, as the tumor can be easily confused with a pneumonia in imaging processes [5, 8]. Thereafter, the tumor will be classified according to the histology and stage. Nowadays, an additional molecular pathology diagnostic is state of the art. This characterization will finally lead to the treatment decision for the individual patient.

### **1.1.2 Treatment of non-small cell lung cancer in the clinics**

Regarding treatment, targeted therapies play a central role in lung cancer. In 2022 there are around 80 different drugs approved by the U.S. Food and Drug Administration (FDA) for the treatment of NSCLC, including different small molecule inhibitors and cytostatic chemotherapeutics [9]. According to the guidelines of the National Comprehensive Cancer Network (NCCN) from the year 2022 (Version 1.2023), the panel for molecular biomarker testing for advanced stage NSCLC should at least include the *epidermal growth factor receptor (EGFR)*, *anaplastic lymphoma kinase (ALK)*, *Kirsten rat sarcoma (KRAS)*, *ros proto-oncogene 1 (ROS1)*, *serine/threonine-protein kinase B-Raf (BRAF)*, *neurotrophic tyrosine receptor kinase (NTRK) 1/2/3*, *hepatocyte growth factor (HGFR/MET) exon 14 skipping*, *ret proto-oncogene (RET)* and *human epidermal growth factor receptor 2 (ERBB2/HER2)*. Furthermore, the expression of the *programmed cell death 1 ligand 1 (PD-L1)* needs to be validated. Alterations in these genes influence the therapy by identifying reasonable targets for targeted therapies and help to exclude therapies that are not likely to be beneficial for the patient. Broader molecular profiling of the tumors is however highly recommended by the NCCN to also detect rare driver mutations as actionable targets for approved therapies or to find candidates for ongoing clinical trials [10]. Thereby, the most commonly mutated oncogenic driver gene is represented by *KRAS* with 29 %, followed by *EGFR* and *BRAF* mutations with 19 % and 5 %, respectively. *ALK*, *MET* and *HER2* gain-of-function mutations are detected in 3 % of all NSCLC cases. In 27 % however the oncogenic driver remains unknown [11].

NSCLC in stage I, II and III is primarily treated by surgical removal of the diseased tissue. Depending on the size of the malignancy either a lobe of the lung is removed or one whole lung, referred to as lobectomy or pneumectomy, respectively. The presence of cancer cells in the margin of the removed tissue is an indication for adjuvant therapies like chemo-, radiation or immunotherapy. For NSCLC in these stages harboring specific *EGFR* mutations (*EGFR*

*exon 19* deletion or *exon-21 L858R* mutation) adjuvant treatment with the third generation EGFR-inhibitor osimertinib is an alternative option. For tumors in stage IV, which have per definition metastasized to different organs throughout the body, the first-line therapy is in most cases performed with targeted therapies whenever gene mutations are detected sensitizing the tumor cells for these agents. For example, in the case of a detection of an *EGFR* mutation, the first-line therapy should be the third-generation tyrosine kinase inhibitor (TKI) osimertinib. Also, for *ALK*- or *ROS1*-rearrangement positive NSCLC the preferred therapy is the use of small molecule inhibitors like alectinib or crizotinib, respectively. Additionally, targeted therapies are available for *BRAF*, *RET*, *MET* and *NTRK* mutated NSCLC. If the testing of biomarkers for reasonable targets however was negative, NSCLC with high PD-L1 expression ( $\geq 50\%$ ) should be treated with the PD-L1 inhibitor pembrolizumab alone or in combination with chemotherapies, while for tumors with lower PD-L1 expression only combinations of chemo- and immunotherapies are indicated [10, 12].

In summary, a wide variety of targeted therapies has evolved for the treatment of NSCLC over the past decades. Considering the trend for the 5-year survival rates increasing from 16.4 % for the year of diagnosis in 1975 – 1977 to 25.1 % for 2009 – 2015, this development brought also substantial benefits for the patients with an ongoing positive trend [4].

Nevertheless, mainly due to secondary mutations in the corresponding target genes, activation of bypass signaling pathways or changes in the cellular phenotype, patients almost exclusively develop resistances towards those small molecule inhibitors [13]. For EGFR-TKI for example patients eventually develop resistance 10-14 months after the start of the therapy [14]. Facing the truth, Hardtstock *et al.* also showed that only 26.3 % of NSCLC patients were even tested for the described targetable driver mutations in Germany between 2011 and 2016, although the data provided strong evidence that patients treated with targeted therapies had an increased overall survival compared the cohort not tested for mutations [15].

The latest targeted therapies receiving approval by the U.S. Food and Drug Administration (FDA) for advanced NSCLC on May 28, 2021, was sotorasib (AMG510) and adagrasib (MRTX894) on December 12, 2022 [16, 17]. Both specifically target *KRAS* harboring a transition from glycine to cysteine at codon 12 (G12C) of the gene. Sotorasib is used in the current treatment of stage IV NSCLC in *KRAS*<sup>G12C</sup>-mutated tumors, however only after progression of the tumor after prior systemic therapies failed [10].

### 1.1.3 The biology of *KRAS*

Having discovered the development of sarcoma in rats after infection with Moloney's leukemogenic virus (MLV) or murine erythroblastosis virus in the 1960s by Dr. Jennifer Harvey and Werner Kirsten [18-20], the genes in those viruses responsible for transformation were termed Ha-ras and Ki-ras. The human homologues *HRAS* and *KRAS* as well as a third RAS-family member *NRAS* were detected 15 years later in cancer cell lines [20-22]. According to the



enormous capability of mutated *RAS* genes for oncogenic transformation and the high frequency of gain-of-function mutations in these genes in cancer, many efforts have been made to understand the biology and mode-of-action of these proteins [23].

Nowadays, the function of *RAS* proteins is well understood. All *RAS* proteins including *KRAS* are GTPases and function as binary switches in an on- or off-state depending on the bound guanine nucleotide. *KRAS* is thereby activated when bound to guanine triphosphate (GTP) and vice versa inactivated when bound to guanine diphosphate (GDP). The exchange of GDP with GTP is mediated via a guanosine exchange factor (GEF), while the inactivation is based on hydrolysis via the intrinsic GTPase activity of *KRAS* and further catalyzed by GTPase activating proteins (GAP) [24]. Post-translational, *RAS* proteins become farnesylated and are thereby located at the plasma membrane. Under physiologic conditions the activation of the son of sevenless (SOS) GEFs via growth factor receptor bound protein 2 (GRB2) is mediated by growth factor receptor signaling, G-protein coupled receptors and members of the integrin family [25]. GTP-bound *KRAS* results in proliferation, inhibition of apoptosis and angiogenesis mainly by downstream signaling via the phosphatidylinositol 3-kinase / mammalian target of rapamycin (PI3K/mTOR) and mitogen-activated protein kinase (MAPK) signaling pathways [26]. Besides these two major signaling axes, there are in total around 20 downstream effectors activated by GTP-bound *RAS*. Noteworthy, different GEFs for *RAS*-like (*RAL*) GTPases are also activated by *RAS* resulting in a shift of the cellular phenotype towards migration and glycolysis [27]. In the context of cancer harboring gain-of-function mutations in *RAS* genes, these cellular effects translate into high proliferation rates, chemo-resistance but also cell migration, invasion and metastasis of the corresponding tumors [28, 29].

#### 1.1.4 *KRAS* mutations in lung cancer

Due to its central role in cellular signaling concerning cell cycle progression and survival, *RAS* genes of course represent classical proto-oncogenes and indeed harbor gain-of-function mutations in frequently different cancer types. While *NRAS* is typically mutated in melanomas, thyroid cancer and leukemia, *KRAS* mutations are commonly observed in lung, pancreatic and colorectal cancer [25, 30]. Even more, as mentioned above (Chapter 1.1.2), *KRAS* is eventually the most commonly mutated oncogenic driver in NSCLC, detected in 29 % of all cases [11]. For patients with lung cancer, *KRAS* mutations go hand in hand with a poor prognosis regarding the overall survival compared to *EGFR* mutations or *KRAS/EGFR* wild type cohorts [31].

Looking specifically into lung adenocarcinoma, *KRAS* mutations are in more than 80 % located in codon 12 of the gene [32]. These missense mutations result in a transition of glycine with different other amino acids, like valine or aspartic acid. However, in 39 % of all *KRAS*-mutations in lung adenocarcinoma a transition from glycine to cysteine is detected in codon 12, referred to as *KRAS*<sup>G12C</sup>-mutation [32]. The heterogeneity of *KRAS* mutations has however also

implications on the signaling processes of the tumor cells. For example, KRAS<sup>G12C</sup> as well as KRAS<sup>G12V</sup> preferentially activate RAL proteins while AKT exhibits lower phosphorylation in comparison to other mutated forms of KRAS. At the same time, the type of KRAS mutations influences the binding affinity between RAS and rapidly accelerated fibrosarcoma (RAF) and in the clinics certain KRAS mutations preferentially metastasize to specific locations [30].

Missense mutations affecting either codon 12 or codon 13 of the KRAS gene attenuate the hydrolysis of GTP by interfering with the interaction between KRAS and GAP and additionally reducing the intrinsic GTPase activity, consequently GTP-bound KRAS accumulates in the corresponding cells [33]. The GAP-mediated hydrolysis of GTP is comparably reduced in KRAS<sup>G12C</sup>, KRAS<sup>G12A</sup>, KRAS<sup>G12D</sup> and KRAS<sup>G12R</sup>. However, the KRAS<sup>G12C</sup> mutation shows the highest intrinsic hydrolysis rate of GTP compared to other codon 12 missense mutations, still allowing active cycling between GTP and GDP, but nevertheless lowered compared to the wildtype form [34]. In the end, tumorigenesis is mediated by constitutively active KRAS independent of growth factors resulting in unregulated activation of pro-proliferative and anti-apoptotic downstream signaling pathways [35].

KRAS mutations in lung cancer also have a vast influence on the composition of immune cells in the TME and inflammatory processes. Via the induction of nuclear factor kappa light chain enhancer of activated B cells (NF-κB), a variety of chemokines and cytokines including the tumor necrosis factor α (TNF-α), Cys-X-Cys Chemokines (CXCL)-1,2,5 and 8 and interleukin (IL)-1 are secreted by KRAS mutated cells. Furthermore, expression of IL-10, transforming growth factor β (TGF-β) and granulocyte-macrophage colony-stimulating factor (GM-CSF) is induced by the PI3K/mTOR and RAF/MEK/ERK signaling pathway [36].

### 1.1.5 Inhibition of KRAS<sup>G12C</sup> with covalent allele-specific inhibitors

According to the high incidence and the vast influence on cellular signaling, KRAS<sup>G12C</sup> represents a perfect target for anti-cancer therapies in the course of personalized medicine. For many decades however, KRAS was considered to be “undruggable” due to the protein structure with a lack of binding sites for small molecule inhibitors and its high affinity to guanine nucleotides [37, 38]. Different approaches to inhibit KRAS indirectly by using for example farnesyltransferase inhibitors or inhibitors for proteins downstream of KRAS eventually failed in clinical trials [39]. In 2013, Ostrem *et al.* revealed a new pocket, termed the switch-II pocket (S-IIP), in KRAS with crystallography directly leading to the development of the first compounds to specifically inhibit oncogenic KRAS<sup>G12C</sup> [40]. One of the first effective KRAS<sup>G12C</sup>-inhibitors was ARS-853. This small molecule inhibitor covalently binds to the mutational introduced cysteine in codon 12 within the S-IIP via an acrylamide warhead and thereby inhibiting the exchange of GDP with GTP. ARS-853 can exclusively access the binding pocket when KRAS is in the inactive GDP-bound conformation [41]. Therefore, only KRAS with active

cycling between the guanine nucleotides is susceptible for this class of inhibitors which is however the case for KRAS<sup>G12C</sup> as described above (Chapter 1.1.4).

While ARS-853 showed selective efficacy in KRAS<sup>G12C</sup>-mutated cell lines *in vitro*, the substance has a poor bioavailability making *in vivo* drug testing unfeasible. Keeping the acrylamide warhead and changing the molecular scaffold to a quinazoline core, both the covalent binding to KRAS<sup>G12C</sup> as well as the pharmacodynamics were improved in the ARS-853 successor ARS-1620. While showing lower IC<sub>50</sub>-values in KRAS<sup>G12C</sup>-mutated cell lines compared to ARS-853, ARS-1620 also exhibited selective efficacy in KRAS<sup>G12C</sup> mouse models. Furthermore, proteomic cysteine profiles pointed towards low off-target effects of the allele-specific inhibitor [42].

The first KRAS<sup>G12C</sup>-inhibitor tested in clinical trials was AMG510 (sotorasib) in 2018 [43]. While showing high parallels concerning the molecular structure to ARS-1620, AMG510 additionally binds to the histidine at position 95 of KRAS, leading to a significantly higher potency compared to its predecessors [44]. In clinical trials sotorasib showed on the one hand tolerable safety levels with common adverse drug reactions being diarrhea, nausea and fatigue and only in rare cases severe side effects were observed. On the other hand, phase III clinical trial of sotorasib demonstrated the efficacy of the treatment in NSCLC. A significantly increased progression-free survival (PFS) as well as overall response rate (ORR) compared to the chemotherapeutic agent docetaxel was described for the KRAS<sup>G12C</sup>-inhibitor for patients with KRAS<sup>G12C</sup>-mutated NSCLC having experienced a progressive disease after standard chemotherapy plus immunotherapy [45]. Still, the ORR was 28.1 %, demonstrating that a major issue of this therapy is primary resistance towards KRAS<sup>G12C</sup>-inhibition. Secondly, different preclinical models also suggested adaptive resistance mechanisms leading to secondary resistances in the corresponding tumor cells. While clinical data for secondary resistances are sparse, a recently published study showed that 45 % of patients initially responding towards the KRAS<sup>G12C</sup>-inhibitor developed resistance towards the therapy [45, 46]. The second KRAS<sup>G12C</sup>-inhibitor recently receiving an accelerated approval for the treatment of advanced NSCLC by the FDA adagrasib (MRTX849) is also defined as an irreversible and allele-specific KRAS<sup>G12C</sup>-inhibitor and demonstrated a comparable efficacy as well as safety profile as sotorasib during clinical trials [47].

### **1.1.6 Resistance mechanisms for KRAS<sup>G12C</sup>-inhibitors**

To unravel the above-described resistance mechanisms and thereby suggesting strategies for combination strategies and patient stratification many efforts have been made in recent years in biomedical research. Refining the patient stratification and defining predictive biomarkers could help to eventually push KRAS<sup>G12C</sup>-inhibitors to the first-line therapy for cancers with a specific genetic background. Furthermore, defining effective combination therapies for specific subgroups of NSCLC patients could on the one hand help to increase the ORR and on the

other hand eliminate drug-tolerant persister cells, reducing the chance for the development of secondary resistances. Like the well-described T790M mutation in the *EGFR* gene, occurring after prolonged treatment with first- or second-generation EGFR-TKIs, acquired resistance in clinical trials towards *KRAS*<sup>G12C</sup>-inhibition also included secondary *KRAS* mutations for example in codon 12 (G12D, G12R, G12W), codon 13 (G13D) as well as amplification of *KRAS*<sup>G12C</sup>. But also acquired activating mutations downstream of *KRAS* in *RAF1*, *BRAF* and *MAP2K1* or activating mutations of *NRAS* were observed in the corresponding cohort [46]. Besides these specific mutations for acquired resistances in the clinics, different general resistance mechanisms were suggested in preclinical models including epithelial-mesenchymal transition (EMT), growth factor receptor signaling as well as cooperative effects of *KRAS* with other oncogenes, depicting potential candidates for predictive biomarkers or combination therapies.

### ***Epithelial-mesenchymal transition***

During embryonal development a physiological change takes place in which embryonic epithelial cells convert into mesenchymal migratory cells [48]. This process referred to as EMT is also observed in wound healing processes where epithelial cells gain mesenchymal traits to support tissue regeneration [49]. Finally, also carcinoma cells are described to undergo EMT during tumor progression. However, epithelial cancer cells typically do not become fully mesenchymal but show partial EMT with co-expression of both epithelial and mesenchymal markers. It is discussed that this transition plays a crucial role for invasion of cancer cells through the basement membrane and thereby for the formation of metastasis but also the interconnection between EMT and chemoresistance as well as aggressiveness was described for different tumor entities [50]. The EMT-phenotype of the corresponding cancer cells can be defined by the expression level of specific marker proteins. Cytokeratins (CKs), E-cadherin (CDH1) and mucin-1 (MUC-1) are for instance proteins typically marking epithelial cells, while vimentin (VIM), N-cadherin (CDH2) or matrix-metallo proteinases (MMPs) are classical mesenchymal biomarkers [51, 52]. Alterations in the genotype but also epigenetic changes during the evolution of cancer cells in tumor progression can result in this partial EMT-phenotype. However, in many cases the transition is induced by cells of the tumor microenvironment (TME). Here, for example the secretion of the TGF- $\beta$ 1 by fibroblasts mediates the activation of SMAD signaling pathways in cancer cells via paracrine signaling and thereby results in the expression of EMT transcription factors [48, 52].

Long time before *KRAS*<sup>G12C</sup>-inhibitors were developed, Singh *et al.* described an interconnection between EMT and the *KRAS* dependency in lung and pancreatic cancer cell lines. Here, cancer cells with a “*KRAS*-addiction” concurrently showed epithelial characteristics and differentiation [53]. Furthermore, by inducing EMT with the TGF- $\beta$ , it was observed that *KRAS*<sup>G12C</sup>-mutated H358 and LU65 cells gained resistance towards sotorasib and gene set

enrichment analysis (GSEA) across a panel of different *KRAS*<sup>G12C</sup>-mutated cell lines pointed towards enrichment of EMT-related genes in the resistant cell lines. The co-inhibition of *KRAS*<sup>G12C</sup>, the PI3K and the Src homology region 2 domain-containing phosphatase-2 (SHP2, also known as PTPN11), mediating the signaling from growth factor receptors to *KRAS*, resulted in this study in significantly reduced growth of the tumor cells showing an EMT-phenotype [54]. Finally, also clinical data suggest a decisive role of the EMT regarding *KRAS*-targeted therapies. In a clinical study, RNA sequencing of *KRAS*<sup>G12C</sup>-mutated tumors of deceased patients having received sotorasib also showed enrichment of EMT-related genes treatment compared to their tumors prior to the targeted therapy [55]. In summary, literature suggests a decisive role of EMT concerning the sensitivity for *KRAS*-targeted therapies and EMT might thereby represent a promising candidate for a predictive biomarker.

The question whether targeting EMT in cancer is beneficial is under controversial debate. On the one hand, interfering with the EMT-phenotype could increase drug sensitivity and eventually reduce migration and invasion and thereby keep the cancer cells localized. On the other hand, it is still uncertain whether EMT is eventually obligatory for the formation of metastasis and restoring the epithelial phenotype by inducing mesenchymal-epithelial transition (MET) could lead to higher proliferation and activation of quiescent tumor cells [56]. Still, inhibitors interfering with EMT in cancer are available. The TGF- $\beta$  type I receptor inhibitor galunisertib was already evaluated in clinical trials. Here, galunisertib improved the response to neoadjuvant chemoradiation in colorectal cancer and prolonged OS in combination with sorafenib in hepatocellular carcinoma [57, 58].

### ***Growth factor receptor signaling***

With *KRAS* playing the central role in the downstream signaling of growth factor receptors (GFRs), *KRAS*-mutated NSCLC carrying co-mutations in GFRs like *ALK* or *EGFR* exhibits low response rates towards TKI therapies [59]. Vice versa, pre-clinical models also suggest a lower efficacy of *KRAS*-inhibitors for tumor cells with constitutively active GFRs.

A CRISPRi screen in the *KRAS*<sup>G12C</sup>-mutated pancreatic cancer cell line MIA PaCa-2 and the subsequent drug testing with ARS-1620 suggested a variety of different possible resistance mediators. The knockdown of for example genes that are involved in receptor tyrosine kinase (RTK) signaling, like fibroblast growth factor receptors (FGFRs), insulin like growth factor 1 receptor (IGF1R) and AXL including their direct downstream mediators sensitized the pancreatic cancer cell line for *KRAS*<sup>G12C</sup>-inhibition. Also, the knockdown of the stem cell marker CD44 resulted in a higher sensitivity towards ARS-1620 in this study [60]. The combination of ARS-1620 with specific RTKIs could *in vitro* also decrease the viability in different cancer cell lines compared to the respective monotherapies. It was described here that the MAPK pathway becomes reactivated after *KRAS*<sup>G12C</sup>-inhibition via increased phosphorylation of RTKs as part of an adaptive secondary resistance mechanism. Here, the

cell lines also showed specific dependencies on for example FGFR or EGFR, respectively [61]. As RTK signaling would shift KRAS into a more GTP-bound state where KRAS<sup>G12C</sup>-inhibitors cannot bind to the oncoprotein, inhibition of GFRs could result in a higher engagement of KRAS<sup>G12C</sup> [41]. Thereby, it is suggested that overexpression or gain-of-function mutations of GFRs negatively influence the sensitivity towards KRAS<sup>G12C</sup>-inhibitors and that combination with RTKIs could sensitize the cells for the treatment. Clinical trials for the co-inhibition of KRAS<sup>G12C</sup> and RTKs are ongoing, using the EGFR-antibody cetuximab or the pan-HER TKI tarloxotinib together with adagrasib or sotorasib, respectively [62, 63].

### **Frequently occurring KRAS co-mutations**

Finally, non-targetable concomitant mutations in KRAS<sup>G12C</sup>-mutated tumors need to be considered regarding the efficacy of the therapy. Frequently detected *KRAS*-comutations are detected in the tumor-suppressors Kelch-like ECH-associated protein 1 (*KEAP1*), serine/threonine kinase 11 (*STK11*) and tumor protein 53 (*TP53*), which also further determine different subgroups of patients that are linked to therapeutic efficacies in lung adenocarcinoma [64]. The tumor suppressor TP53 that is crucial to maintain genomic integrity in healthy cells shows loss-of-function in 39 % of all *KRAS*<sup>G12C</sup>-mutated tumors [65, 66]. The serine threonine kinase *STK11* harbors mutations in 20 – 28 % of all *KRAS*<sup>G12C</sup>-mutated tumors and regulates cellular metabolism by phosphorylation of AMP-activated protein kinase (AMPK)-related proteins, while loss-of-function is further linked with the phenotype of a “cold” tumor regarding the immune system [66]. Lastly, *KEAP1* which mediates the ubiquitination of NF-E2-related factor 2 (*NRF2*) responsible for the transcription of cytoprotective genes under oxidative stress is co-mutated in 13 – 24 % of all cases [66, 67]. Loss-of-function of this tumor suppressor has a major influence on the tumor microenvironment in regards of composition of immune cells in the TME and negatively influences therapy responses towards chemotherapy and radiation, while at the same time proliferation is induced [66, 67]. Lung adenocarcinoma harboring *KRAS* mutations together with *STK11* or *KEAP1* mutations also go hand in hand with a poor prognosis for immunotherapy compared to *KRAS* wildtype tumors with mutated *STK11* or *KEAP1*, showing the cooperative effect of these mutations [68]. In an exploratory biomarker analysis during the phase 2 clinical trial of sotorasib a higher response rate was described for patients with *STK11* mutation but *KEAP1* wildtype. Vice versa, whenever *KEAP1* was mutated a lower percentage of patients showed response towards sotorasib. However, this study was not statistically powered, and further investigations are necessary due to strong overlaps between the different groups [69]. While loss-of-function of *KEAP1* and *TP53* could be potential predictive biomarkers for *KRAS*-targeted therapies, they are impossible to target in the clinics in the current state. *STK11* mutations could be possibly coped via treatment with the antidiabetic drug metformin, activating the AMPK pathway suggested in different *in vitro* studies [70, 71].

### ***Cooperative effects between KRAS and MYC***

Regarding cooperative effects of KRAS with other oncoproteins, it is indispensable to also mention the transcription factor c-MYC. A synergistic effect of those two central oncoproteins was described for hematopoietic tumors, breast cancer and also lung adenocarcinoma [72]. In *Kras*<sup>G12D</sup> mouse tumor models, malignancies that are solely induced by the *Kras* mutation represented the histopathology of lung adenomas with very defined tumor margins. Whenever now *Myc* was concordantly overexpressed in these *Kras*<sup>G12D</sup>-mutated cells, the adenoma proceeded to an invasive lung adenocarcinoma. At the same time, the tumors harboring both the *Kras*<sup>G12D</sup> mutation as well as the *Myc* overexpression exhibited a significantly higher proliferation compared to those tumors only driven by the *Kras* mutation. Finally, the *Kras*<sup>G12D</sup> mouse models also pointed out that the cooperation of the two oncogenes mediates immune evasion by secretion of Il23 and Ccl9 recruiting Pd-I1 expressing and Vegf-secreting macrophages into the tumor microenvironment while T cells and NK cells are repulsed. However, interrupting the *Myc* overexpression restored the immune surveillance after a short period in this study [73]. In the same transgenic mouse model, it was further observed that the cooperation of *Kras* and *Myc* has a substantial influence also on lipid metabolism. Activating the *Myc* expression in *Kras*<sup>G12D</sup> mouse models resulted in higher cholesterol synthesis as well as uptake and subsequent storage in lipid droplets in the tumor cells [74]. Also, regarding the immunity in lung cancer there is evidence that the two oncogenes have cooperative effects. Oncogenic KRAS signaling was demonstrated to reduce the expression of genes involved in anti-tumor interferon (IFN) pathways by positively regulating the *MYC* expression. This effect could be however reversed by KRAS<sup>G12C</sup> inhibitors to some extent, while simultaneous knock-down of *MYC* had a substantial greater effect on the expression of IFN-related genes like signal transducer and activator of transcription 2 (*STAT2*), Interferon regulatory factor (*IRF*) 7, *IRF9* and others [75]. Hence, a *MYC*-overexpression independent of KRAS-signaling might also attenuate the positive effects regarding anti-tumor immunity induced by KRAS<sup>G12C</sup>-inhibitors. Considering the tremendous influence of the KRAS and c-MYC cooperation regarding tumorigenesis, proliferation, invasion, metabolism and immunity, c-MYC is another promising candidate for further investigation as a predictive biomarker for KRAS-targeted therapies.

Specifically targeting *MYC* in cancer is however difficult. Inhibitors which mainly interfere in the protein-protein interaction of *MYC* and its dimerization partner *MAX* display poor pharmacokinetics and bioavailability [76]. Still, *MYC* can be alternatively targeted by indirect approaches by for example inhibiting the bromodomain protein *BRD4* with the inhibitor *JQ1* [77].

In the end, multiple resistance mechanisms towards KRAS<sup>G12C</sup>-inhibitors are suggested in literature and for further investigation of predictive biomarkers as well as testing of combination

strategies to overcome these resistances, pre-clinical tumor models resembling the pathologic situation in the clinics are crucial.

## **1.2 *In vitro* tumor models for automation and mode-of-action studies**

A majority of experiments in cancer research are still performed using 2D cell cultures or animal models. While cancer cells in 2D are comparably cheap, highly reproducible, and not labor intensive, the cultures fail to represent the complexity of native tumors in many aspects and thereby could result in misleading data also regarding drug testing. The unphysiological flat and elongated cell shape with lost apical-basal cell polarity, altered gene expression leading to artificial high proliferation, poor cell differentiation as well as the reduced cell-cell and cell-extracellular matrix interactions are just some of the reasons making 2D cultures a comparably poor *in vitro* tumor model [78]. Considering the low success rates of clinical trials in oncology of less than 5 % [79], there is a high demand for more predictive pre-clinical models. Nowadays, a wide variety of different 3D *in vitro* tumor models are established for cancer research that can partially cope the issues of 2D cultures and better mimic the *in vivo* situation. Besides organoids and bioprinted scaffolds, frequently used 3D tumor models include tumor spheroids and cultures on decellularized tissue as a biological 3D scaffold [80].

In the era of personalized medicine in cancer therapy there is however also strong interest in automated drug testing in a larger scale on the one hand to provide the best available therapy for each patient or to evaluate the efficacy of a wide variety of new substances in a fast and cost-effective way. On the other hand, decades of cancer research showed the vast influence of non-malignant cells in the TME, the ECM and tissue architecture on therapy response of cancer cells [81, 82] leading to a high demand for complex model systems at the same time. As a matter of fact, the higher the complexity of the 3D *in vitro* model is, the less it is suitable for automation. Vice versa, if a specific drug should be tested pre-clinically regarding its mode-of-action and efficacy, the models should represent the *in vivo* situation as close as possible. Thereby, the choice of the *in vitro* model highly depends on the underlying research question. For this work, two different 3D *in vitro* models were used. While tumor spheroids served as a model for establishing a workflow for automated drug testing in a robotic platform, 3D models based on decellularized tissue of the porcine small intestine were investigated regarding patient stratification for KRAS<sup>G12C</sup>-mutated tumors and safety testing of oncolytic viruses (OVs) in NSCLC.

### **1.2.1 Spheroids as 3D tumor model for automated drug testing**

Per definition 3D tumor spheroids are described as cultures of tumor cells that are self-assembling under conditions in which the interactions between the cells outweigh cell-substrate interactions [83]. These conditions can be created by either using scaffolds to mimic the ECM in native tissue like hydrogels or culturing cells in systems where no attachment to other substrates is possible, referred to as anchorage-dependent or anchorage-independent



tumor spheroids, respectively [84]. These models are compared to other 3D *in vitro* models less expensive and labor-intensive but can also be used in a larger scale, making spheroids especially interesting for bridging the gap between high throughput screening (HTS) with automated drug testing and 3D cell culture.

A big downside of anchorage-dependent tumor spheroids for drug testing are however the gel matrices themselves, containing undefined combinations of growth factors and components. Furthermore, considering automated drug testing and analysis of tumor spheroids by imaging, spheroids in gel matrices are not always found in the same Z-plane of the specimen [83]. Here, anchorage-independent spheroids in a floating culture are advantageous. Using for example ultra-low attachment (ULA) 96-well-plates, seeding suspensions of tumor cells ideally leads to the formation of a single 3D spheroid per well usually within 48 h [85]. Another drawback of the spheroid technology is the fact, that not all cancer cells have the intrinsic capability to form these 3D structures. Primarily the spheroid formation capability of cancer cells of different entities is interconnected with the formation of adherens junctions by E-cadherin (CDH1) [86-88].

Compared to 2D cultures, tumor spheroids represent important characteristics also observed in solid tumors which have a substantial influence on drug sensitivity including gradients of oxygen and nutrients, altered metabolism, cell-cell and cell-ECM interactions as well as heterogenous cell populations [89]. The tumor spheroids can either consist out of only tumor cells but can also be co-cultured with non-malignant cells including fibroblasts and immune cells to partially mimic the TME [90-92].

Regarding the predictivity of spheroids for therapeutic agents, there is growing evidence that the models are more representative for the *in vivo* situation compared to conventional 2D cultures. In tumor spheroids from head and neck squamous cell carcinoma (HNSCC) displaying an EMT phenotype and gene expression comparable to the clinics, significantly higher resistance towards cisplatin and cetuximab were observed compared to 2D monolayer cultures [93]. The testing of the KRAS<sup>G12C</sup>-inhibitor ARS-1620 in 2D monolayers, 3D spheroids and cell line derived xenografts also demonstrated that the IC<sub>50</sub>-values of the spheroids were directly predictive for the efficacy in the xenografts, which was not the case for the 2D cultures [42]. Finally, the comparison of breast cancer cells in 2D and 3D spheroids to patient-derived xenografts as well as the corresponding native tumors, pointed out an artificial high amount of KI-67 and caspase-3-positive cells in 2D. Subsequently, the cells in 2D displayed sensitivity while the 3D spheroids showed resistance towards the chemotherapeutic agent paclitaxel [94]. Considering an automated generation of spheroids with subsequent drug testing, a methodology needs to be established that allows high reproducibility of models as well as easy-to-perform and cost-effective viability assays to determine the therapeutic efficacy of the corresponding anti-cancer drugs.

### 1.2.2 Decellularized tissue as biological matrix for 3D tumor models

With a lack of tissue ECM in tumor spheroids the suitability of these models for cancer research is still controversially discussed [95]. Scaffold based 3D *in vitro* models also enhance cell-ECM interactions and represent an alternative for testing drug efficacy. Therefore, different materials are used for the scaffolds including hydrogels, solid scaffolds but also decellularized native tissue. In comparison to other approaches, decellularized native tissue provides a natural ECM environment as well as tissue architecture for the cells.

To produce decellularized tissue, it is mandatory to thoroughly remove all cellular components from the original organ until mainly the ECM remains. The main components of the decellularized tissue are represented by collagens, elastin, fibronectin, laminin and matricellular proteins [96]. While the process of decellularization is labor-intensive and difficult, cell-ECM as well as cell-cell interactions are promoted in these models and a strong bioactivity as well as low immunogenicity is described for these biological scaffolds [97]. The low immunogenicity is based on the conservation of the ECM between different species [98]. Additionally, with the preservation of the ECM structure the 3D architecture of the respective tissue is also conserved in the biological scaffold [96].

Regarding cancer research, the ECM is known to play a central role in the TME. Both the physical properties as well as the adhesion to ECM affect signaling processes, the phenotype and the polarity of the corresponding cells [99, 100]. Via the interaction of cellular ECM receptors, signaling processes including for example focal adhesion signaling supporting cell proliferation and survival are promoted [101]. The crosstalk between the ECM and cancer cells is also crucial for migratory and invasive processes. During mesenchymal cell migration integrins are necessary for the adhesion of cells and invasion is further depending on the active degradation of the ECM [102]. Also, the efficacy of drug treatment in cancer is highly influenced by the ECM in the TME. On the hand, the ECM alone creates a physical barrier resulting in lower drug delivery in solid tumors. On the other hand, activation of the pro-proliferative and anti-apoptotic PI3K/AKT and MAPK pathways by cell-ECM interactions can mediate a higher chemoresistance in cancer cells [99]. Thereby, a 3D *in vitro* model resembling a natural ECM environment for the cancer cells leading to an *in vivo* like phenotype and signaling is crucial for predictive pre-clinical test systems.

Here, decellularized porcine jejunum was chemically decellularized with sodium deoxycholate (DOC) and applied as a biological matrix for the establishment of KRAS<sup>G12C</sup>-biomarker 3D *in vitro* tumor models. The decellularized tissue contains the preserved ECM structure of the former submucosa (SIS) and mucosa (muc) including the basement membrane. Histological analysis of the SISmuc models demonstrated the conservation of both the mucosal as well as submucosal layer earlier, including former crypt structures. Seeding of the NSCLC cell lines HCC827 and A549 on the biological matrix resulted in the formation of cellular monolayers

with close cell-cell contacts and colonization of the former crypts and reasonable therapy responses of the cells towards the first-generation TKI gefitinib were observed. Noteworthy, artificial high proliferation indices of the cell lines in 2D were reduced to values representative for the clinical situation in these 3D models [103]. SISmuc models also hold the possibility for modular expansion with other cell types to mimic the TME. Formation of tumoral clusters surrounded by fibroblasts were observed on the 3D models when SW480 colon cancer cells were co-cultured on the biological matrix and the phenotype of the colorectal tumor models matched primary colon cancer in regards of tissue architecture and proliferation [104]. Besides targeted therapies and chemotherapeutic agents, also the efficacy of a ROR1-specific chimeric antigen receptor (CAR)-T-cell therapy was evaluated on lung and breast cancer SISmuc models, demonstrating the versatility of the models [105].

Data evaluated from HCC827 NSCLC SISmuc tumor models were also further integrated previously into *in silico* signaling network topologies, which allowed the simulation of cellular responses regarding signaling nodules but also therapy responses towards monotherapy and combination therapies, underlining the *in vitro* results [106]. Also, for colorectal cancer 3D SISmuc models the *in silico* model was successfully adapted leading to a combined *in vitro* / *in silico* model for drug target prediction [107]

### **1.3 Treatment of non-small cell lung cancer with oncolytic viruses**

Besides CAR-T-cell therapy and immune checkpoint inhibitors as promising treatments in the field of immunotherapies, also OVs as anti-cancer therapy attracted attention in recent years. The idea of using oncolytic virotherapy emerged in 1904, where regression of leukemia was found in a patient after an influenza infection and 8 years later it was observed that injection of rabies vaccine was beneficial for the treatment of cervical cancer [108]. With several clinical trials of using wild-type viruses to treat cancer failing due to severe side effects according to the pathogenicity of the viruses, techniques for gene engineering allowed to attenuate the pathogens and make the pathogens more specific for cancer cells [109]. Mechanistically, the therapeutic efficacy of OVs is based on the one hand on the induction of cell lysis in the corresponding tumor cells as well as on the other hand on the activation of anti-tumor immunity due to the release of tumor antigens and danger-associated molecular patterns [110]. The selectivity for cancer cells of the respective OVs can be mediated by retargeting of the virus to specific receptors for cellular entry. Also, the high proliferation rates in cancer cells support the viral replication compared to healthy cells [111].

While many OVs are currently investigated in clinical trials, so far only one OV is approved by the FDA and used for the treatment of melanoma. Talimogene laherparepvec (T-VEC) is based on HSV-1 attenuated via the deletion of two viral infected cell protein (ICP) 34.5 genes reducing the neurotoxicity and increasing the selectivity for cancer cells. The additional deletion of ICP47 and insertion GM-CSF further support anti-tumor immunity [112]. With a large genome,

high infectivity as well as strong lytic activity, the double-stranded neurotropic DNA-virus HSV-1 is widely used as basis for the development of OV<sub>s</sub> [113]. HSV-1 enters the host cells either by fusion of the virus with the cell membrane or by endocytosis [114]. After gene expression and DNA replication in the nucleus, the virions are reassembled in the infected cells and released by exocytosis or by triggering cell lysis of the host cells [115].

One major issue however for the application of OV<sub>s</sub> in solid tumors is the delivery of the therapeutic agent. Here, the barriers formed by the tumor stroma can reduce the therapeutic outcome of OV<sub>s</sub> regarding reduced viral penetration and spread between the tumor cells. Especially in tumors with desmoplastic stroma reactions the ECM is a limiting factor for viral spread [116]. Also, the crosstalk of tumor cells and non-malignant cells like fibroblasts in the TME can highly influence the activity of OV<sub>s</sub> [117]. However, not only the efficacy of the OV<sub>s</sub> is decisive for the transfer into clinical application but also the safety of the therapy. By definition OV<sub>s</sub> should only infect and lyse cancer cells but not normal cells [118]. Unspecific viral infections and spread would result in a risk for severe side effects like for example neurotoxicity in the case of HSV-1 based OV<sub>s</sub> [119].

Thereby, for pre-clinical efficacy and especially safety testing of emerging OV<sub>s</sub> *in vitro*, a test system is mandatory comprising of a physiologic tissue architecture including the ECM as well as non-malignant cells for defining a preliminary risk profile besides the therapeutic efficacy of the corresponding viruses. These aspects cannot be modeled in conventional 2D cultures. Here, the capability of NSCLC SIS<sub>muc</sub> tumor models co-culturing tumor cells and fibroblasts was evaluated for safety and efficacy testing of a novel genetically engineered HSV-1 for the treatment of lung cancer in a pre-clinical setting.

#### **1.4 Genotype of lung cancer cell lines used in this study**

For drug testing and investigation of predictive biomarkers for KRAS<sup>G12C</sup>-targeted therapies, six different NSCLC cell lines were used. H358 (NCI-H358) cells originate from lung adenocarcinoma of a male patient with unspecified age [120]. Besides a heterozygous KRAS<sup>G12C</sup> mutation, homozygous deletion of TP53 is reported for the cells [121]. HCC44 cells are derived from a lung adenocarcinoma of 54-year-old woman [120]. Carrying a homozygous KRAS<sup>G12C</sup>-mutation, the cell line harbors a *c-MYC* amplification, making HCC44 cells a promising candidate to potentially study the cooperative effects of KRAS and MYC. Besides multiple TP53 mutation, as well as loss-of-function mutations in *STK11* and *KEAP1* are described for HCC44 cells [121]. The remaining four KRAS<sup>G12C</sup>-mutated cell lines were kindly provided by the Charles River Research Laboratories and are derived from patient derived xenograft (PDX) models. KRAS<sup>G12C</sup>-mutated LXFA 983 cells additionally harboring a TP53 deletion are derived of a brain metastasis of a lung adenocarcinoma of a 59-year-old male patient [122, 123]. LXFL 1072 cells originate from the primary tumor of a 41-year-old female patient and histologically refer to a large cell carcinoma [122]. Besides the KRAS<sup>G12C</sup>-mutation,

a *KEAP1* mutation is reported [123]. LXFL 1674 cells are derived from the primary tumor of a *KRAS*<sup>G12C</sup>-mutated lung large cell carcinoma from a female patient at the age of 45 [122]. The cell line additionally harbors an amplification of the wild-type *c-MYC* gene and carries a *TP53* and *KEAP1* mutation [123]. Originating from the primary lung adenocarcinoma of a 57-year-old male patient, LXFA 2184 cells show an amplification of the *EGFR* gene as well as a mutation in *TP53*, besides the *KRAS*<sup>G12C</sup>-mutation [122, 123]. No therapy took place prior to surgery of the patients of which the cell lines LXFA 983 and LXFL 1072 derived, while potential neo-adjuvant therapies of the corresponding patients are unknown for the cell lines LXFL 1674 and LXFA 2184 [122].

The lung adenocarcinoma cell lines HCC827 and A549 were used for SIS muc tumor models to test the efficacy and safety of OV. HCC827 cells harbor a heterozygous activating exon 19 deletion in the *EGFR* gene as well as a mutation in the *TP53* allele and are derived from a 39-year-old female patient [120, 121, 124]. A549 cells originating from male patient aged 58 carry a homozygous *KRAS*<sup>G12S</sup>-mutation and missense mutations in the genes *KEAP1* and *STK11* [120, 121].

### Table 1 Genotype of NSCLC cell lines used in this work

Mutations of selected genes in H358, HCC44, HCC827 and A549 cells according to the TRON Cell Line Portal [121]. Mutations of the PDX-derived cell lines LXFA 983, LXFL 1072, LXFL 1674 and LXFA 2184 are provided by Charles River Discovery Research Services [123].

Gene Cell line	<i>KRAS</i>	<i>EGFR</i>	<i>MYC</i>	<i>TP53</i>	<i>STK11</i>	<i>KEAP1</i>	
H358	▼ p.G12C	□	□	▼	□	□	□ Wild-type
HCC44	▼ p.G12C	□	▼	▼	▼	▼	▼ Undefined mutation
LXFA 983	▼ p.G12C	□	□	▼	□	□	▼ Deletion
LXFL 1072	▼ p.G12C	□	□	□	□	▼	▼ Stop gained
LXFL 1674	▼ p.G12C	□	▼	▼	□	▼	▼ Inframe deletion
LXFA 2184	▼ p.G12C	▼	□	▼	□	□	▼ Missense
HCC827	▼	▼	□	▼	□	□	▼ Amplification
A549	▼ p.G12S	□	□	□	▼	▼	

## 1.5 Aims of the Thesis

The efficacy of KRAS<sup>G12C</sup>-inhibitors in the clinics is limited and eventually resistance mechanisms towards the therapy develop in a substantial number of responders. To address this issue, 3D KRAS<sup>G12C</sup>-biomarker should be established for the identification of possible resistance mechanisms and predictive biomarkers for KRAS<sup>G12C</sup>-targeted therapies. Recent research in 2D cultures and *in vivo* models suggest an interconnection between EMT as well as GFR signaling with the sensitivity towards KRAS<sup>G12C</sup>-inhibitors. Furthermore, a cooperative effect of Kras and Myc was described for Kras<sup>G12D</sup>-mouse models which could potentially also influence the efficacy of these therapies. Hence, the KRAS<sup>G12C</sup>-biomarker models on the SISmuc models should be characterized by immunofluorescence staining, western blot and RNAseq with a specific focus on EMT and the expression of *c-MYC*. Via a subsequent drug testing in 2D and 3D models regarding proliferation, viability, and apoptosis after treatment with the KRAS<sup>G12C</sup>-inhibitor ARS-1620, these candidates for predictive biomarkers should be evaluated and surrogate models for drug testing of combination therapies should be defined. Thereby, it should eventually be addressed whether the combination of KRAS<sup>G12C</sup>-inhibitors with RTKIs or other small molecule inhibitors could be beneficial in a defined mutational background to break resistances.

Furthermore, the treatment of NSCLC with OV<sub>s</sub> emerges as a novel therapeutic approach to treat this tumor entity, while there is a lack of suitable *in vitro* models to test this therapy in a pre-clinical setting. Therefore, 3D SISmuc tumor models should be validated in this study for their capability to perform a risk and safety assessment *in vitro*. A novel OV based on HSV-1 was provided by the Fraunhofer IGB Stuttgart (Prof. Bailer, Dr. Funk) in a non-attenuated and attenuated version. The 3D tumor models should be cocultured with non-malignant cells and infected with the corresponding viruses to get insight into the specificity of the novel OV<sub>s</sub> for tumor cells. Infection should thereby be investigated via the validation of specific viral proteins with immunofluorescence staining and oncolytic effects should be evaluated by determining changes in proliferation and the number of tumor cells on the model.

Finally, there is also a high demand for a reproducible and automated testing of targeted therapies for pre-clinical studies as well as for patient stratification in the course of personalized medicine. Thereby 3D *in vitro* models are considered to be more predictive compared to 2D cultures. In cooperation with engineers from the Fraunhofer ISC in Würzburg (M.Sc. Königer, M.Sc. Mahdy) a proof-of-concept process should be developed for an automated generation of 3D spheroids including a subsequent drug testing. To establish this process, a suitable lung cancer cell line should be defined, which reproducibly forms compact spheroids and additionally shows response towards a targeted therapy, to further define suitable viability assays for automation in a two-arm-robot system. Here, live-dead staining as well as changes in the spheroid morphology should be investigated as possible viability assays which can be performed *in situ* and thereby be readily translated to automation.

## 2 Material and Methods

### 2.1 Material

#### 2.1.1 Cells

Table 2 List of cell lines and primary cells

NAME	SOURCE	CATALOGUE NO.
<b>Cell-lines</b>		
A549	DSMZ	Cat# ACC 107
CI-huFIB	InSCREENex, Braunschweig	Cat# INS-CI-1010
GFP-tagged CI-huFIB	InSCREENex, Braunschweig	N/A
H358 (NCI-H358)	ATCC	Cat# CRL-5807
HCC44	DSMZ	Cat# ACC 534
HCC827	DSMZ	Cat# ACC 566
LXFA 2184	Charles River, Freiburg	N/A
LXFA 983	Charles River, Freiburg	N/A
LXFL 1072	Charles River, Freiburg	N/A
LXFL 1674	Charles River, Freiburg	N/A
<b>Primary Cells</b>		
Human dermal fibroblasts	University Hospital Würzburg*	N/A
Primary lung fibroblasts*	University Hospital Würzburg**	N/A

\* Isolated and provided by Heide Häfner (Chair of Tissue Engineering and Regenerative Medicine, Würzburg) or \*\*Lisa Bauer (Chair of Tissue Engineering and Regenerative Medicine, Würzburg); Ethical approval numbers: 182/10 and 280/18.

#### 2.1.2 Cell culture

Table 3 List of Media, Supplements and Materials for cell culture

REAGENT OR RESOURCE	SOURCE	CAT. NO:
<b>Culture Media and Supplements</b>		
DMEM, high glucose, GlutaMax™, HEPES	Gibco by ThermoFisher	Cat# 32430-027
Fetal Calf Serum (FCS)	PAN Biotech (GER)	Lot# P150508
RPMI Medium 1640, GlutaMax™ Supplement	Gibco by ThermoFisher (GER)	Cat# 61870-010
Sodium Pyruvate	Invitrogen (GER)	Cat# P2256
<b>Devices and Disposable Materials</b>		
Axiovert 40C	Zeiss (GER)	N/A
Biological Safety Cabinet Safe 2020	ThermoFisher (GER)	Cat# 51026638
Cell Culture Aspirator	Integra Biosciences (GER)	N/A

<b>Costar® 96-well plate with ULA coating</b>	Corning (USA)	Cat# 3471
<b>Cryo Tubes, Nunc (1.8 ml)</b>	ThermoFisherScientific (GER)	Cat# 368632
<b>DMSO</b>	Sigma-Aldrich (GER)	Cat# D2438
<b>Dulbecco's Phosphate Buffered Saline w/o Ca<sup>2+</sup> and Mg<sup>2+</sup></b>	Sigma-Aldrich (GER)	Cat# D8537
<b>Dulbecco's Phosphate Buffered Saline with Ca<sup>2+</sup> and Mg<sup>2+</sup></b>	Sigma-Aldrich (GER)	Cat# D8662
<b>EDTA</b>	Sigma-Aldrich (GER)	Cat# E9884
<b>EVOS Core Cell Imaging System</b>	Invitrogen (GER)	Cat# AMEX1100
<b>Freezing container Mr. Frosty™</b>	VWR (GER)	Cat #479-0966
<b>Hemocytometer Neubauer improved</b>	A. Hartenstein (GER)	Cat# ZK16
<b>Heraeus BBD 6220</b>	Thermo-Fisher (GER)	Cat# 51020241
<b>Heraeus Multifuge X1R</b>	Thermo-Fisher (GER)	Cat# 15682027
<b>Metal Cell Crowns</b>	Chair of Tissue Engineering and Regenerative Medicine, Würzburg (GER)	N/A
<b>Pasteur pipettes</b>	Brand (GER)	Cat# 747725
<b>Penicillin / Streptomycin</b>	Sigma-Aldrich (GER)	Cat# P4333
<b>Petridishes 60/15mm / 145/20mm</b>	Greiner Bio-One (GER)	Cat# 627102 Cat# 639161
<b>SISmuc**</b>	Chair of Tissue Engineering and Regenerative Medicine, Würzburg	N/A
<b>Tissue Culture Flask 75 cm<sup>2</sup> / 150 cm<sup>2</sup></b>	Techno Plastic Products TPP (CH)	Cat# 90076 Cat# 90151
<b>Tissue Culture Test Plate 12-/ 24-/ 96-well</b>	Techno Plastic Products TPP (CH)	Cat# 92012 Cat# 92024 Cat# 92096
<b>Trypan Blue solution</b>	Sigma-Aldrich (GER)	Cat# T8154
<b>Trypsin/EDTA Solution</b>	Invitrogen by ThermoFisher (GER)	Cat# R001100
<b>Water bath with immersion thermostat</b>	Lauda (GER)	N/A



<b>Cell-Specific Media and Solutions</b>		
<b>A549, H358, HCC44, LXFA 983, LXFL 1072, LXFL 1674 and LXFA 2184 Growth Medium</b>	RPMI Medium 1640, GlutaMax™ Supplement (Gibco) + 10 % FCS (PAN-Biotech)	N/A
<b>HCC827 Growth Medium</b>	RPMI Medium 1640, GlutaMax™ Supplement (Gibco) + 20 % FCS (PAN-Biotech)	N/A
<b>PBS w/o Ca<sup>2+</sup> and Mg<sup>2+</sup> with EDTA</b>	2mM EDTA in PBS	N/A
<b>Primary Lung or dermal Fibroblast Growth Medium</b>	DMEM, high glucose, GlutaMax™, HEPES (Gibco) + 1 mM Sodium Pyruvate (Invitrogen) + 10 % FCS (PAN-Biotech)	N/A

\*\* Registration reference number of approval for explantations #2531-2-12, Ethics Committee of the District of Unterfranken

### 2.1.3 Drugs and Growth Factors

*Table 4 List of inhibitors, drugs, and growth factors for the treatment of cells*

<b>NAME</b>	<b>SOURCE</b>	<b>CATALOGUE NO.</b>
<b>Small molecule inhibitors</b>		
<b>ARS-1620</b>	MedChemExpress (USA)	Cat# HY-U00418
<b>Alisertib (MLN8237)</b>	Selleckchem (USA)	Cat# S1133
<b>Crizotinib (PF-02341066)</b>	Selleckchem (USA)	Cat# S1068
<b>Erdafitinib (JNJ-42756493)</b>	Selleckchem (USA)	Cat# S8401
<b>Galunisertib (LY2157299)</b>	Selleckchem (USA)	Cat# S2230
<b>Gefitinib (ZD1839)</b>	Selleckchem (USA)	Cat# S1025
<b>SHP099 HCl</b>	Selleckchem (USA)	Cat# S8278
<b>Drugs</b>		
<b>Metformin HCl</b>	Selleckchem (USA)	Cat# S1950
<b>Growth factors</b>		
<b>hTGF-β1</b>	Cell Signaling (USA)	Cat# 8915

### 2.1.4 Decellularization

Table 5 List of chemicals for the decellularization of porcine jejunum

REAGENT / SUBSTANCE	SOURCE	CATALOGUE NO.
DNase I	Roche (GER)	Cat# 10104159001
Dulbecco's Phosphate Buffered Saline w/o Ca <sup>2+</sup> and Mg <sup>2+</sup>	Sigma-Aldrich (GER)	Cat# D8537
Dulbecco's Phosphate Buffered Saline with Ca <sup>2+</sup> and Mg <sup>2+</sup>	Sigma-Aldrich (GER)	Cat# D8662
PBS <sup>-</sup> Dulbecco	Biochrom (UK)	Cat# L182-500
Sodium desoxycholate	Sigma-Aldrich (GER)	Cat# D6750-500

### 2.1.5 Reagents for assays and commercial kits

Table 6 List of reagents and kits for assays

REAGENT / KIT	SOURCE	CATALOGUE NO.
<b>Assays</b>		
Calcein AM	Thermo Fisher (GER)	Cat# C1430
MTT	Serva (GER)	Cat# 20395
MTT reagent	3 mg/ml MTT in ultrapure water pH 7.2	N/A
MTT working solution	MTT reagent in growth medium (1:3)	N/A
Propidium Iodide	Sigma-Aldrich (GER)	Cat# P4170
<b>Commercial Kits</b>		
Caspase-Glo® 3/7 3D assay	Promega (GER)	Cat# G8981
CellTiter-Glo® Luminescent Cell Viability Assay	Promega (GER)	Cat# G7570
M30 Apoptosense® (PEVIVA®)	Teco Medical Group (GER)	Cat# 10011

### 2.1.6 RNA isolation and RT-qPCR

Table 7 Chemicals and reagents for RT-qPCR

<b>REAGENT OR RESOURCE</b>	<b>SOURCE</b>	<b>CAT. NO.</b>
<b>RNA isolation and RT-qPCR</b>		
<b>Buffer RLT</b>	QIAGEN (NL)	Cat# 79216
<b>Ethanol absolute</b>	Chemsolute (GER)	Cat# 2246
<b>Labcycler Basic</b>	SensoQuest (GER)	Cat# 011-103
<b>RNAprotect</b>	QIAGEN (NL)	Cat# 76104
<b>RNeasy Fibrous Tissue Mini Kit</b>	QIAGEN (NL)	Cat# 74704
<b>RNeasy Micro Kit</b>	QIAGEN (NL)	Cat# 74004
<b>Stainless Steel Beads</b>	QIAGEN (NL)	Cat# 69989
<b>TissueLyser LT</b>	QIAGEN (NL)	Cat# 85600
<b>β-Mercaptoethanol</b>	Carl Roth (GER)	Cat# 4227.1
<b>RT-qPCR</b>		
<b>CFX96 Dx Real-Time PCR Detection System</b>	Bio Rad (USA)	Cat# DHF-04580
<b>iScript™ cDNA Synthesis Kit</b>	Bio Rad (USA)	Cat# 1708890
<b>SsoAdvanced Universal SYBR Green Supermix</b>	Bio Rad (USA)	Cat# 1725270

### 2.1.7 Primers

Table 8 List of primers used for qPCR

<b>GENE</b>	<b>SENSE (5' → 3')</b>	<b>ANTISENSE (5' → 3')</b>
<b>Gene of Interest</b>		
<b>CDH1</b>	CCCATCAGCTGCCAGAAAATGA	CTGTCACCTTCAGCCATCCTGTTT
<b>KRT18</b>	GAGGGCTCAGATCTTCGCAA	CCAGCTGCAGTCGTGTGATA
<b>MYC</b>	TCTCCGTCCTCGGATTCTCT	TTCTTGTTCCCTCAGAGTCG
<b>SNAI1</b>	CGAGTGGTTCTTCTGCGCTA	CTGCTGGAAGGTAACTCTGGA
<b>SNAI2</b>	TGCGATGCCAGTCTAGAAA	AAAAGGCTTCTCCCCCGTGT
<b>VIM</b>	TTCTCTGCCTCTTCCAACTTT	CGTTGATAACCTGTCCATCTCTA
<b>Housekeeping Gene</b>		
<b>HPRT1</b>	TGACCTTGATTTATTTTGCATACC	CGAGCAAGACGTTTCAGTCCT
<b>RPL6</b>	ATTCCCGATCTGCCATGTATTC	TACCGCCGTTCTTGTCACC

### 2.1.8 Protein isolation and Western Blot

Table 9 Chemicals and reagents for protein biochemistry

<b>REAGENT OR RESOURCE</b>	<b>SOURCE/ COMPOSITION</b>	<b>CATALOGUE NO.</b>
<b>Protein Isolation and precipitation</b>		
<b>cOmplete™ Protease-Inhibitor</b>	Roche (GER)	Cat# 04693132001
<b>DC Protein Assay</b>	Bio Rad (USA)	Cat# 5000111
<b>Laemmli Buffer (5 x)</b>	1.5 mM Tris Base pH 6.8 10 % Glycerol 5 % β-Mercaptoethanol 2 % SDS 0.01 % Bromophenol blue	N/A
<b>Modified RIPA Lysis Buffer</b>	137 mM NaCl 50 mM NaF 20 mM Tris base pH 8 10% Glycerol 1% Nonidet P40 0.5 % Deoxycholic acid sodium 0.1 % SDS	N/A
<b>β-Mercaptoethanol</b>	Carl Roth (GER)	Cat# 4227.1
<b>Glycerol</b>	Carl Roth (GER)	Cat# 3783.1
<b>NaCl</b>	Carl Roth (GER)	Cat# HN00.3
<b>Bromophenol blue</b>	Car Roth (GER)	Cat# A512.1
<b>Tris base</b>	Sigma-Aldrich (GER)	Cat# T6066
<b>NaF</b>	Sigma-Aldrich (GER)	Cat# 201154
<b>Nonidet P40</b>	AppliChem (GER)	Cat# A1694
<b>Deoxycholic acid sodium</b>	Carl Roth (GER)	Cat# 3484.2
<b>SDS</b>	Carl Roth (GER)	Cat# CN30.3
<b>Western Blot</b>		
<b>10 % separation gel</b>	2.5 mL Lower Tris 3.3 mL Acrylamide 2.2 mL H <sub>2</sub> O 2.0 mL Glycerol 14 μL 40 % APS 14 μL TEMED	N/A
<b>5 % stacking gel</b>	1.25 mL Upper Tris 0.5 mL Acrylamide 3.2 mL H <sub>2</sub> O	N/A

	12 µL 40% APS	
	12 µL TEMED	
<b>APS</b>	Carl Roth (GER)	Cat# 9592.1
<b>Biometra Fastblot B44 blotting chamber</b>	Biometra GmbH (GER)	N/A
<b>Electrophoresis buffer (10 x)</b>	1920 mM Glycine 250 mM Tris base 1.5 % SDS in ultrapure water	N/A
<b>FluorChem Q imaging station</b>	Biozym Scientific (GER)	N/A
<b>Glycine</b>	Carl Roth (GER)	Cat# 3908.3
<b>Lower Tris (4 x)</b>	1.5 M Tris base pH 6.8 0.4 % SDS	N/A
<b>Mini-PROTEAN Tetra Vertical Electrophoresis Cell</b>	Bio Rad (USA)	Cat# 1658001FC
<b>Nitrocellulose Blotting Membrane</b>	Whatman, Maidstone (GB)	Cat# WHA7193004
<b>Stripping buffer</b>	1.5 % Glycine 0.1 % SDS 1.0 % Tween-20 in ultrapure water	N/A
<b>TBS (10 x)</b>	1500 mM NaCl 500 mM Tris base In ultrapure water	N/A
<b>TBS-T</b>	10 % TBS (10 x) 0.5 % Tween-20 in deionized water	N/A
<b>TEMED</b>	Carl Roth (GER)	Cat# 2367.2
<b>Upper Tris (4 x)</b>	0.5 M Tris base pH 6.8 0.4 % SDS	N/A
<b>WesternBright Chemilumineszenz Substrat Quantum kit</b>	Biozym (GER)	Cat# 541013
<b>Whatman filter paper</b>	Hartenstein (GER)	Cat# GB46

### 2.1.9 Antibodies

Table 10 Primary and secondary antibodies for Immunofluorescence Staining and Western Blotting

ANTIBODY	SUPPLIER	CAT. NO.	RRID
<b>Primary Antibodies for Immunofluorescence staining</b>			
Mouse anti-VP21/VP22a [LP13]	Bio Rad (USA)	Cat# MCA406	AB_322110
Mouse monoclonal anti-Cytokeratin, pan (Mixture)	Sigma-Aldrich (GER)	Cat# C2562	AB_476839
Mouse monoclonal anti-E-cadherin [Clone 36]	BD-Biosciences (GER)	Cat# 610181	AB_397581
Rabbit anti-CD44 [EPR1013Y]	Abcam (UK)	Cat# ab51037	AB_868936
Rabbit anti-Collagen IV	Abcam (UK)	Cat# ab6586	AB_305584
Rabbit monoclonal anti-Ki67 [SP6]	Abcam (UK)	Cat# ab16667	AB_302459
Rabbit monoclonal anti-Muc1 [EPR1023]	Abcam (UK)	Cat# #ab84597	AB_10672326
Rabbit monoclonal anti-Vimentin [EPR3776]	Abcam (UK)	Cat# ab92547	AB_10562134
<b>Secondary Antibodies for Immunofluorescence staining</b>			
Donkey polyclonal anti-Mouse IgG (H+L), Alexa Fluor 555	Life Technologies (GER)	Cat# A-31570	AB_2536180
Donkey polyclonal anti-Mouse IgG (H+L), Alexa Fluor 647	Life Technologies (GER)	Cat# A-31571	AB_162542
Donkey polyclonal anti-Rabbit IgG (H+L), Alexa Fluor 555	Life Technologies (GER)	Cat# A-31572	AB_162543
Donkey polyclonal anti-Rabbit IgG (H+L), Alexa Fluor 647	Life Technologies (GER)	Cat# A-31573	AB_2536183
<b>Primary Antibodies for Western Blotting</b>			
Mouse anti-alpha-tubulin [DM1A]	Cell Signaling (USA)	Cat# 3873	AB_1904178
Rabbit anti-AKT (pan) [C67E7]	Cell Signaling (USA)	Cat# 4691	AB_915783
Rabbit anti-AMPK $\alpha$ [D5A2]	Cell Signaling (USA)	Cat# 5831	AB_10622186
Rabbit anti-c-Myc [Y69]	Abcam (UK)	Cat# ab32072	AB_731658

<b>Rabbit anti-MAPK (p44/42) [137F5]</b>	Cell Signaling (USA)	Cat# 4695	AB_390779
<b>Rabbit anti-MET [D1C2]</b>	Cell Signaling (USA)	Cat# 8198	AB_10858224
<b>Rabbit anti-Phospho-AKT (Ser473) [D9E]</b>	Cell Signaling (USA)	Cat# 4060	AB_2315049
<b>Rabbit anti-Phospho-AMPK<math>\alpha</math>1 (Ser485)/AMPK<math>\alpha</math>2 (Ser491)</b>	Cell Signaling (USA)	Cat# 4185	AB_2169402
<b>Rabbit anti-Phospho-MAPK (Thr202/Tyr204) [D13.14.4E]</b>	Cell Signaling (USA)	Cat# 4370	AB_2315112
<b>Rabbit anti-Phospho-MET (Tyr1234/1235) [D26]</b>	Cell Signaling (USA)	Cat# 3077	AB_2143884
<b>Secondary Antibodies for Western Blotting</b>			
<b>Goat anti-mouse IgG (H + L)-HRPO</b>	Jackson Immuno Research (USA)	Cat# 115-035-146	AB_2307392
<b>Goat anti-rabbit IgG (H + L)-HRPO</b>	Jackson Immuno Research (USA)	Cat# 111-035-144	AB_2307391

### 2.1.10 Histology and staining

Table 11 List of buffers, chemicals and material for histology and staining

<b>REAGENT OR RESOURCE</b>	<b>SOURCE</b>	<b>CAT. NO.</b>
<b>Buffers and Chemicals</b>		
<b>Antibody diluent</b>	DCS Innovative Diagnostic Systems (GER)	Cat# AL120R500
<b>Citric acid</b>	Carl Roth (GER)	Cat# 1.00244.1000
<b>Donkey-Serum</b>	Sigma-Aldrich (GER)	Cat# D9663
<b>Entellan®</b>	Merck (GER)	Cat# 1079600500
<b>Eosin 1% aqueous solution</b>	Morphisto GmbH (GER)	Cat# 10177.01000
<b>Ethanol 99,8 %</b>	Carl Roth (GER)	Cat# K928.4
<b>Fluoromount-G™ DAPI</b>	Inivitrogen (GER)	Cat# SBA-0100-20
<b>Haematoylin solution acidic</b>	Morphisto GmbH (GER)	Cat# 10231
<b>Isopropanol</b>	Carl Roth (GER)	Cat# T910
<b>Paraffin</b>	Sigma-Aldrich (GER)	Cat# 6642.8
<b>Roti-Histofix 4%</b>	Carl Roth (GER)	Cat# P087
<b>Triton™ X-100</b>	Sigma-Aldrich (GER)	Cat# T8787

<b>Tween®-20</b>	Sigma-Aldrich (GER)	Cat# P9416
<b>Xylol</b>	Carl Roth (GER)	Cat# 9713
<b>Citrate buffer (10x stock solution)</b>	42 g/L Citric acid monohydrate 17.6 g/l Sodium hydroxide in deionized water (pH 6.0)	N/A
<b>Washing buffer (PBS-T)</b>	10 % (v/v) PBS (10x) 0.5 % (v/v) Tween®-20 in deionized water	N/A
<b>Devices and Disposable Material</b>		
<b>Cassette Printer</b>	Vogel Medizintechnik (GER)	N/A
<b>Cooling Plate</b>	Leica (GER)	N/A
<b>Fluorescence Microscope BZ-9000</b>	Keyence (GER)	N/A
<b>Microscope Slide Printer</b>	Vogel Medizintechnik (GER)	N/A
<b>Microscope Slides</b>		
<b>Superforst®</b>	Thermo Fisher (GER)	Cat#AAAA000086
<b>Polylysine™</b>	Thermo Fisher (GER)	Cat#10219280
<b>Microtome Blades A35 / R35 / S35</b>	Pfm medical	Cat# 20750011 Cat# 20750005 Cat# 20750000
<b>Microtome LEICA SM 2010R</b>	Leica BioSystems	Cat# 1492010
<b>Paraffin oven UNpa</b>	Memmert (GER)	CAT# UN55pa
<b>Spin Tissue Processor STP 120</b>	Thermo Fisher (GER)	Cat# 36-101-3476
<b>Steamcooker Multi Gourmet FS 20</b>	Braun (GER)	N/A
<b>Tissue drying oven TDO 66</b>	Medite (GER)	Cat# 02-6600-00
<b>Tissue Embedding Center</b>	Leica (GER)	N/A
<b>Tissue float bath GFL1052</b>	GFL (GER)	N/A



### 2.1.11 Plaque assays

Table 12 List of chemicals for plaque assays

<b>REAGENT/SUBSTANCE</b>	<b>SOURCE/COMPOSITION</b>	<b>CAT. NO.</b>
<b>Crystal Violet</b>	Carl Roth (GER)	Cat# T123.1
<b>Crystal Violet solution</b>	2 g/L Crystal Violet 11 % Formaldehyde 2 % Ethanol 20 g/L PFA	
<b>Ethanol 99,8 %</b>	Carl Roth (GER)	Cat# K928.4
<b>Human IgG</b>	Sigma-Aldrich (GER)	Cat# I4506
<b>Formaldehyd 37 %</b>	Carl Roth (GER)	Cat# 7398.1

### 2.1.12 General laboratory equipment

Table 13 List of general laboratory equipment and devices

<b>REAGENT, RESOURCE OR DEVICE</b>	<b>SOURCE</b>
<b>Accu-Jet Pro Pipettor</b>	Brand (GER)
<b>Autoclaves</b>	
<b>DXDX-45 Bench-top Autoclave</b>	Systec GmbH (GER)
<b>Steam sterilizer</b>	HP Medizintechnik (GER)
<b>Technoclav</b>	Integra Biosciences AG (CH)
<b>Centrifuge Tube 15 ml / 50 ml</b>	Greiner Bio-One (GER)
<b>Centrifuges</b>	
<b>Centrifuge 5417R</b>	Eppendorf (GER)
<b>Mutlifuge X12</b>	Thermo Fisher Scientific (GER)
<b>Multifuge X1R</b>	Thermo Fisher Scientific (GER)
<b>Cold Storage room, 4 °C</b>	Genheimer (GER)
<b>Descosept®</b>	Dr. Schumacher GmbH (GER)
<b>Duran® laboratory bottles 100 ml / 250ml / 1,000 ml</b>	Schott
<b>Freezers</b>	
<b>-20 °C: Comfort</b>	Liebherr (GER)
<b>-80 °C: HFU586 Basic</b>	Heraeus (GER)
<b>Fume hood</b>	Prutcher Laboratory Systems (AT)
<b>Ice machine AF-80</b>	Scotsman (I)
<b>Liquid Nitrogen storage tank MVE 815 P190</b>	German-cryo (GER)
<b>Magnetic stirrer 720-HPS</b>	VWR (GER)

<b>Medical gloves nitrile</b>	Medline (GER)
<b>Multichannel Pipette Research plus, 12-channel</b>	Eppendorf (GER)
<b>Parafilm</b>	Carl Roth (GER)
<b>Pipette Research Plus 0.5–10 µl / 20-200 µl / 100-1,000 µl</b>	Eppendorf (GER)
<b>Pipette Tips 0.5-20 µl / 2-200 µl / 50-1,000 µl</b>	Eppendorf (GER)
<b>Reaction Tubes 1.5 ml / 2.0 ml</b>	Sarstedt (GER)
<b>Rocking Shaker</b>	VWR (GER)
<b>Scalpel blades</b>	Bayha (GER)
<b>Serological Pipettes 5 ml/ 10 ml/ 25 ml/ 50 ml</b>	Greiner Bio-One (GER)
<b>Tecan Reader Infinite 200</b>	Tecan Group (CH)
<b>Tweezers</b>	Assistent (GER)

### 2.1.13 Software

*Table 14 Software for data analysis, figure design and citation*

<b>SOFTWARE</b>	<b>SOURCE</b>	<b>VERSION</b>
<b>BioRender.com</b>	BioRender (US)	N/A
<b>BZ-II Analyzer</b>	Keyence (GER)	2.1
<b>BZ-II Viewer</b>	Keyence (GER)	2.1
<b>CFX Manager™</b>	Bio Rad (USA)	3.1
<b>Endnote</b>	Clarivate Analytics (US)	X9.3.3
<b>ImageJ</b>	National Institutes of Health (US)	1.52q
<b>OriginPro</b>	OriginLab Corporation (USA)	9.9
<b>Prism</b>	GraphPad Software, Inc. (US)	8.4.3
<b>Tecan i-control</b>	Tecan Group (CH)	1.11.1.0

## 2.2 Methods

### 2.2.1 Decellularization of porcine jejunum

Jejunal segments including the associated vessel system of house pigs (German landrace, local supplier) were surgically explanted and provided for the process of decellularization. Remaining intestinal contents were removed by washing the lumen at least 3 times with PBS w/o  $\text{Ca}^{2+}$  and  $\text{Mg}^{2+}$  ( $\text{PBS}^-$ ) by sealing one end of the tissue with a clipper and adding the buffer from the contralateral side to the intestinal tube. After manual removing of the buffer for washing, the lumen was refilled with  $\text{PBS}^-$  and closed on both sides. Subsequently the associated vascular system was rinsed with 500 mL  $\text{PBS}^-$  via a cannula placed in a main arteria of the mesenteric vessel system connected to a peristaltic pump running at maximal pressure of 80 mmHg with up to 40 rpm. In the case of remaining visible blood in the vessel system, the process was repeated. Thereafter,  $\text{PBS}^-$  was removed from the lumen before refilling with deoxycholic acid (DOC) diluted to a final concentration of 22.5 % in deionized water. In total, 3 times 500 mL DOC solution were pumped through the vasculature with an additional exchange of the DOC solution in the lumen after each round. Subsequently, the tissue was placed in a DOC solution filled plastic bucket and the lumen was connected to the peristaltic pump running at 30 rpm with the opposite side unclosed overnight.

The day after surgery, the tissue was removed from the bucket and the vasculature and lumen were rinsed 2 times with  $\text{PBS}^-$ , before the lumen was filled with DOC solution and 2 L DOC solution were pumped through the vessels system in four steps. Thereafter, the luminal side and vasculature was rinsed 4 times with  $\text{PBS}^-$  and perfused overnight in a plastic bucket filled with  $\text{PBS}^-$ , as described above.

After removing the tissue from the overnight incubation construction, both the luminal side and the vasculature were washed 6 times with  $\text{PBS}^-$ , increasing the maximal pump pressure to 100 mmHg limited at 40 rpm. Finally, the vasculature system and surrounding connective tissue were separated from the former mucosal and submucosal layers and the SISmuc was cut into pieces of 10 cm. The SISmuc was afterwards incubated in beakers containing  $\text{PBS}^-$  with 1 % penicillin / streptomycin on a rocking shaker for 30 min at 4 °C.  $\text{PBS}^-$  with penicillin / streptomycin was renewed 3 times prior to the digestion of remaining DNA in the tissue with 0.33 mg/mL DNase diluted in prewarmed PBS with  $\text{Ca}^{2+}$  and  $\text{Mg}^{2+}$  ( $\text{PBS}^+$ ) supplemented with 1 % penicillin / streptomycin. The tissue was incubated at 37 °C for 2 h for DNA digestion before washing with  $\text{PBS}^-$  for 3 times on a rocking shaker for 30 min at 4 °C. The SISmuc was incubated overnight in  $\text{PBS}^-$  on a rocking shaker at 4 °C. Finally, the tissue was sterilized by gamma radiation with 25 kGy. The sterile and ready prepared SISmuc for 3D tumor models was stored at 4 °C in  $\text{PBS}^-$  until the use for cell culture.

## **2.2.2 Cell culture**

### **2.2.2.1 2D cell culture**

All cells were cultured under standard conditions (37 °C, 5 % CO<sub>2</sub>). NSCLC cell lines A549, H358 and HCC44 cells as well as PDX-derived cell lines LXFA 983, LXFL 1072, LXFL 1674 and LXFA 2184 were cultured in RPMI 1640 GlutaMAX™ supplemented with 10 % fetal calf serum (FCS). HCC827 cells were cultured in RPMI 1640 GlutaMAX™ supplemented with 20 % FCS. Primary human lung fibroblasts (hLF) from healthy tissue and human dermal fibroblasts (hdF) were cultured in DMEM, high glucose, GlutaMAX™ supplemented with 1 mM sodium pyruvate and 10 % FCS. Primary hLF were isolated at the institute from biopsies of healthy lung tissue with informed consent according to ethical approval granted by the Institutional Ethics Committee of the University Hospital Würzburg (protocol code 99/20-am). The immortalized human fibroblast cell line huFIB was cultured in human Fibroblast medium (huFIB Medium), including basal supplements provided by the company InSCREENex (Braunschweig, Germany).

Cells were thawed in a 37 °C water bath after storage in liquid nitrogen at -180 °C and directly transferred to the respective T75 or T150 cell culture flasks containing prewarmed growth medium. The day after thawing, cell culture medium was changed. Culture medium was subsequently renewed every 2<sup>nd</sup> to 3<sup>rd</sup> day and cells were passaged twice a week using Trypsin/EDTA after reaching 80 – 90 % confluency. Cells were counted in a Neubauer counting chamber diluted 1:2 in trypan blue. For freezing of cells,  $1 \times 10^6$  cells/mL were resuspended in 70 % growth medium, 20 % FCS and 10 % dimethyl sulfoxide (DMSO) before overnight storage in cryovials in a freezing container at -80 °C. Afterwards, cells were stored at in liquid nitrogen at -180 °C. Unless otherwise stated, cells were centrifuged at 300 x g for 5 min.

Primary cells were used for experiments until passage 5, while cell lines were cultured over 20 passages. After thawing, the cells were sub-cultivated at least once before carrying out the according experiments.

### **2.2.2.2 2D cultures for immunohistochemistry**

For subsequent immunofluorescence staining,  $2 \times 10^4$  H358 or  $3 \times 10^4$  LXFA 983, LXFL 1072, LXFL 1674 and LXFL 2184 cells were seeded per well of a 24-well plate on a round glass cover slip and cultured for 4 days with a medium change on the 2<sup>nd</sup> day. In the case of additional treatment with ARS-1620, the cells were allowed to attach for 24 h before the inhibitor treatment for 72 hours. Medium containing the inhibitor was renewed after 48 h of treatment.

### **2.2.2.3 Preparation of SISmuc tumor models**

SISmuc pieces were placed in a Petri dish with sterile forceps and the tubular tissue was cut open with a scalpel. The required size of SISmuc was cut out with a scalpel with the tissue

placed unfolded and the luminal side facing upwards on the Petri dish. To fix the decellularized tissue between two metal rings, so called cell crowns, the matrix was placed over the inner metal ring. The outer ring was positioned over the inner ring and transferred to a 12-well plate. Thereafter, 1.5 mL and 1 mL growth medium were added outside and inside of the cell crown, respectively, to prevent the tissue from drying out. The prepared models were incubated overnight under standard conditions and checked for bacterial contamination before the seeding of cells on the following day.

Directly before seeding tumor cells on the models, the growth medium was removed from the cell crowns, and in total  $1 \times 10^5$  tumor cells were added in 500  $\mu$ l of the corresponding growth medium to the inner compartment. For coculture models with fibroblasts,  $1 \times 10^5$  cells of each cell type were seeded in 250  $\mu$ l growth medium each. The models were incubated for 2 h under standard conditions before the addition of 1 mL growth medium in the inner and outer compartment of the cell crowns. For cocultures of HCC827 tumor cells with human dermal fibroblasts, a mixture of 1:2 of the cell specific growth media was used (DMEM, high glucose, GlutaMAX™ supplemented with 1 mM sodium pyruvate and 10 % FCS + RPMI 1640 GlutaMAX™ supplemented with 20 % FCS). The 3D models were cultured for 14 days for characterization and testing of targeted therapies or 18 days in the case of infection with oncolytic viruses.

H358 and HCC44 tumor models were cultured statically, while models seeded with HCC827 and A549 as well as the PDX-derived cell lines LXFA 983, LXFL 1072, LXFL 1674 and LXFA 2184 were placed on an orbital shaker running at 100 rpm to enhance tissue generation. Medium was changed every 2<sup>nd</sup> to 3<sup>rd</sup> day by removing the medium with a Pasteur pipette from the cell crowns and 1.5 mL and 1 mL fresh growth medium were added to the inner and outer compartment of the cell crown, respectively.

#### **2.2.2.4 Treatment of SIS muc tumor models with targeted therapies**

All tested inhibitors were administered on the SIS muc tumor models via the growth medium. After 11 days in culture, the complete medium was removed from the cell crowns and exchanged with fresh medium containing the corresponding inhibitor in the desired concentration. For the solvent control, DMSO was diluted in growth medium. The treatment was renewed after 48 h by a medium change. SIS muc models were treated in total for 72 h in the last three days of culture.

#### **2.2.2.5 Stimulation of H358 cells with TGF- $\beta$**

H358 tumor models were prepared as described above (Chapter 2.2.2.3). After 72 h in culture, 2 ng/mL human TGF- $\beta$ 1 with carrier was administered on the models via the growth medium. TGF- $\beta$ 1-containing medium was renewed every 2<sup>nd</sup> or 3<sup>rd</sup> day for the remaining culture time of 11 days.

### **2.2.2.6 Infection of SIS muc tumor models with oncolytic viruses**

SIS muc tumor models were cultured under semi-dynamic conditions on an orbital shaker running at 100 rpm before the infection with the corresponding virus. Thereafter, cultures were changed to static conditions. On day 11 of culture, the virus was diluted in growth medium with a final multiplicity of infection (MOI) of 0.1 or 1.0 and medium was removed from the cell crowns. The diluted virus was added in a volume of 1 mL to the inner compartment of the cell crowns, while 1.5 mL fresh growth medium without any virus were added to the outer compartment. For the control models, growth medium without virus was also used in the inner compartment of the cell crown. Tissue was fixed on the respective days post infection (dpi) with 4 % paraformaldehyde (PFA) for 4 h at room temperature and the supernatant was collected for viral plaque assays from the inner compartment and stored at  $-80^{\circ}\text{C}$ . A partial medium change was performed daily after 3 dpi until 7 dpi by removing 0.5 mL from the inner and outer compartment of the cell crown and adding the same volume of fresh growth medium.

### **2.2.2.7 Spheroid cultures and drug treatment**

For the generation of 3D tumor spheroids,  $1 \times 10^3$  H358 or HCC827 cells were seeded in 100  $\mu\text{l}$  growth medium per well in a costar® ULA-coated 96-well plate with round bottom (Corning Inc., New York, USA) using a multichannel-pipette. For H358 and GFP-tagged ISX huFIB coculture spheroids, 500 cells per cell type were seeded together in 100  $\mu\text{l}$  mixed medium of RPMI 1640 GlutaMAX™ supplemented with 10 % FCS and huFIB Medium with basal supplements 1:2. Plates were centrifuged for 5 min at 300 x g and afterwards carefully transferred to the incubator with special attention to not mechanically disturb the cells by shaking. The formation and the morphology of the spheroids were visually checked every 24 h and brightfield pictures of representative wells were recorded. Treatment of H358 spheroids with ARS-1620 was conducted 24 h after seeding the cells, by slowly adding 100  $\mu\text{l}$  of the inhibitor diluted in growth medium (2-fold concentrated) to avoid mechanical disruption, resulting in a final volume of 200  $\mu\text{l}$  per well. For the solvent control, the corresponding volume of DMSO was diluted in growth medium and added to the spheroids. H358 spheroids were treated with ARS-1620 for a total of 72 h and brightfield pictures of treated and control spheroids were recorded every 24 h.

For Sphericalplates 5D (Kugelmeiers AG, Erlenbach, CH), wells were pre-wetted with 1 mL growth medium per well followed by subsequent centrifugation for 1 min at 1,000 x g. Medium was removed, and wells were pre-loaded with 0.5 mL growth medium before HCC827 cells were seeded in a concentration of either 50 or 100  $\text{cells}/\text{microwell}$  in 0.5 mL growth medium. Plates were incubated under standard conditions and brightfield pictures were recorded every 24 h of culture.

### **2.2.3 Histology**

#### **2.2.3.1 Fixation of samples and paraffin embedding**

Cells cultured in 2D on glass cover slips were washed once with prewarmed PBS<sup>+</sup> before fixing the cells with 4 % PFA for 10 min at room temperature. Cells were washed again with PBS<sup>+</sup> before the addition of PBS<sup>-</sup> and storage of the cells at 4 °C until staining was performed.

For fixation of spheroids, the spheroids cultured in ULA-coated 96-well plates were collected with a 1000 µl pipette in a 2 mL reaction tube with conical shaped bottom. Spheroids were allowed to sink to the bottom of the tube by gravity before the supernatant was carefully removed from the 3D models. The spheroids were washed 3 times with PBS<sup>-</sup> before the addition of 4 % PFA for 10 min at room temperature. After removing the PFA, spheroids were washed twice with PBS<sup>-</sup> and subsequently between 10 and 20 spheroids per sample were embedded in HistoGel™. Thereafter, the specimen was placed in filter paper in an embedding cassette for subsequent paraffin embedding.

SISmuc tumor models were washed once with PBS<sup>+</sup> before fixation of the tissue with 4 % PFA for 2 h at room temperature. Thereafter, the tissue was removed from the cell crowns and the region seeded with cells was cut out with a scalpel and placed within filter paper in an embedding cassette.

Embedding cassettes containing the spheroids or SISmuc were placed overnight in a tissue transfer processor according to the program in Table 15. Thereafter the samples were cast in paraffin blocks using a tissue blocking station.

Therefore, the embedding cassettes containing the samples were prewarmed in a liquid paraffin bath for 20 min before the samples were removed from the cassettes. Spheroids in HistoGel™ were directly placed in base molds while the SISmuc was cut in 3 pieces with a scalpel and placed perpendicular in the base molds filled with liquid paraffin. The paraffin blocks were allowed to cool down on a cooling plate for at least 30 min before the blocks were removed from the molds.

#### **2.2.3.2 Microtomy**

Samples in paraffin blocks were cooled down at on a 4 °C cooling plate for 20 min before sectioning on the slide microtome. Sections of 5 µm were prepared with the slide microtome for H&E as well as immunofluorescence staining. The floating sections were mounted on microscope slides via the transfer to deionized water with a hairbrush and subsequently briefly dipped in 50 °C deionized water. Superfrost™ or polylysine-coated microscope slides were used for H&E and immunofluorescence staining, respectively. The specimens were stored overnight at 37 °C in a drying oven before staining.

**Table 15 Program or schedule for paraffin embedding as well as dehydration and rehydration of samples prior to H&E or immunofluorescence staining.**

Dehydration, Clearing, Paraffin Embedding		Deparaffination, Rehydration	
Reagent	Time [min.]	Reagent	Time [min.]
Deionized H <sub>2</sub> O	60	Xylol I	10
Ethanol, 50 %	60	Xylol II	10
Ethanol, 70 %	60	Ethanol, 96 % I	3 x Dipping
Ethanol, 80 %	60	Ethanol, 96 % II	3 x Dipping
Ethanol, 96 %	60	Ethanol, 70 %	3 x Dipping
Isopropanol I	60	Ethanol, 50 %	3 x Dipping
Isopropanol II	60	Deionized H <sub>2</sub> O	Swiveling
Isopropanol / Xylene 1:2	60		
Xylene I	60		
Xylene II	60		
Paraffin I	90		
Paraffin II	90		

### **2.2.3.3 Deparaffination and rehydration**

Microscope slides with SISmuc or spheroid sections were incubated at 60 °C for 30 min and directly transferred to xylol twice for 10 min. Afterwards the samples were rehydrated in a series of decreasing ethanol concentrations from 96 % to 50 %, before the slides were finally placed in deionized water until disturbances cleared (Table 15).

### **2.2.3.4 H&E staining**

Samples were placed in hematoxylin for 6 min after deparaffination and rehydration (Chapter 2.2.3.3). The dye was washed out with deionized water before incubation under running tap water for 5 min. Thereafter, the samples were placed in eosin for 6 min and washed with deionized water. The samples were briefly dipped in 70 % ethanol and placed for 2 min in 96 % ethanol, 5 min in isopropanol and 10 min in xylol, before mounting of the samples with Entellan<sup>®</sup> and drying overnight.

### **2.2.3.5 Immunofluorescence staining of cells in 2D**

Cells cultured in 2D on glass cover slips in 24-well plates were stained directly in the well-plate. After fixation (Chapter 2.2.3.1), the PBS<sup>-</sup> was removed, cells were permeabilized for 5 min with 500 µl of 0.2 % Triton X-100 in PBS<sup>-</sup> per well. Samples were washed 3 times with PBS-T for 5 min and blocked with 400 µl 5 % donkey serum in antibody diluent solution for 20 min. Blocking solution was removed and 200 µl of the corresponding primary antibody diluted 1:200 in antibody diluent solution were added per well. The plate was sealed with parafilm and



incubated overnight at 4 °C on a rocking shaker. After washing 3 times with PBS-T, the secondary antibody was added in a dilution of 1:400 in antibody diluent solution for 1 h at room temperature. Finally, the samples were washed 3 times with PBS-T and mounted with Fluoromount G containing DAPI. Samples were dried overnight at room temperature before imaging.

### **2.2.3.6 Immunofluorescence staining of 3D models**

SISmuc and spheroid sections were deparaffinized and rehydrated (Chapter 2.2.3.3) and heated in citrate buffer pH 6 for 20 min in a steam cooker. Subsequently, the microscope slides were placed in deionized water and sections were edged with a liquid blocker pen, before the transfer to PBS-T. Placed in a moisture chamber, the samples were blocked for 20 min with 100 µl 5 % donkey serum in antibody diluent solution. The sections were afterwards covered with the primary antibody, diluted 1:100 in antibody diluent solution and incubated overnight at 4 °C. For each replicate a negative control was included, using only antibody diluent solution without primary antibody. Samples were washed 3 times with PBS-T for 5 min, before the addition of the secondary antibody diluted 1:400 in antibody diluent solution for 1 h protected from light at room temperature. After a final washing for 3 times with PBS-T in the dark, the samples were mounted with Fluoromount G containing DAPI and dried overnight before imaging.

### **2.2.3.7 Microscopy**

Pictures of H&E and immunofluorescence staining were recorded with digital Keyence Microscopes (BZ-9000 and BZ-X810). Cy5 or TRIT-C filters were used for the detection of conjugated Alexa Fluor 647 or 555 fluorophores, respectively. At least three non-overlapping and representative areas were imaged for each replicate. Within the same experiment, the exposure time for each channel was not varied and the unspecific background signals were excluded with the corresponding negative controls.

## **2.2.4 In vitro assays for drug efficacy assessment**

### **2.2.4.1 CellTiter-Glo® viability assay and determination of IC<sub>50</sub>**

Sensitivity of cell lines towards targeted therapies in 2D were determined by CellTiter-Glo® Luminescent Viability assay (Promega). Therefore, either  $3 \times 10^3$  H358,  $1 \times 10^3$  HCC44,  $5 \times 10^3$  LXFA 983,  $6 \times 10^3$  LXFL 1072,  $6 \times 10^3$  LXFL 1674 or  $4.5 \times 10^3$  LXFA 2184 cells were seeded in 100 µl growth medium per well of a white 96-well plate with clear bottom. Cells were allowed to attach for 24 h before the addition of the corresponding inhibitor. For the treatment, the inhibitor stock solution was diluted in growth medium to a final concentration of 24 µM or 48 µM and a serial dilution of 1:2 was performed to the lowest applied concentration of 46.9 nM or 93.7 nM, respectively. In the case of metformin, concentrations ranged from 40 mM to 39 µM. The DMSO control contained the volume of solvent according to the highest concentration of the inhibitor in the assay. For the evaluation of combination therapies with ARS-1620 in HCC44

cells in 2D, a corresponding serial dilution of the inhibitor was performed in growth medium containing 1  $\mu\text{M}$  ARS-1620. After 24 h in culture, medium was removed and 100  $\mu\text{l}$  growth medium containing the inhibitor were added. For each concentration and the control, technical triplicates were used. The treatment was repeated after 48 h and cells were treated in total for 72 h.

CellTiter-Glo® Viability assay was performed according to the manufacturer's protocol. In brief, medium containing the inhibitor was removed, and cells were washed once with PBS<sup>+</sup> before the addition of 100  $\mu\text{l}$  growth medium and 100  $\mu\text{l}$  CellTiter-Glo® reagent to each well. Luminescence was measured without attenuation and with an integration time of 1000 ms in a microplate reader, after shaking the plate for 2 min and incubation of 10 min at room temperature in the dark. Via the analysis of the non-linear regression of the luminescence including interpolation of unknown values of the curve, the IC<sub>50</sub> values were determined with GraphPad Prism.

#### **2.2.4.2 Caspase-Glo® 3D assay and determination of EC<sub>50</sub>**

Apoptosis induction in spheroids was measured by a Caspase-Glo® 3D assay to determine the dose-dependent activation of caspase 3 and 7 after treatment. H358 cells were seeded at a density of  $1 \times 10^3$  per well in 75  $\mu\text{l}$  growth medium in a ULA-coated 96-well plate and allowed to form spheroids for 24 h. Subsequently the cells were treated with increasing concentrations of ARS-1620 ranging from 93.8 nM to 24.0  $\mu\text{M}$ . Therefore, 25  $\mu\text{l}$  growth medium containing the 4-fold concentration of ARS-1620 were added carefully to the wells resulting in a final medium volume of 100  $\mu\text{l}$  per well. For each concentration technical triplicates were performed. For the untreated control, DMSO was added according to the highest concentration of the inhibitor treatment. Spheroids were treated for 72 h and finally 100  $\mu\text{l}$  Caspase Glo reagent were added to each well with a multichannel pipette. After incubation for 30 min at room temperature protected from light, luminescence was measured in a microplate reader without attenuation and with an integration time of 1000 ms. The EC<sub>50</sub> was determined by non-linear-regression analysis with GraphPad Prism.

#### **2.2.4.3 MTT viability assay of SIS muc tumor models**

The relative viability of tumor cells on SIS muc tumor models after inhibitor treatment was evaluated by quantitative MTT assays. After treatment of SIS muc models (as described in Chapter 2.2.2.4) in duplicates per condition, the medium containing the inhibitor or solvent control was removed and growth medium containing 1  $\text{mg}/\text{mL}$  MTT was added to the inner and outer compartment of the cell crown. One SIS muc model unpopulated with cells was included to determine the background absorbance of the biological matrix. Tumor models were incubated under standard conditions for 3 h, before the MTT solution was removed. Cell crowns were subsequently disassembled and the SIS muc was placed in a 50 mL falcon tube containing 2 mL isopropanol 0.04 N HCl. After incubation for 1 h on an orbital shaker at room

temperature, the extracted dye was collected in 15 mL tubes and 1 mL of fresh isopropanol 0.04 HCl was added to the SISmuc. The extracts were again collected in the corresponding 15 mL tubes, after 30 min incubation on an orbital shaker. This step was repeated until the dye was completely washed out from the SISmuc. After mixing thoroughly, 200 µl of the collected dye were transferred to a 96-well plate in triplicates for each sample. Absorbance was measured in a microplate reader at 570 nm with 10 flashes and a reference wavelength of 630 nm. To calculate the relative viability, the background absorbance of the empty SISmuc was subtracted and the viability of models treated with the solvent control was defined as 100 % viability.

#### **2.2.4.4 Determination of relative cell numbers, proliferation indices and invasive cells**

KI-67 or collagen IV immunofluorescence staining with DAPI-counterstaining was performed to calculate the proliferation index, the relative cell number on the model or invasiveness of tumor cells, respectively. For each replicate at least five immunofluorescence pictures of representative non-overlapping areas of the model were imaged at a 20-fold magnification and subsequently quantitatively analyzed. Therefore, the total number of cells (all DAPI-stained nuclei) as well as the KI-67-positive cells or cells inside the matrix (DAPI-positive nuclei within the collagen of the matrix which were not located on the surface of the SISmuc) were manually counted with ImageJ and the mean proliferation index, relative cell numbers or percent of invasive cells per replicate were evaluated according to the following formulas:

*Proliferation index [%] = (KI67/DAPI-double-positive cells) / (DAPI-positive cells)*

*Relative cell numbers [%] = (DAPI-positive cells "treated") / (DAPI-positive cells "control")*

*Invasive cells [%] = (DAPI-positive cells inside the SISmuc) / (DAPI-positive cells)*

#### **2.2.4.5 Evaluation of fold increase of apoptosis by M30 ELISA**

For the determination of the fold increase of apoptosis, 100 µl supernatant of the inner compartment of the cell crowns were collected of the corresponding tumor models directly before treatment (T0) as well as 24 h (T1), 48 h (T2) and 72 h (T3) after the first treatment and stored at -80 °C before the measurement. The concentration of caspase-cleaved keratin 18 (M30 neo-epitope) was measured with a M30 Apoptosense® ELISA (Peviva) according to the manufacturer's protocol. If necessary, the samples were diluted in cell culture medium to fit the range of the standard curve. The reagents were allowed to reach room temperature before use. For the washing buffer, the provided wash tablet was dissolved in 500 mL deionized water. The M30 Conjugate was diluted 1:25 in M30 Conjugate Dilution Buffer. Thereafter, 25 µl of the standards, the controls "high" and "low" as well as the samples were pipetted in duplicates into the provided pre-coated 96-well plate. Thereafter, 75 µl of the diluted M30 conjugate dilution were added with a multi-channel pipette to each well. Sealed with a tape, the plates were incubated on an orbital shaker at room temperature for 4 h. Plates were manually washed 5 times with 230 µl washing buffer per well and 200 µl of TMB Substrate were added to each

well with a multi-channel pipette. After 20 min incubation in the dark, 50  $\mu$ l Stop Solution were added per well and the plate was briefly placed on an orbital shaker to ensure complete mixing. After 5 min incubation at room temperature the absorbance at 450 nm was measured with a microplate reader.

With the provided standards, the sigmoidal standard curve was interpolated with the software Origin using the fitting function "Sigmoidal logistic function, type 1 (Slogistic 1)", and the concentration of M30 [U/L] was determined for the samples according to the function. For diluted samples, the values were multiplied with the dilution factor. As the inhibitor treatment was renewed 48 h after the initial treatment in the SISmuc tumor models, the T3 values were added to the T2 values to calculate the final concentration of M30. Each sample was thereafter normalized to its corresponding T0 value for each timepoint (T1, T2, T3) to determine the increase of apoptosis over time for each replicate of the treated samples as well as the controls. The mean value for the increase of apoptosis was determined for all controls at the respective time points and subsequently the increase of apoptosis of the treated samples were divided by the increase of apoptosis of the controls for the final calculation of the fold increase of apoptosis over the control at each timepoint.

#### **2.2.4.6 Viral plaque assay**

The plaque assays were performed according to Todo *et al.* [125]. Vero cells were seeded at a density of  $2.4 \times 10^5$  cells per well in a 12-well plate and incubated under standard conditions for 4 h. The supernatant of the infected SISmuc tumor models containing the virus was stepwise diluted 1:10, with dilutions ranging from  $10^{-1}$  to  $10^{-6}$ . Growth medium was removed from Vero cells and 400  $\mu$ l of the diluted virus stock solution were added in triplicates. After 4h incubation under standard conditions, 400  $\mu$ l growth medium supplemented with 400  $\mu$ g/mL human IgG were added per well. After 4 days in culture, cells were fixed with crystal violet solution for 10 min at room temperature und the wells were subsequently rinsed with deionized water. The plaques were counted manually, and the titer was calculated according to the following formula:

$$\text{Titer [pfu/ml]} = (\text{Mean Plaque count} * \text{Dilution Factor}) / (\text{Inoculum volume})$$

#### **2.2.4.7 Determination of spheroid area, diameter and circularity**

Brightfield pictures of spheroids were recorded every 24 h with an EVOS™ Cell Imaging system, starting 24 h after seeding the H358 cells in the ULA-coated 96-well plates. For each condition, at least five representative spheroids were recorded for each timepoint. Pictures were imported in ImageJ and the spheroids were encircled at the border with the freehand selection tool and the area, Ferret's diameter and circularity were analyzed by ImageJ's implemented measurement tool. The spheroid area and Ferret's diameter at different timepoints were normalized to the respective values of the spheroids after 24 h in culture.

#### **2.2.4.8 Live-Dead Staining of Spheroids**

For *in situ* staining of living and dead cells in H358 spheroid cultures, calcein AM and propidium iodide diluted in PBS<sup>-</sup> were directly added in the corresponding concentrations to the wells successively. For calcein AM, final concentrations of 1  $\mu$ M, 2  $\mu$ M and 3  $\mu$ M were tested. Propidium iodide was added to reach final concentrations of 1.0  $\mu$ g/mL, 2.5  $\mu$ g/mL or 5.0  $\mu$ g/mL. The spheroids were incubated with the dyes for 3 h under standard conditions and images were recorded with a Keyence Microscope BZ-9000, using the TRIT-C filter for propidium iodide (Excitation 535 nm / Emission 617 nm) and GFP filter for calcein AM (Excitation 495 nm / Emission 515 nm). Specificity of the dyes was determined by simultaneous recording of brightfield pictures of the specimen as well as unstained spheroids.

#### **2.2.5 Expression analysis**

##### **2.2.5.1 RNA Isolation**

For RNA isolation of cells cultured in 2D, 5 x 10<sup>5</sup> H358 or HCC44 cells were used per sample and directly lysed in RLT Buffer containing  $\beta$ -mercaptoethanol (10  $\mu$ L per 1 mL buffer). Thereafter, RNA was isolated with the RNeasy Micro Kit (Qiagen) according to the manufacturer's protocol.

SISmuc tumor models were washed once with PBS<sup>-</sup> and cell crowns were disassembled. The tissue was stored in RNAprotect® at 4 °C until the isolation of RNA. RNA of SISmuc tumor models was isolated with a RNeasy Fibrous Tissue Kit (Qiagen). Therefore, the tissue that has beforehand been minced with a scalpel was placed together with 300  $\mu$ L RLT lysis buffer supplemented with  $\beta$ -mercaptoethanol (10  $\mu$ L per 1 mL buffer) in a 2 mL reaction tube. A heat sterilized steel bead was added per sample and the tubes were placed in a Tissue Lyser for 2 min at 20 Hz. The lysate was transferred to a fresh 1.5 mL reaction tube and 590  $\mu$ L RNase-free water were added. After addition of 10  $\mu$ L Proteinase K solution and thoroughly mixing, the samples were incubated at 55 °C for 10 min. Samples were centrifuged for 3 min at 10,000 x g and the supernatant was transferred to a fresh 1.5 mL reaction tube. Ethanol 96 % was added to the lysate and mixed well. Thereafter, the sample was transferred to a RNeasy Mini spin column and RNA was isolated according to the manufacturer's protocol.

In the final step, RNA isolated from 2D cultures or SISmuc tumor models was eluted with 30  $\mu$ L RNase-free water and RNA-concentrations were measured with a NanoQuant Plate™ in a microplate reader and stored at -80 °C.

##### **2.2.5.2 RT-PCR**

For the reverse transcription of RNA to cDNA, the isolated RNA was diluted to a final concentration of 1,000 ng in 15  $\mu$ L RNase-free water. A mastermix was prepared containing 1  $\mu$ L iScript Reverse Transcriptase and 4  $\mu$ L iScript Reaction Mix per sample and subsequently 5  $\mu$ L of this mastermix were added to the diluted RNA. The samples were placed in the thermal

cycler for 5 min at 25 °C, 30 min at 42 °C and 5 min at 85 °C. The transcribed cDNA was stored at -20 °C until the use for qPCR.

### 2.2.5.3 qPCR

Primers used for the first time were tested in a gradient PCR to determine the optimum annealing temperature and the products were checked on an agarose gel for specific amplification of the gene of interest before use (Data not shown).

The cDNA was diluted in ultrapure water to a concentration of 7.5 µg/µl. Primers (400 nM) and SsoAdvanced universal SYBR Green supermix (Bio Rad) were thawed on ice. The Supermix was protected from light. All solutions were carefully mixed and briefly centrifuged before use. A mastermix was prepared for every primer pair according to Table 16 and placed on ice protected from light. As housekeeping genes *HPRT1* and *RPL6* were used for normalization. cDNA was pipetted in duplicates in the 96-well plate and the mastermix was subsequently added. For every primer pair a negative control was included with ultrapure water instead of cDNA.

**Table 16 Mix for qPCR per well**

<b>REAGENT</b>	<b>VOLUME</b>
SsoAdvanced SYBR Green supermix	5 µl
Primer Forward (400 nM)	1 µl
Primer Reverse (400 nM)	1 µl
cDNA (15 ng / Well)	2 µl
Water	1 µl
Final volume / Well	10 µl

The plate was sealed and briefly centrifuged, before running the qPCR on a CFX96 Dx Real-Time PCR Detection System (Bio Rad) with the following program (Table 17):

**Table 17 Thermal cycling protocol for qPCR**

	Activation/ Denaturation	Amplification			Denaturation	Melt- Curve
		Denaturation	Annealing/Extension	Cycles		
Temp.	95 °C	95 °C	60 °C	40	95 °C	65 –95 °C
Time	30 sec	10 sec	25 sec		10 sec	5 sec/step

Changes in gene expression were evaluated according to the Pfaffel method [126]. For the housekeeping genes the geometric mean was calculated.

#### **2.2.5.4 RNAseq**

RNA was isolated from HCC44 and H358 SIS muc tumor models with or without treatment with 1  $\mu\text{M}$  ARS-1620 as described above (Chapter 2.2.5.1). RNA of 4 biological replicates were provided for RNA sequencing for each condition. RNA sequencing was performed by the Core Unit SysMed of the University Hospital Würzburg with a TruSeq-mRNA library preparation after polyA-enrichment. Sequencing was performed with NSQ 500, 400 M reads, single-end and 950 pM loading concentration. Data were evaluated by the Chair of Bioinformatics in Würzburg (Prof. Dandekar, M.Sc. Caliskan, M.Sc. Crouch, Dr. Liang, M.Sc. Yu).

#### **2.2.5.5 Protein Isolation and measurement of protein concentration**

For the isolation of proteins from the SIS muc tumor models, a modified RIPA-buffer was used. SIS muc tumor models seeded with the corresponding tumor cells as well as an empty SIS muc were washed twice with cold PBS<sup>-</sup> before the disassembling of the cell crowns. The tissue was subsequently placed in a 6-well plate on ice and 800  $\mu\text{l}$  lysis buffer were added to each well. After incubation at 4 °C for 30 min on an orbital shaker, the lysis buffer containing the protein was collected in 1.5 mL reaction tubes and centrifuged at 10,000 x g for 10 min at 4 °C. Supernatant was transferred to fresh 1.5 mL reaction tubes and stored at -80 °C, unless directly used for measuring the protein concentration.

The protein concentration was determined with a DC Protein Assay kit (Bio Rad). Standards were prepared with BSA diluted in ultrapure water with concentrations between 0  $\mu\text{g}/\text{mL}$  and 2000  $\mu\text{g}/\text{mL}$ . Cell lysates were diluted 1:2 in ultrapure water to match the range of the standard curve. For the standards as well as the diluted samples, 5  $\mu\text{l}$  were pipetted in duplicates into a 96-well plate. The alkaline copper solution was prepared by diluting the provided solution "S" (surfactant) with "A" (copper solution) 1:50. Per well 25  $\mu\text{l}$  of this alkaline copper solution were added to each well, followed by reagent "B" (folin) in a volume of 200  $\mu\text{l}$ . After 15 min incubation at room temperature protected from light, the absorbance at 750 nm was measured with a microplate reader and the protein concentration was calculated according to the function of the linear standard curve. The values of the empty SIS muc were subtracted from the samples, to calculate the final protein concentration for western blotting.

#### **2.2.5.6 Protein precipitation**

According to the measured protein concentration, 100  $\mu\text{g}$  of protein were adjusted with ultrapure water in a 2 mL reaction tube to reach a final volume of 100  $\mu\text{L}$ . After that 400  $\mu\text{L}$  methanol were added and samples were mixed thoroughly. Afterwards, 100  $\mu\text{L}$  chloroform and 300  $\mu\text{L}$  ultrapure water were added, mixed, and the samples were centrifuged at 14,000 rpm for 10 min. The supernatant corresponding to the aqueous phase was discarded and another 800  $\mu\text{l}$  methanol were added and the solution was mixed. After centrifugation at 14,000 rpm for 10 min, the supernatant was discarded and the pellet containing the proteins was dried in a drying oven at 37 °C for 15 min. Finally, the pellet was resolved in 15  $\mu\text{l}$  ultrapure water and

5  $\mu$ l Laemmli buffer. The samples were subsequently heated for 5 min at 95 °C and stored at -20 °C until electrophoresis was performed.

#### **2.2.5.7 Western Blot**

Per lane of a 10 % SDS gel 80  $\mu$ g protein of the corresponding sample were loaded. The proteins were subsequently blotted semi-dry on a 0.2  $\mu$ m nitrocellulose membrane with 1  $\text{mA}/\text{cm}^2$  and maximal voltage of 11 V for 2 h, before blocking with 5 % milk in TBS-T for 1 h at room temperature. Primary antibodies were diluted according to the supplier's instruction in either 5 % milk or 5 % BSA in TBS-T, respectively, and the blots were incubated in a 50 mL centrifuge tube overnight at 4 °C on a rolling shaker. Subsequently, the blots were washed 3 times with TBS-T for 10 min, before the incubation with the HRP-conjugated secondary antibody for 1h at room temperature on a rolling shaker. After another washing step with TBS-T (3 x 10 min), the blots were covered with developing solution (WesternBright Chemiluminescence Substrate, Biozym) and visualized on an Imaging Station FluorChem Q (Biozym).

The blots were stripped for the detection of additional target proteins as well as the housekeeping protein by using a mild stripping buffer twice for 10 min or 0.1 % sodium azide in 5 % milk in TBS-T for 30 min. Thereafter, the blots were incubated with the corresponding primary antibody overnight and the secondary antibody for 1 h at room temperature. Subsequently the blots were re-analyzed as described above.

For the quantification of protein expression, ImageJ's implemented analysis tool was used to determine the density of bands of the western blots according to Stael *et al.* [127]. Each sample was normalized to its loading control before comparison of the protein expression.

#### **2.2.6 Statistical analysis**

Assuming that data were distributed normally, the statistical significance was determined with unpaired t-tests. Prism 8 (GraphPad) was used for the calculation of p-values. p-values  $\leq 0.05$  were considered as significant; \*:  $p \leq 0.05$ , \*\*:  $p \leq 0.01$ , \*\*\*:  $p \leq 0.001$ .



### 3 Results

#### 3.1 Patient stratification for KRAS<sup>G12C</sup>-mutated NSCLC

With a high frequency of intrinsic and acquired resistances as well as poor ORRs for KRAS<sup>G12C</sup>-targeted therapies in the clinics, the definition of predictive biomarkers and effective combination therapies to break these resistances could increase the therapeutic efficacy of KRAS<sup>G12C</sup>-inhibitors for specific subgroups of patients. Therefore, KRAS<sup>G12C</sup>-biomarker models were established on the SISmuc and investigated together with the Chair of Bioinformatics in Würzburg in a joint project with a specific focus on EMT and *c-MYC*-expression as potential predictive biomarker. For developing KRAS<sup>G12C</sup>-biomarker models on the SISmuc suitable for stratification and subsequent drug testing of KRAS<sup>G12C</sup>-inhibitors, first and foremost corresponding tumor cells are crucial for the recellularization of the biological matrix SISmuc. Here, the two KRAS<sup>G12C</sup>-mutated NSCLC cell lines H358 and HCC44 were tested as candidate cells for these models since the cell lines show decisive difference in the *c-MYC* gene. HCC44 cells harbor an amplification of the wildtype *c-MYC* gene, which is not the case for H358 cells. Therefore, HCC44 cells represent an ideal cell line to further study the cooperative effect of the KRAS and *c-MYC* oncoproteins if the amplification goes hand in hand with *c-MYC* overexpression.

##### 3.1.1 Differential EMT-phenotype and ARS-1620 sensitivity in KRAS<sup>G12C</sup>-mutated cell lines in 2D

Before establishment of 3D tumor models on the SISmuc, the cell lines H358 and HCC44 were characterized in conventional 2D cultures. Here, the characterization of the EMT-phenotype of the two cell lines in 2D pointed towards a comparatively progressed EMT in HCC44 cells. This was indicated by a lack of expression of the epithelial markers E-cadherin (CDH1) and MUC-1 in these cells, whereas H358 cells expressed both markers. Epithelial cytokeratins (PCK), however, were expressed by both cell lines throughout the monolayer. Expression of VIM could be detected in all HCC44 cells, while a substantial proportion of H358 cells was negative for the mesenchymal marker. In summary, both cell lines showed a partial EMT-phenotype in 2D while the staining pointed towards a more progressed transition phenotype in HCC44 cells (Figure 1).

Additionally, a differential sensitivity of the two cell lines towards the KRAS<sup>G12C</sup>-inhibitor ARS-1620 was observed. H358 cells in 2D cultures displayed an IC<sub>50</sub>-value towards ARS-1620 of 680 nM, whereas the IC<sub>50</sub> in HCC44 cells was more than ten-fold higher with 8.85 μM. ARS-1630, an enantiomer of ARS-1620 with less activity regarding KRAS<sup>G12C</sup>-inhibition was tested in parallel as a control, and while the IC<sub>50</sub> for this small-molecule-inhibitor was nearly 20-fold increased compared to ARS-1620 in H358 cells with 13.17 μM, only a minor difference in the IC<sub>50</sub> values of HCC44 cells with 9.80 μM was evaluated (Figure 2 A,B).

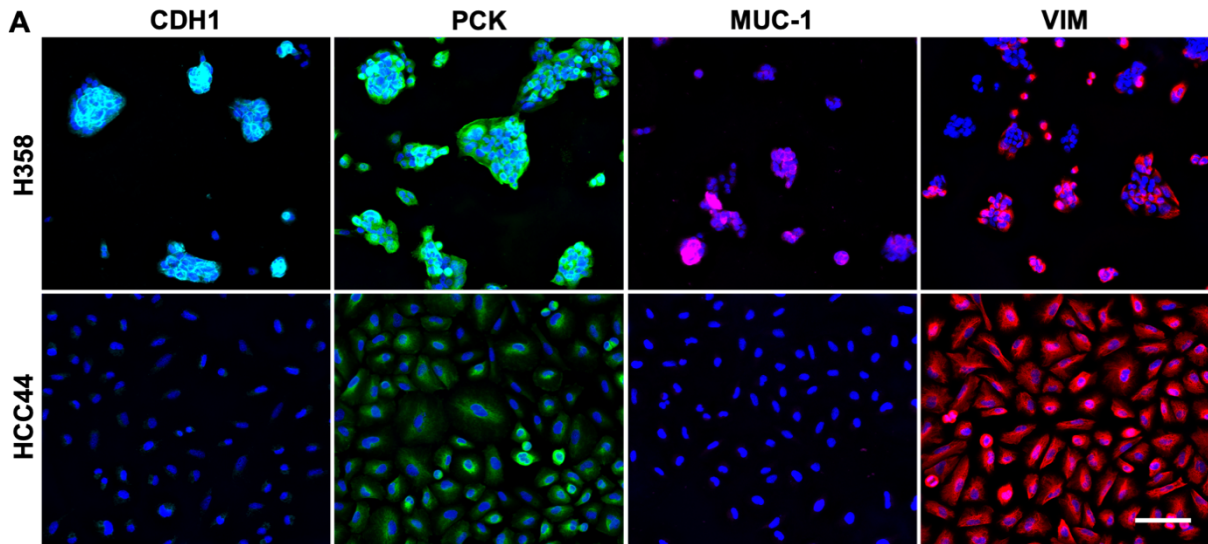


**Figure 1 Immunofluorescence staining of EMT-markers in H358 and HCC44 cells**

Both cell lines were cultured for 96 hours on glass cover slips and subsequently stained for the epithelial markers CDH1 (lightblue), PCK (green), MUC-1 (purple) and the mesenchymal marker VIM (red). Cells were counterstained with DAPI (blue). Scale bar = 100  $\mu$ M; n = 4. Adapted figure was published in Peindl *et al.* [128].

In 2D cultures, the untreated cell lines H358 and HCC44 displayed high proliferation indices of  $91.3 \pm 0.9$  % and  $98.6 \pm 0.5$  %, respectively. The treatment with 1  $\mu$ M ARS-1620 for 72 hours resulted only in significantly reduced proliferation in H358 cells with  $13.3 \pm 5.9$  % but not in HCC44 cells ( $96.7 \pm 0.8$  %; Figure 2 C, D). Taken together, these results suggested resistance towards ARS-1620 in HCC44 cells in 2D cultures, whereas H358 displayed sensitivity towards the inhibitor in the sub micromolar range.

### 3.1.2 Advanced NSCLC phenotype in *MYC*-overexpressing *KRAS*<sup>G12C</sup>-mutated HCC44 cells in 3D

After characterization of H358 and HCC44 cells regarding EMT and ARS-1620 sensitivity in 2D, the cell lines were tested for their capability to build *KRAS*<sup>G12C</sup>-biomarker models based on the SIS muc and the tissue architecture, marker expression and proliferation of the models was investigated.

H&E staining after 14 days in static culture revealed major differences between the two 3D tumor models. While H358 cells formed a continuous mono- or multi-layer on top of the biological matrix and colonized the former crypt structures (Figure 3 A), HCC44 cells exhibited an invasive growth indicated by a large proportion of tumor cells penetrating through the preserved ECM. Here, HCC44 cells especially lined the former interface between the mucosa and submucosa. Further the cells partially failed to create a continuous layer on top of the matrix (Figure 3 B). Staining of the preserved porcine collagen IV of the decellularized tissue further confirmed the invasiveness of HCC44 cells in 3D (Figure 3 C). Quantification of cells on top or inside the biological scaffold pointed out that  $42.7 \pm 5.1$  % of all HCC44 cells were

detected within the biological matrix, while only  $2.3 \pm 0.5$  % H358 showed invasive growth (Figure 3 D).

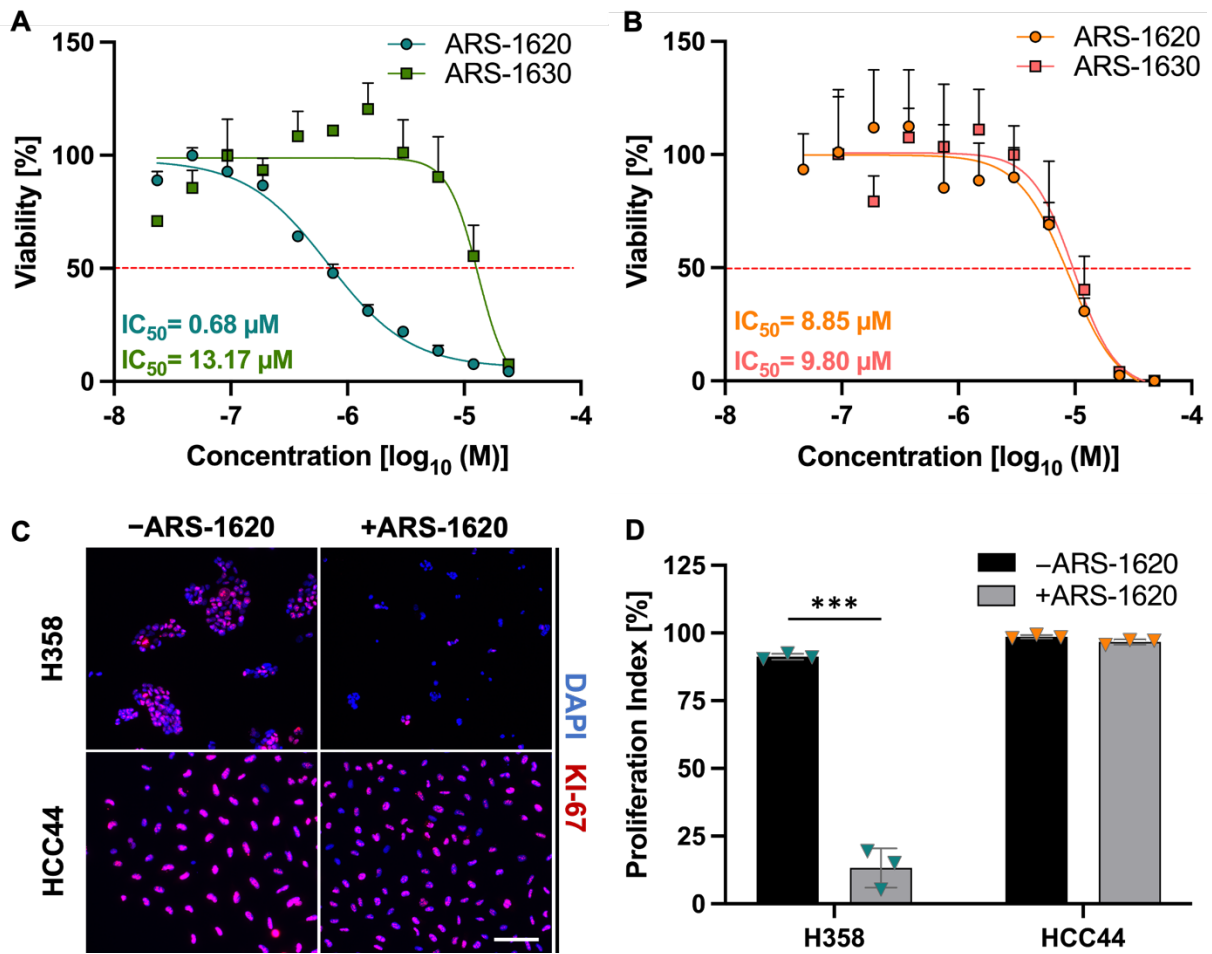


**Figure 2 Drug testing of ARS-1620 in H358 and HCC44 cells in 2D**

$IC_{50}$ -values for ARS-1620 and ARS-1630 were determined with CellTiter-Glo® viability assays after 72 h treatment of **(A)** H358 and **(B)** HCC44 cells;  $n=1$  with three technical replicates. **(C)** H358 and HCC44 cells were stained for KI-67 (red) with DAPI-counterstaining (blue) with or without treatment applying  $1 \mu\text{M}$  ARS-1620 for 72 hours and **(D)** proliferation indices were subsequently determined; scale bar =  $100 \mu\text{m}$ ,  $n = 3$ . Significance was determined with unpaired t-tests. \*\*\*:  $p \leq 0.001$ . Adapted figure was published in Peindl *et al.* [128].

Characterization of the two KRAS<sup>G12C</sup>-biomarker models further indicated that the progressed EMT phenotype in HCC44 cells observed in 2D cultures was conserved in the 3D SIS muc tumor models. Immunofluorescence staining of CDH1, and MUC-1 pointed out low expression in HCC44 tumor models comparable to 2D culture conditions, but solid expression of these epithelial markers in H358 tumor models was observed. Both H358 and HCC44 cells in 3D however co-expressed epithelial PCK and mesenchymal VIM. Furthermore, the proportion of H358 cells expressing the mesenchymal marker VIM was increased compared to 2D cultures. The stem cell marker CD44 was on the other hand only detected in HCC44 tumor models (Figure 4 A).

Compared to 2D cultures, RT-qPCR indicated a shift to a more mesenchymal and thereby dedifferentiated phenotype in both cell lines in 3D tumor models. While for H358 in 3D the epithelial marker CDH1 was higher expressed, the expression of epithelial cytokeratins (PCK) was reduced and vice versa mesenchymal VIM increased. HCC44 cells showed lower expression of both epithelial CDH1 and PCK, as well as a higher expression of VIM when cultured on the SISmuc compared to 2D conditions (Figure 4 B).

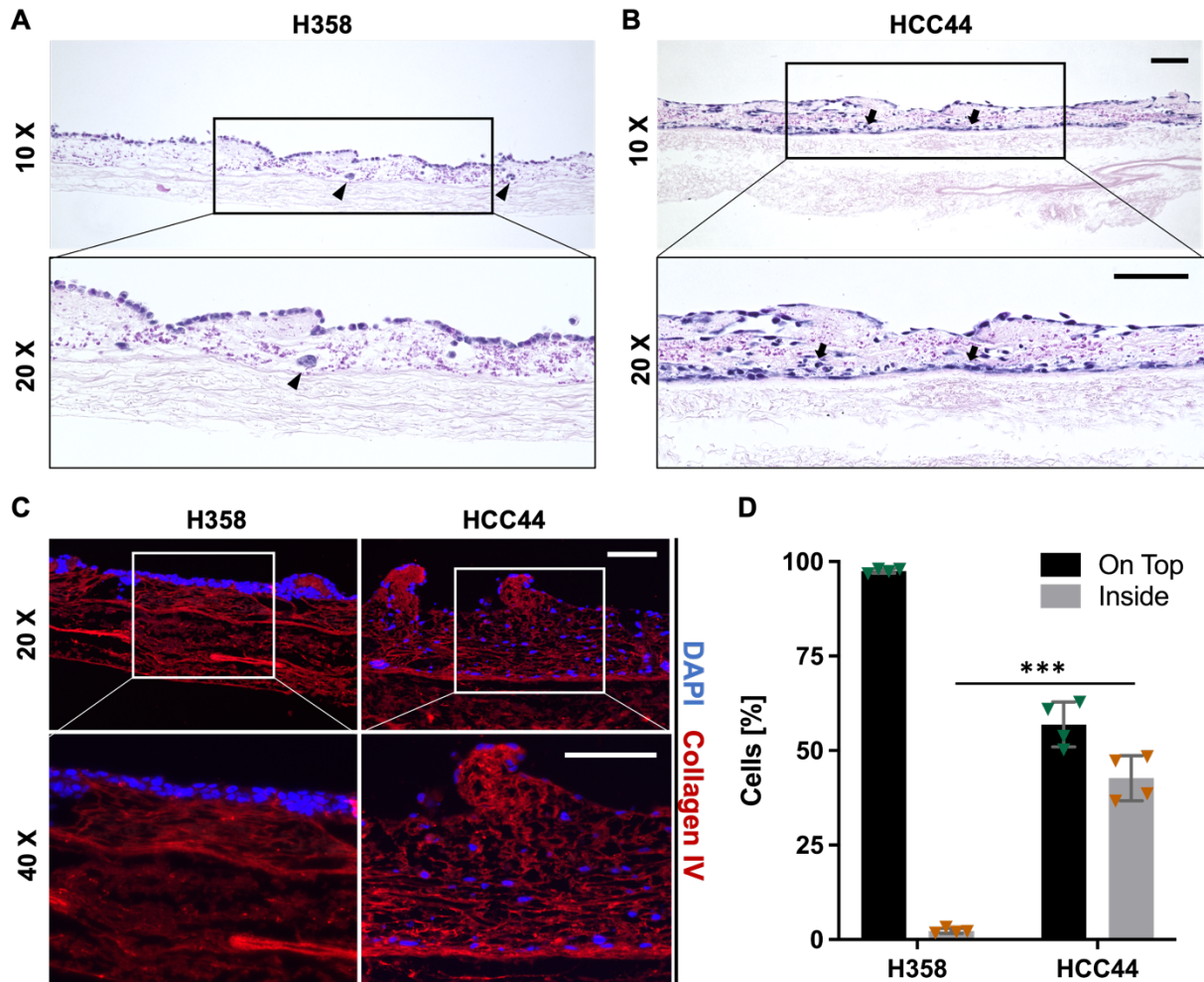
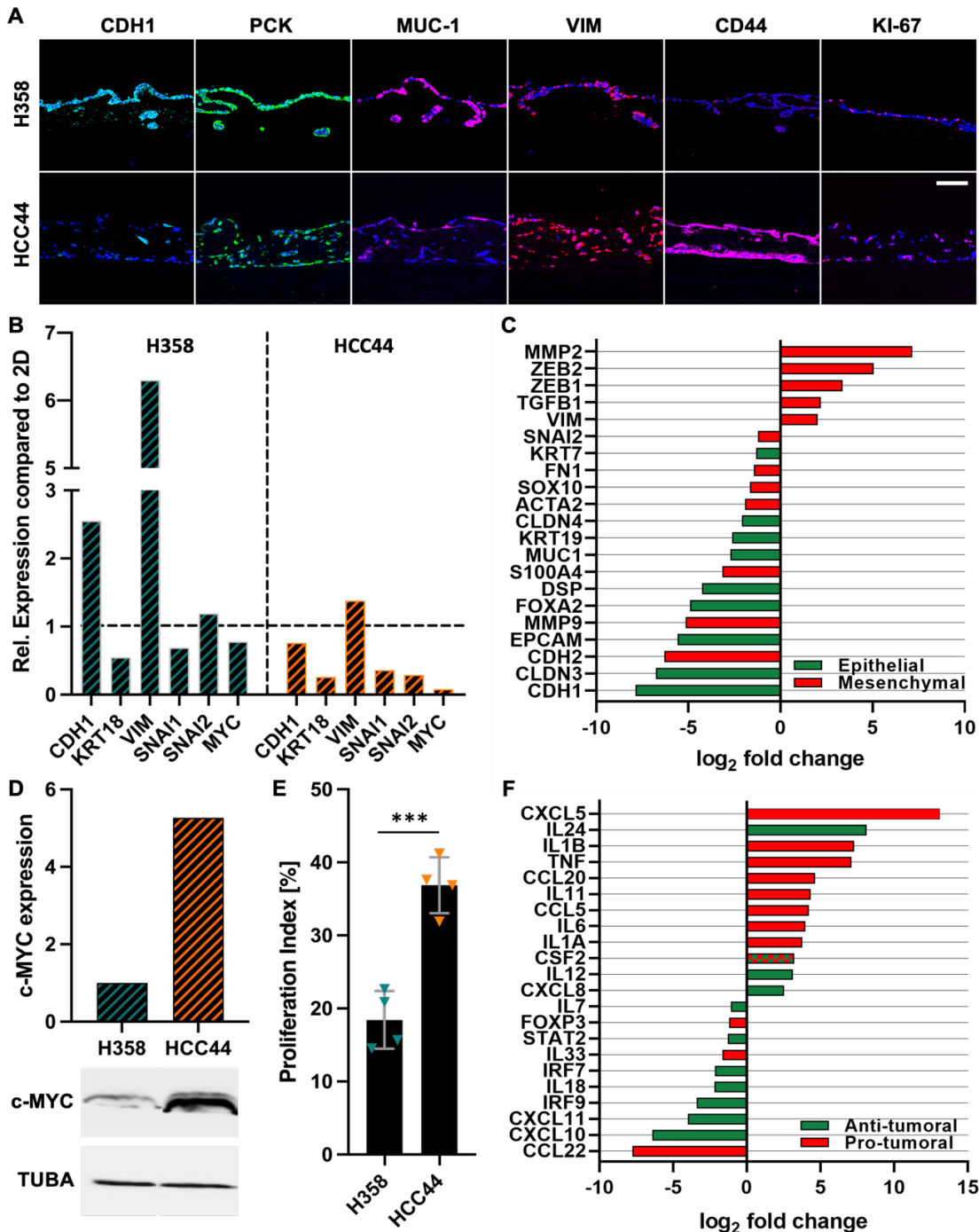


**Figure 3 H&E and collagen IV staining of H358 and HCC44 3D tumor models**

H&E staining of SISmuc tumor models after 14 days in static culture seeded with (A) H358 or (B) HCC44 cells. Black arrowheads indicate cells in the crypts, black arrows exemplary point at invasive cells. n=3. (C) Collagen IV (red) staining of the SISmuc with DAPI counterstaining (blue) of H358 and HCC44 tumor models. n=4. (D) Quantitative evaluation of H358 and HCC44 cells with invasive growth (“Inside”) or on top of the matrix based on the collagen IV staining. n=4. Significance was determined with unpaired t-tests: \*\*\*:  $p \leq 0.001$ . Scale bars A-C = 100  $\mu\text{m}$ . Adapted figure was published in Peindl *et al.* [128].

Although, EMT progressed in both models compared to 2D cultures, HCC44 models were still defined as more mesenchymal compared to H358 models, indicated by RNA sequencing of both models. Among differential expressed genes (DEGs) comparing H358 and HCC44 tumor models, multiple epithelial and mesenchymal markers were detected. Here, neither of the cells

could be clearly defined as completely epithelial or mesenchymal, respectively. Important mesenchymal markers including the central EMT transcription factors *ZEB1* and *ZEB2* as well as *TGFB1* and *VIM* were significantly higher expressed by HCC44 cells. At the same time, epithelial markers tended to show higher expression in H358 cells like *CDH1*, *CLDN3*, *EPCAM* and *FOXA2* among others. Still, also single mesenchymal markers including *CDH2* and *MMP2* were higher expressed by H358 cells in 3D compared to HCC44 cells (Figure 4 C). In total, the data hold evidence that both cell lines in 3D showed a partial EMT, while the phenotype is more progressed in HCC44 cells.



Regarding the expression of *c-MYC* in the SISmuc tumor models, RT-qPCR indicated lower expression compared to 2D cultures in both cell lines (Figure 4 B). Still, Western-Blot revealed

that HCC44 cells harboring the *c-MYC* amplification exhibited a 5.3-fold higher expression of the transcription factor compared to H358 cells in the models on protein level (Figure 4 D). Thereby, HCC44 cells on the SISmuc represent a suitable *in vitro* model for further studying the described cooperative effect of KRAS and MYC *in vivo* in NSCLC.

Additionally, HCC44 cells also showed a significantly higher proliferation than H358 cells. For both cell lines in 3D the artificial high proliferation indices of more than 90 % in 2D cultures were clearly reduced. While HCC44 cells were KI-67-positive in  $36.9 \pm 3.1$  %, the proliferation index in H358 cells in 3D was significantly lower with  $18.4 \pm 3.4$  % after 14 days in culture (Figure 4 E).

The KRAS<sup>G12C</sup>-biomarker models also exhibited decisive differences in their immunophenotype. Multiple chemokines described in the literature as pro-tumoral supporting immune evasion and tumor-associated inflammation were detected to be higher expressed by HCC44 cells. DEGs detected by RNAseq included important mediators like *IL24*, *IL1B*, *TNF* and *CCL20* among other candidates. Vice versa specific anti-tumoral chemokines supporting anti-tumor immunity including *CXCL10*, *CXCL11* and *IL18* or involved in interferon signaling (*IRF7*, *IRF9*, *STAT2*) showed a higher expression in H358 cells (Figure 4 F).

---

#### Figure 4 Characterization of H358 and HCC44 SISmuc tumor models

H358 and HCC44 were cultured on the SISmuc for 14 days. **(A)** Immunofluorescence staining of CDH1 (lightblue), PCK (green), MUC-1 (purple), VIM (red), CD44 (purple) and KI-67 (red) with DAPI counterstaining (blue) in H358 and HCC44 3D models after 14 days in culture. Scale bar = 100  $\mu$ m;  $n \geq 2$ . **(B)** RT-qPCR of EMT-related genes and *c-MYC* of H358 and HCC44 tumor models. Relative gene expression was evaluated compared to the corresponding cell line in 2D cultures.  $n=1$ . **(C)** EMT-related DEGs of RNAseq comparing HCC44 versus H358 3D models. Positive  $\log_2$  fold changes indicate higher expression in HCC44 tumor models, while negative  $\log_2$  fold changes show genes with higher expression in H358 tumor models. Differences in expression were considered significant with an adjusted p-value < 0.05.  $n = 4$ . **(D)** Western Blot of *c-MYC* and TUBA as housekeeping protein of H358 and HCC44 tumor models with quantification.  $n = 1$ . **(E)** Proliferation indices of H358 and HCC44 cells on the SISmuc after 14 days in culture. Significance was determined with unpaired t-tests; \*\*\*:  $p \leq 0.001$ ;  $n = 4$ . **(F)** Immune system related DEGs validated by RNAseq comparing HCC44 versus H358 3D models. Positive  $\log_2$  fold changes indicate higher expression in HCC44 tumor models, while negative  $\log_2$  fold changes show genes with higher expression in H358 tumor models. Differences in expression were considered significant with an adjusted p-value < 0.05.  $n = 4$ . Adapted figure was published in Peindl *et al.* [128].

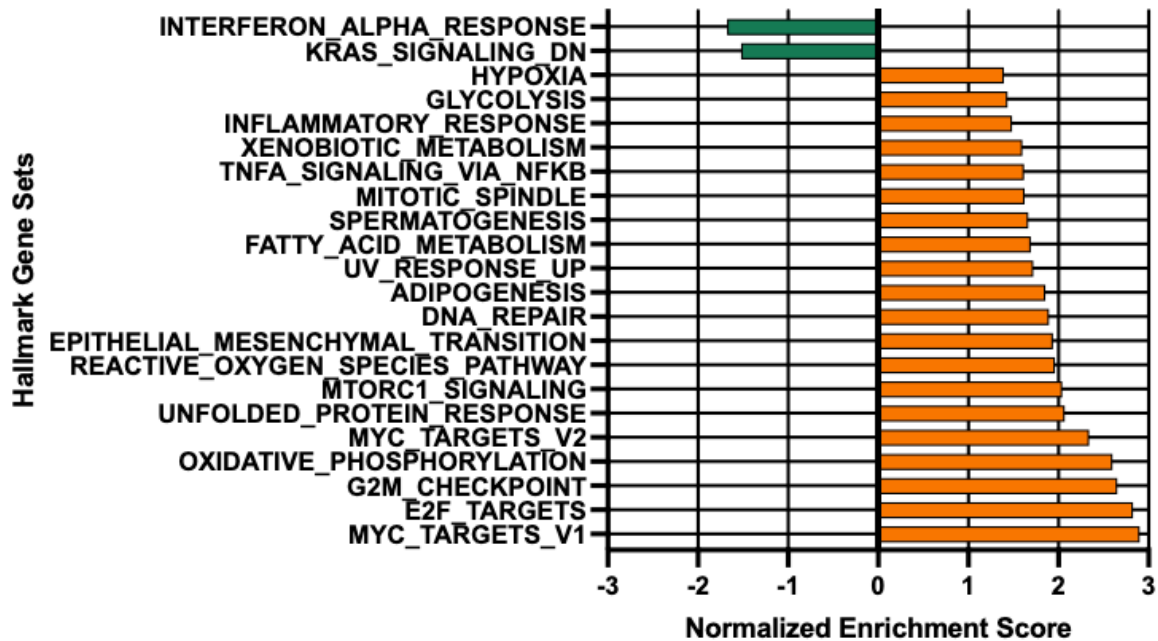


**Figure 5 GSEA hallmark analysis of H358 versus HCC44 3D tumor models**

H358 and HCC44 tumor models were cultured for 14 days. Negative Normalized Enrichment Scores shows enriched gene sets in H358 tumor models. Gene sets with positive Normalized Enrichment Scores are enriched in HCC44 tumor models. Enrichments were considered significant with an adjusted p-value < 0.05; n=4.

Finally, the gene set enrichment analysis (GSEA) comparing the H358 to HCC44 tumor models further underlined the described observations on the one hand. A comparatively more advanced EMT in HCC44 cells is indicated (“EPITHELIAL\_MESENCHYMAL\_TRANSITION”). The higher *c-MYC* expression in HCC44 cells resulted in upregulation of corresponding target genes (“MYC\_TARGETS\_V1, MYC\_TARGETS\_V2”). At the same time the high proliferation state of HCC44 cells was represented by enriched gene sets connected to cell cycle progression (“E2F\_TARGETS, G2M\_CHECKPOINT, MITOTIC\_SPINDLE”). In addition, a more inflammatory and immune evasive phenotype of HCC44 cells is pointed out via enrichment of related gene sets (“TNFA\_SIGNALING\_VIA\_NFKB, INFLAMMATORY\_RESPONSE”). Vice versa, interferon alpha response was increased in H358 tumor models (“INTERFERON\_ALPHA\_RESPONSE”). On the other hand, also significant differences in the metabolism of the two different KRAS<sup>G12C</sup>-mutated cell lines were indicated, pointing towards enhanced oxidative phosphorylation and adipogenesis in HCC44 cells (“OXIDATIVE\_PHOSPHORYLATION, ADIPOGENESIS”). Stimulation of angiogenesis was pointed out by the enrichment of gene sets upregulated in hypoxic conditions (“HYPOXIA, REACTIVE\_OXYGEN\_SPECIES\_PATHWAY”). Last but not least, the GSEA also held evidence that KRAS-signaling itself plays a more central role in H358 cells. Target genes

downregulated via KRAS-signaling ("KRAS\_SIGNALING\_DN") were lower expressed by H358 cells (Figure 5).

In summary, the characterization of these two KRAS<sup>G12C</sup>-biomarker *in vitro* models demonstrated decisive differences between the cell lines H358 and HCC44 in 3D concerning invasion, EMT, *c-MYC* expression, proliferation, anti-tumor immunity, metabolism, and angiogenesis. Thereby, HCC44 cells represented a more advanced and aggressive phenotype compared to H358 models throughout the evaluated aspects.

### 3.1.3 Resistance towards KRAS<sup>G12C</sup>-inhibition in HCC44 3D tumor models

After characterization and definition of differences in the phenotypes between the two KRAS<sup>G12C</sup>-biomarker SISmuc models, H358 and HCC44 tumor cells on the SISmuc were tested for their sensitivity towards the covalent and allele-specific KRAS<sup>G12C</sup>-inhibitor ARS-1620.

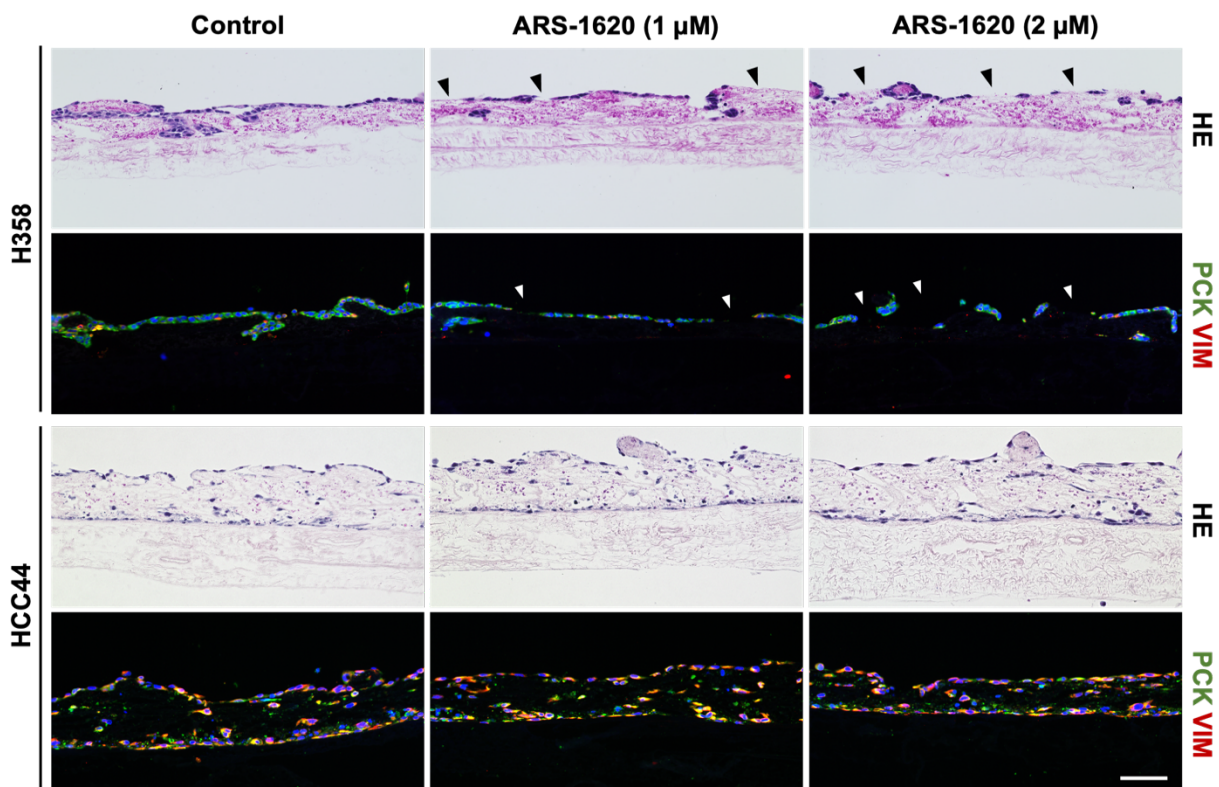


**Figure 6 Tissue architecture of H358 and HCC44 tumor models after ARS-1620 treatment** H&E and PCK (green) and VIM (red) immunofluorescence staining of KRAS<sup>G12C</sup>-biomarker models after treatment with 1 or 2  $\mu\text{M}$  ARS-1620 for 72 hours compared to the DMSO control. Black and white arrowheads indicate gaps in the cell layer of H358 models after treatment. Scale bar = 100  $\mu\text{m}$ . n = 2.

H&E staining of H358 tumor models after treatment with either 1 or 2  $\mu\text{M}$  ARS-1620 for 72 hours showed larger cell-free gaps in the cell layer on the SISmuc, which was intact in the untreated control. The tissue architecture of HCC44 models in contrast was not altered after treatment in comparison to the control. Furthermore, the EMT-phenotype of both cell lines did



not show considerable changes after applying the small molecule KRAS-inhibitor, demonstrated by immunofluorescence staining of the epithelial and mesenchymal marker PCK and VIM, respectively (Figure 6).

Treating the models with increasing concentrations of ARS-1620 of up to 5  $\mu\text{M}$  resulted in a dose-dependent reduction of cell viability in the MTT-assay to less than 50 % in H358 cells in 3D (Figure 7 A), The viability of HCC44 3D models remained at around 100 % viability of the control even at the highest concentration (Figure 7 B). Regarding the proliferation of the tumor cells on the biological scaffold after ARS-1620 treatment, a significant reduction from  $18.4 \pm 3.4$  % in the control to  $4.8 \pm 0.8$  % of the proliferation index was observed in H358 but not in HCC44 cells, still expressing in KI67 in  $34.5 \pm 2.5$  % of all cells no matter the KRAS-inhibitor (Figure 7 C). The relative cell numbers compared to the control in both models were however significantly reduced after treatment with 1  $\mu\text{M}$  ARS-1620 in both KRAS<sup>G12C</sup>-biomarker models. Still, the HCC44 cell numbers were lowered by only  $13.2 \pm 3.7$  % while for H358 cells a reduction of  $34.8 \pm 4.8$  % was determined compared to the control (Figure 7 D). In addition, a dose- and time-dependent increase of apoptosis was evaluated in the M30-apoptosis ELISA in H358 tumor cells on the SISmuc. The rate of apoptosis increased up to 10-fold for the highest concentrations of ARS-1620 after 72 hours of treatment. Noteworthy the apoptosis was unaltered compared to the control in the first 24 hours and rapidly increased after 48 hours of treatment in a dose dependent-manner (Figure 7 E). In parallel, only minor increases in apoptosis of HCC44 cells were detected after 24 hours treatment, while after 72 hours of ARS-1620 treatment no considerable changes in apoptosis compared to the untreated control were observed (Figure 7 F).

On protein level, the phosphorylation of the two major KRAS downstream signaling mediators AKT and ERK as well as of MET and AMPK was evaluated. Western blots revealed that while ARS-1620 reduced the phosphorylation of AKT, phosphorylated ERK and MET were completely abolished in H358 cells after treatment. Phosphorylation of these proteins remained unaltered in HCC44 cells with or without ARS-1620 treatment (Figure 8 A, B). AMPK was only weakly or not expressed by both KRAS<sup>G12C</sup>-mutated cell lines in the 3D model (Figure 8 A). The expression of *c-MYC* was additionally only reduced in H358 cells after ARS-1620 treatment but not in HCC44 cells (Figure 8 A, C).

In summary, the data hold strong evidence that HCC44 cells also display resistance and H358 cells sensitivity towards ARS-1620 on the SISmuc tumor models as also observed in 2D cultures. These findings were further underlined by RNAseq of the models after ARS-1620 treatment. Here, the Principal Component Analysis (PCA) pointed out major changes in gene expression only in H358 cells after treatment with ARS-1620 compared to the control, while HCC44 cells untreated versus treated showed a major overlap and thereby pointed towards high similarity (Figure 9 A).

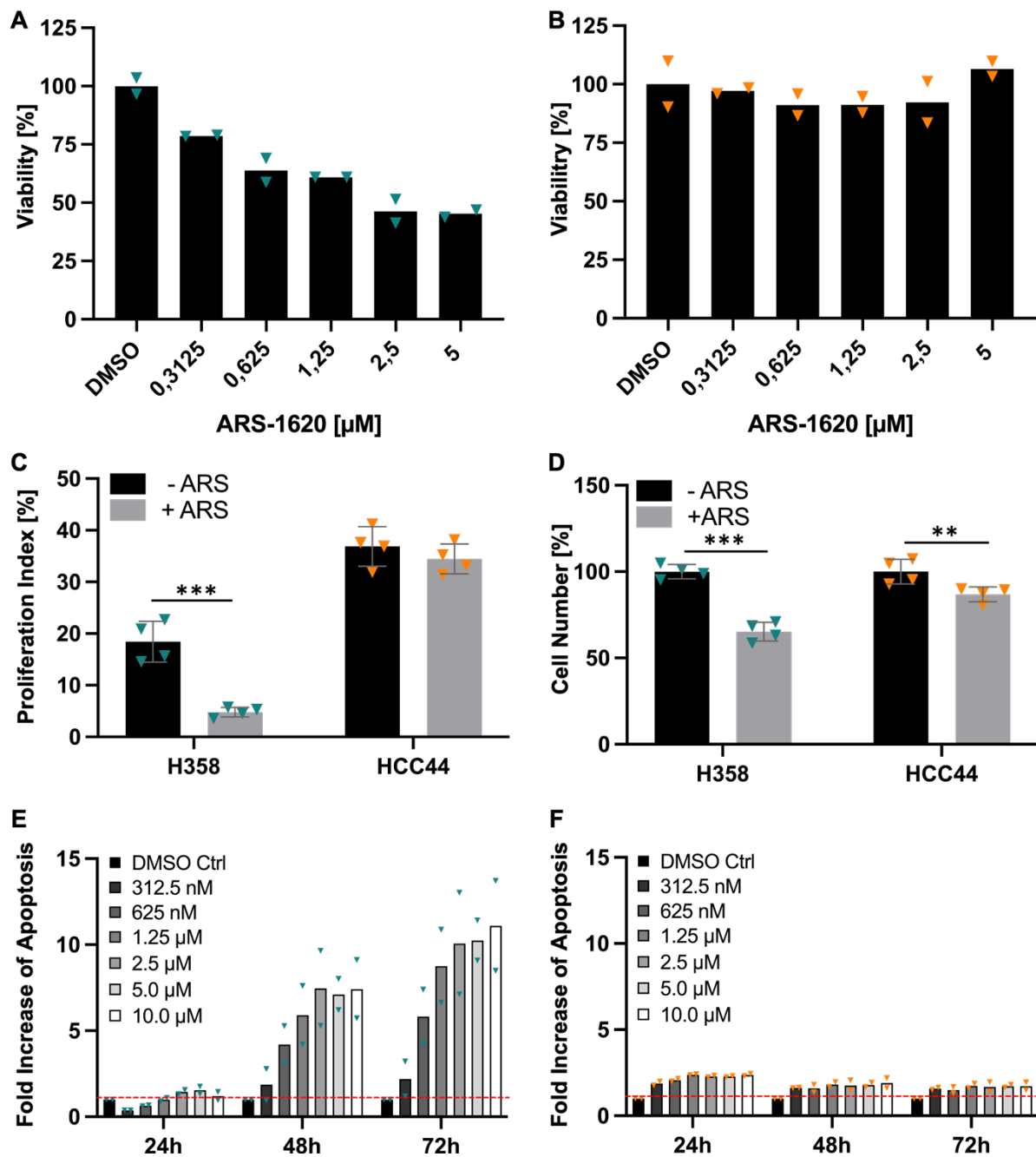


**Figure 7 Quantitative ARS-1620 drug testing of H358 and HCC44 tumor models**

H358 and HCC44 tumor models were cultured for 14 days and treated with ARS-1620 in the last 72 hours of culture. **(A)** Viability evaluated with MTT-assays after treatment with increasing concentrations of ARS-1620 in H358 and **(B)** HCC44 cells on the SISmuc. **(C)** Proliferation indices and **(D)** relative cell numbers determined by KI-67 and DAPI staining of H358 and HCC44 cells comparing DMSO control to treatment with 1  $\mu\text{M}$  ARS-1620. Significance was determined with unpaired t-tests; \*\*:  $p \leq 0.01$ , \*\*\*:  $p \leq 0.001$ ;  $n = 4$ . **(E)** M30-ELISAs showing the fold increase of apoptosis over the DMSO control after 24, 48 and 72 hours of treatment with indicated concentrations of ARS-1620 in H358 or **(F)** HCC44 tumor models.  $n = 2$ . Adapted figure was published in Peindl *et al.* [128].

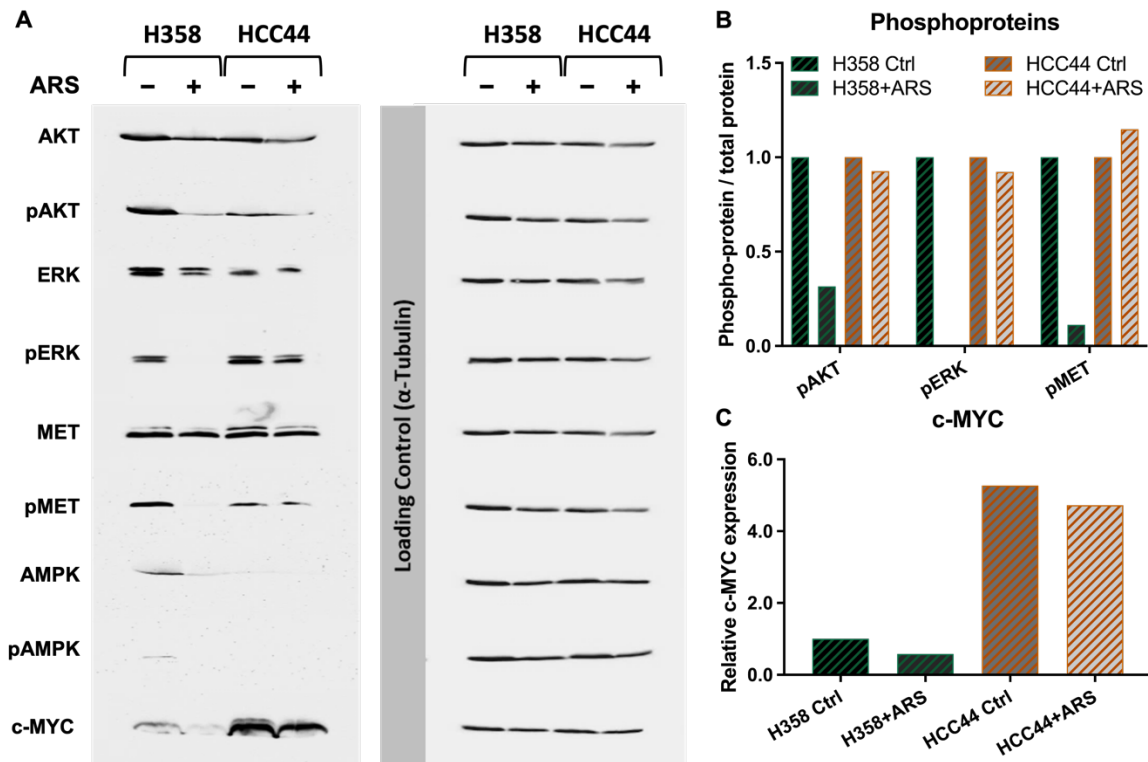


**Figure 8 Western blot of H358 and HCC44 tumor models after ARS-1620 treatment**

**(A)** Proteins were isolated of H358 and HCC44 tumor models after treatment with 1  $\mu$ M ARS-1620 for 72 hours and the corresponding untreated controls. Alpha-tubulin was used as a housekeeping protein.  $n = 1$ . **(B)** Quantification of phosphoproteins and **(C)** c-MYC after normalization to the loading control for H358 and HCC44 tumor models with or without ARS-1620 treatment.  $n = 1$ . Adapted figure was published in Peindl *et al.* [128].

Accordingly, 995 DEGs were detected in H358 tumor models after the treatment, compared to 79 in HCC44 tumor models. Among the most profoundly downregulated genes after ARS-1620 treatment in H358 cells the negative feedback regulator of the MAPK signaling *DUSP6*, the EGFR-ligand *TGFA* and lysyl oxidase (*LOX*) were detected. The transmembrane serine protease *TMPRSS2*, the membrane anchoring protein *EFR3B* and *PCP4L1* were among the most significantly differentially expressed genes expressed higher after treatment (Figure 9 B). In HCC44 cells *MMP1*, *EGR1* and *CD177* showed a highly significant reduced expression after treatment with ARS-1620 besides different pseudogenes, while *EIF3CL* was the only higher expressed gene among the 10 most significantly regulated genes (Figure 9 C).

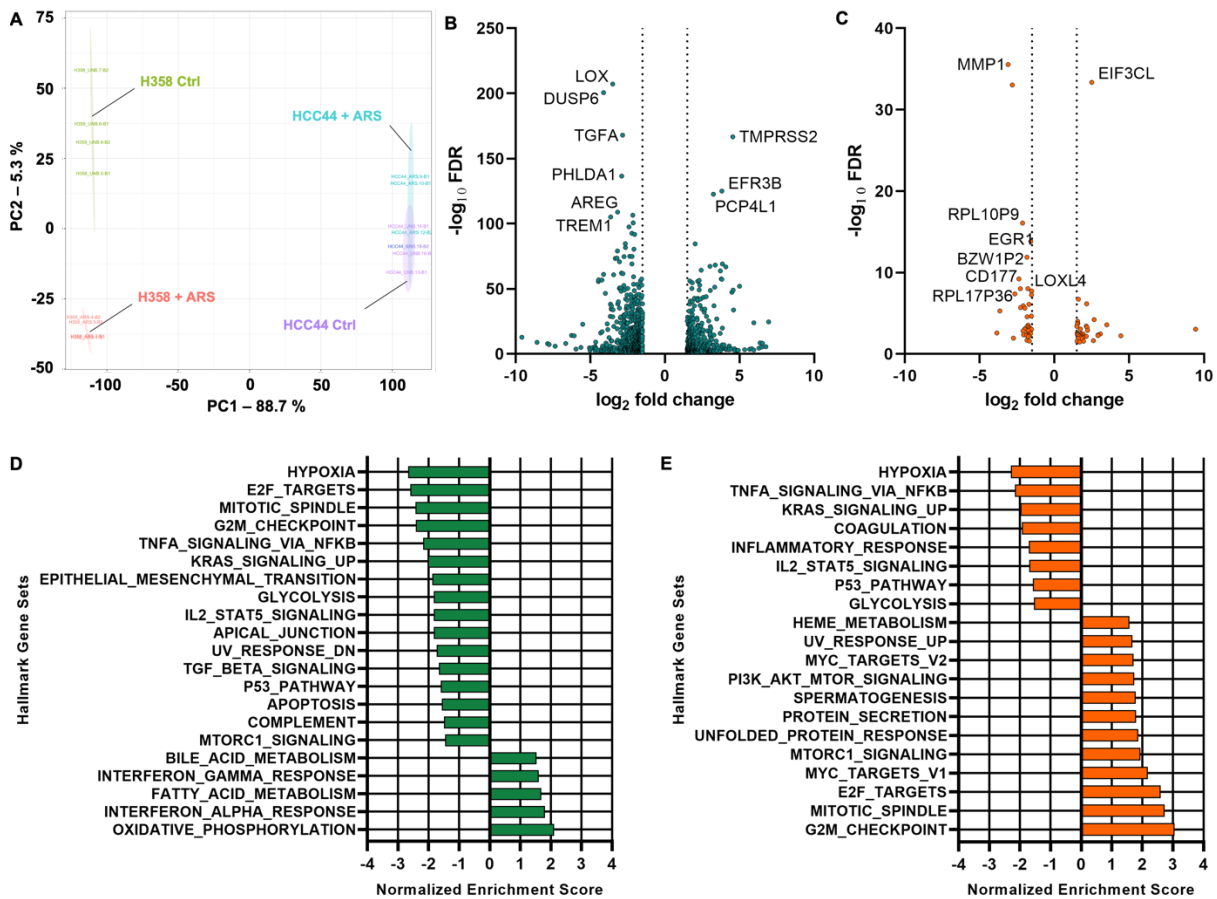


**Figure 9 RNAseq of H358 and HCC44 3D tumor models after ARS-1620 treatment**

H358 and HCC44 cells were cultured on the SIS muc for 14 days and treated with 1  $\mu$ M ARS-1620 for the last 72 hours in culture. **(A)** PC analysis of H358 and HCC44 RNAseq samples.  $n = 4$ . Volcano plots showing the DEGs of **(B)** H358 cells or **(C)** HCC44 cells after treatment with ARS-1620. Negative  $\log_2$  fold changes indicate lower expression after treatment and vice versa. Most significantly changed DEGs are labeled. Genes with a  $\log_2$  fold change of more than 1.5 and an adjusted  $p$ -value  $< 0.05$  were considered as significantly differentially expressed.  $n = 4$ . **(D, E)** GSEA hallmark analysis of H358 and HCC44 tumor models after ARS-1620 treatment compared to the untreated control. Negative NESs are enriched in the untreated control, while positive NESs account for hallmarks enriched after treatment. Enrichments were considered significant with an adjusted  $p$ -value  $< 0.05$ ;  $n=4$ .

GSEA of H358 tumor models also pointed towards a profound change of the phenotype after ARS-1620 treatment. As indicated by the lower expression of KI67 in the immunofluorescence staining, the reduced proliferation after ARS-1620 treatment was also demonstrated by significantly lower NESs of proliferation related hallmarks (“E2F\_TARGETS, G2M\_CHECKPOINT, MITOTIC\_SPINDLE”). Vice versa, these three hallmarks were enriched in HCC44 cells after treatment. Noteworthy, the GSEA also held evidence that KRAS<sup>G12C</sup> was substantially inhibited by ARS-1620 in both cell lines as gene sets upregulated by KRAS signaling were significantly lower expressed (“KRAS\_SIGNALING\_UP”).

The hallmark gene set for EMT was lower in both 3D tumor models after ARS-1620 treatment, although only reaching statistical significance in H358 models. Furthermore, hallmark gene sets involved in inflammation (“TNFA\_SIGNALING\_VIA\_NFKB, INFLAMMATORY RESPONSE, COAGULATION, COMPLEMENT”) as well as in hypoxia were lower expressed in both models after treatment. In H358 tumor models interferon alpha and gamma responses were increased and a shift in metabolism from glycolysis to oxidative phosphorylation and fatty acid metabolism was indicated. Finally, HCC44 models showed higher expression of MYC target genes (“MYC\_TARGETS\_V1, MYC\_TARGETS\_V2”) after ARS-1620 treatment (Figure 9 D, E).

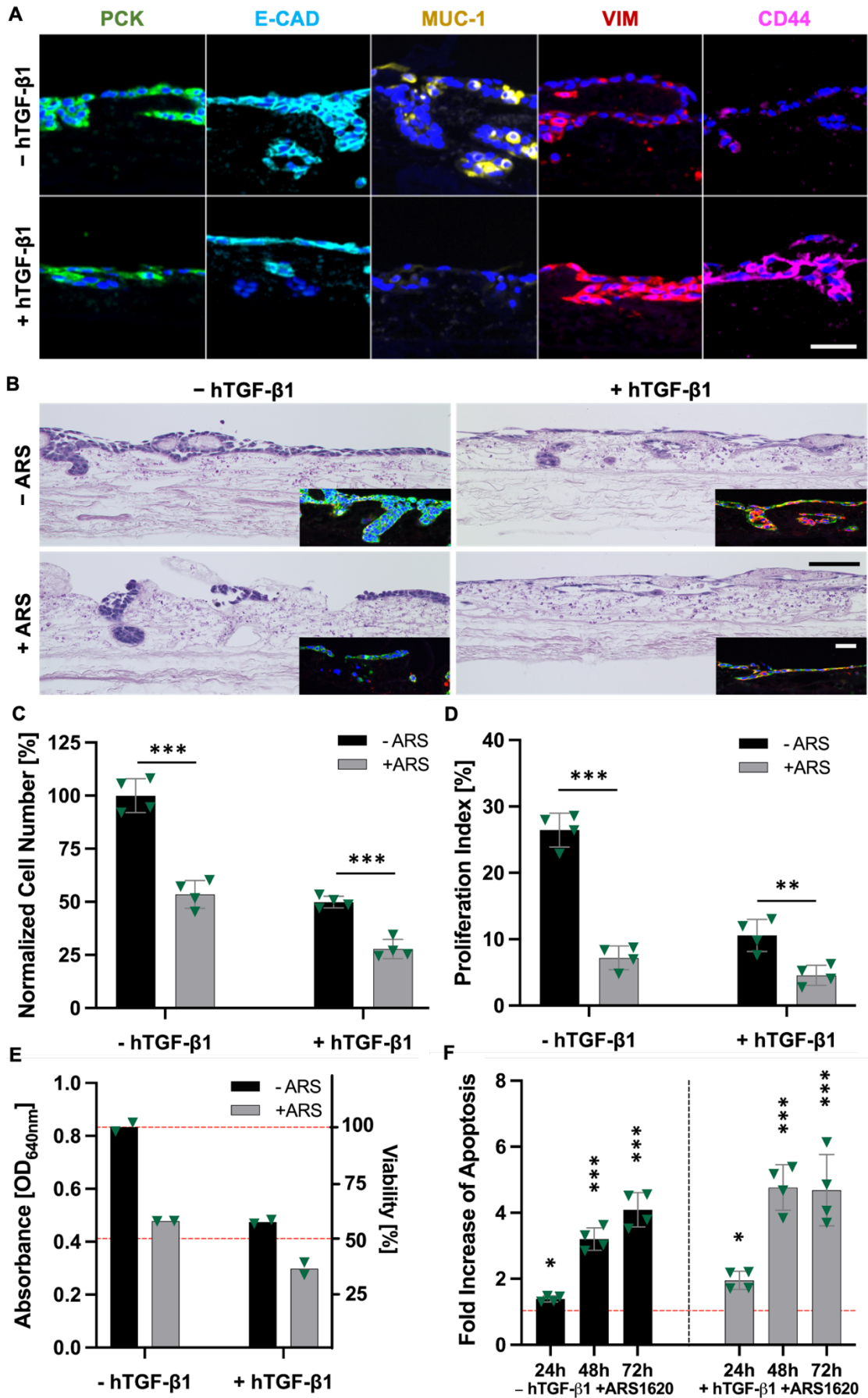
To put it in a nutshell, drug testing of ARS-1620 in both models clearly pointed towards resistance regarding proliferation, apoptosis, signaling and viability in HCC44 tumor models. Vice versa H358 3D models displayed sensitivity towards the treatment and hence the two KRAS<sup>G12C</sup>-biomarker models with decisive differences in their phenotype could serve as surrogate models for the following investigation of resistance mechanisms and testing of combination therapies with KRAS<sup>G12C</sup>-inhibitors.

### 3.1.4 TGF- $\beta$ induced EMT is insufficient to mediate drug resistance

As the ARS-1620 resistant HCC44 tumor models showed a progressed EMT phenotype in comparison to H358 tumor models the question arose whether EMT is a possible mediator of primary resistance towards KRAS<sup>G12C</sup>-inhibition as described in the literature. To address this question, EMT was induced in H358 cells via TGF- $\beta$  stimulation prior to ARS-1620 treatment. Addition of 2 ng/mL TGF- $\beta$  changed the expression of epithelial, mesenchymal and stem cell markers in H358 cells on the SISmuc. Immunofluorescence staining demonstrated that a proportion of H358 cells lost the expression of CDH1 after TGF- $\beta$  treatment. Furthermore, TGF- $\beta$  treated H358 became negative for the epithelial marker MUC-1, which was solidly expressed in naïve H358 cells. The mesenchymal marker VIM and the stem cell marker CD44 got higher expressed compared to the unstimulated control. At the same time, the epithelial height of the cell layer formed by H358 cells appeared flattened in comparison, suggesting reduced apical-basal cell polarity (Figure 10 A, B) and a minor but nevertheless significant increase of invasive cells from  $0.6 \pm 0.2$  % to  $1.3 \pm 0.2$  % was determined after TGF- $\beta$  treatment (Figure S1).

H&E as well as immunofluorescence staining of PCK and VIM suggested reduced cell numbers after ARS-1620 treatment in both specimen no matter the TGF- $\beta$  treatment. However, TGF- $\beta$  alone resulted in lower cell numbers compared to the untreated control (Figure 10 B). These findings were confirmed via the quantification of cells on the corresponding models, where the cell numbers were significantly decreased after ARS-1620 treatment with or without prior TGF- $\beta$  addition. ARS-1620 or TGF- $\beta$  treatment alone reduced the cell numbers to

53.3 ± 4.2 % or 49.9 ± 2.4 of the control, respectively. The combined treatment with both ARS-1620 and TGF-β further reduced the cell numbers to 27.8 ± 3.9 % (Figure 10 C).



In accordance, the proliferation index of TGF- $\beta$  stimulated H358 cells, reduced to  $10.6 \pm 2.1$  % compared to  $26.4 \pm 2.2$  % in the control, further decreased to only  $4.6 \pm 1.3$  % after additional ARS-1620 treatment (Figure 10 D). The MTT-assay also demonstrated reduced viability in H358 tumor models after ARS-1620 treatment compared to the respective control, with or without TGF- $\beta$  stimulation (Figure 10 E). Finally, the M30 ELISA confirmed a comparable increase of apoptosis after ARS-1620 treatment in both models no matter the addition of TGF- $\beta$  (Figure 10 F). Thereby, the results suggest that TGF- $\beta$  induced EMT is not sufficient to mediate a primary resistance in H358 cells towards KRAS<sup>G12C</sup>-inhibition.

Vice versa it was also investigated whether the inhibition of the TGF- $\beta$  receptor I (T $\beta$ RI) could possibly revert the EMT phenotype of HCC44 cells and thereby change the sensitivity towards ARS-1620.

Treating HCC44 cells with 5  $\mu$ M of the T $\beta$ RI-inhibitor galunisertib for 7, 11 or 14 days in 3D models, the latter one with additional 48 hours pre-treatment in 2D culture, did not change the expression of the EMT-markers E-Cadherin, PCK and VIM compared to the untreated control (Figure 11 A). In 2D cultures, galunisertib alone or in a constant combination with 1  $\mu$ M ARS-1620 failed reduce the viability of HCC44 cells even at high concentrations (Figure 11 B). Also, in HCC44 3D tumor models, the combined treatment with galunisertib and ARS-1620 did not result in significant differences compared to the monotherapy with the KRAS<sup>G12C</sup>-inhibitor in the MTT-assay (Figure 11 C). Hence, the EMT phenotype in HCC44 cells appeared to be independent of the T $\beta$ RI and galunisertib failed to sensitize HCC44 cells for KRAS<sup>G12C</sup>-inhibition.

---

### Figure 10 ARS-1620 sensitivity of TGF- $\beta$ stimulated H358 tumor models

(A) Immunofluorescence staining of PCK (green), E-CAD (lightblue), MUC-1 (yellow), VIM (red) and CD44 (purple) with DAPI counterstaining (blue) of H358 cells on the SISmuc with or without stimulation with 2 ng/mL h-TGF- $\beta$ 1 for 11 days in culture. n = 2. (B) H&E and PCK (green), VIM (red) immunofluorescence staining of H358 tumor models after treatment with 1  $\mu$ M ARS-1620 compared to the untreated control with or without h-TGF- $\beta$ 1 stimulation.; n=2. (C) Normalized cell numbers and (D) proliferation indices of H358 cells on the SISmuc with or without h-TGF- $\beta$ 1 and ARS-1620 treatment, respectively. n = 4. (E) Quantification of MTT assay of H358 tumor models after treatment with 1  $\mu$ M ARS-1620 and stimulation with h-TGF- $\beta$ 1 or the combination of both compared to the untreated control. n = 2. (F) Increase of apoptosis over the control validated with M30-ELISAs after ARS-1620 treatment with 1  $\mu$ M in H358 cells on the SISmuc with or without prior h-TGF- $\beta$ 1 stimulation. n = 4. Scale bars = 100  $\mu$ m. Significance was determined with unpaired t-tests; \*: p < 0.05, \*\*: p  $\leq$  0.01, \*\*\*: p  $\leq$  0.001. Adapted figure was published in Peindl *et al.* [128].

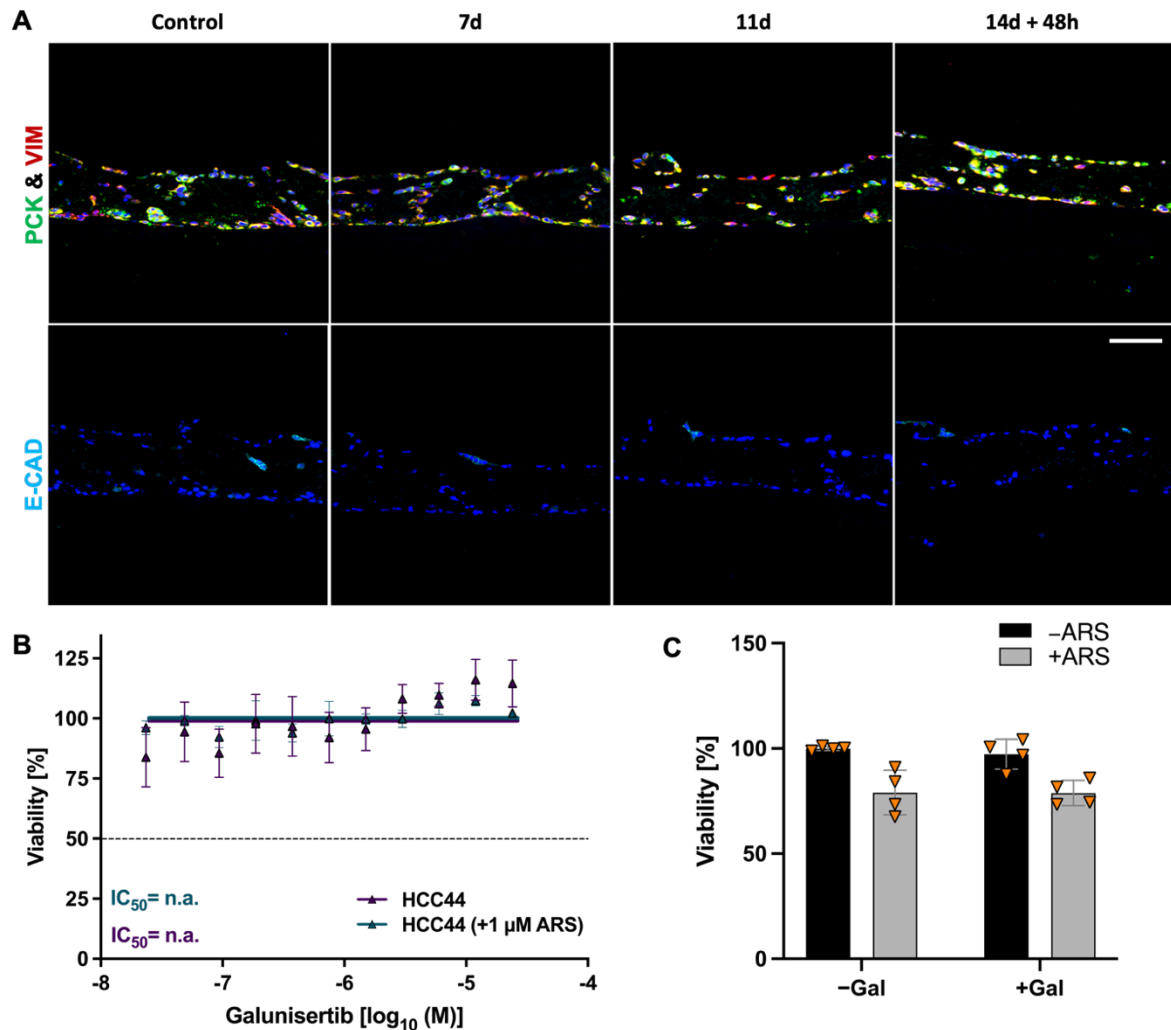


**Figure 11 Inhibition of the T $\beta$ RI in HCC44 cells with galunisertib**

(A) Immunofluorescence staining of PCK (green), VIM (red) and E-CAD (lightblue) with DAPI counterstaining (blue) of HCC44 tumor models after treatment with 5  $\mu$ M galunisertib for 7, 11 and 14 days. For the 14 days treatment, the cells were additionally pre-treated with galunisertib for 48 hours before seeding the cells on the SISmuc. Scale bar = 100  $\mu$ m. n = 2. (B) CellTiter-Glo® viability assay of HCC44 cells in 2D treated for 72 hours with increasing concentrations of Galunisertib alone or in a constant combination with 1  $\mu$ M ARS-1620. n=1 with three technical replicates. (C) MTT-assays of HCC44 3D tumor models after treatment with 5  $\mu$ M galunisertib or 1  $\mu$ M ARS-1620 and the combination of both inhibitors for 72 hours. n = 4.

### 3.1.5 No correlation between KRAS<sup>G12C</sup>-inhibitor sensitivity with EMT, MYC-expression or stemness in PDX-derived cells

For investigating EMT, *c-MYC* expression or stemness as potential predictive biomarkers for the sensitivity towards KRAS<sup>G12C</sup>-inhibition, the two KRAS<sup>G12C</sup>-biomarker models based on HCC44 and H358 cells can only be regarded as a first indicator. Therefore, a panel of four different KRAS<sup>G12C</sup>-mutated NSCLC cell lines derived from PDXs were characterized in both 2D and 3D with a subsequent drug testing of ARS-1620. Under both culture conditions, the four cell lines showed considerable differences in their EMT-phenotype. LXFA 983 exhibited



the most epithelial characteristics among the four specimens, indicated by a solid expression of PCK and E-cadherin as epithelial markers while the cells were negative for mesenchymal VIM as well as the stem cell marker CD44. LXFL1072 cells on the other hand displayed a change in EMT between 2D and 3D culture conditions. In 2D the cells were defined with a progressed EMT phenotype, demonstrated by high VIM and low PCK expression. In 3D, the tumor cells differentiated in a mesenchymal-epithelial transition (MET) into a more epithelial state with PCK and E-Cadherin expression while VIM as well as CD44 was low or negative, respectively. LXFL 1674 and LXFA 2184 cells showed in contrast a highly progressed EMT under both conditions. Both PDX-derived tumor cells co-expressed PCK and VIM while in LXFA 2184 cells PCK expression was weak. At the same time, the two cell lines were negative for E-Cadherin and CD44 positive, respectively (Figure 12 A).

Regarding the expression of *c-MYC* in the four PDX-derived cell lines on the 3D tumor models, also major differences were detected. LXFL 1674 and LXFL1072 displayed the highest expression of the transcription factor. LXFA 983 cells showed the lowest expression of *c-MYC* among the four cell lines and LXFA 2184 cells exhibited intermediate protein levels of *c-MYC* (Figure 12 B, C). Taking the different phenotype regarding EMT, *MYC*-expression and stemness into consideration, the models represented suitable surrogate models to eventually unravel the correlation between these markers and drug sensitivity.

Drug testing of the KRAS<sup>G12C</sup>-inhibitor however pointed against a direct correlation of EMT, stemness or the *MYC*-expression with ARS-1620 sensitivity. Epithelial LXFA 983 cells with the lowest *c-MYC* expression showed the highest IC<sub>50</sub>-value in 2D with 14.6 μM and displayed only a minor decrease of viability to 93.2 ± 1.0 % after treatment with 1 μM ARS-1620 in 3D. LXFL 1674 and LXFA 2184 cells with the progressed EMT phenotype in 2D showed the lowest IC<sub>50</sub>-values towards ARS-1620 with 1.1 μM and 4.4 μM, respectively. In 3D, LXFL 1674 cells with the highest *MYC* expression were the second most sensitive model towards ARS-1620 with a viability of 74.9 ± 3.3 % after treatment and LXFA 2184 cells showed an intermediate response with 86.2 ± 2.4 % viability. Finally, LXFL 1072 cells that underwent MET when cultured on the SISmuc were the most sensitive cell line in 3D with 67.0 ± 6.9 % viability after treatment while they showed a comparatively high IC<sub>50</sub>-value of 7.6 μM in 2D (Figure 12 D, E). In the 3D models based on PDX-derived cell lines, the cells with high *c-MYC* expression concordantly showed the most pronounced reduction of viability after ARS-1620 treatment. All in all, none of the candidate biomarkers was thereby directly predictive across all KRAS<sup>G12C</sup>-mutated cells tested in this study in either 2D or SISmuc tumor models for ARS-1620 sensitivity. Nevertheless, none of the SISmuc models based on the PDX-derived cells demonstrated a strong response towards KRAS<sup>G12C</sup>-inhibition, but rather intermediate sensitivity in the case of LXFL 1072 and LXFL 1674 models.

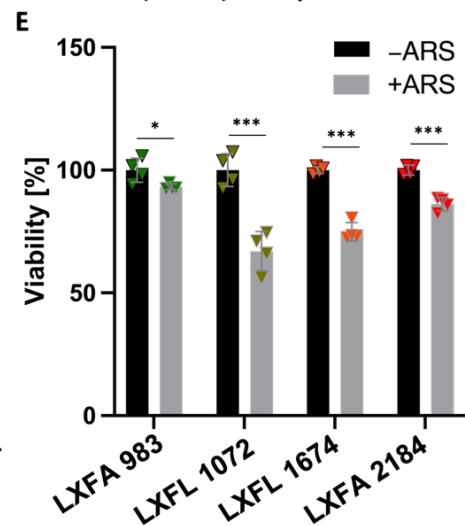
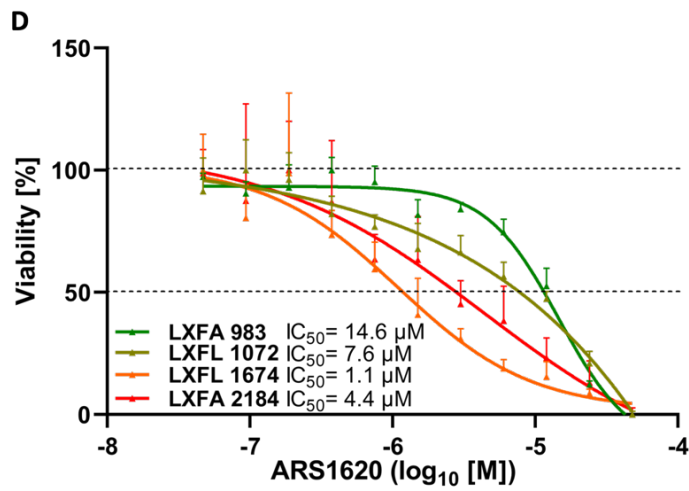
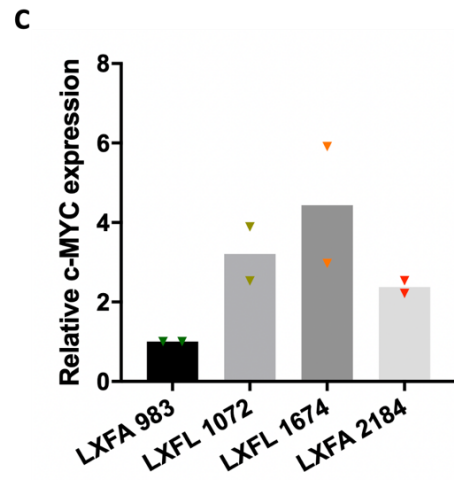
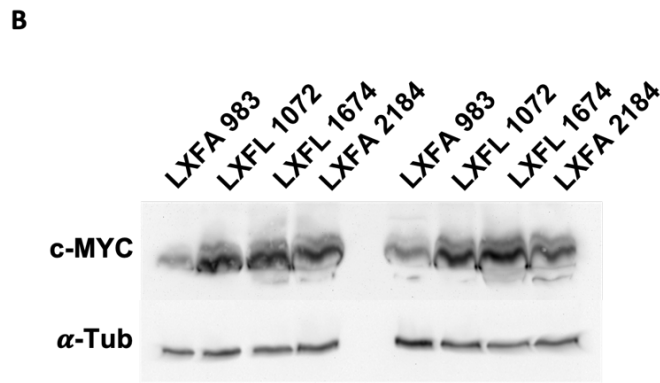
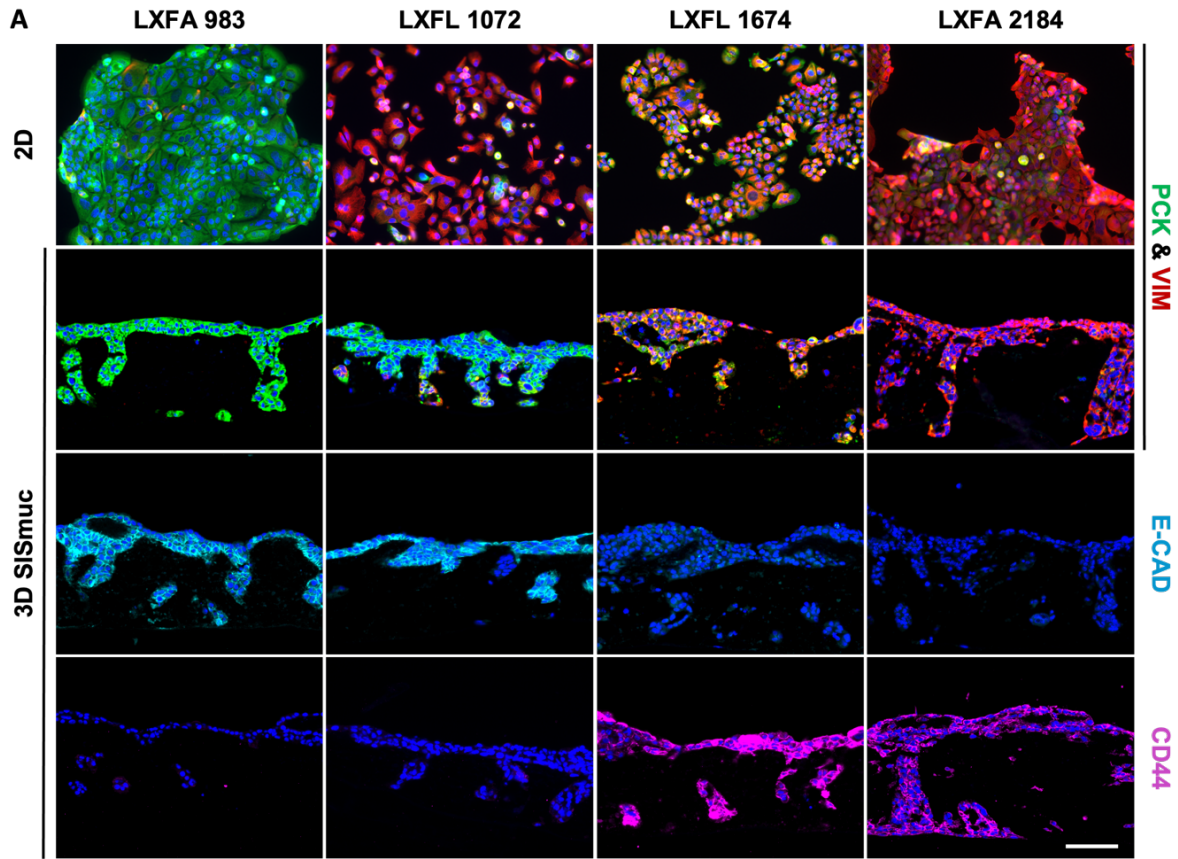


## Figure 12 Characterization and drug testing of KRAS<sup>G12C</sup>-mutated PDX-derived NSCLC cells

(A) Immunofluorescence staining of PCK (green), VIM (red), E-CAD (lightblue) and CD44 (purple) with DAPI-counterstaining (blue) of PDX-derived cell lines in 2D or 3D SIS muc tumor models. Scale bar = 100  $\mu$ m. n = 2. (B) c-MYC western blot of PDX-derived cell lines in 3D after 14 days in culture with alpha-Tubulin as housekeeping protein and (C) quantification after normalization. n = 2. (D) CellTiter-Glo® viability assay of PDX-derived cell lines after treatment with increasing concentrations of ARS-1620 for 72 hours in 2D with calculated IC<sub>50</sub>-values. One representative curve of two independent experiments with three technical replicates is plotted. n = 2. (E) Quantification of MTT-assay of PDX-derived cell lines on the SIS muc after treatment with 1  $\mu$ M ARS-1620 for 72 hours. Significance was determined with unpaired t-tests; \*: p < 0.05, \*\*\*: p  $\leq$  0.001. n = 4. Adapted figure was published in Peindl *et al.* [128].

### 1.1.1 Co-inhibition of AURKA to break resistance in HCC44 3D tumor models

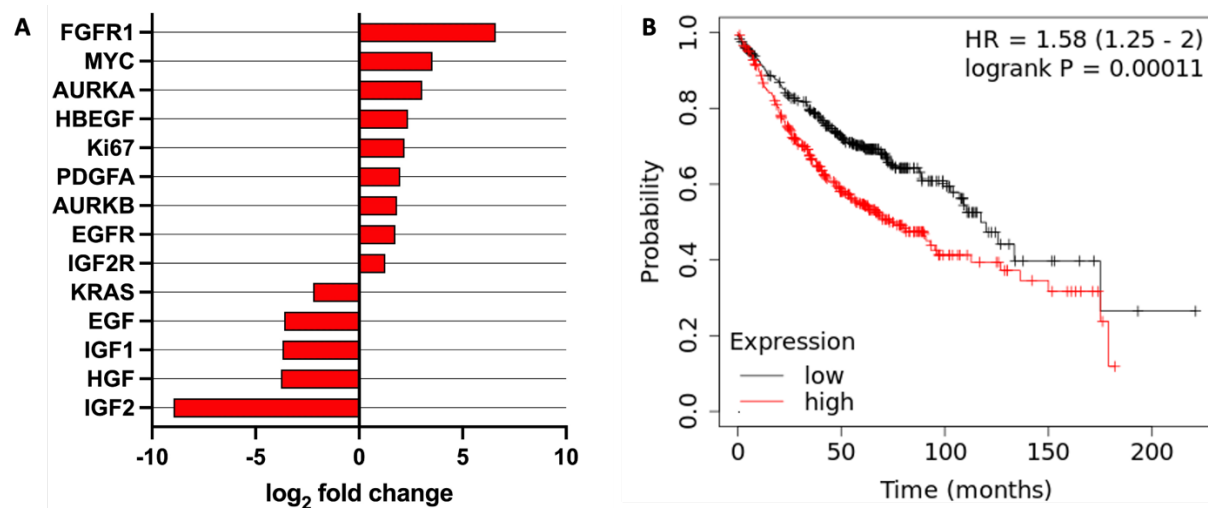


### Figure 13 Candidates for resistance mechanisms in HCC44 tumor models

(A) DEGs related to possible resistance mechanisms in HCC44 tumor models compared to H358 3D models. Positive log<sub>2</sub> fold changes indicate higher expression in HCC44 tumor models, while negative log<sub>2</sub> fold changes show genes with higher expression in H358 tumor models. Differences in expression were considered significant with an adjusted p-value < 0.05. n = 4. (B) Kaplan-Meier plot of overall survival analysis of 719 LUAD patients including all stages and both genders comparing high and low expression of AURKA. Median survival for the low expression and high expression cohort is 117 and 73 months, respectively. Data were generated with the Kaplan-Meier Plotter (kmplot.com [129]).

After characterization and investigation of biomarkers in KRAS<sup>G12C</sup>-biomarker SIS muc tumor models, it was next evaluated whether primary resistance against ARS-1620 can be broken by combinations of targeted therapies. For this HCC44 cells on the SIS muc exhibiting primary resistance towards KRAS<sup>G12C</sup>-inhibition and being deeply characterized were used as a test system. Considering DEGs in HCC44 cells compared to H358 cells on the SIS muc, several

possible targets for co-inhibition together with ARS-1620 were revealed. Different growth factor receptors and growth factors were highly expressed in HCC44 tumor models, including the *FGFR1*, the *EGFR* as well as *HBEGF* and *PDGFA*. Also, the aurora kinases A and B showed higher expression in HCC44 tumor models (Figure 13 A). Hence, different RTKI were tested for their efficacy as either monotherapy or in combination with ARS-1620: Erdafitinib targeting the FGFR 1-4, gefitinib inhibiting the EGFR and the multi-RTKI crizotinib. Also, the SHP2-inhibitor SHP099 was included, as this phosphatase acts as a mediator between RTKs and KRAS signaling. Taking the loss-of-function mutation of *STK11* in HCC44 cells into consideration, the AMPK activator metformin was also tested for anti-cancer effects in those cells. Considering the fact that high expression of *AURKA* has also a negative predictive value in LUAD looking at survival analysis (Figure 11 B), also the AURKA-inhibitor alisertib was included in drug testing.

Selected inhibitors were pre-tested in 2D cultures on HCC44 cells. Here, none of the tested substances could sensitize the cells for ARS-1620. For the FGFR-inhibitor erdafitinib  $IC_{50}$ -values of 6.0  $\mu$ M or 6.6  $\mu$ M were evaluated for the monotherapy and the combination with 1  $\mu$ M ARS-1620, respectively (Figure 14 A). Also, for metformin the  $IC_{50}$ -values were not considerably altered between the monotherapy and the combination in 2D with 902 and 952  $\mu$ M, respectively (Figure 14 B). Low  $IC_{50}$ -values were observed for crizotinib and alisertib in HCC44 cells with 1.0  $\mu$ M and 0.2  $\mu$ M, however also without considerable changes when combined with ARS-1620 (Figure 14 C, D). As the  $IC_{50}$  for alisertib was far in the sub-micromolar range, the cytocompatibility of the small-molecule-inhibitor together with ARS-1620 was checked on primary human lung fibroblasts (hLF). Here, even high concentrations of up to 24  $\mu$ M were insufficient to reach the  $IC_{50}$  value in the non-malignant cells (Figure 14 D).

In contrast to 2D cultures, for the 3D tumor models all tested inhibitors showed an enhanced effect of the combinatorial treatment together with ARS-1620 compared to the respective monotherapies. Metformin treatment alone increased the viability of HCC44 cells on the SIS muc and when combined with ARS-1620 had the same effect as ARS-1620 monotherapy. SHP099 alone or in combination with gefitinib, as well as erdafitinib only marginally sensitized HCC44 cells towards the KRAS<sup>G12C</sup>-inhibitor. As indicated by the low  $IC_{50}$ -value in 2D, crizotinib alone or in combination with ARS-1620 was the second most effective therapy to reduce the viability of HCC44 cells in 3D (Figure 15 A).

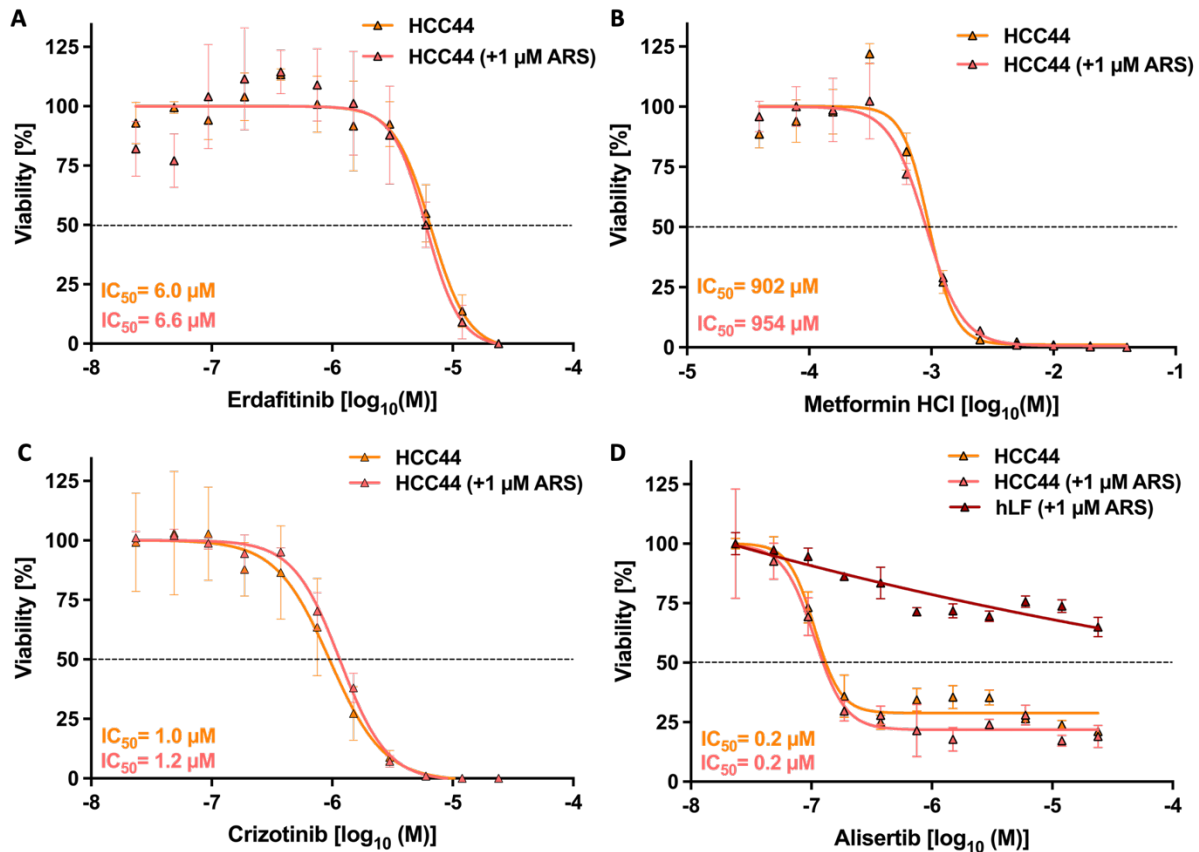


**Figure 14 Testing of combination therapies in HCC44 cells in 2D**

CellTiter-Glo® viability assays of HCC44 cells after treatment for 72 hours with increasing concentrations of (A) erdafitinib, (B) metformin HCl, (C) crizotinib and (D) alisertib. Inhibitors were tested as monotherapies (orange) or in a constant combination with 1 μM ARS-1620 (pink). Alisertib in combination with ARS-1620 was additionally tested on primary human lung fibroblasts (hLF, red).  $n = 1$  with three technical replicates. Adapted figure was published in Peindl *et al.* [128].

Combined inhibition of AURKA with alisertib and KRAS<sup>G12C</sup> with ARS-1620 resulted in significantly reduced viability compared to the control of  $64.3 \pm 1.2\%$ , compared to  $88.6 \pm 2.4\%$  and  $74.4 \pm 1.4\%$  for the respective monotherapies with alisertib or ARS-1620 alone (Figure 15 A, B). This result was further underlined by a substantial reduction of cell numbers to less than 50% of the untreated control in HCC44 tumor models after the treatment with alisertib alone or in combination with ARS-1620 (Figure 15 C). The proliferation index of HCC44 cells in 3D was only significantly reduced when alisertib was combined ARS-1620 with  $29.3 \pm 4.2\%$ , but not for the respective monotherapies (Figure 15 D). H&E staining of HCC44 models after treatment with alisertib alone clearly suggested a reduced number of tumor cells compared to the untreated control. This effect was even more pronounced when alisertib was combined with ARS-1620 (Figure 15 E).

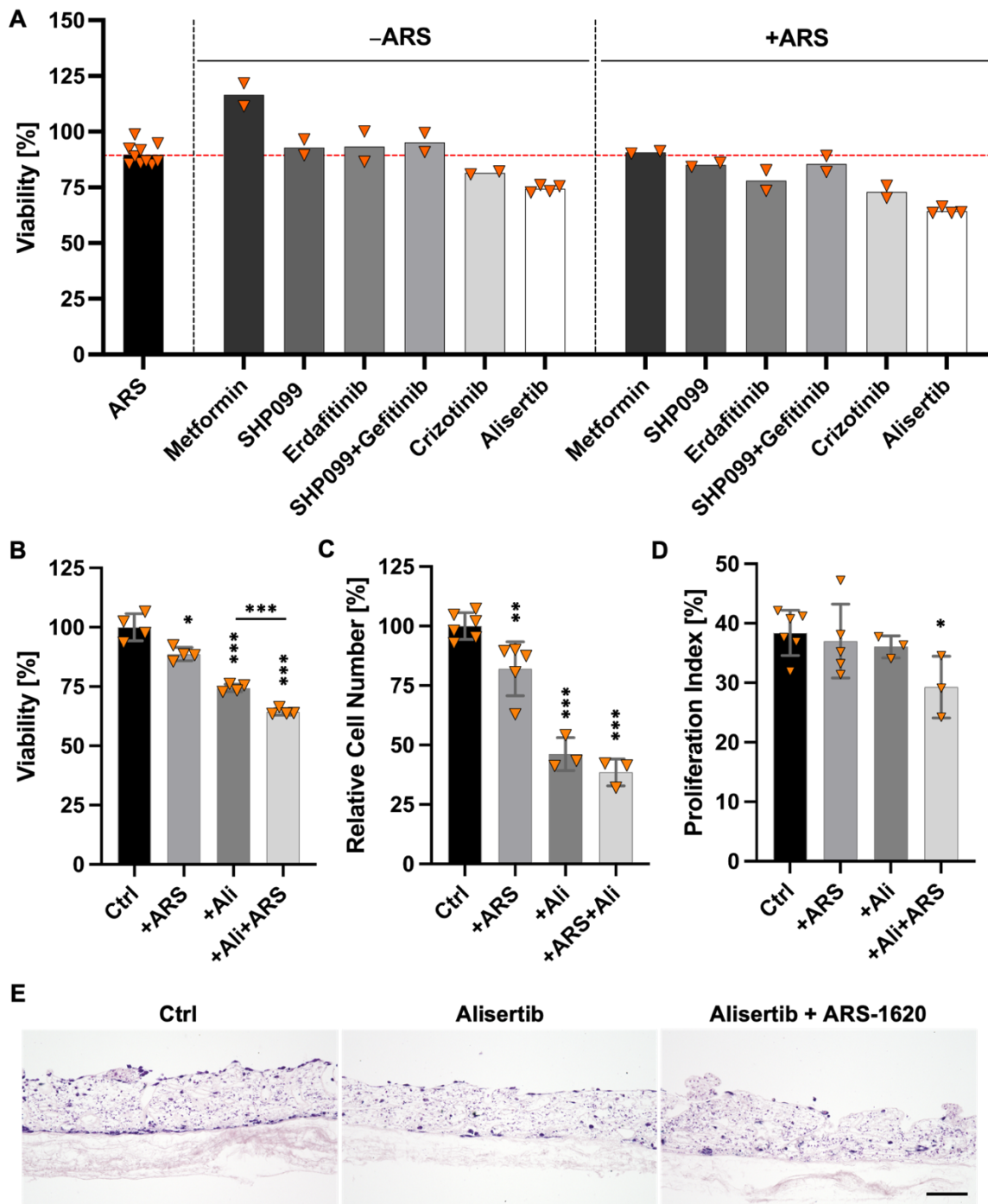


**Figure 15 Testing of combination therapies in HCC44 cells in 3D**

(A) MTT-viability assays of HCC44 tumor models after treatment with the indicated substances for 72 hours. For metformin 1 mM was applied, while 5 μM were used for the remaining inhibitors. Models were treated with either the monotherapy (-ARS) or in combination with 1 μM ARS-1620 (+ARS). n ≥ 2. (B) Quantification of MTT-assays, (C) relative cell numbers and (D) proliferation indices of HCC44 cells on the SIS muc after treatment with 1 μM ARS-1620, 5 μM alisertib or the combination of both inhibitors. Significance was determined with unpaired t-tests; \*: p < 0.05, \*\*: p ≤ 0.01, \*\*\*: p ≤ 0.001; n ≥ 3. (D) H&E staining of HCC44 tumor models after treatment with alisertib alone or in combination with ARS-1620 compared to the untreated control. Scale bar = 100 μm. n = 2. Adapted figure was published in Peindl *et al.* [128].

Finally, a minor reduced expression of *c-MYC* was indicated for HCC44 cells after the inhibition of AURKA. On mRNA level, RT-qPCR pointed out slightly but significantly lower expression of *c-MYC* after treatment with alisertib alone or in combination with ARS-1620 compared to the untreated control (Figure 16 A). The western blot of *c-MYC* suggested a lower expression after the combination therapy compared to the control and the respective monotherapies. However, replicates showed wider deviation on protein levels (Figure 16 B).

Taken together, combined inhibition of the AURKA and KRAS<sup>G12C</sup> was most effective in overcoming the primary resistance in HCC44 cells in 3D, demonstrated by reduced viability, cell numbers and proliferation.

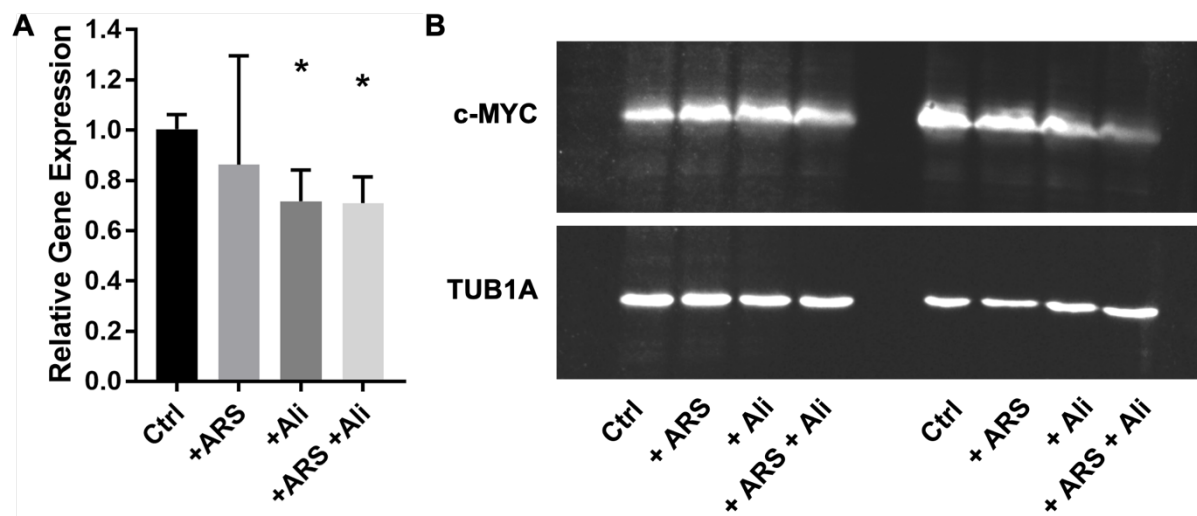


**Figure 16** *c-MYC* expression after combined KRAS<sup>G12C</sup> and AURKA inhibition

**(A)** RT-qPCR of HCC44 cells in 3D after treatment with 5  $\mu$ M alisertib or 1  $\mu$ M ARS-1620 or the combination of both inhibitors for 72 hours depicting the relative gene expression of *c-MYC* compared to the untreated control. Significance was determined with unpaired t-tests; \*:  $p < 0.05$ ;  $n=3$ . **(B)** Western Blot showing the expression of *c-MYC* and alpha-Tubulin as loading control of HCC44 3D tumor models. The models were treated with 5  $\mu$ M alisertib or 1  $\mu$ M ARS-1620 or the combination of both inhibitors for 72 hours;  $n=2$ .

### 3.1.6 Efficacy of combined AURKA and KRAS<sup>G12C</sup>-inhibition in *MYC*-overexpressing and KRAS-mutated cells in 3D tumor models

Considering the promising result of the combination therapy using ARS-1620 together with alisertib in HCC44 tumor models, the combined inhibition of AURKA and KRAS<sup>G12C</sup> was next tested for its efficacy in the remaining KRAS<sup>G12C</sup>-biomarker models including H358 tumor models and the PDX-derived cell lines LXFA 983, LXFL 1072, LXFL 1674 and LXFA 2184 on the SIS muc.

Here, H358 tumor models showed a minor reduction of viability of only 16.8 % compared to the control after the treatment with alisertib alone and the combination of alisertib and ARS-1620 could only reduce the viability by less than 10 % compared to the ARS-1620 monotherapy. Also, in LXFA 983 tumor models, resistance towards alisertib was observed and

even combined inhibition of AURKA and KRAS<sup>G12C</sup> failed to reduce the viability in these tumor cells. In contrast, LXFL 1072 and LXFL 1674 tumor models were however sensitized towards ARS-1620 treatment by alisertib, as the combination therapy reduced the viability to 51.2 % or 53.8% of the untreated control, respectively. Alisertib alone also showed a reasonable effect on both tumor models with a viability of 76.4 % for LXFL 1072 and 78.5 % for LXFL 1674 tumor models after treatment with the AURKA-inhibitor. An intermediate response towards the combination therapy was indicated in LXFA 2184 tumor models compared to the monotherapy with ARS-1620 with 86.2 % versus 75.0 % viability, while alisertib alone did not show effects concerning viability on those cells (Figure 17).

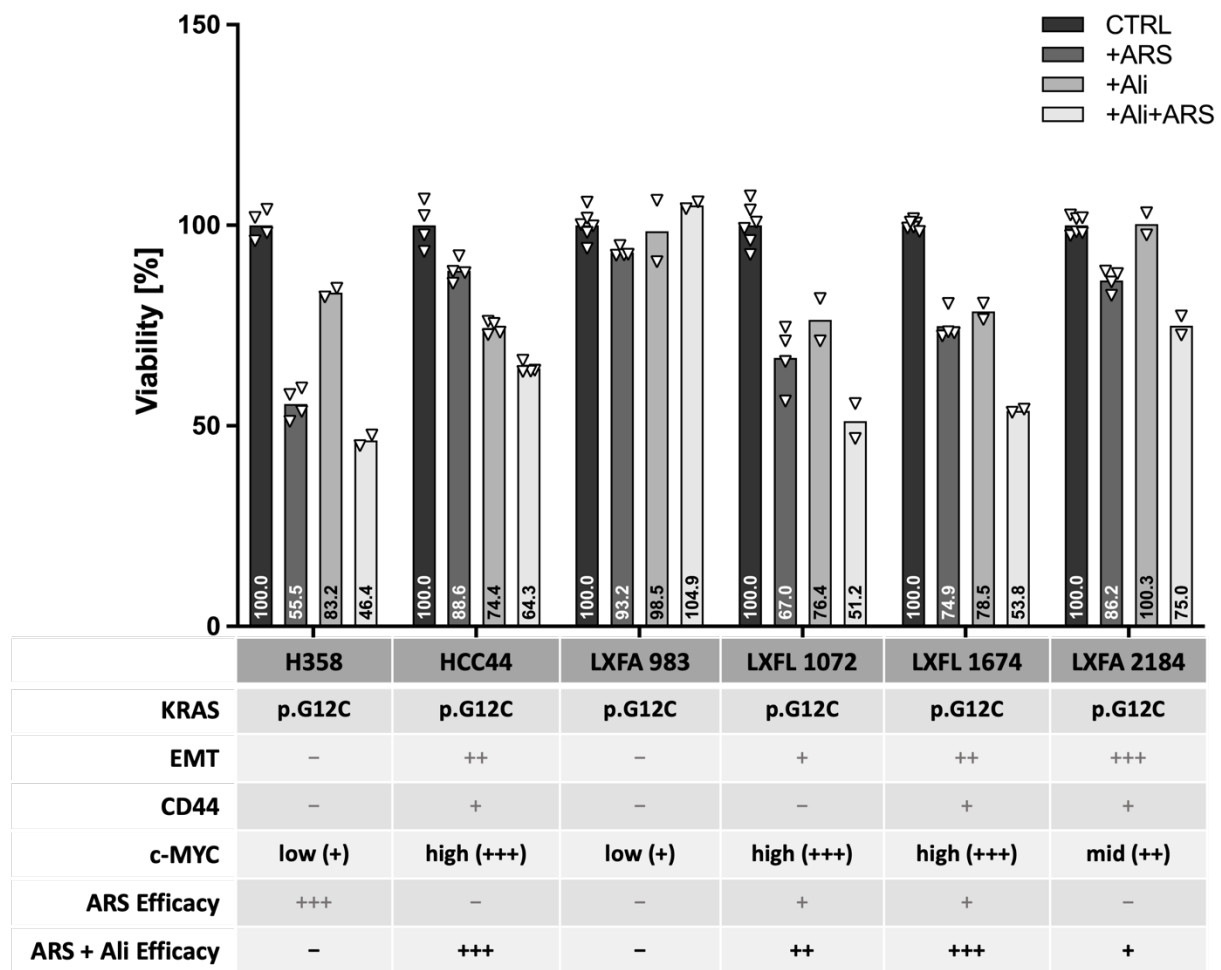


**Figure 17 Marker expression and drug sensitivity of KRAS<sup>G12C</sup>-biomarker models**

Quantification of MTT viability assays of the KRAS<sup>G12C</sup>-biomarker models using H358 and HCC44 cells, as well as the PDX-derived cell lines LXFA 983, LXFL 1072, LXFL 1674 and LXFA 2184 cells after the treatment with either 1 μM ARS-1620, 5 μM alisertib or the combination of both. The table indicates the EMT-phenotype, the CD44 and c-MYC-expression as well as the therapy response towards the monotherapy with ARS-1620 in the corresponding cells. The efficacy of the combinatorial treatment (ARS + Ali) is stated in comparison to ARS-1620 monotherapy. n ≥ 2. Adapted figure was published in Peindl *et al.* [128].



Taking these data as well as the characterization of the 3D models into consideration, neither EMT, nor CD44 and *c-MYC* expression could directly predict the efficacy of the ARS-1620 monotherapy across the KRAS<sup>G12C</sup>-biomarker models. However, the level of *c-MYC* expression directly correlated with the efficacy of the combined inhibition of AURKA and KRAS<sup>G12C</sup> throughout the 6 different tumor models. While for H358 and LXFA 983 tumor models with low *c-MYC* expression no combined effect of alisertib and ARS-1620 was observed, *c-MYC* overexpressing HCC44, LXFL 1072 and LXFL 1674 cells on the SIS muc displayed a reduced viability compared to the respective monotherapies. LXFA 2184 cells in 3D with an intermediate *MYC*-expression also exhibited an intermediate reduction of viability after treatment with the combination therapy (Figure 16).

### **3.2 SIS muc tumor models as a platform for safety and efficacy testing of a genetically modified HSV-1 for the treatment of NSCLC**

While the capability of SIS muc tumor models was previously demonstrated for testing a variety of anti-cancer therapies, including chemotherapies, targeted therapies, and immunotherapies, it was investigated here whether the 3D *in vitro* models also further allow the efficacy and safety evaluation of oncolytic viruses (OVs). The establishment of SIS muc tumor models for testing of viral therapies was performed within a joint project of the Fraunhofer IGB (Stuttgart), Fraunhofer IZI (Leipzig), Fraunhofer ITEM (Braunschweig, Regensburg) and Fraunhofer ISC (Würzburg). Therefore, OVs based on HSV-1 were provided by the Fraunhofer IGB Stuttgart (Prof. Bailer, Dr. Funk) for this approach using a newly established platform vector which was further functionalized to increase the specific infection of tumor cells.

#### **3.2.1 Infection of NSCLC cells with genetically modified HSV-1 in 3D tumor models**

To get insight into the capability of the provided genetically modified HSV-1 to infect NSCLC cells in a 3D environment, *EGFR*-mutated HCC827 and *KRAS*-mutated A549 cells cultured on the SIS muc were infected with the non-attenuated HSV1-based platform virus (P) and the functionalized equivalent (PZ) targeting the *EGFR* with a multiplicity of infection (MOI) of 0.1. SIS muc models infected with the P- or PZ-virus, respectively, were prepared by Dr. Bauer (Fraunhofer ISC, Würzburg) beforehand and infection as well as oncolytic effects were evaluated during this study.

Four days post infection (dpi) of HCC827 cells on the 3D models, the HSV1-specific proteins VP21/22a were firstly detected in a small proportion of tumor cells for both the P- and PZ-viruses. The amount of infected HCC827 cells steadily increased over time from 5 to 7 dpi. After 7 dpi HCC827 were almost exclusively positively stained for VP21/22a, demonstrating that both viruses were able to infect the *EGFR*-mutated cells in 3D (Figure 18 A).

VP21/22a positive A549 cells on the one hand were visible after 3 dpi with the P- and PZ-viruses. On the other hand, the number of infected cells barely increased in comparison to

HCC827 cells and even after 7 dpi a substantial proportion of tumor cells was not infected accounting for both OV<sub>s</sub> (Figure 18 B).

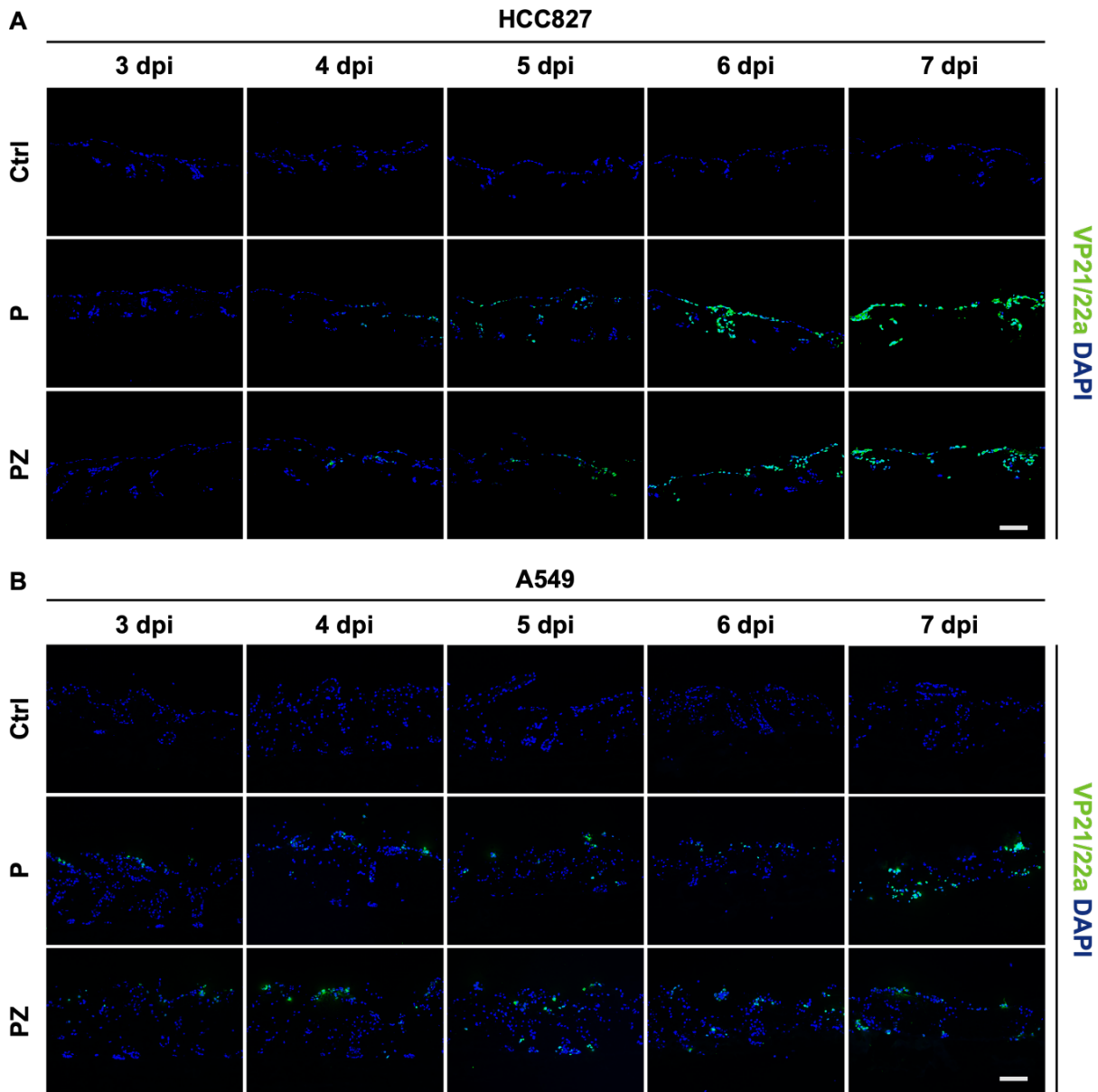


**Figure 18 Infection of HCC827 and A549 monoculture models with oncolytic viruses**

Immunofluorescence stainings of the HSV1-specific proteins VP21/22 a (green) and DAPI-counterstaining (blue) for **(A)** HCC827 or **(B)** A549 SIS<sub>muc</sub> models after 3 dpi to 7 dpi using the non-attenuated oncolytic viruses P and PZ. Tumor models were infected with a MOI of 0.1 after 11 days in culture. Scale bar= 100  $\mu$ m; n=1.

Regarding the oncolysis of the genetically modified HSV-1, anti-tumoral effects were validated by quantitative determination of tumor cells on the models and changes in proliferation. Both the P- and PZ-virus reduced the relative number of HCC827 tumor cells on the SIS<sub>muc</sub> to 72.4 % and 73.3 % of the control after 7 dpi, respectively, whereas after 5 dpi and 6 dpi no considerable effects were observed (Figure 19 A a). Proliferation indices of HCC827 cells, validated by KI67 stainings, showed a decrease after 6 dpi from 15.3 % in the uninfected

control to 11.4 % or 11.6 % for the P- and PZ-virus infected models, respectively. Also, after 7 dpi the OV treated models exhibited lower proliferation with 14.4 % and 16.7 % for the P- and PZ-virus compared to 24.8 % in the control (Figure 19 A b). For A549 cells neither a clear tendency of the relative cell numbers on the models nor a reduced proliferation after infection with the P- and PZ-viruses was indicated. Noteworthy, A549 cells exhibited low proliferation indices of less than 5 % when cultured on the SISmuc in general, no matter the infection with OVs (Figure 19 B a,b).

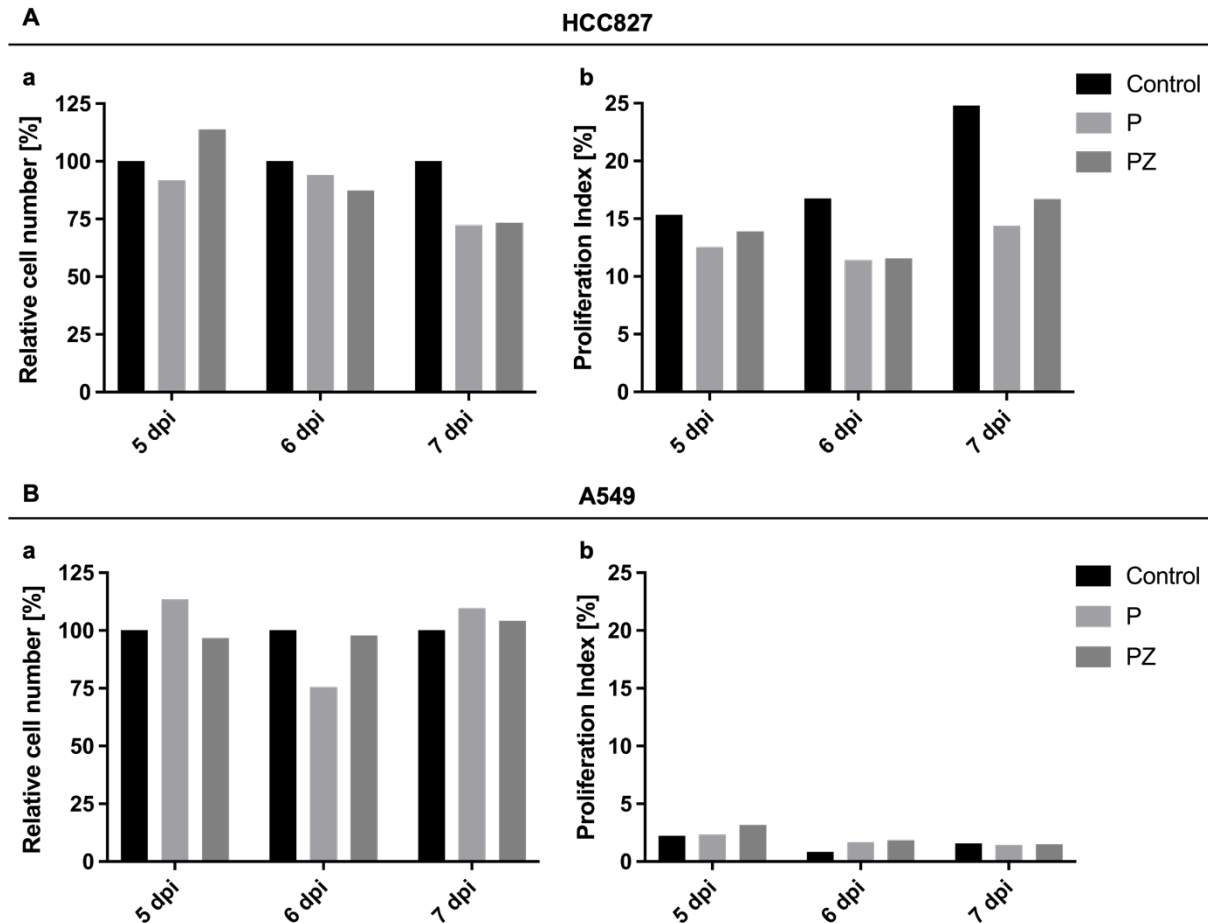


**Figure 19 Oncolytic effects of the P- and PZ-virus on NSCLC cells in 3D**

Quantification of relative cell numbers and proliferation indices of **(A)** HCC827 and **(B)** A549 tumor cells on the SISmuc at different timepoints after infection with the indicated viruses compared to the uninfected control. Tumor cells were infected with a MOI of 0.1 after 11 days in culture. Cell numbers were normalized to the respective uninfected control at each time point. n=1.

### 3.2.2 Co-cultures with fibroblasts for safety evaluation of oncolytic viruses

After demonstrating the infection of NSCLC cells with the genetically modified and non-attenuated HSV1 in the 3D model, it is crucial to further investigate the infectivity of the OVs also in non-malignant cells for safety testing of this therapeutic approach. Here, SISmuc tumor models hold the possibility to modularly expand the tissue with other cell types, including

primary fibroblasts. Co-culture models of NSCLC cell lines and fibroblasts were subsequently infected with both P- and PZ-viruses for a preclinical risk-assessment of this therapy.

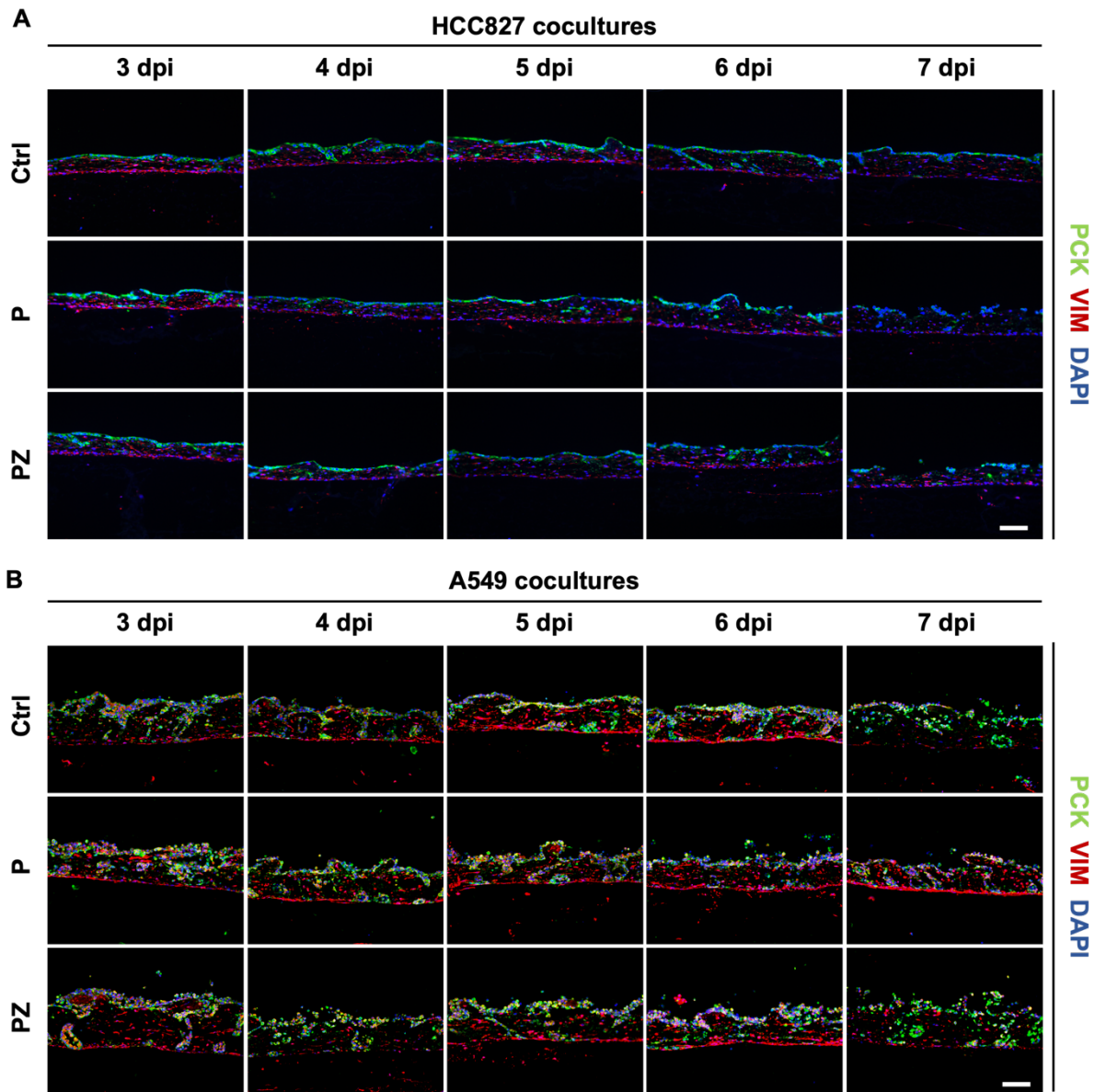


**Figure 20 Cocultures of NSCLC cells with human fibroblasts for safety testing of oncolytic viruses**

Immunofluorescence stainings of the epithelial marker PCK (green), the mesenchymal marker VIM (red) with DAPI-counterstaining (blue) of **(A)** HCC827 or **(B)** A549 cells cocultured with fibroblasts on the SISmuc after different timepoints post-infection. After 11 days in culture the models were infected with the P- or PZ-virus using a MOI of 0.1. Scale bar= 100  $\mu$ m; n=1.

To discriminate the tumor cells from non-malignant fibroblasts in the co-culture models, epithelial CKs and the mesenchymal marker VIM were used. The tissue architecture pointed towards oncolytic effects in HCC827 tumor models by both viruses indicated via a reduction of tumor cells starting at 6 dpi. After 7 dpi with the P- and PZ-viruses larger gaps in the HCC827 monolayer were clearly visible. Tissue architecture of A549 models was however not altered after infection compared to the control even at later timepoints after infection. Furthermore, the

mesenchymal fibroblasts neither exhibited a clear reduction in cell number nor in the morphology after viral infection compared to the respective uninfected controls (Figure 20 A, B). Also, the quantitative evaluation of HCC827 tumor cells on the models pointed towards an enhanced oncolytic effect in the co-cultures of both genetically modified HSV-1 compared to the beforehand tested monocultures, suggested by a reduction of tumor cells to 57.1 % or 54.5 % after 6 dpi and 30.6 % and 42.9 % after 7dpi for the P- and PZ-virus, respectively (Figure 21 A a). In accordance, the proliferation indices of HCC827 cells reduced from 24.4 % in the control to 8.0 % and 4.2 % after the infection after 6 dpi and from 25.0 % to 1.2 % and 5.4 % for the P- and PZ-virus (Figure 21 A b). In parallel to the monocultures, oncolytic effects of the OVVs regarding the number and the proliferation indices of the tumor cells were again not observed for A549 tumor cells also when cocultured with fibroblasts. The low proliferation of A549 cells in monoculture was further reduced in cocultures, independent of viral infections (Figure 21 B a, b).

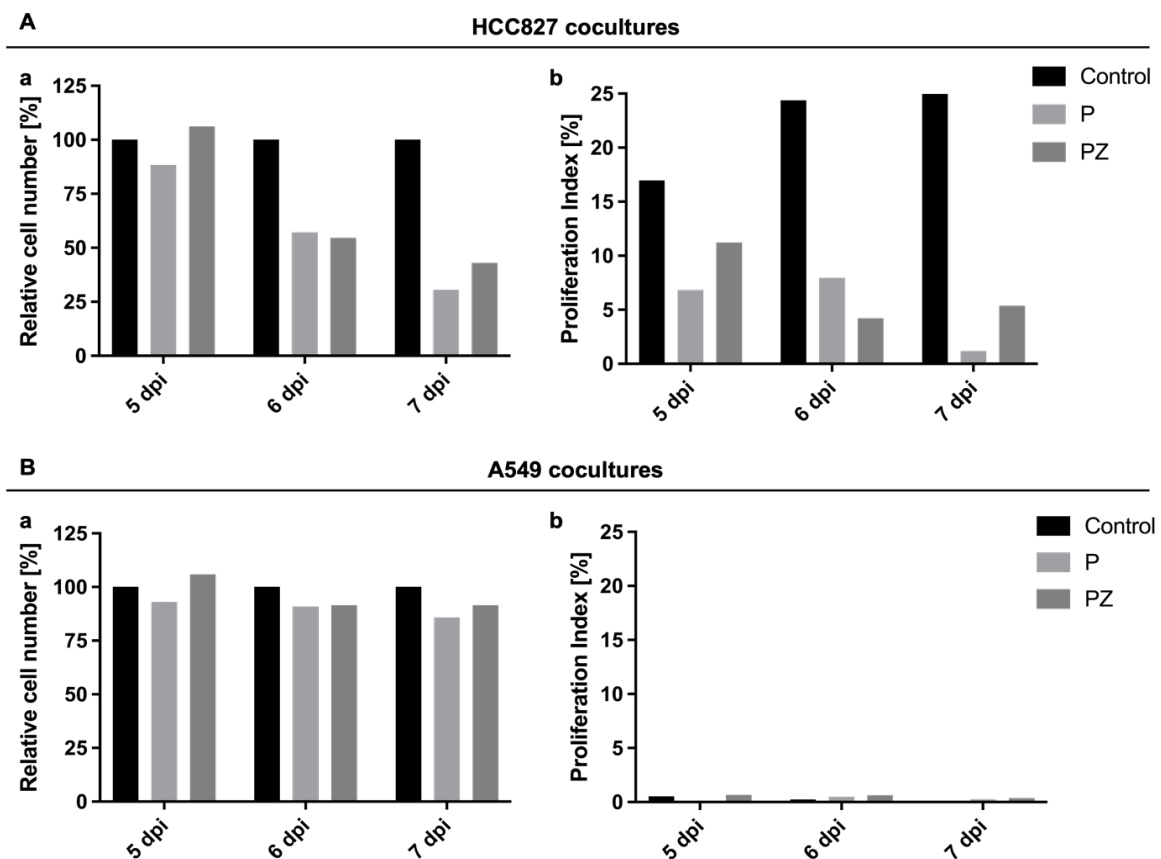


**Figure 21 Oncolytic effects of P- and PZ-virus on NSCLC cells in co-cultures**

**(A)** HCC827 or **(B)** A549 cells co-cultured with human fibroblasts were infected with the indicated OVVs with a MOI of 0.1 and **(a)** relative cell numbers and **(b)** proliferation indices based on KI67 staining were determined for the tumor cells after 5, 6 and 7 dpi. Cell numbers were normalized to the respective uninfected control at each time point. n=1.

While the tissue architecture of the coculture models did not hold evidence for negative effects of the OVVs on the non-malignant cells, the staining of VP21/22a clearly pointed infection of

both tumor cells and fibroblasts for both non-attenuated OV. Starting at 5 dpi, only few VP21/22a positive fibroblasts could be detected. However, after 6 and 7 dpi a large proportion of fibroblasts showed infection with the P- or PZ-Virus, indicating low specificity for cancer cells of the non-attenuated HSV-1 based OV in the 3D models (Figure 22 and S2).

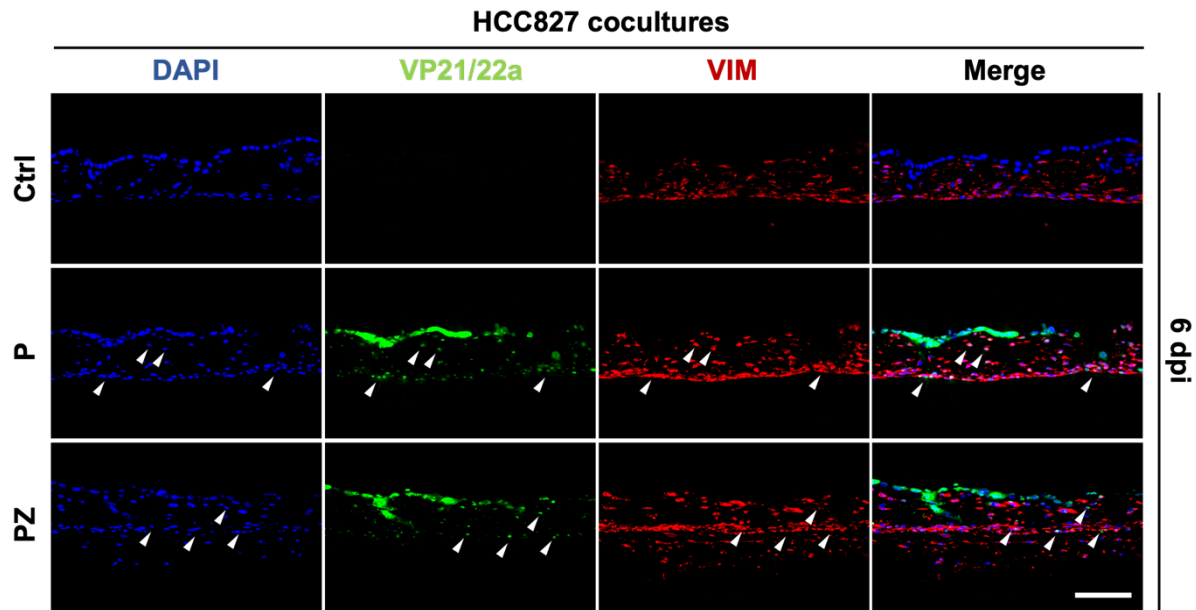


**Figure 22 Safety testing of P- and PZ-virus on coculture models**

Immunofluorescence staining of VP21/22a (green), VIM (red) with DAPI-counterstaining (blue) of HCC827 co-culture models after infection with either the P- or the PZ-virus at 6 dpi. Cells were infected with a MOI of 0.1. White arrowheads indicate VP21/22a positive fibroblasts. Scale bar = 100  $\mu$ m; n=1.

### 3.2.3 Infection of co-culture models with attenuated oncolytic viruses

Both the non-attenuated P- and PZ-viruses could successfully infect the tumor cells both in mono- and cocultures and oncolytic effects were observed in HCC827 tumor models. Still, due to the infection of the primary fibroblasts in the co-culture models the treatment could not be considered safe at least regarding the preliminary testing in this preclinical *in vitro* model. In parallel, the OV. were externally also tested by the partner at the Fraunhofer IZI *in vivo* and in accordance with the *in vitro* results also here infection of non-malignant cells was observed leading to neurotoxic side-effects of the OV. To increase the safety of the treatment, the viruses were further genetically modified by the cooperation partners at the Fraunhofer IGB by partially deleting the gene *UL39* and targeted mutagenesis of *UL37*. These genes are decisive for the replication of the virus in non-proliferating cells and the retrograde axonal transport of viral particles, respectively. According to the assumed reduced neurotoxicity as well as the attenuation the platform vector was termed PNA (platform, prevented neurotoxicity, attenuation) and PNAZ for specifically targeting the EGFR for viral entry.

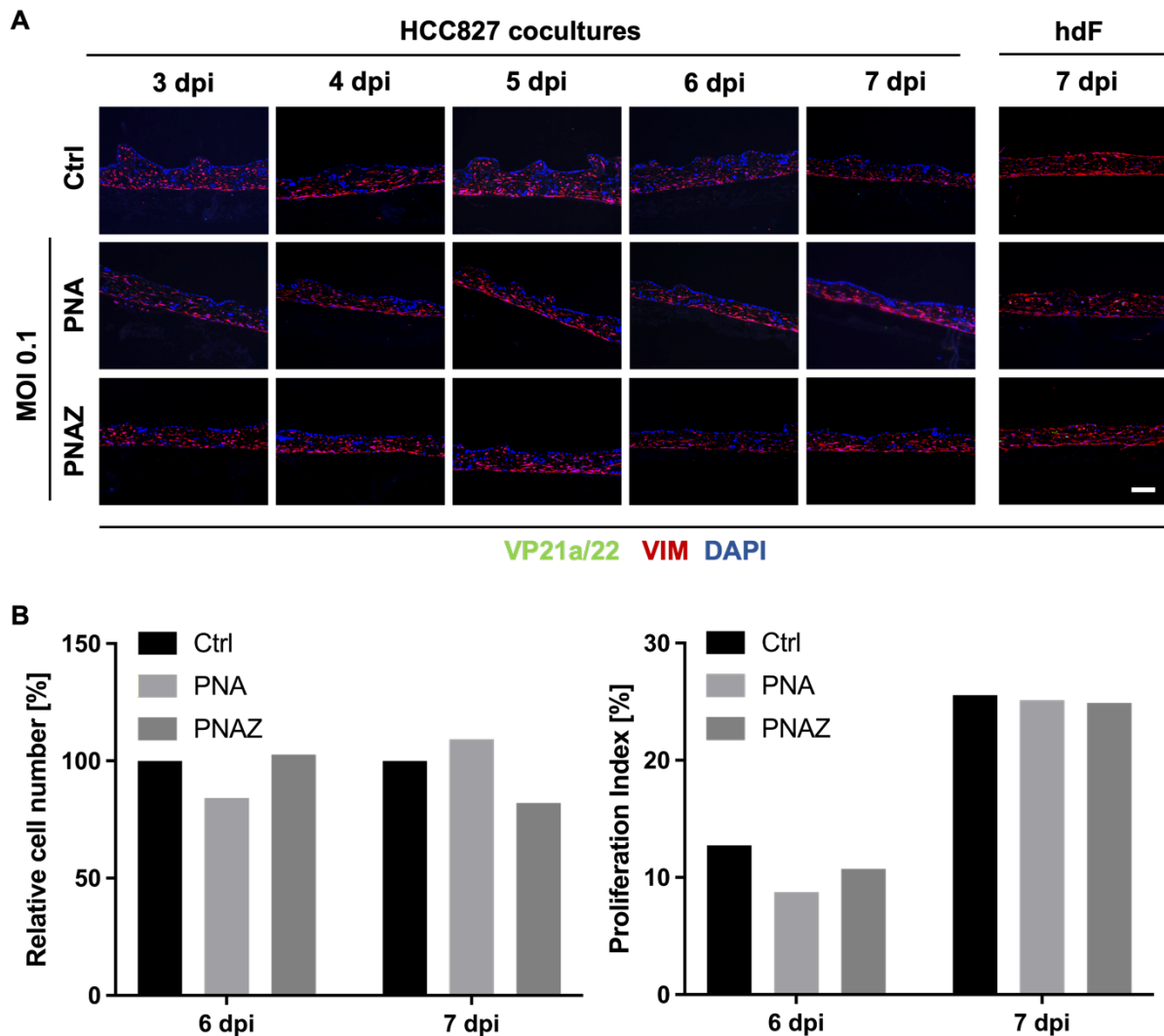


**Figure 23 Infection of HCC827 coculture models with attenuated oncolytic viruses**

(A) Immunofluorescence staining of VP21/22a (green), vimentin (red) with DAPI-counterstaining (blue) of HCC827 coculture models or fibroblast monocultures on the SIS muc at indicated timepoints after infection with the attenuated oncolytic viruses PNA or PNAZ with a MOI of 0.1. (B) Quantification of relative cell numbers and the proliferation indices based on KI67 staining of HCC827 tumor cells co-cultured with fibroblasts after 6 and 7 dpi with the indicated oncolytic viruses. Cell numbers were normalized to the respective uninfected control at each time point. Scale bar = 100  $\mu$ m; n=1.

Both the PNA as well as the PNAZ-virus however clearly failed to infect HCC827 cells cocultured with primary fibroblasts and SIS muc models with only fibroblasts at a MOI of 0.1. The viral protein VP21/22a was not detected between 3 dpi and 7 dpi in HCC827 coculture models. Also, after 7 dpi no VP21/22a positive fibroblasts were visible in the fibroblast monocultures (Figure 23 A). Furthermore, no anti-tumoral effects were indicated by the relative cell numbers and the proliferation indices of the tumor cells only showing minor deviations from the uninfected controls (Figure 23 B). The viral titers determined by plaque-assays further proved the inability of the attenuated viruses to replicate under these conditions as the titers

steadily decreased between 3 and 7 dpi from 14,500 PFU/mL to 1,080 PFU/mL for the PNA-virus and from 6,250 PFU/mL to 3,080 PFU/mL for the PNAZ-virus (Figure S3).

Since the PNA or PNAZ virus using a MOI of 0.1 failed to infect the tumor cells on SIS muc models, the MOI was increased to 1.0. Although a ten-fold higher MOI was used for infection with the attenuated OV of HCC827 co-culture models, no VP21/22a positive cells were detected after 3 dpi or 5 dpi. Eventually after 7 dpi for both the PNA and PNAZ virus few infected tumor cells were visible, while even after 7 dpi no infection of the primary fibroblasts was indicated in the immunofluorescence staining (Figure 24 A). In accordance with the low infection rates, only minor effects on the cell count and proliferation indices were evaluated. While the number of tumor cells was even increased after 3 dpi with 117.6 % and 129.4 % of the uninfected control for the PNA or PNAZ infected models, a reduction of tumor cells was observed 5 dpi and 7 dpi. Here, the PNA-virus resulted in a reduction of the tumor cells to 78.8 % after 5 dpi and 87.0 % after 7 dpi, whereas the PNAZ-virus reduced HCC827 cells to 84.9 % and 82.7 % after 5 dpi or 7 dpi, respectively. Regarding the proliferation of HCC827 cells, the lowest proliferation indices were evaluated after 3 dpi with 8.8 %, 12.3 % and 10.1 % for the control and the PNA- or PNAZ-infected models. After 5 dpi, the proliferation indices were reduced after PNA and PNAZ infection to 24.8 % and 22.9 % compared to 28.6 % in the control. For the latest timepoint, the control showed a proliferation index of 35.7 % while the PNA or PNAZ infection resulted in 29.7 % and 27.2 % (Figure 24 B). Finally, the viral titers also exhibited a definitive decrease from 45,800 PFU/mL after 3 dpi to 2,380 PFU/mL after 7 dpi for the PNA-virus, while for the PNAZ-virus the titers decreased from 33,300 PFU/mL to 2,500 PFU/mL from 3 to 7 dpi (Figure S3).

Infection with the attenuated platform virus was further tested on the human monocytic cell line THP1 on the SIS muc, to also model immune cells as part of the TME besides fibroblasts. No VP21/22a-positive THP1 cells were detected after 7 dpi with the attenuated platform-virus PNA while the cell number was 108.4 % of the uninfected control, suggesting no susceptibility of the immune cells for the virus (Figure 25 A, B).

In summary both OV still demonstrated low infection rates, minor oncolytic effects as well as poor replication applying a MOI of 1.0 in the HCC827 coculture models on the SIS muc. However, regarding the safety testing of the attenuated OV, primary fibroblasts and monocytic cells were not infected even at the higher MOI on the 3D models. This result was in agreement by parallelly performed *in vivo* experiments by the partner group at the Fraunhofer IZI, providing evidence for a reduced neurotoxicity of the attenuated OV in the corresponding mouse models.



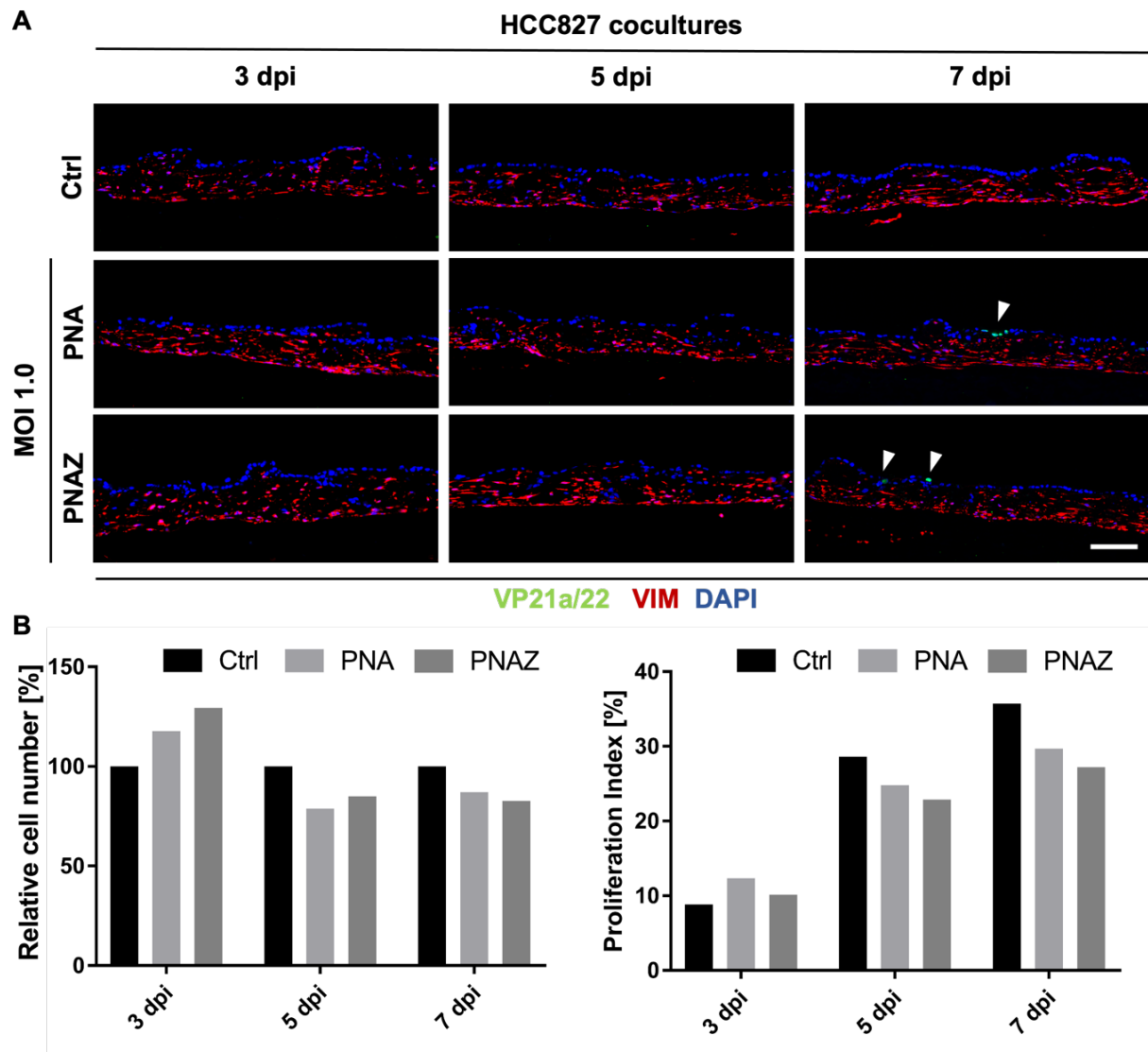


**Figure 24 Increased MOI for infection of HCC827 co-cultures models with attenuated oncolytic viruses**

**(A)** HCC827 cells cocultured with fibroblasts were infected with the oncolytic viruses PNA- or PNAZ at a MOI of 1.0 and stained for VP21/22a (green), vimentin (red) with DAPI-counterstaining (blue) after 3, 5 or 7 dpi. White arrowheads indicate VP21/22a positive HCC827 cells after 7 dpi. **(B)** Relative cell numbers on the models and proliferation indices determined by KI67 staining of HCC827 cells co-cultured with fibroblasts on the SIS muc after infection with the attenuated oncolytic viruses at a MOI 1.0 compared to the uninfected control. Cell numbers were normalized to the respective uninfected control at each time point. Scale bar = 100  $\mu$ m; n=1.

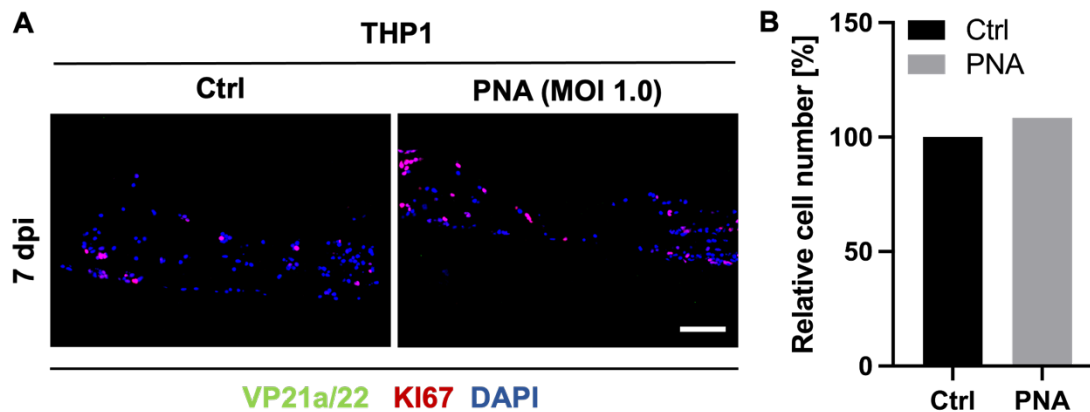


**Figure 25 THP1 models after infection with attenuated oncolytic viruses**

**(A)** Immunofluorescence staining of VP21/22a (green), vimentin (red) with DAPI-counterstaining (blue). THP1 cells were cultured on the SISmuc and infected with the PNA-virus at a MOI of 1.0 for 7 days. **(B)** Subsequent determination of the relative cell numbers of the corresponding models. Cell numbers were normalized to the respective uninfected control at each time point. Scale bar = 100  $\mu$ m; n=1.

### 3.2.4 Efficacy of attenuated oncolytic viruses on advanced stage NSCLC models

Assuming safety of the attenuated OV's using MOIs of 1.0, the PNA- and PNAZ-viruses were examined for their capability to induce oncolysis in HCC44 SISmuc tumor models. This KRAS<sup>G12C</sup>-mutated cell line exhibits invasive growth and comparatively increased proliferation rates as described above (see Chapter 3.1.2), thereby representing an *in vitro* model for a more advanced and aggressive NSCLC.

Using a MOI of 1.0 of PNA- or PNAZ-virus for infection of HCC44 tumor models, no infection was observed 3 dpi. After 5 dpi rare VP21/22a-positive HCC44 cells were detected, while after 7 dpi a substantial proportion of tumor cells showed infection with the attenuated OV's (Figure 26 A). Accordingly, no decrease in the relative cell numbers was visible 3 dpi with 122.0 % and 95.2 % of the control after infection with the PNA- or PNAZ-virus, respectively. Lower amount of tumor cells was however indicated after 5 dpi with 76.8 % for the PNA-virus and 78.6 % for the PNAZ-virus compared to the uninfected control. This effect was eventually more pronounced after 7 dpi with only 67.5 % or 62.8 % of tumor cells on the model after infection with the PNA- or PNAZ-virus. Proliferation indices however did neither show a clear tendency nor considerable reductions after the treatment with OV's. Still, higher proliferation indices of HCC44 cells in comparison to beforehand used HCC827 or A549 cells were validated with 20.1 %, 31.9 % and 30.4 % for the uninfected controls for the time points 3, 5 and 7 dpi (Figure 26 B). The plaque-assays further pointed out higher virus concentrations after 3 dpi compared to beforehand used HCC827 models, with viral titers of 91,700 PFU<sub>/mL</sub> for the PNA-virus and 123,000 PFU<sub>/mL</sub> for the PNAZ-virus. A drop of the viral titers for the PNA- and PNAZ-virus was observed at 5 dpi with 32,500 PFU<sub>/mL</sub> and 39,200 PFU<sub>/mL</sub>. At the last timepoint, 7 dpi, the viral concentration increased for the PNA-virus with 110,000 PFU<sub>/mL</sub>, while for the

PNAZ-virus the concentration remained relatively unaltered in comparison to 5 dpi with 43,000 PFU/mL (Figure S3). By this, the highest virus titers with the attenuated OVVs were validated for the infection of HCC44 tumor models. Thereby, both attenuated OVVs showed enhanced infection rates, increased oncolysis as well as higher replication in the invasive and highly proliferative HCC44 cells in 3D compared to HCC827 tumor models.

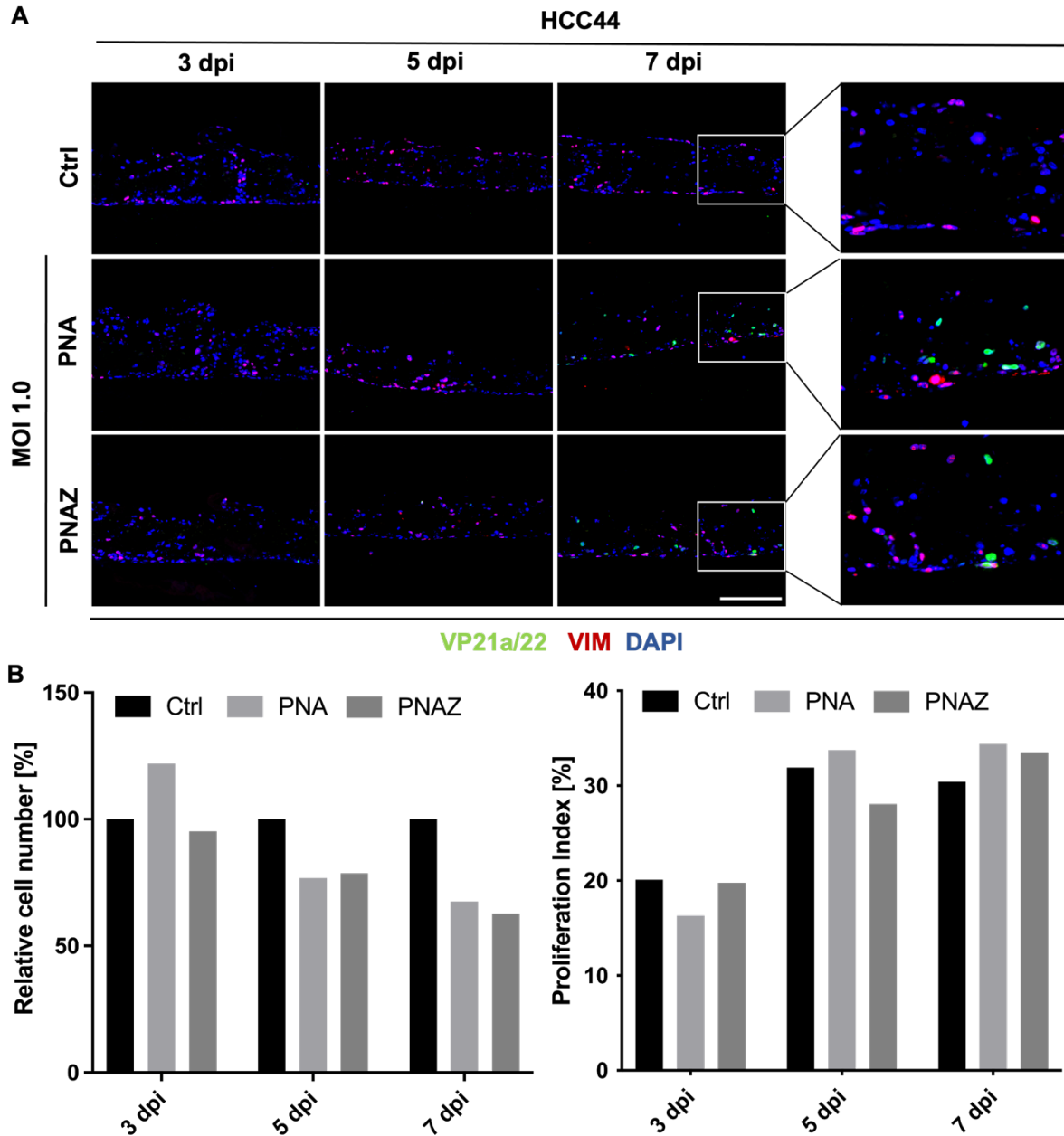


**Figure 26 Infection of HCC44 tumor models with attenuated oncolytic viruses**

**(A)** VP21/22a (green), vimentin (red) immunofluorescence staining with DAPI-counterstaining (blue) of HCC44 cells on the SISmuc 3, 5 or 7 days after infection with the attenuated oncolytic viruses PNA or PNAZ at a MOI of 1.0. **(B)** Oncolytic effects regarding relative cell numbers on the models and proliferation indices of HCC44 cells after infection with the indicated virus compared to the uninfected control after 3, 5 or 7 dpi. Scale bar = 200  $\mu$ m; n=1.

### 3.3 Automation of 3D tumor models

The development and testing of individualized therapies became a central aspect in the field of oncology in recent years, going hand in hand with a high demand for platforms to test these therapies in a larger scale with little effort. Here, an automated platform for testing anti-cancer therapies was developed within a Bavarian research network for personalized medicine (FORTiTher). For this approach, a model system is crucial that on the hand shows 3D architecture to mimic *in vivo* conditions but is on the other hand also capable of high-throughput testing, cost-effective as well as simple to set up. These requirements are met by 3D tumor spheroids, displaying a reasonable model system for the translation into an automated process. In the following, a workflow for spheroid generation including drug testing was established for the direct translation into a robotic platform by the cooperating engineers of the Fraunhofer ISC in Würzburg (M.Sc. Königer, M.Sc. Mahdy).

#### 3.3.1 Inability of HCC827 cells for spheroid formation

Prerequisites for the establishment of a proof-of-concept process for automated spheroid generation with efficacy validation of targeted therapies is a cell line carrying a targetable biomarker mutation rendering the cells sensitive towards a corresponding small molecule inhibitor. *EGFR*-mutated HCC827 cells, showing sensitivity towards *EGFR*-TKIs, are a possible candidate cell line and were hence tested for their capability to form compact 3D spheroids under different settings.

In a first approach, HCC827 cells were seeded in 96-well-plates with ultra-low-attachment (ULA) coating, preventing the attachment of the tumor cells to the plastic surface. Tumor cells were seeded in culture medium supplemented with either 20 or 10 % FCS. For the former condition, HCC827 cells failed to form compact spheroids within 96 hours of culture. The cells formed only loose aggregates including the accumulation of peripheral cellular debris. Furthermore, considerable proportions of cells were not integrated into the aggregates. Reduction of FCS to 10 % in the culture medium enhanced spheroid generation capability of HCC827 cells. Still, no single spheroid per well could be generated and multiple spheroids with different sizes and varying morphology were observed. Additionally, disintegrated single cells and cellular debris were detected in the periphery of the aggregates (Figure 27 A).

Subsequently, a Sphericalplate 5D (Kugelmeiers) containing a micro-structured well bottom was evaluated for the capability to refine spheroid formation of HCC827 cells. While disintegrated cells and cellular debris were drastically reduced under these conditions compared to ULA-coated 96-well plates, neither 50 nor 100 cells per microwell were suitable to induce the formation of single compact spheroids in this test system. Again, multiform spheroids were detected within single microwells, making a reliable testing of therapy efficacy challenging (Figure 27 B, C).

According to the failed formation of compact single spheroids by HCC827 cells the cell line was excluded as candidate for a proof-of-concept process for automation.

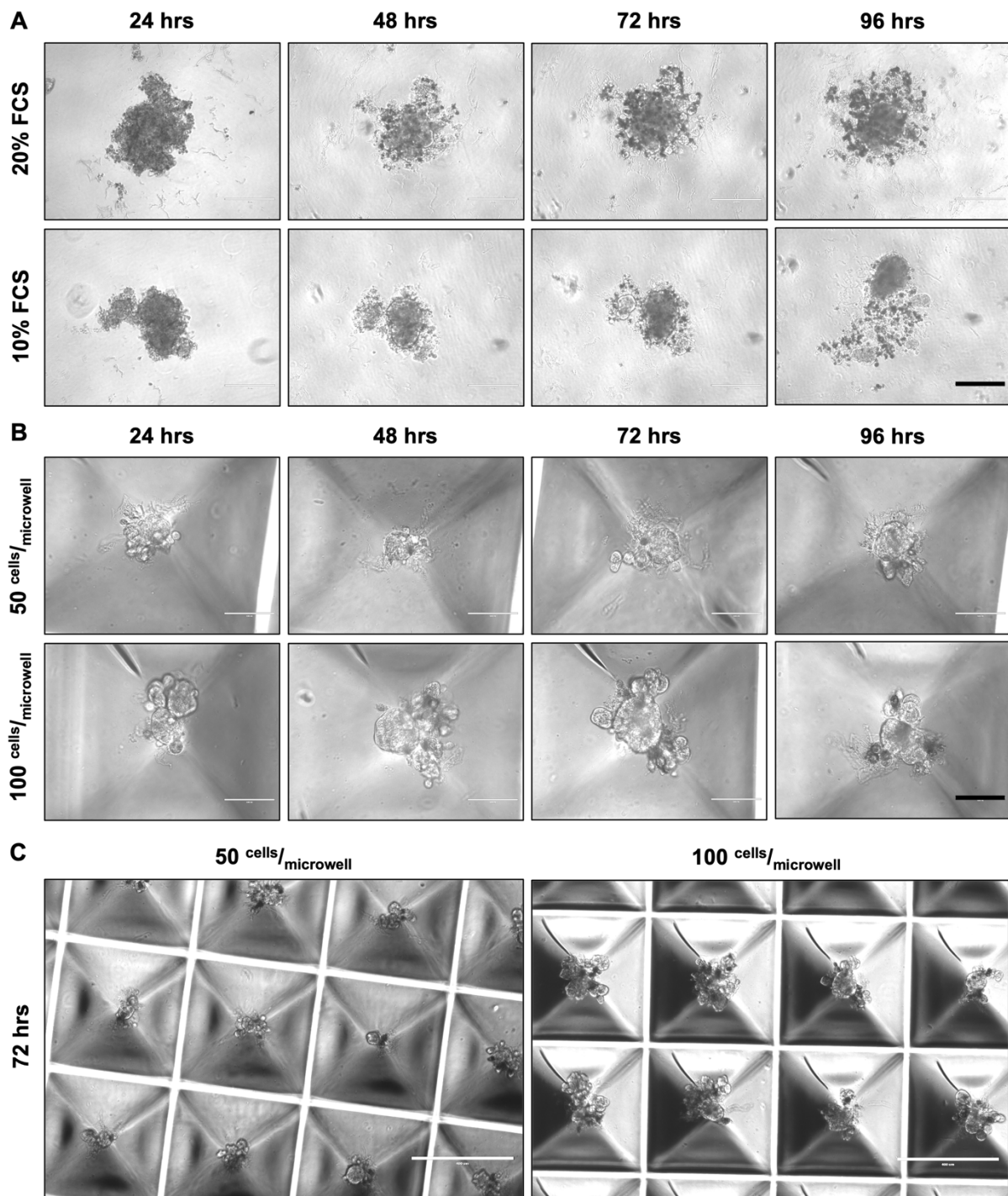


**Figure 27 HCC827 spheroid generation approach under different culture conditions**

**(A)** Brightfield pictures of 1,000 HCC827 cells after 24, 48, 72 and 96 h in culture seeded in ULA-coated 96-well plates. Cells were cultured in medium containing either 10 % or 20 % FCS. Scale bar = 400  $\mu$ m. **(B)** Brightfield images of single microwells with either 50 or 100 HCC827 cells seeded per microwell in Sphericalplates 5D (KUGELMEIER'S) at different timepoints of culture; Scale bar = 100  $\mu$ m. **(C)** Overview over multiple microwells in Sphericalplates 5D (KUGELMEIER'S) seeded with HCC827 cells after 72 hrs; Scale bar = 400  $\mu$ m.

### 3.3.2 Formation of compact spheroids in ULA-coated plates by H358 cells

Another promising candidate for a suitable NSCLC cell line is represented by *KRAS*<sup>G12C</sup>-mutated H358 cells, for which the sensitivity towards the *KRAS*-targeted therapy with ARS-1620 in 2D and 3D SISmuc models was described above (Chapter 3.1.1 and 3.1.3).

In contrast to HCC827 cells, H358 reproducibly formed round and compact spheroids in ULA-coated 96-well plates within 24 h of culture after seeding. Additionally, exclusively one single spheroid was generated per well and the 3D aggregates remained stable up to 168 h in culture. The amount of cellular debris and number of disintegrated single cells in the periphery of the core spheroid remained low in comparison to HCC827 cells (Figure 28 A). H&E staining of H358 spheroids demonstrated that the tumor cells were arranged in a dense manner with close cell-cell-contacts throughout the aggregate and no signs of necrosis were detected after 5 days in culture. Epithelial markers including E-cadherin, PCK and MUC-1 were expressed throughout the spheroids as well as the mesenchymal marker VIM, pointing towards a partial EMT in the 3D spheroids (Figure 28 B).

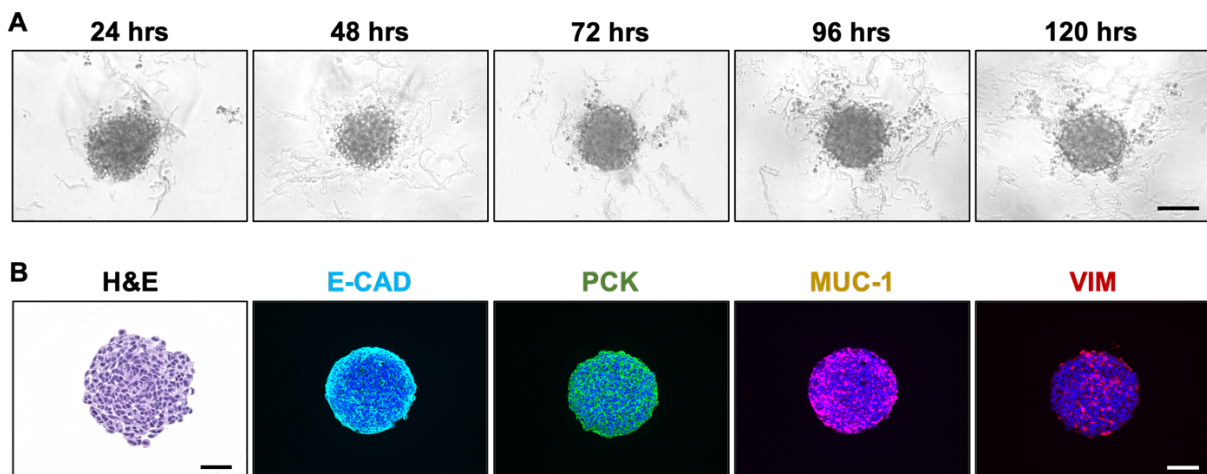


**Figure 28 H358 spheroids in ULA-coated 96-well plates**

(A) Brightfield pictures of 1,000 H358 cells seeded in ULA-coated 96-well plates at different timepoints in culture. Scale bar = 100  $\mu$ m; n = 3 with 5 technical replicates. (B) H&E staining and immunofluorescence staining of E-CAD (lightblue), PCK (green), MUC-1 (purple) and VIM (red) with DAPI (blue) counterstaining of H358 spheroids after 5 days in culture. Scale bar = 100  $\mu$ m; n = 1.

Furthermore, H358 tumor spheroids exhibited high uniformity regarding the morphology. After 24 h in culture the spheroid areas deviated by 10 % between the replicates. The aggregates further compacted within the first 48 h in culture, indicated by a minor reduction in size, and from this timepoint on the deviations in spheroid areas were 6 % or less between the replicates, demonstrating high reproducibility. The initial size of the spheroids after 24 h was re-reached at 96 h in culture and afterwards the area of the spheroids steadily increased over time until 168 h in culture (Figure 29 A). H358 spheroids could further be successfully co-cultured with

immortalized human fibroblasts (ISX huFIB), thereby giving the possibility to partially mimic the TME in this 3D model. GFP signals from the tagged huFIB were detected throughout the H358 spheroids, pointing towards the incorporation of the non-malignant cells into the aggregates (Figure 29 B).

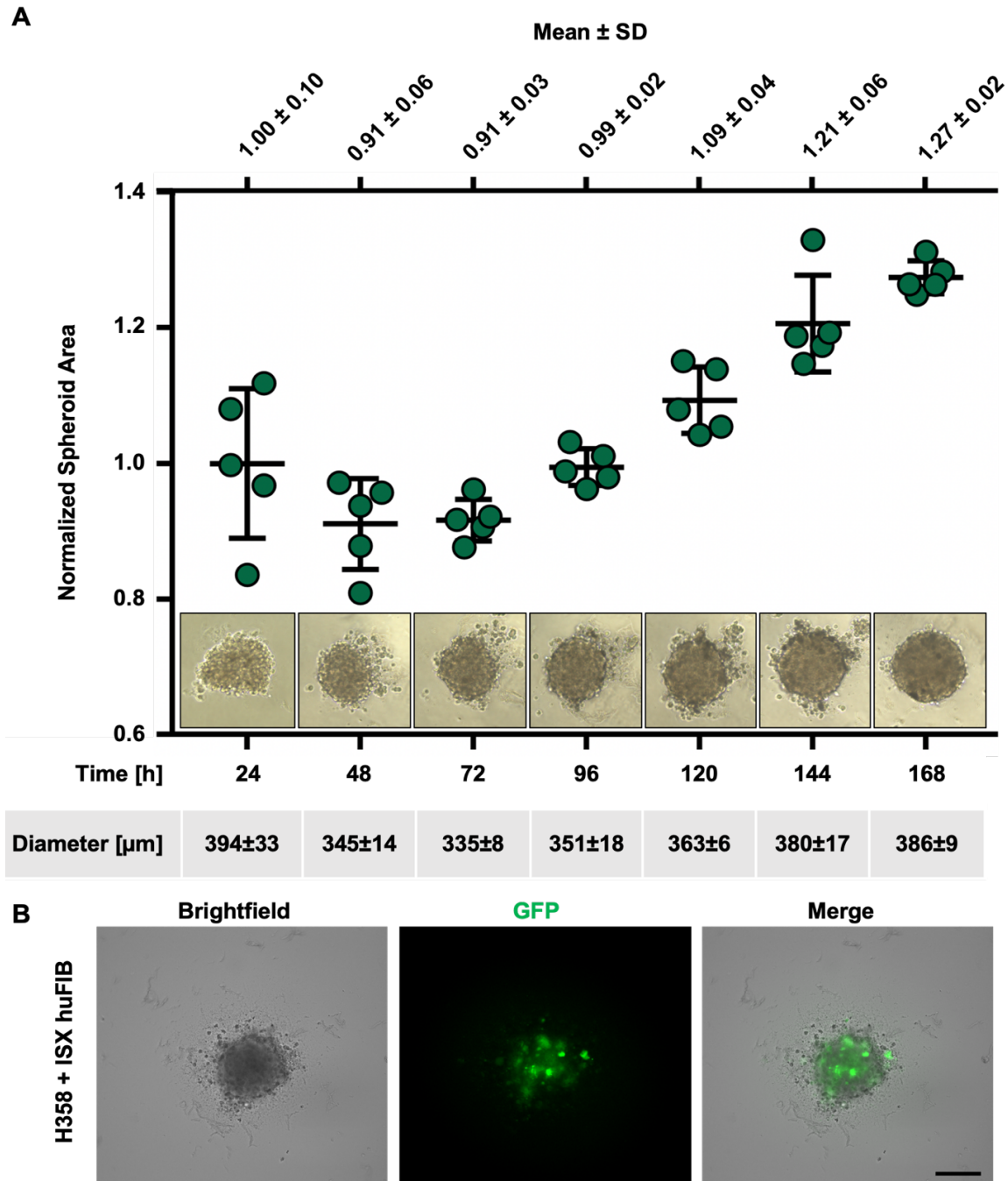


**Figure 29 H358 spheroids in ULA-coated 96-well plates**

**(A)** Spheroid area after normalization to the mean area of spheroids after 24 h in culture. Spheroids were cultured for 168 h and brightfield images were recorded every 24 h of the same five spheroids. The mean Ferret's diameter of the spheroids at different timepoints is indicated with standard deviations. N=5. **(B)** Coculture spheroids of H358 cells and GFP-tagged ISX huFIB cells. Both cell lines were seeded simultaneously in ULA-coated 96-well plates and images were recorded after 4 days in culture. N=5; Scale bar = 200  $\mu$ m.

### 3.3.3 Sensitivity of H358 spheroids towards KRAS<sup>G12C</sup>-inhibition

After validating the capability of H358 cells to reproducibly form compact spheroids, the sensitivity of the 3D models towards the KRAS<sup>G12C</sup>-inhibitor ARS-1620 was determined in order to have an efficient targeted therapy for the automated proof-of-concept process available. Brightfield microscopy of H358 spheroids treated with increasing concentrations from 62.5 nM up to 500 nM of ARS-1620 applied 24 h after seeding the cells suggested that the size of the spheroids was decreasing in both a dose- as well as time-dependent manner compared to the untreated control. At the same time, ARS-1620 treatment resulted in a dose-dependent increase of cellular debris and disintegrated cells in the spheroid cultures (Figure 30 A, B).

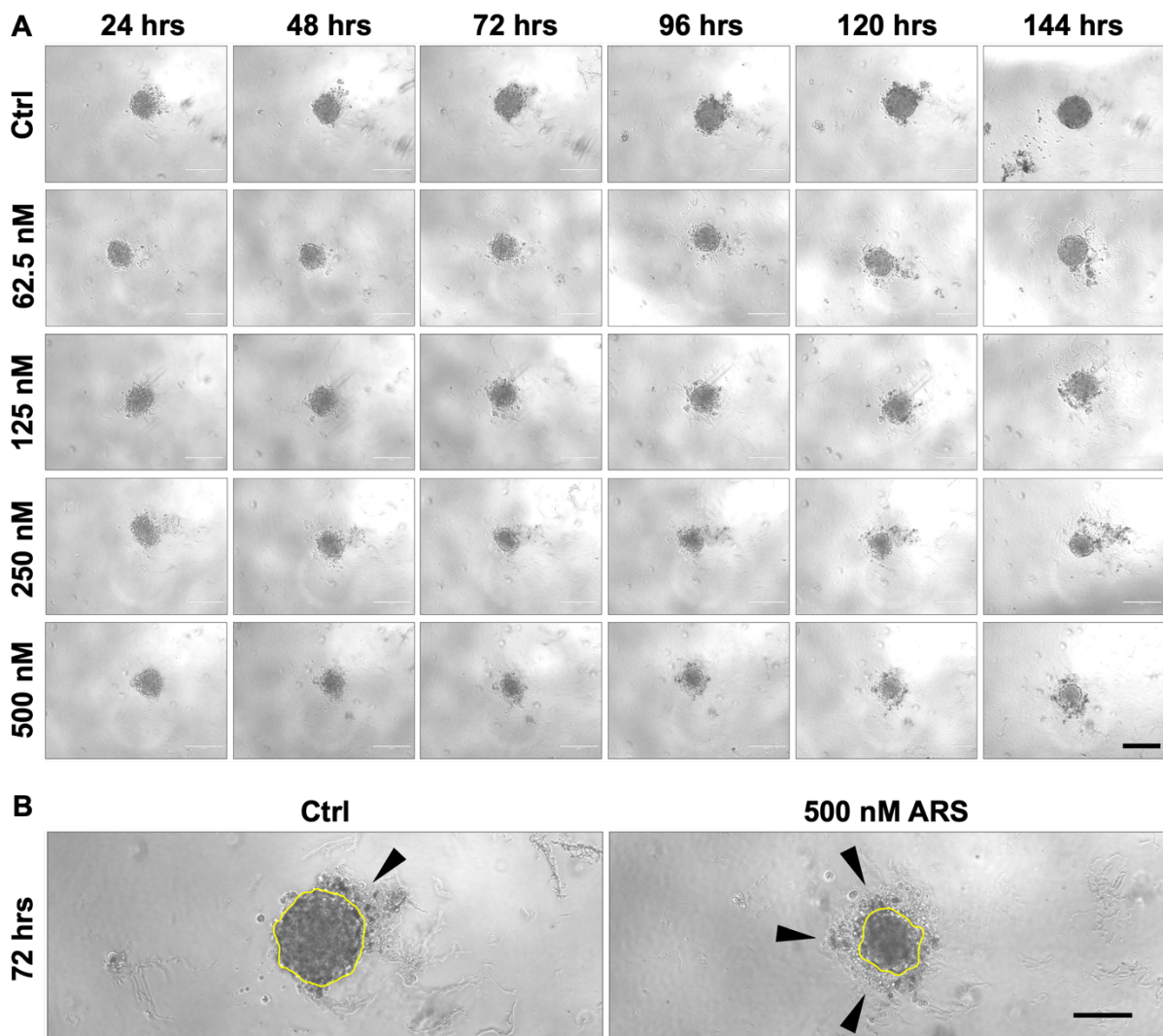


**Figure 30 Morphology of H358 spheroids after ARS-1620 treatment**

(A) Brightfield pictures of H358 spheroids at different timepoints of culture after treatment with indicated concentrations of ARS-1620 compared to the DMSO control. Scale bar = 400  $\mu$ m; N = 5. (B) Magnified view of H358 spheroids after treatment with 500 nM ARS-1620 for 72 h compared to the DMSO control. Core spheroids are bordered with a yellow line. Black arrowheads indicate disintegrated, peripheral cells and debris. Scale bar = 200  $\mu$ m.



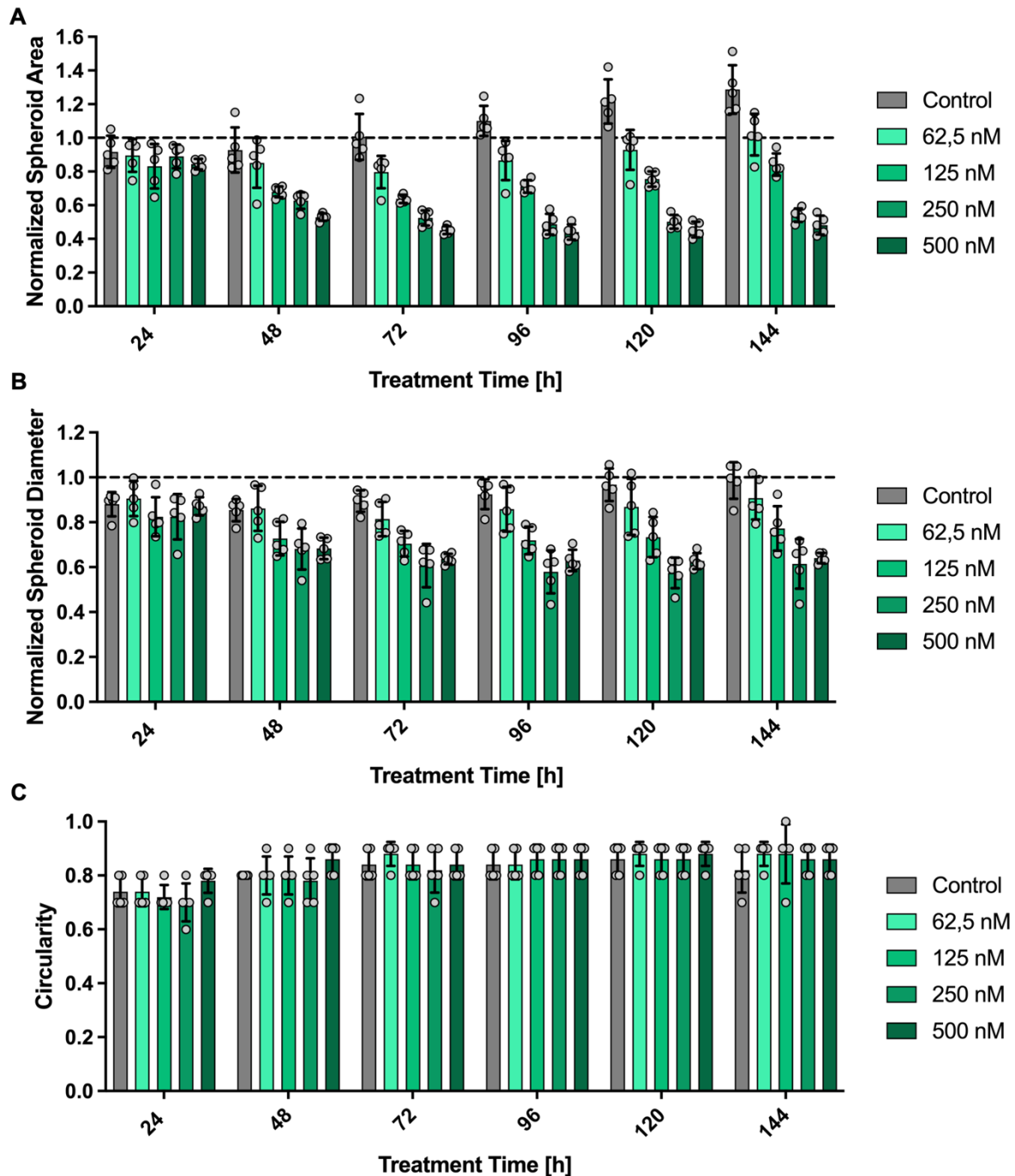


**Figure 31 Morphological changes in H358 spheroids after ARS-1620 treatment**

(A) Area and (B) Ferret's diameter after normalization, as well as (C) circularity of H358 spheroids after treatment with indicated concentrations of ARS-1620 at different timepoints compared to the untreated control. Data were generated by manual measurements of brightfield images of 5 representative spheroids recorded every 24 h of culture. N=5.

Measurement and subsequent quantification of the area and the Ferret's diameter of H358 spheroids confirmed the reduction of size of the 3D aggregates after treatment. While 24 h after treatment with different concentrations of ARS-1620 no major differences were detected regarding the area and the diameter of the spheroids, 48 h after treatment the dose-dependent

reduction of areas could be validated. For 500 nM ARS-1620 the spheroid area was reduced to 52.9 % after the treatment at this timepoint. The effect was even more pronounced after 72 hours of treatment where the spheroid area was reduced to 45.2 % for the highest concentration. The dose-dependent reduction in spheroid areas was further conserved over the remaining time in culture (Figure 31 A). In parallel, similar effects were observed for the Ferret's diameter of the spheroids, where the treatment concordantly resulted in a dose- and time-dependent reduction (Figure 31 B). However, the circularity of the aggregates, which can be further considered to get insight into the morphological changes of the models, did not show any major differences between the control and the spheroids treated with different concentrations of ARS-1620 at any given timepoint (Figure 31 C). Nevertheless, the data point towards sensitivity of H358 tumor spheroids towards ARS-1620 in the sub-micromolar range of concentrations.

Assays used for 2D cultures are often difficult to translate to 3D cultures and M30 ELISAs, which were used for 3D SIS muc tumor models in this study, failed to measure apoptosis induction in 3D spheroids (Data not shown). To address whether ARS-1620 eventually induced apoptosis in the H358 tumor spheroids, a luminescence-based assay was performed to detect caspase-3 and -7 activation in the cells. Here, caspase activity started to increase at ARS-1620 concentrations higher than 100 nM and reached a plateau above 3  $\mu$ M of the inhibitor. Thereby an excitatory concentration 50 ( $EC_{50}$ ) for caspase activation in H358 spheroids with ARS-1620 of 640 nM was determined, pointing out the sensitivity of the models for the KRAS<sup>G12C</sup>-inhibitor and demonstrating the induction of caspase-mediated apoptosis after treatment (Figure 32).

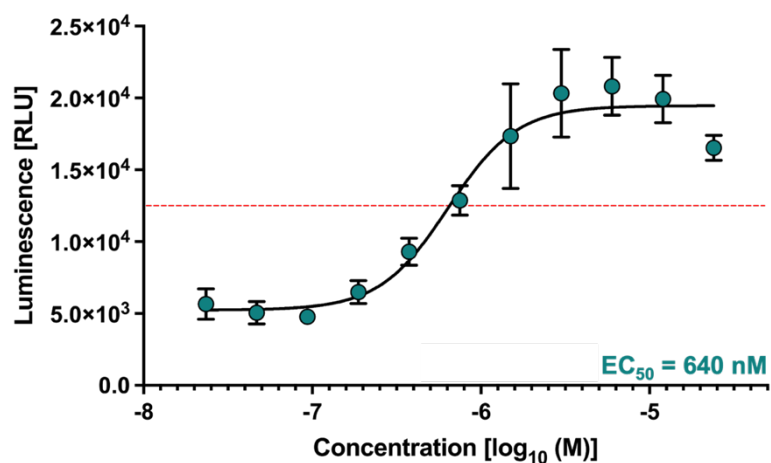


**Figure 32 Caspase-3 and -7 activation in ARS-1620 treated H358 spheroids**

H358 spheroids were treated for 72 h with ARS-1620 concentrations ranging from 23.5 nM to 24  $\mu$ M. Caspase-3 and -7 activation was measured with a Caspase-Glo® 3/7 assay and an  $EC_{50}$  of 640 nM was calculated. The graph shows one representative curve; n=2 with three technical replicates.

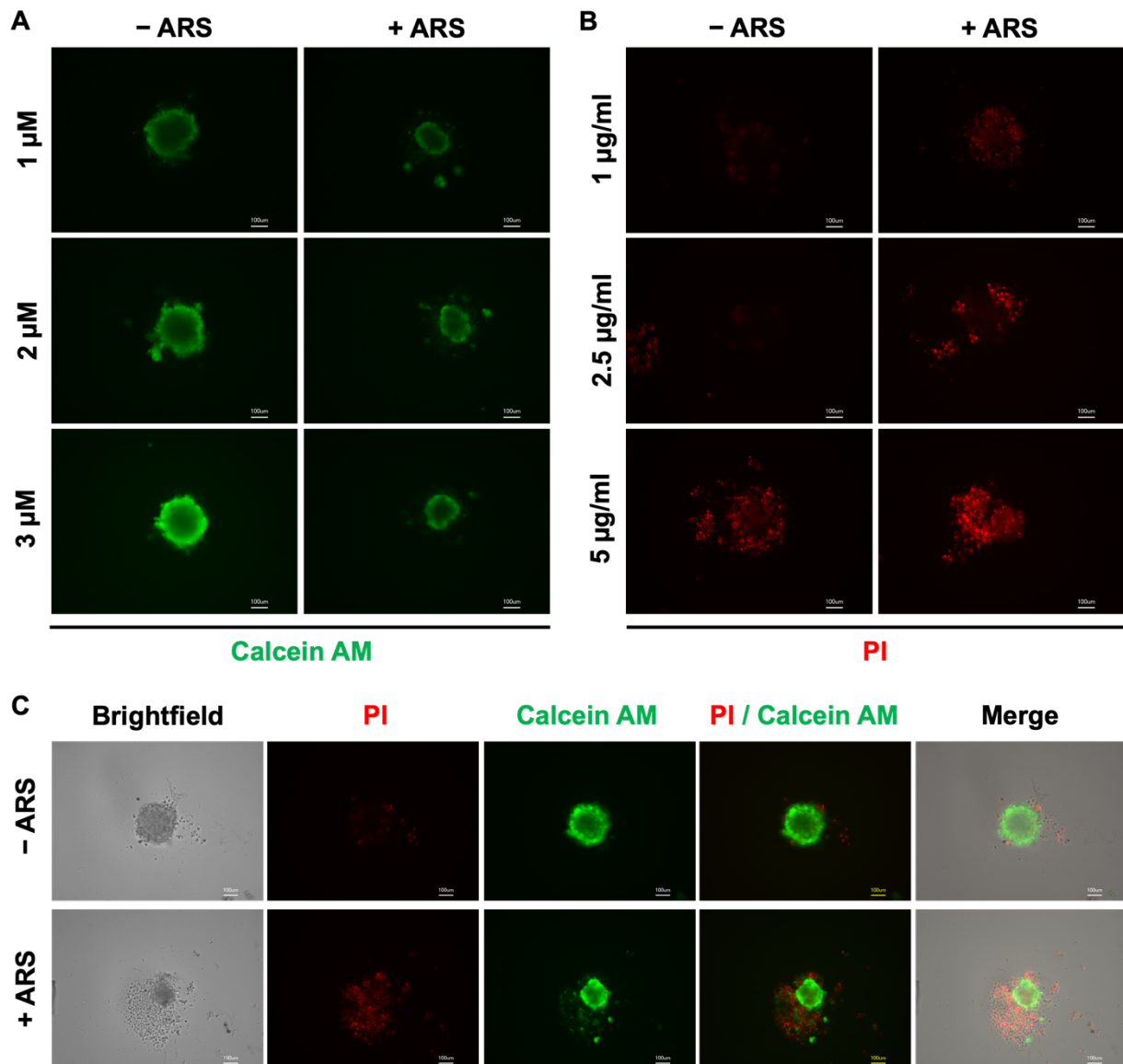


**Figure 33 Live-dead staining of H358 spheroids**

*In situ* staining of H358 spheroids after 4 days in culture with or without 1  $\mu\text{M}$  ARS-1620 treatment for 72 hours using different concentrations of **(A)** calcein AM or **(B)** propidium iodide; N=2. **(C)** Brightfield images and double-staining with 2.5  $\mu\text{g}/\text{mL}$  propidium iodide and 1  $\mu\text{M}$  calcein AM of H358 spheroids *in situ* after 72 h treatment with 1  $\mu\text{M}$  ARS-1620 compared to the control. N=2; scale bars = 100  $\mu\text{m}$ .

To finally confirm the localization of the dead versus the living cells in the 3D cultures *in situ* without the necessity of a challenging medium change or fixation of the spheroids with following staining procedures in an automated process, a live-dead staining based on calcein AM and propidium iodide (PI) was tested for its capability to detect viable and necrotic or apoptotic cells. The different applied concentrations of 1, 2 or 3  $\mu\text{M}$  calcein AM were throughout sufficient to stain living cells in the 3D spheroids. However, the core of the spheroid exhibited reduced signals compared the surface, indicating poor penetration of the dye into the core of

the spheroids independent of the applied concentration (Figure 33 A). The staining with propidium iodide in contrast only delivered weak signals using a concentration of 1  $\mu\text{g}/\text{mL}$ . Applying 2 or 3  $\mu\text{g}/\text{mL}$  propidium iodide however allowed to clearly identify the dead cells and pointed out an increase of dead cells after treatment with ARS-1620 compared to the control spheroids (Figure 33 B). Merging of calcein AM and PI staining eventually provided evidence about the specific localization of dead and living cells in the 3D cultures. The disintegrated cells including the peripheral debris were mainly stained by PI while the intact spheroid itself was stained by calcein AM. Overlay with the brightfield image also demonstrated the specificity of the applied staining dyes (Figure 33 C).

Taken together, the reduction of spheroid sizes, the activation of caspase-3 and -7 as well as the live-dead staining after ARS-1620 treatment pointed out the sensitivity of H358 tumor spheroids towards the KRAS<sup>G12C</sup>-inhibitor. Thereby, ARS-1620 proved to be suitable for a targeted therapy drug testing in H358 spheroids in a proof-of-concept automation process of 3D NSCLC models.

### 3.3.4 Transfer of methodology to other cell types

To validate the established methods for H358 spheroids for a general automation of 3D models, it is mandatory to show that the workflow can be readily translated also to other cell types and tumor entities. Therefore, the breast cancer cell line MDA-MB 231 and adipose-derived stem cells (ASCs) used by partners in the research consortium (Prof. Blunk, M.Sc. Watzling, Department of Trauma, Hand, Plastic and Reconstructive Surgery, University Hospital Würzburg) were tested for their capability to form spheroids under the pre-defined conditions and subsequently a live-dead staining with calcein AM and PI was performed.

In parallel to the generation of H358 cells in ULA-coated 96-well plates, 1,000 MDA-MB 231 cells or ASCs were seeded in each well. Additionally, a coculture approach of the two cell lines was performed, seeding 500 cells of each cell type simultaneously. Here, MDA-MB 231 cells alone clearly failed to form compact spheroids under these conditions. For 96 h in culture only loose, single cells could be detected. Still, live-dead staining held evidence that the breast-cancer cells stayed viable as the floating cells were almost exclusively stained by calcein but not PI. In contrast, ASCs formed compact spheroids with clearly defined borders within 24 h in culture and remained stable for at least 96 h. Noteworthy, disintegrated cells in the periphery were completely absent in these models. Live-dead staining showed only weak signals for PI while the spheroids were positively stained by calcein AM. Coculturing ASCs and MDA-MB 231 also resulted in the generation of compact spheroids within 24 h of culture. However, the 3D aggregates appeared less densely structured compared to ASC monoculture spheroids and single peripheral disintegrated cells were detected after prolonged culture time. Also, for the coculture 3D spheroids only minor signals were detected for PI staining, while calcein AM exclusively stained all cells (Figure 34).

Although, MDA-MB 231 as well as HCC827 cells failed to form compact spheroids with the applied methodology (described above; see Chapter 3.3.1), cell lines with a high intrinsic capability for spheroid formation could be directly translated into the process of spheroid formation and subsequent live-dead staining.

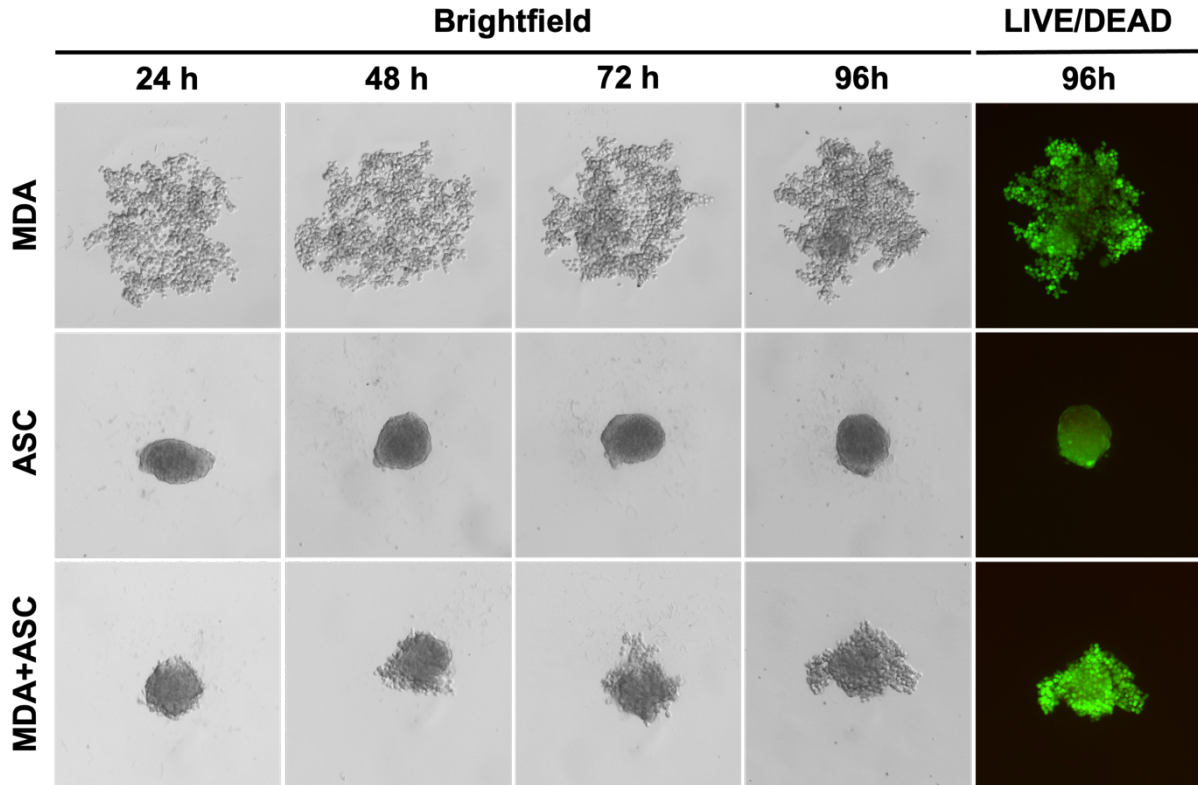


**Figure 34 MDA-MB231, ASC and co-culture spheroids**

Brightfield images at different timepoints of culture of MDA-MB 231, ASCs or coculture of both cell lines seeded in ULA-coated 96-well plates, as well as live-dead staining with 2.5  $\mu\text{g}/\text{mL}$  propidium iodide and 1  $\mu\text{M}$  calcein AM after 96 h in culture. Pictures were recorded with an automated microscopy unit in the robotic platform without defined scale bar. N=3.

### 3.3.5 Translation of the manual process to automation in a robotic platform

After definition of a manual workflow for the generation of 3D NSCLC spheroids and the validation of two different *in situ* assays to determine the efficacy of targeted therapies by microscopy, the single process steps as well as the specific time schedule for the method was specifically defined to finally allow translation into the robotic platform.

The workflow starts with detachment of the cells in 2D cultures und subsequent cell counting. Afterwards, a cell suspension with a final concentration of  $1 \times 10^4 \text{ cells}/\text{mL}$  must be prepared to subsequently seed 100  $\mu\text{l}$  growth medium containing 1,000 cells in each single well of the ULA-coated 96-well plates. After centrifugation the plate is placed in an incubator for 24 h before the first brightfield picture of the spheroids is recorded. Directly afterwards the treatment with the targeted therapy to be tested is performed using a range of concentrations, also including a solvent control. From now on, brightfield pictures are again recorded every 24 h until day 4

in culture. In the last step, a live-dead staining is performed using 1  $\mu\text{M}$  calcein AM and 2,5  $\mu\text{g}/\text{mL}$  PI. After 2h incubation under standard conditions, fluorescence pictures are recorded, and the 3D culture is discarded afterwards (Figure 35). The efficacy of the tested anti-cancer therapies should be evaluated by an automated detection and evaluation of the spheroid areas in comparison to the untreated control as well as by live-dead staining, giving the further possibility to automatically quantify the ratio of pixels in the PI versus the calcein AM staining. To simplify the translation of spheroid generation and subsequent drug testing, the process was further broken down into the single steps the two-arm robot needs to perform within the workflow. These steps include cell detaching and counting, adjusting cell suspension, and seeding, brightfield imaging, drug treatment and live-dead staining. Via this modularization of the workflow, adaptations regarding time schedule, tested anti-cancer drugs and the number of cells for spheroid generation can be readily adapted for the desired experiment. The modular steps were further subdivided into single actions, representing the necessary movements of the robot, the required material as well as the exact volumes of reagents. Finally, a decision tree was implemented based on a counter system adding plus 1 after each round of brightfield imaging. Thereby, the following step in the experimental procedure is clearly defined throughout the workflow (Figure 36). This process could eventually be translated into the robotic platform by the cooperating engineers of the Fraunhofer ISC in Würzburg (data not shown, unpublished data).

In summary, a proof-of-concept process for automated drug testing based on H358 spheroids and the KRAS<sup>G12C</sup>-inhibitor ARS-1620 could be defined and the validation of therapeutic efficacy by *in situ* measurement of spheroid areas as well as live-dead staining with calcein AM and PI was established.

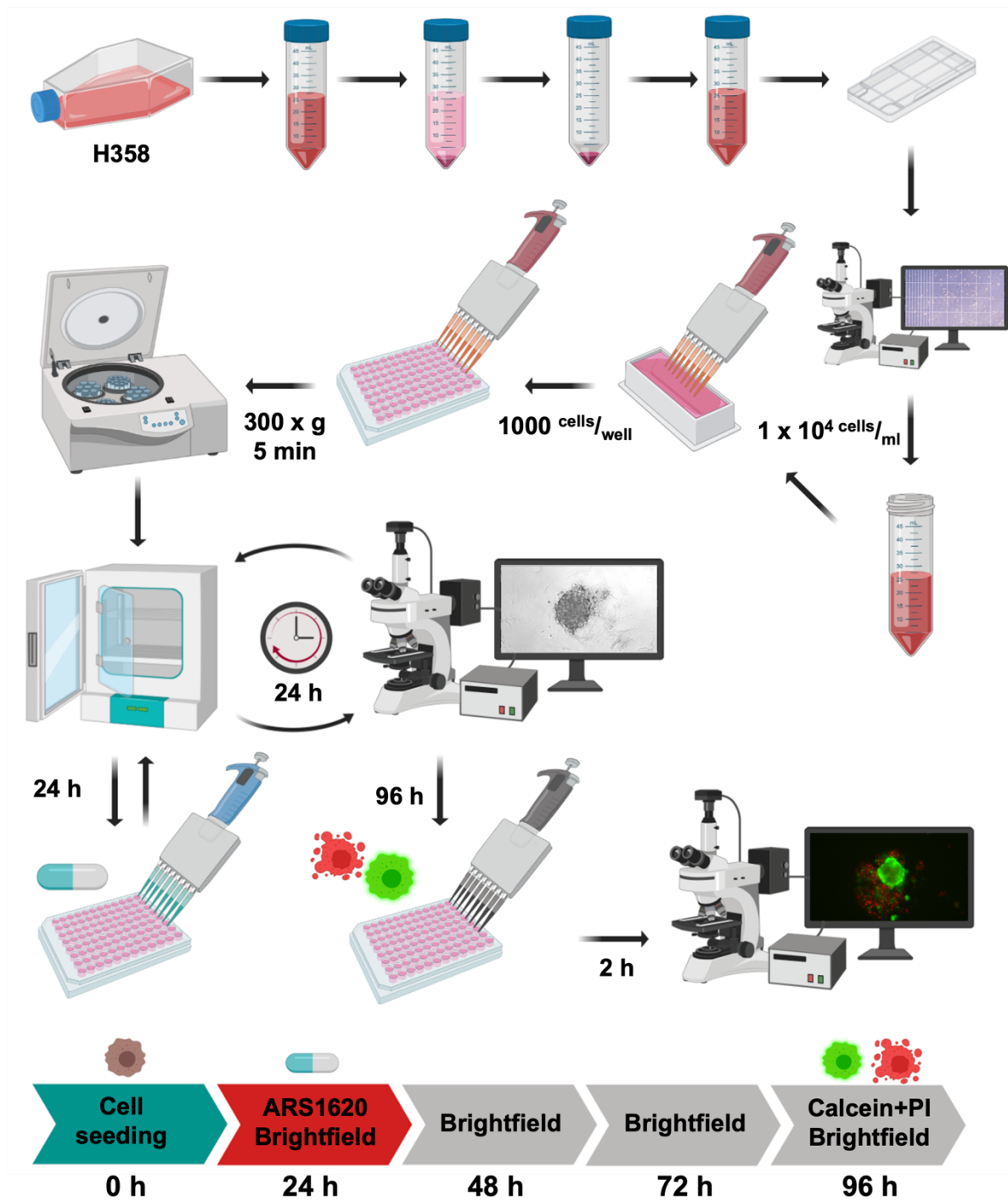


**Figure 35 Schematic workflow of spheroid generation and drug testing**

The schematic workflow depicts the single working steps necessary to be translated to the robotic system for H358 spheroid generation and subsequent testing of targeted therapies, here represented by ARS-1620. The time schedule illustrates the different timepoints in culture when specific work steps need to be performed. Figure was created with BioRender.

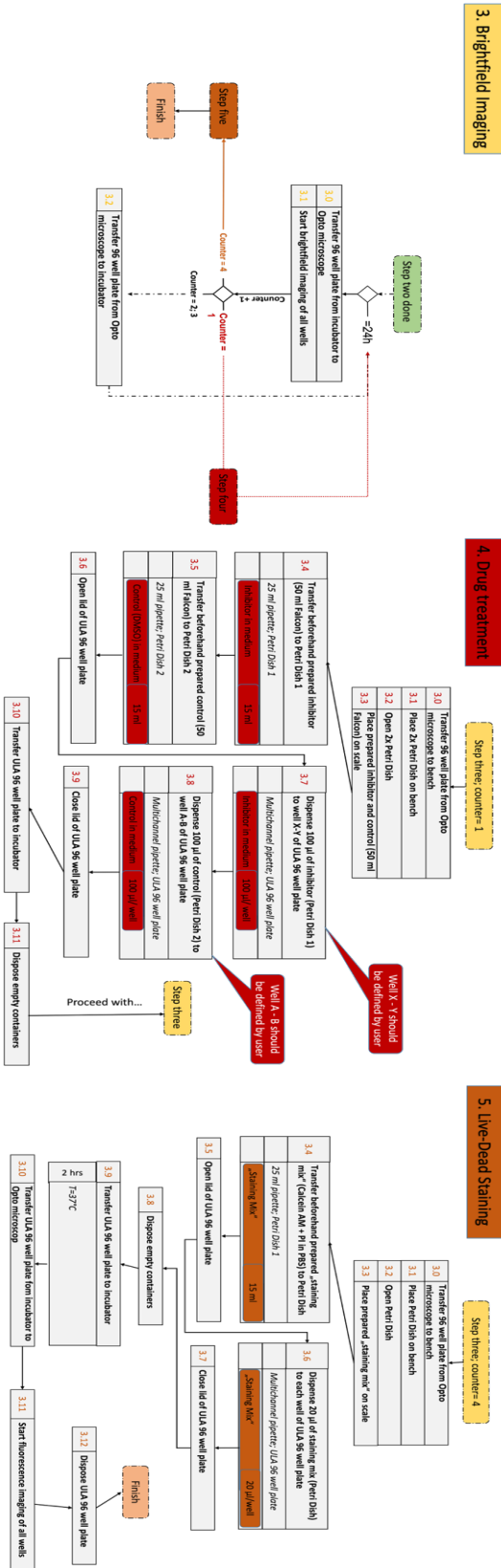
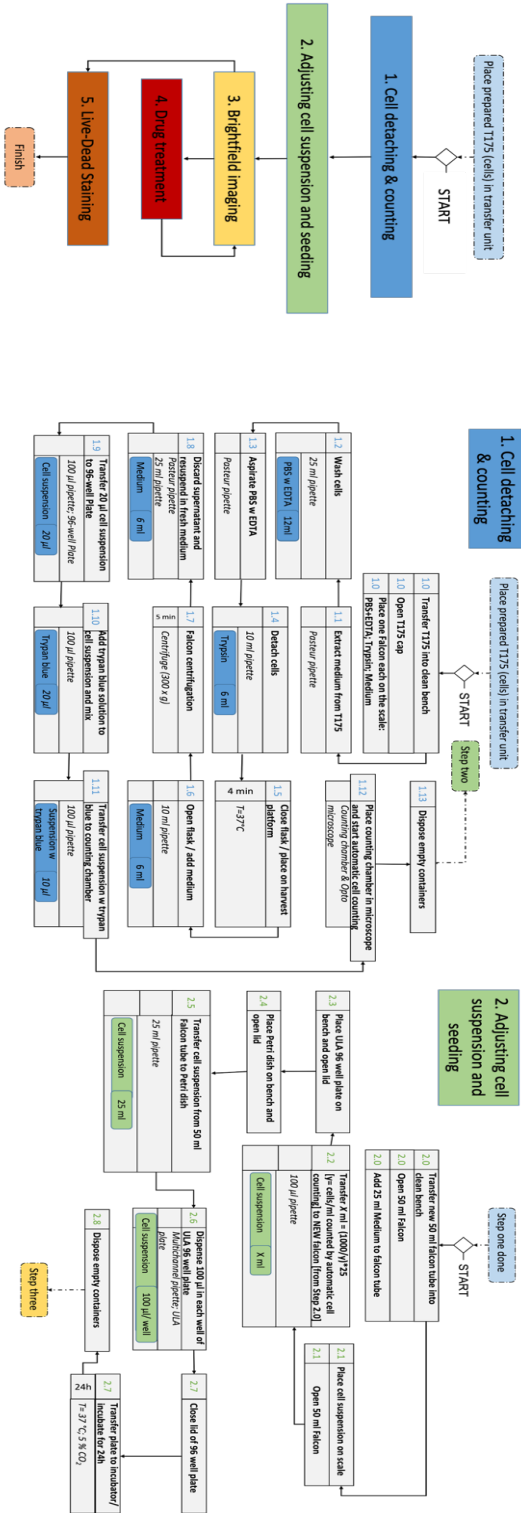


Figure 36 Detailed workflow for translation into the robotic platform

The chart shows the defined steps including the single actions with volumina, reagents and time schedules as a template for programming the robot. In total, the process of spheroid generation can be subdivided in five subprocesses. The subprocess = brightfield imaging can be further used to implement a counter system, allowing to define a decision tree for the next acquired subprocess.



## 4 Discussion

In this thesis, KRAS<sup>G12C</sup>-biomarker could be successfully developed and characterized with a specific focus on EMT and *c-MYC* expression. While the described phenotype of *in vivo* mouse models in regards of high proliferation, invasion and immune modulatory characteristics was observed on the SISmuc models, the drug testing with the KRAS<sup>G12C</sup>-inhibitor ARS-1620 demonstrated that neither EMT nor *c-MYC* expression were directly predictive for KRAS-targeted therapy in the test system. HCC44 cells on the SISmuc showing a limited response towards ARS-1620 could be defined as a surrogate model to test combination strategies to break resistances. With combined inhibition of AURKA and KRAS<sup>G12C</sup> in this tumor models being most effective to overcome the resistant phenotype in this model, testing of alisertib and ARS-1620 among the panel of different KRAS<sup>G12C</sup>-mutated cells on the SISmuc suggested the expression of *c-MYC* as a predictive biomarker for the efficacy of this combination therapy.

The SISmuc tumor models could be further introduced as an *in vitro* test system for safety and efficacy assessment using a novel HSV-1 based OV. Here, definite differences regarding the specificity of the non-attenuated versus the attenuated virus became evident in the coculture models, according to the infection of fibroblasts. While fibroblasts were not permissive for the attenuated virus, oncolytic effects were reduced in parallel in the 3D models. The attenuated virus furthermore exhibited specific infection of HCC44 cells, representing a more advanced and aggressive NSCLC phenotype.

Finally, H358 cells showing a reproducible formation of compact spheroids, met the requirements for establishing a proof-of-concept process for automated development of 3D spheroids with a subsequent drug testing. A live-dead staining as well as the area measurement of the spheroids after treatment with ARS-1620 could be introduced as *in situ* assays to determine the drug efficacy, which was eventually successfully translated to the robotic platform.

### 4.1 Patient stratification for KRAS-mutated NSCLC based on SISmuc tumor models

#### 4.1.1 KRAS-biomarker models as representers for different phenotypes

Although both harboring the KRAS<sup>G12C</sup> mutation, the characterization pointed out decisive differences in the phenotype of H358 and HCC44 cells. In accordance with earlier publications [130, 131], in 2D a more progressed EMT was observed in HCC44 cells compared to H358 cells, indicated by the expression patterns of epithelial and mesenchymal markers. However, H358 dedifferentiated when cultured in 3D on the SISmuc pointed out by higher expression of the mesenchymal marker VIM compared to 2D, evaluated by RT-qPCR and immunofluorescence staining. Nevertheless, immunofluorescence staining, the enriched EMT hallmark as well as the DEGs of EMT markers from RNAseq analysis hold evidence that EMT is more progressed in HCC44 cells not only in 2D but also on the SISmuc models. Noteworthy, central EMT-transcription factors showed different expression between the tumor models.

While SNAI1 and TWIST were not significantly changed, ZEB1 as well as ZEB2 showed higher expression in HCC44 cells, whereas SNAI2 was controversially higher expressed in H358 cells. As previously described for 2D cultures, EMT transcription factors are not exclusively differentially expressed and further show low dynamics when the EMT phenotype is altered, contributing to the partial EMT state observed in cancers [132]. Considering the controversial discussed role of EMT for invasive potential of cancer cells, which was also observed here in HCC44 SISmuc models, it is further known that Snail and Twist expression alone in mouse tumor models is not capable to induce metastasis, while ZEB1, being higher expressed in HCC44 models, resulted in invasion and metastasis in the same *in vivo* models [56]. In the 3D models based on KRAS<sup>G12C</sup>-mutated PDX-derived cell lines a higher invasiveness with more progressed EMT was indicated by the tissue architecture but was however not quantified. In contrast, the successfully induced EMT in H358 cells by stimulation with TGF- $\beta$  only resulted in negligible increase of invasion compared to HCC44 cells in the ground state, demonstrating that induction of EMT alone might not be sufficient for invasion through the basement membrane.

While the importance of EMT for invasion was not clearly unraveled by the models, a definitive correlation between EMT and the stemness character of the tumor cells was pointed out. The cell surface glycoprotein CD44 is described as a stem cell marker for a variety of tumor entities including NSCLC [133]. In all KRAS-biomarker models investigated, CD44 was expressed in the cells with progressed EMT-phenotype while cells with epithelial characteristics were defined as CD44 negative. The connection of EMT and stemness observed on the tumor models is in agreement with the literature, showing that EMT induces stemness properties in cancer cells by a variety of signaling processes [134, 135].

Additionally, H358 and HCC44 tumor models also exhibited decisive differences in the proliferation of the tumor cells. However, this aspect could only be evaluated on the 3D models. In 2D the proliferation rates for both cell lines were artificially high, pointing out a major problem of drug testing in conventional cell culture. Reduction of proliferation rates to physiologic levels in 3D models is described to have an immense impact on the predicted drug response [136, 137]. In NSCLC the mean proliferation index validated for lung adenocarcinoma is 25.8 % and high indices over 25 % are negative prognostic factors independent of the cancer stage [138]. Thereby, H358 and HCC44 with a mean proliferation index of 18.4 % and 36.9 %, respectively, are representative for the clinical situation, in contrast to 2D cultures where both cell lines exhibited more than 90 % proliferation.

Finally, also the expression of *c-MYC* showed decisive differences between the KRAS<sup>G12C</sup>-biomarker models. HCC44 cells harboring an amplification of the wildtype *c-MYC* gene [139] displayed higher expression of *c-MYC* on both protein as well as mRNA level compared to H358 cells. High *c-MYC* expression in this cell line is also described in the literature [140]. The

overexpression of *MYC* might also contribute to the higher proliferation in HCC44 cells. Regarding, the *c-MYC* expression in the SISmuc models based on the PDX-derived cell lines, the expression of the transcription factor was the highest for the two models exhibiting partial EMT, LXFL 1072 and LFXL 1674. The latter one also carrying an amplification of *c-MYC* [123]. It is well studied that overexpression of *c-MYC* is an inducer of EMT in cancer [141, 142]. Still, the completely mesenchymal LXFA 2184 cells showed lower expression of *c-MYC*. A complete mesenchymal transformation is however usually not observed for tumor cells in the clinics [143].

In summary, the KRAS-biomarker models displayed decisive differences in EMT, stemness, proliferation, invasion as well as *MYC*-expression and thereby represented different phenotypes as a perfect basis for subsequent drug testing and investigation of potential biomarkers.

#### **4.1.2 HCC44 cells on the SISmuc as surrogate models for advanced stage NSCLC with MYC and KRAS cooperation**

Comparing HCC44 to H358 tumor models, HCC44 cells on the SISmuc proved to represent NSCLC in an advanced stage with a more malignant phenotype. The high proliferation rates, progressed EMT as well as invasive growth are typical characteristics of aggressive tumors. Also, the co-mutations in HCC44 point towards high aggressiveness of this lung adenocarcinoma cell line. Harboring mutations in *TP53*, *STK11* and *KEAP1* [144] together with the *KRAS* gain-of-function mutation points towards an immunologically “cold” tumor with chemoresistance, poor prognosis and low benefits of treatment with immune checkpoint inhibitors [68, 145].

Additionally, although not in a black and white pattern, the expression of cytokines and chemokines supporting a pro-tumoral immune microenvironment showed higher expression in HCC44 3D models. IL1B, highly expressed in HCC44 cells, for instance is a mediator of tumor-associated inflammation, angiogenesis, and metastasis in lung cancer [146]. The pro-inflammatory IL-6 and TNF- $\alpha$  both displaying significantly higher expression in HCC44 models are described to positively regulate the proliferation and invasion in NSCLC [147]. Vice versa chemokines initiating the migration and activation of immune cells supporting tumor suppression and anti-tumor immunity CXCL10 or CXCL11 [148] exhibited lower expression in HCC44 cells compared to H358 cells in 3D. Last but not least, also the GSEA pointed out a more inflammatory phenotype in HCC44 tumor models, while H358 cells showed an enriched interferon alpha response. The latter one is reported to have a variety of anti-tumoral effects, including the direct inhibition of tumor growth as well as attraction and activation of immune cells in the TME [149].

Also, the cooperative effect of KRAS and MYC described for *in vivo* models was well represented in HCC44 tumor models. Kortlever *et al.* observed invasive tumor growth in *Myc*-

overexpressing and *Kras*-mutated lung adenocarcinoma in mouse models [73]. In agreement HCC44 cells exhibited invasive growth and penetration through the preserved basement membrane of the biological matrix SISmuc. The described increased proliferation index determined with KI67 staining of tumors in the same mouse models harboring high *Myc* expression and *Kras* mutation was also evident in HCC44 cells compared to *KRAS*-mutated H358 cells with lower expression of the transcription factor. Finally, the immune evasion in the corresponding *in vivo* models was mediated by IL23 and Ccl9, resulting in repulsion of T-cells and NK-cells but recruitment of macrophages inducing angiogenesis [73]. While IL23 was not differentially expressed in HCC44 compared to H358 tumor models, on the SISmuc models low expression of *CXCL10* and *CXCL11* was evaluated in HCC44 models, both chemokines are responsible for attracting T-cells and NK-cells [150]. *Ccl9* on the other hand is a murine gene, of which the human homologue is *CCL15* [151], showing no differential expression between the two *KRAS*<sup>G12C</sup>-biomarker models. Still, *CCL5* and *CXCL5* were highly expressed by HCC44 cells mediating the recruitment of macrophages into the TME [150]. Further considering the enriched hallmark gene set for hypoxia, induction of angiogenesis would be suggested for HCC44 tumor models.

Regarding the influence of *KRAS* and *MYC*-cooperation for metabolism, alterations in lipid metabolism are described pointing towards increased cholesterol uptake and storage of lipids in droplets [74]. While the responsible genes for this altered metabolism detected in the *in vivo* model described by Hall *et al.* were not expressed in a similar pattern in HCC44 models, GSEA clearly showed a significant increase in adipogenesis related genes of the HCC44 tumor cells harboring the *MYC*-amplification and the *KRAS*<sup>G12C</sup> mutation cultured on the SISmuc models. Finally, considering the influence of *KRAS* and *MYC* cooperativity on the immune system in the TME described by Mugarza *et al.* [75], concordant results were evaluated for the *KRAS*<sup>G12C</sup>-biomarker models on the SISmuc. There it was observed that the downregulation of interferon pathways is mediated in *KRAS*-mutated cancer cells via the expression of *MYC*. In parallel, GSEA comparing *KRAS*-mutated HCC44 cells overexpressing *c-MYC* to *KRAS*-mutated H358 cells with low *c-MYC* expression revealed an enrichment of the interferon alpha response in H358 tumor models. The described responsible interferon-related genes *IRF7*, *IRF9* and *STAT2* [75] all showed in accordance with this study comparably lower expression in HCC44 tumor models.

To put it in a nutshell, the *in vivo* described effects of *KRAS* and *MYC* cooperativity in regards of invasion, proliferation, metabolism, and immune evasion were represented in HCC44 SISmuc tumor models *in vitro* and contribute to the advanced stage, aggressive phenotype of this NSCLC cell line.

#### 4.1.3 Differential sensitivity of H358 and HCC44 tumor models towards KRAS<sup>G12C</sup>-inhibition

Suggested by the advanced stage and aggressive NSCLC phenotype in HCC44 cells, the tumor models exhibited low sensitivity towards the KRAS<sup>G12C</sup>-inhibitor ARS-1620 in comparison to H358 cells. In agreement with Janes *et al.* [42] and Misale *et al.* [152] an IC<sub>50</sub>-value in the sub-micromolar range was determined for H358 cells while HCC44 cells showed an intermediate sensitivity with an IC<sub>50</sub>-value between 5.0 and 10.0 μM. Cultured in 3D on the SISmuc however reduced the sensitivity of both KRAS<sup>G12C</sup>-mutated cell lines towards ARS-1620, as 50 % viability of the cells were determined for H358 cells between 1.25 μM and 2.5 μM, while for HCC44 cells no considerable reduction of viability was observed even applying 5 μM. Noteworthy, this finding is in contrast with the original publication, in which ARS-1620 was described for the first time, where the IC<sub>50</sub>-values were drastically reduced in 3D models using spheroids compared to the same cells in 2D [42]. In accordance, a strong sensitivity of H358 3D spheroids towards ARS-1620 was also observed in this study, establishing the proof-of-concept process for automated drug testing. Nevertheless, ARS-1620 treatment with 1 μM resulted in a significant reduction of the proliferation indices and a dose-dependent induction of apoptosis in H358 tumor models, whereas HCC44 models neither displayed lower proliferation nor increased apoptosis after treatment.

On protein level it was revealed, that ARS-1620 reduced the phosphorylation of the two major downstream mediators of KRAS, namely AKT and ERK in H358 but not HCC44 cells. Here, however the phosphorylation of ERK was distinct, whereas phosphorylated AKT remained in H358 cells to some extent even after ARS-1620 treatment. As the PI3K/AKT/mTOR signaling is dependent on both KRAS as well as RTKs, it is hypothesized that both signals need to be inhibited to completely suppress AKT phosphorylation [153]. Furthermore, KRAS<sup>G12C</sup> mainly activates RAL GTPases and the ERK pathway, while the phosphorylation of AKT is lower for this mutated form of KRAS even compared to the wild-type protein [154].

The GSEA comparing the gene expression of untreated versus ARS-1620 treated 3D models, further pointed out the resistant phenotype in HCC44 cells. Proliferation and cell cycle related gene sets that were significantly reduced in ARS-1620 treated H358 tumor models, showed enrichment in HCC44 models after the treatment. Here, it needs to be emphasized that ARS-1620 substantially inhibited KRAS<sup>G12C</sup> in both cell lines demonstrated by reduced expression of genes that are usually upregulated by KRAS signaling. This demonstrates that proliferation and survival in HCC44 models was independent of KRAS signaling.

Nevertheless, both H358 and HCC44 tumor models also showed parallel downregulation of the hallmark gene sets for hypoxia, TNF-α and glycolysis after treatment with ARS-1620. Regarding hypoxia, signaling of mutant KRAS was described to enhance hypoxic induction via the hypoxia inducible factor (HIF)-1α [155]. The downstream signaling of KRAS also modulates

the TME in a pro-inflammatory way including the transcription of *TNFA* [36]. KRAS is also responsible for elevated glycolysis in both lung and pancreatic cancer cells by increasing the expression of the glucose transporter *GLUT1* and glycolytic enzymes via the ERK signaling pathway [156]. Thereby considering the inhibition of KRAS with ARS-1620 in both models the observed results are comprehensible.

Looking into the DEGs of H358 tumor models after treatment with ARS-1620, *LOX* and *DUSP6* were lower expressed with high significance. While *LOX* is induced under hypoxic conditions by HIFs [157] and thereby underlines the reduced hypoxic signaling, the lower expression of the tumor suppressor *DUSP6* is based on the decreased MAPK-signaling after KRAS-inhibition. *DUSP6* is expressed by MAPK-signaling and encodes a MAPK phosphatase that negatively regulates this signaling pathway via a feedback loop [158]. Accordingly, the lower expression demonstrates that the MAPK signaling pathway is inhibited by ARS-1620 in H358 tumor models. *TMPRSS2* showing higher expression after treatment of H358 models is in contrast described to be a favorable prognostic factor in lung adenocarcinoma [159]. Comparatively, only few genes showed differential expression in HCC44 models. Two of which where the lower expressed *MMP1*, also being strongly associated with KRAS according to the STRING database [160], and the higher expressed *EIF3CL*. The latter one could however contribute to a putative resistance mechanism of HCC44 cells, as EIF3C promotes cell growth, protein synthesis but also proliferation [161].

In summary, the data proved that H358 tumor models displayed sensitivity towards the treatment with the KRAS<sup>G12C</sup>-inhibitor, while HCC44 tumor models exhibited a resistant phenotype. Thereby the models perfectly suited as surrogate models for responders or non-responders, respectively, towards KRAS-targeted therapies.

#### **4.1.4 Neither EMT nor c-MYC are exclusive predictive biomarkers for KRAS-targeted therapies**

In contrast to previous publication, drug testing in 6 different KRAS<sup>G12C</sup>-biomarker models on the SISmuc did not show a direct correlation between ARS-1620 sensitivity and the EMT-phenotype of the corresponding cells. While HCC44 cells with a comparatively progressed EMT showed resistance towards KRAS<sup>G12C</sup>-inhibition, the models based on the PDX-derived models did not confirm EMT as generally valid predictive biomarker for KRAS-targeted therapies. LXFA 983 cells exhibited the most epithelial phenotype in regards of EMT-marker expression in both 2D and 3D but depicted however the lowest sensitivity towards ARS-1620 under both conditions. In contrast, LXFA 1674 cells with a partial EMT were among the most sensitive cell lines in both 2D and 3D. Additionally, the GSEA of H358 tumor models indicated reduced EMT after ARS-1620 treatment, pointing against EMT as acquired resistance mechanism for KRAS<sup>G12C</sup>-inhibition. Finally, TGF- $\beta$  induced EMT was not sufficient to mediate resistance towards ARS-1620 considering viability, proliferation, and apoptosis, although EMT

could be successfully induced in H358 cells demonstrated by reduced apical-basal cell polarity, reduced E-cadherin and increased *VIM* as well as *CD44* expression. This finding contradicts the results of Adachi *et al.* where the  $IC_{50}$ -value towards sotorasib for TGF- $\beta$  treated H358 and LU65 cells significantly increased in 2D cultures compared to the naïve cells [54]. The treatment with TGF- $\beta$  is described to result in a higher ratio of GTP-bound KRAS and thereby should lead to lower occupancy of KRAS<sup>G12C</sup> with the corresponding inhibitor [162]. The reason why TGF- $\beta$  did not induce resistance towards ARS-1620 on SISmuc models remained elusive. However, parallel observations were made for EGFR-biomarker models on the SISmuc where the treatment with TGF- $\beta$  did concordantly not mediate resistance towards the EGFR-inhibitor gefitinib [128], which is also controversially described in literature for 2D cultures [163]. Still, TGF- $\beta$  signaling is just one among different EMT-inducing pathways. Other EMT-inducers like WNT-, NOTCH- or HH-signaling were also described to mediate chemoresistance for a variety of cell lines of different tumor entities [164].

Besides the EMT-phenotype, also the expression of *c-MYC* did not correlate with ARS-1620 sensitivity in the KRAS<sup>G12C</sup>-biomarker models. While HCC44 cells harboring a *c-MYC* amplification and overexpression were resistant towards ARS-1620, the two cell lines with the highest *c-MYC* expression among the PDX-derived cell lines exhibited a higher sensitivity towards the KRAS<sup>G12C</sup>-inhibitor compared to their counterparts LXFA 983 and LXFA 2184, showing lower levels of *c-MYC*. Noteworthy, with a viability of around 70 % after treatment with ARS-1620 neither LXFL 1674 nor LXFL 1072 models can be however defined as sensitive towards the treatment. Thereby, *MYC* might be still represent a contributor to a diminished therapeutic efficacy of KRAS-inhibition, while it on the other hand was not general predictive on the SISmuc models. Via stabilization and activation *c-MYC* is regulated by KRAS signaling [162] and *c-MYC* is described as mediator of resistance for a multitude of different anti-cancer therapies [165-167]. Additionally, the inhibition of *MYC* by omomyc in KRAS<sup>G12D</sup> mouse models massively increased the overall survival of the corresponding mice [168]. By evaluating genetic alterations of patients treated with sotorasib Zhao and her colleagues also found low response rates in all KRAS<sup>G12C</sup>-mutated tumors harboring an additional *c-MYC* amplification [169]. However, the corresponding genotype was only detected in 3 out of 43 patients in this clinical study and several other putative mutations rendering resistance to the treatment were detected in other patients, underlining the hypothesis that overexpression of *MYC* reduces the sensitivity towards KRAS<sup>G12C</sup>-inhibition but is not an exclusive mechanism. With additional respect to the *MYC* and KRAS cooperativity in regards of metabolism, invasion and the immune TME described above (Chapter 12.1.2), the expression of *MYC* in KRAS<sup>G12C</sup>-mutated tumors represents a reasonable biomarker for the clinics, even though it was not exclusively predictive for KRAS-targeted therapies in this work.

#### 4.1.5 Sensitizing effect of AURKA inhibition for KRAS-inhibition in MYC-overexpressing tumor cells

Drug testing with a panel of different inhibitors on HCC44 cells, pointed out a generally higher chemoresistance in 3D models compared 2D cultures. Besides it is worth to mention, that for all tested combinations an additive effect of ARS-1620 was observed in 3D, while the  $IC_{50}$ -values comparing mono- to combination therapies did not show major differences. This underlines the influence of the applied *in vitro* model system for the prediction of therapeutic efficacy. Finally, there was evidence that MTT-assays underestimated the efficacy of certain drugs in comparison to the evaluated relative cell number on the models after treatment. The MTT assay quantifies cell viability via the determination of mitochondrial activity, as the tetrazolium salt MTT is reduced to formazan by dehydrogenases in the mitochondria [170]. The underestimation of growth inhibition by this assay was previously described for a variety of inhibitors and here especially metabolism and oxidative stress can influence the outcome of this viability assay [171]. Thereby, especially the results of MTT assays applying drugs strongly interconnected with cellular metabolism need to be interpreted with caution. Here, for example metformin was combined with ARS-1620, as HCC44 cells additionally harbor a *STK11* mutation. In the MTT-assay an increased viability was observed after metformin treatment, while metformin as an AMPK-activator massively changes the cellular metabolism and regulates mitochondrial activity [172].

Regarding the drug testing to break primary resistance in HCC44 models, interfering with the RTK signaling only resulted in negligible reduction of viability in HCC44 models, also when combined with ARS-1620. Combining RTKIs or the SHP2-inhibitor with KRAS<sup>G12C</sup>-inhibitors is justified by the fact that active GFR signaling favors the GTP-bound confirmation of KRAS in which KRAS<sup>G12C</sup>-inhibitors fail to bind to the oncoprotein [41]. However, GSEA of HCC44 tumor models pointed out that KRAS<sup>G12C</sup> is essentially occupied by ARS-1620 monotherapy in HCC44 cells, as reduced enrichment of KRAS regulated genes was significantly pointed out. This strongly indicates that the reason for the intrinsic resistance of the KRAS<sup>G12C</sup>-mutated cell line is located downstream of KRAS. Still, crizotinib inhibiting c-MET and ALK [173] showed a low  $IC_{50}$ -value in 2D and was the second most effective inhibitor in 3D for HCC44 cells. Western blot of H358 tumor models after treatment with ARS-1620 revealed that after KRAS<sup>G12C</sup>-inhibition the phosphorylation of c-MET was diminished in H358 cells, suggesting a positive feedback regulation in H358 models. This was however not observed in HCC44 cells, where phosphorylation of MET remained unaltered after ARS-1620 treatment. RNAseq data further provided evidence that the c-MET ligand HGF was higher expressed by H358 cells in the ground state compared to HCC44 cells, but ARS-1620 treatment did not change the expression of the growth factor in both models. Thereby, it is suggested that the observed



feedback loop is not based on paracrine but on intrinsic signaling and might be interrupted in HCC44 cells and causative for the measured effects of crizotinib.

From the panel of different inhibitors tested to overcome the primary resistance of HCC44 tumor models towards ARS-1620, the AURKA inhibitor alisertib proved to be most efficient, and the sensitizing effect of alisertib directly correlated with the expression of *c-MYC* in the corresponding KRAS<sup>G12C</sup>-models. The results of the 3D *in vitro* models based on H358 and HCC44 cells were further used to define an *in silico* signaling network for KRAS<sup>G12C</sup>-mutated cancer cells by the Chair of Bioinformatics in Würzburg. The network considers the characterization, the sensitivity towards KRAS-targeted therapies as well as reported co-mutations. The network topology allows simulated drug-testing also of combinatorial treatments and confirmed the *in vitro* results, demonstrating increased apoptosis of HCC44 cells after combined AURKA and KRAS<sup>G12C</sup> inhibition in the *in silico* model [128].

As a member of the family of serine/threonine kinases the AURKA is a crucial component for cell division and regulator of mitosis, thereby also representing an oncogene [174]. It is reported, that AURKA can upregulate the expression of *c-MYC* and vice versa *c-MYC* binds to the AURKA promoter leading to a higher expression of the kinase [175]. In *MYC*-overexpressing HCC44 tumor models also a high expression of AURKA was shown, while in H358 tumor models with low *MYC*-expression exhibited lower AURKA expression. The highest efficacy of combined AURKA- and KRAS<sup>G12C</sup>-inhibition was evaluated for the two cell lines HCC44 and LXFL1674 harboring a *c-MYC* amplification and overexpression, as well as for LXFL 1072 with high *c-MYC* expression. At the same time, H358, LXFA 983 and LXFL 2184 tumor models with comparatively lower *MYC* expression either showed no or only a marginal sensitivity for AURKA-inhibition with alisertib. This correlation strongly suggests that *c-MYC* expression is predictive for the efficacy of this combination therapy in the corresponding cell line. However, on protein as well as on transcriptional level only a slight reduction of *MYC* expression was suggested after alisertib treatment, seeming disproportionate to the therapeutic effect in regards of viability. Xue *et al.* described that AURKA mediated reactivation of KRAS<sup>G12C</sup> after prolonged KRAS<sup>G12C</sup>-inhibitor treatment and immunoprecipitation demonstrated that KRAS<sup>G12C</sup> does not only interact with CRAF but also with AURKA itself. In line, the authors found that the knock-out of AURKA resulted in enhanced efficacy of KRAS<sup>G12C</sup>-inhibition on the one hand and that reactivation of KRAS after prolonged treatment was prevented on the other hand [176]. Using the AURKA-inhibitor VIC-1911 there is also evidence that synergistic effects of AURKA- and KRAS<sup>G12C</sup>-inhibitors was significantly more pronounced in sotorasib-resistant cells compared to sotorasib-sensitive cells [177]. Noteworthy, high efficacy in this study was described for the cell lines H1792 and HCC44, in contrast to low efficacy in H358 cells. The NSCLC cell line H1792 also carries an amplification of the *MYC* gene [178]. Recently, a phase I clinical trial started for locally advanced or

metastatic NSCLC with KRAS<sup>G12C</sup> mutation testing a AURKA inhibitor alone and in combination with sotorasib [179].

To this end, taking the data of this work and recent research into consideration, it is strongly suggested that AURKA is activated in *MYC*-overexpressing NSCLC and attenuates the efficacy of KRAS<sup>G12C</sup>-inhibitors. AURKA-inhibitors hold the capability to increase the therapeutic efficacy of KRAS-targeted therapies in the corresponding lung cancer cells. Hence, the expression of *c-MYC* in KRAS<sup>G12C</sup>-mutated NSCLC is strongly suggested as a predictive biomarker for the combined inhibition of KRAS<sup>G12C</sup> and AURKA.

#### **4.2 Efficacy and safety assessment of oncolytic viruses on SIS muc tumor models**

With immune checkpoint inhibitors (ICIs) showing beneficial outcomes in lung cancer in the clinics, OV partially depending on comparable mechanisms by combining cell lysis and activation of the immune system appear promising for the treatment of this tumor entity. Viral infections can thereby enhance the local infiltration of immune cells in the TME, as for example described for CD8+ T cells after infection with adenovirus [180]. Pro-inflammatory signals additionally support the recruitment of natural killer (NK) cells and antigen-presenting cells (APC) in the TME after infection with OVs [181]. Thereby the treatment with OVs could additionally sensitize lung cancer for ICIs by modulating the distribution and presence of immune cells in the TME turning a “cold” into a “hot” tumor, suggesting the rational combination of the two immunotherapies [182]. Currently, a multitude of different OVs to treat lung cancer are tested pre-clinically but also several clinical trials are ongoing [183].

2D cultures conventionally used for preclinical testing of OVs *in vitro*, fail to represent the pathologic situation in the clinics and lack the representation of the TME. Accordingly, both the oncolytic efficacy as well as safety testing in 2D may not be representative for cancer *in vivo*. On the one hand, in 2D monolayer cultures the infection of tumor cells by OVs is facilitated, as there is increased contact between the virus and the tumor cells compared to 3D model systems [184]. On the other hand, it was also described that 3D cultures can result in more susceptible tumor cells for viral infection compared to 2D cultures, as it was observed for U-118 MG cells cultured as spheroids infected with the mammalian orthoreovirus T3D [185]. A differential sensitivity towards the myxoma virus, vaccinia virus and maraba virus was similarly observed in ovarian cancer cells cultured in 2D versus 3D spheroids [186]. Also the reduced apical-basal cell polarity contributes to altered susceptibility for viral infection [187]. Furthermore, considering the role of the ECM for limiting viral spread in solid tumors [116], this central aspect is not represented in 2D cultures. Finally, to define the specificity of OVs for infecting tumor cells, direct co-cultures with non-malignant are decisive. Considering these aspects, SIS muc tumor models hold the possibility to co-culture tumor cells and fibroblasts with native ECM and ECM-associated proteins in a 3D environment, and thereby overcome these limitations for preclinical testing of OVs *in vitro*.

In general, the capability for efficacy and safety testing of the novel HSV1-based OVs *in vitro* using SIS muc tumor models could be demonstrated in this work. The non-attenuated platform virus with or without functionalization successfully infected HCC827 tumor cells and induced oncolytic effects in these models, while in A549 both the infection as well as the oncolysis were limited. The viral replication of HSV-1 is closely linked to the proliferation and cell cycle of the host cell. Factors present during the G1/S phase as well as the activation of cyclin-dependent kinases (CDKs) are crucial for the transcription of viral DNA of this virus [188]. Considering the low proliferation indices of A549 cells in 3D of less than 5 % and the interconnection between cell cycle progression and HSV-1 replication, it is suggested that the low proliferation of the tumor cells is causative for the reduced efficacy and lower infection rates in the A549 models. The oncolytic effects on HCC827 cells were further increased for the non-attenuated OVs when the tumor cells were co-cultured with fibroblasts. Primary fibroblasts are described to be in general permissive for HSV-1, although the cells are more effectively infected *in vitro* compared to *in vivo* conditions as a consequence of the ECM building a barrier for viral spread [189]. Hence, additional host cells in cocultures of tumor cells with fibroblasts are provided for viral replication which could result in increased viral titers and thereby higher efficacy of the OVs.

As expected for the OVs without attenuation, the presence of VP21/22a-positive fibroblasts clearly demonstrated that the non-attenuated viruses are not specifically infecting tumor cells. The attenuation of the OVs via the genetic modification of genes involved in the replication in non-proliferating cells and the retrograde axonal transport *UL37* and *UL39* could abolish the infection of fibroblasts in the 3D models going hand in hand with the downside of losing the capability for effectively infecting HCC827 tumor cells even at a higher MOI. Mutations in *UL39* were previously described to reduce viral replication of HSV-1 *in vivo* and leading to reduced neurotoxicity and recombinant HSV-1 harboring a point mutation in *UL37* attenuated viral infection in cell cultures as well as *in vivo* [190, 191]. In accordance to the results on the SIS muc tumor models, knockout of *UL39* further resulted in reduced HSV-1 infection of fibroblasts *in vitro* [192]. Eventually, HCC44 tumor models representing an invasive and more-malignant NSCLC phenotype were successfully infected with the attenuated OVs and resulted in reduced number of tumor cells after infection. *UL39* was partially deleted to limit the viral replication to cells with high proliferation [193] and HCC44 tumor cells exhibited significantly higher proliferation indices compared to HCC827 cells in the 3D models. In summary, the testing of the novel HSV-1 based OVs was successfully carried out in the SIS muc tumor models and demonstrated the efficient attenuation of the OV. This conclusion goes hand in hand with the results of the cooperation partners at Fraunhofer IZI (Leipzig) and Fraunhofer ITEM (Regensburg), where the attenuation of the OV resulted in abolished neurotoxicity in

mouse models and the infection of T-cells with the attenuated virus using different MOIs did not reduce the T-cell viability (data not shown, unpublished data).

Regarding the target control of the OVs, no clear benefit of the PZ- or PNAZ-virus could be observed in comparison to the platform virus on the 3D SISmuc tumor models. Nevertheless, a major drawback of the SISmuc tumor models for testing of OVs in this study was the limitation of downstream assays to validate the oncolytic effects of the viruses. Mainly immunofluorescence staining was carried out to determine the tissue architecture, the number of tumor cells and the proliferation index of the corresponding cells after infection. Regarding the changes in proliferation after infection, it is also reported that HSV-1 infection changes intracellular signaling processes and can up- but also down-regulate the pro-proliferative MAPK pathway [188]. Functional assays to specifically determine apoptotic and necrotic processes or changes in gene expression of the tumor cells after OV-therapy could however not be carried out in this study due to safety issues. Finally, a major pillar of OV-therapy is represented by the activation of the immune system in “cold” tumors besides direct oncolysis [110].

#### **4.3 Established proof-of-concept process for automated drug testing on tumor spheroids**

Using the KRAS<sup>G12C</sup>-mutated NSCLC cell line H358, a proof-of-concept process could be developed including the generation of the 3D models and subsequent drug testing for the transfer to a robotic platform at the Fraunhofer ISC (Würzburg). As previously reported, H358 cells reproducibly formed compact spheroids within 24 hours after seeding the cells under low attachment conditions [194, 195]. This was however not the case for other tested NSCLC cell lines, including HCC827. The ability of HCC827 cells to form spheroids is described controversially. While Ekert *et al.* observed in agreement only loose aggregates for HCC827 cells [196], also the formation of compact HCC827 spheroids in ULA-coated plates is reported by other authors [197, 198]. Thereby, a major drawback of this 3D models is pointed out, namely the aspect that not all cells are capable of forming compact spheroids with the applied methodology as it was similarly reported by other authors [86, 87, 199]. Nevertheless, tumor spheroids proved to be a bona fide 3D model for automation of drug testing with high reproducibility in a larger scale.

After a short delay of 24 h where the deviation in spheroid area was more pronounced, the models compacted and showed low variations in the area, especially after 72 hours and 96 hours in culture, pointing towards reproducible spheroid formation. Hence, a comprehensible culture time for the proof-of-concept process was determined with 96 hours including 72 hours treatment, after which definitive drug effects became evident. H358 cells reliably formed single spheroids per well in the ULA-coated 96-well plates and according to the U-shape of the wells were throughout located in the same Z-stack. Additionally, regarding the automation of 3D

models, the use of ULA-coated plates further spares the time-consuming process of additional agarose-coating of multi-well plates or labor-intensive transfer of spheroids cultured in hanging drops for subsequent assays [85].

After treatment with ARS-1620 a dose- and time-dependent reduction of the spheroid area was observed. This phenomenon was also reported for colorectal HT29 and pancreatic VCaP spheroids after treatment with the anti-cancer drugs irinotecan or MLN4924, respectively [200, 201]. After 72 hours of treatment with ARS-1620, 250 nM of the KRAS<sup>G12C</sup>-inhibitor were sufficient to reduce the spheroid area to less than 50 % of the control, demonstrating the sensitivity of H358 spheroids towards ARS-1620 also described by Janes *et al.* [42]. The efficacy of ARS-1620 on H358 tumor spheroids was further underlined by the induction of apoptosis with an EC<sub>50</sub> in the sub-micromolar range. As previously also reported for HepG2 spheroids after treatment with paclitaxel, doxorubicin or disulfram [202], the live-dead staining finally also demonstrated that the disintegrated cells in the periphery of the core spheroids after treatment were specifically stained by PI and thereby underwent cell death. The cells in the core spheroid remained viable in contrast. This further justifies the area measurement as valid assay to determine drug efficacy. In summary, both the area measurement as well as the live-dead-staining proved to be suitable for determining drug efficacy regarding an easy-to-perform and cost-effective methodology for automation. Both assays can be performed *in situ* without the necessity for a challenging medium change in floating cultures of spheroids, harboring the risk of disrupting the 3D models and creating artefacts conducting to misleading results.

Lastly, the complete process including establishment of H358 spheroids and the subsequent drug testing with ARS-1620 was successfully automated in a robotic platform using a two-arm robotic system (data not shown, unpublished data). Nevertheless, a major drawback of this study is the fact, that only one targeted therapy was tested in a single cell line and no specific thresholds could be suggested for defining the therapeutic efficacy of a specific treatment. While the establishment of spheroids with the applied methodology was also demonstrated for ASC spheroids and MDA-MB 231 / ASC co-culture spheroids, no drugs were applied on these specimens. Therefore, it is mandatory to evaluate the efficacy on a wider variety of anti-cancer therapies also considering spheroids originating from cells of different tumor entities. The ultimate objective of this process is however to test panels of different anti-cancer therapies on patient-derived spheroids to define the best available therapies in the course of personalized medicine.

In this regard, the establishment of patient-derived tumor spheroids was previously described for primary NSCLC with a subsequent drug testing using cisplatin [203]. The successful generation of 3D spheroids from surgical specimen derived from native breast cancer tissue with a success rate of 87 % and the validation of therapeutic efficacy of a panel of different

chemotherapies by evaluating the spheroid area was also recently described by Hofmann *et al.* [204]. In this study the changes in area of the spheroids further directly correlated with the cell viability determined by a luminescence-based ATP assay, further underlining the relevance of area measurement for studying drug efficacy in spheroids. In both studies, comparable ULA-coated microplates were used for the generation of patient-derived spheroids [203, 204].

In summary, a proof-of-concept process for automated drug testing on tumor spheroids could be successfully established and thereby the ground is prepared for studying drug efficacy on patient-derived spheroids in an automated and cost-effective manner in the future, representing a beneficial tool to support clinical decision making for personalized medicine.

## 5 Outlook

The establishment of KRAS<sup>G12C</sup>-biomarker models including characterization of the tumor cells in the 3D environment and the subsequent drug testing of mono- or combination therapies demonstrated the capability of the tumor models for patient stratification in a pre-clinical setting. Thereby it was suggested that this system represents a reasonable *in vitro* surrogate model that could contribute in future studies to a reduction of animal experiments according to the 3R principle. Different combination therapies tested in this study undergo clinical trials at the moment and the evaluation of the clinical efficacy of these therapies will give further insight into the predictivity of the SISmuc tumor models. While a physiologic ECM and tissue-architecture are provided for the tumor cells in the model and co-cultures with fibroblast are established, there is still a lack of other important components of the TME. This especially accounts for immune cells, gaining increasing importance in cancer research according to the high relevance of immunotherapies, like immune checkpoint inhibition. Also, differences in the immune modulatory characteristics of the tumor models based on different cell lines were indicated but could only be investigated on expression but not a functional level due to missing immune cells in the test system. However, first steps towards the implementation of immune cells in SISmuc tumor models were recently performed but asking for further refinement to model this central aspect *in vitro*. Adding immune cells to the test system could also be highly beneficial in regards of pre-clinical testing of novel OV's, of which the anti-tumoral effects are partially also depending on this cell types. Additionally, the biological matrix is of course still dependent on animal material. Providing a for example 3D-printed scaffold exhibiting comparable characteristics as the SISmuc could further reduce the amount of necessary animal material in the future. Finally, the tumor cells used for reseeding the biological matrix were exclusively represented by cell lines, which accumulate decisive changes in the genotype compared to the original cells of the tumor tissue. Using patient-derived cells directly isolated from native diseased tissue and cultured on the SISmuc, the pathological situation in the clinics could be modeled more closely and could further increase the relevance of the test system for personalized medicine. However, the isolation of tumor cells for *in vitro* cultures is challenging and often goes hand in hand with the selection of a specific subtype of tumor cells of the in general heterogenous tumor mass. Also, the recently described advances in the establishment of patient-derived spheroids originating from native tissue of different tumor entities indicate that an automatic drug testing in 3D model systems as described in this study for a cell line is in general feasible. Thereby the proof-of-concept process could be prospectively translated to a versatile tool for testing a wide variety of approved anti-cancer drugs on patient-derived spheroids and support clinical decisions for the most effective and individualized therapy, as for example similar approaches using PDXs are described to be too time-consuming to make a contemporarily suggestion for a suitable therapy.

## Supplemental Information

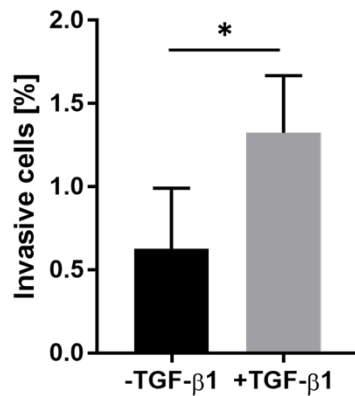


## Figure S 1 Invasion of H358 cells in 3D after TGF-β1 stimulation

H358 cells on the SISmuc were treated with 2 ng/mL TGF-β1 for 11 days in culture. Based on staining of preserved collagen IV of the biological scaffold and DAPI counterstaining, the invasive cells were quantified. \*:  $p \leq 0.05$ ;  $n=4$ .

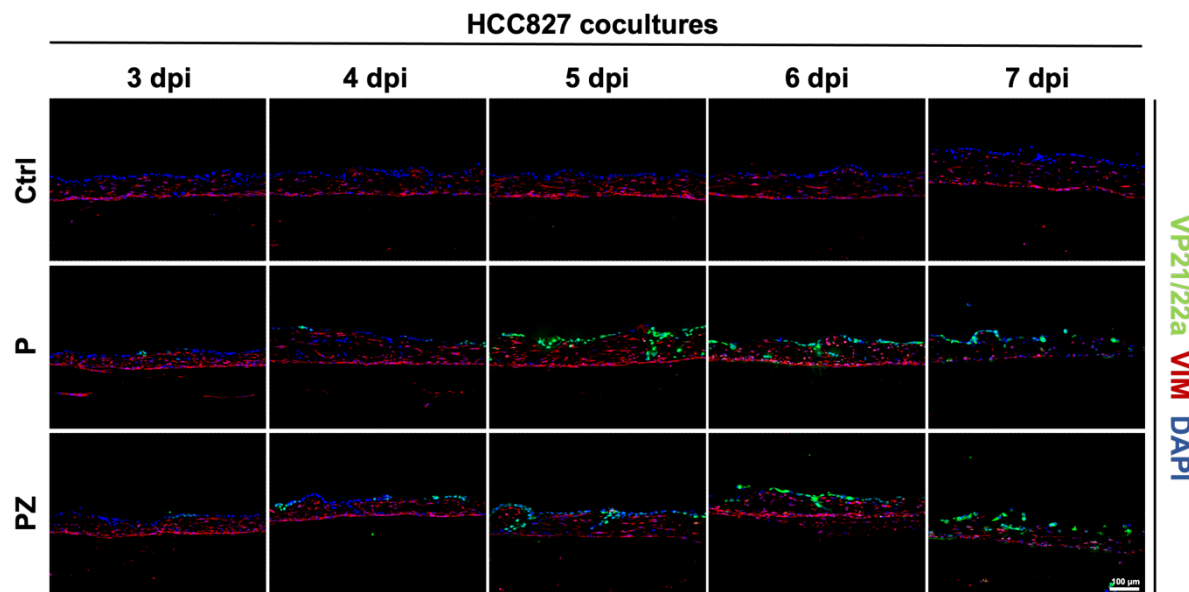


## Figure S 2 Infection of fibroblasts on HCC827 coculture models

Immunofluorescence staining of VP21/22a (green), VIM (red) with DAPI-counterstaining (blue) of HCC827 co-culture models after infection with either the P- or the PZ-virus at different timepoints after infection. Cells were infected with a MOI of 0.1. Scale bar = 100 μm;  $n=1$ .



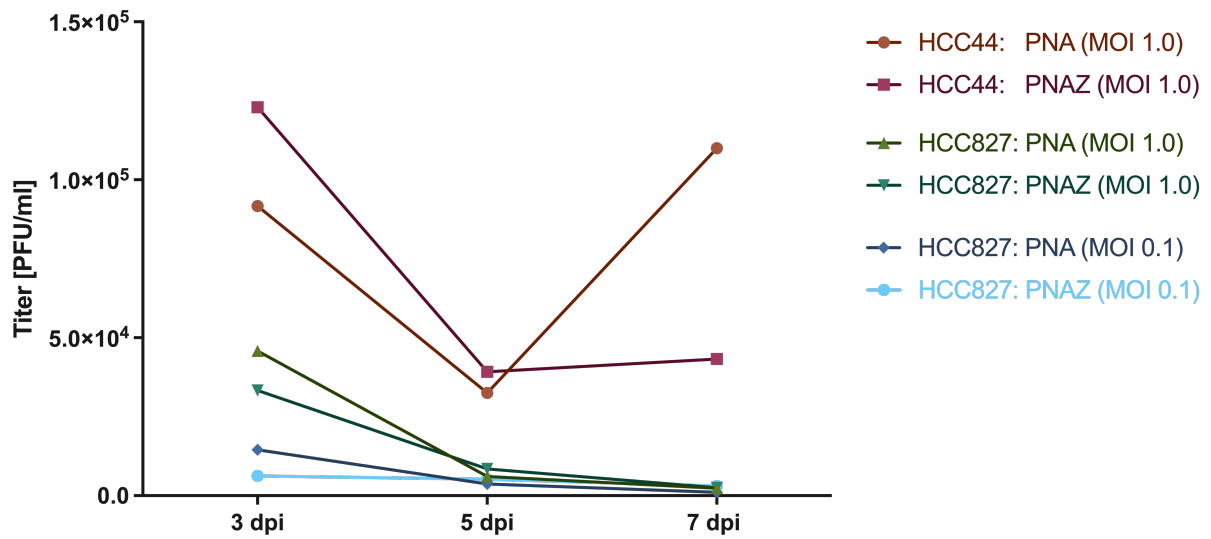


**Figure S 3 Viral titers of attenuated oncolytic viruses in different models and MOIs**

After 11 days in culture HCC827 SIS muc models co-cultured with fibroblasts or HCC44 SIS muc models were infected with the PNA- or PNAZ-virus with the indicated MOI. Viral titers were evaluated 3, 5 and 7 dpi with viral plaque assays. n=1.

**Bibliography**

1. MDPI. *Copyrights and Licensing*. 2023 [cited 2023 25.01.]; Available from: <https://www.mdpi.com/authors/rights>.
2. Murphy, S.L., et al., *Mortality in the United States, 2020*. NCHS Data Brief, 2021(427): p. 1-8.
3. Sung, H., et al., *Global Cancer Statistics 2020: GLOBOCAN Estimates of Incidence and Mortality Worldwide for 36 Cancers in 185 Countries*. *CA Cancer J Clin*, 2021. **71**(3): p. 209-249.
4. Howlader N, N.A., Krapcho M, Miller D, Brest A, Yu M, Ruhl J, Tatalovich Z, Mariotto A, Lewis DR, Chen HS, Feuer EJ, Cronin KA, *SEER Cancer Statistics Review, 1975-2016*. based on November 2018 SEER data submission, posted to the SEER web site, 2019. **National Cancer Institute. Bethesda, MD**.
5. Urs-Nikolaus Riede, G.K., Nikolas Freudenberg, Heinrich Matthys, *Allgemeine und Spezielle Pathologie*. 2 ed, ed. M.W. Ursus-Nikolaus Riede. Vol. 2. 2017, Germany: Springer. 858.
6. TheAmericanCancerSociety. *Lung Cancer Survival Rates*. 2022 [cited 2022 15.11.]; Available from: <https://www.cancer.org/cancer/lung-cancer/detection-diagnosis-staging/survival-rates.html>.
7. Duma, N., R. Santana-Davila, and J.R. Molina, *Non-Small Cell Lung Cancer: Epidemiology, Screening, Diagnosis, and Treatment*. *Mayo Clin Proc*, 2019. **94**(8): p. 1623-1640.
8. K.R. Aigner, F.O.S., T. Allen-Mersh, G. Hortobagyi, D. Khayat, S.M. Picksley, and T.T. P. Sugarbaker, J.F. Thompson, *Onkologie Basiswissen*, ed. F.O.S. K.R. Aigner. Vol. 1. 2016, Heidelberg: Springer.
9. NationalCancerInstitute. *Drugs Approved for Lung Cancer*. 2022 August 29, 2022 [cited 2022 17.11.]; Available from: <https://www.cancer.gov/about-cancer/treatment/drugs/lung>.
10. David S. Ettinger, D.E.W., *NCCN Guidelines Version 5.2022 Non-Small Cell Lung Cancer*. National Comprehensive Cancer Network, 2022.
11. Chevallier, M., et al., *Oncogenic driver mutations in non-small cell lung cancer: Past, present and future*. *World J Clin Oncol*, 2021. **12**(4): p. 217-237.
12. TheAmericanCancerSociety. *Treatment Choices for Non-Small Cell Lung Cancer, by Stage*. 2022 11.11.2022 [cited 2022 19.11.]; Available from: <https://www.cancer.org/cancer/lung-cancer/treating-non-small-cell/by-stage.html>.
13. Facchinetti, F., et al., *Mechanisms of Resistance to Target Therapies in Non-small Cell Lung Cancer*. *Handb Exp Pharmacol*, 2018. **249**: p. 63-89.
14. Sun, R., et al., *Drug resistance mechanisms and progress in the treatment of EGFR-mutated lung adenocarcinoma*. *Oncol Lett*, 2022. **24**(5): p. 408.
15. Hardtstock, F., et al., *Real-world treatment and survival of patients with advanced non-small cell lung Cancer: a German retrospective data analysis*. *BMC Cancer*, 2020. **20**(1): p. 260.
16. Nakajima, E.C., et al., *FDA Approval Summary: Sotorasib for KRAS G12C-Mutated Metastatic NSCLC*. *Clin Cancer Res*, 2022. **28**(8): p. 1482-1486.
17. FDA. *FDA grants accelerated approval to adagrasib for KRAS G12C-mutated NSCLC*. 2022 12.12.2022 [cited 2022 13.12.2022]; Available from: <https://www.fda.gov/drugs/resources-information-approved-drugs/fda-grants-accelerated-approval-adagrasib-kras-g12c-mutated-nsclc>.
18. Harvey, J.J., *An Unidentified Virus Which Causes the Rapid Production of Tumours in Mice*. *Nature*, 1964. **204**: p. 1104-5.
19. Kirsten, W.H. and L.A. Mayer, *Morphologic responses to a murine erythroblastosis virus*. *J Natl Cancer Inst*, 1967. **39**(2): p. 311-35.
20. Parikh, K., et al., *Drugging KRAS: current perspectives and state-of-art review*. *J Hematol Oncol*, 2022. **15**(1): p. 152.

21. Der, C.J., T.G. Krontiris, and G.M. Cooper, *Transforming genes of human bladder and lung carcinoma cell lines are homologous to the ras genes of Harvey and Kirsten sarcoma viruses*. Proc Natl Acad Sci U S A, 1982. **79**(11): p. 3637-40.
22. Hall, A., et al., *Identification of transforming gene in two human sarcoma cell lines as a new member of the ras gene family located on chromosome 1*. Nature, 1983. **303**(5916): p. 396-400.
23. Cox, A.D. and C.J. Der, *Ras history: The saga continues*. Small GTPases, 2010. **1**(1): p. 2-27.
24. Pantsar, T., *The current understanding of KRAS protein structure and dynamics*. Comput Struct Biotechnol J, 2020. **18**: p. 189-198.
25. Gimple, R.C. and X. Wang, *RAS: Striking at the Core of the Oncogenic Circuitry*. Front Oncol, 2019. **9**: p. 965.
26. Jancik, S., et al., *Clinical relevance of KRAS in human cancers*. J Biomed Biotechnol, 2010. **2010**: p. 150960.
27. Guin, S. and D. Theodorescu, *The RAS-RAL axis in cancer: evidence for mutation-specific selectivity in non-small cell lung cancer*. Acta Pharmacol Sin, 2015. **36**(3): p. 291-7.
28. Zago, G., et al., *A family affair: A Ral-exocyst-centered network links Ras, Rac, Rho signaling to control cell migration*. Small GTPases, 2019. **10**(5): p. 323-330.
29. Tao, S., et al., *Oncogenic KRAS confers chemoresistance by upregulating NRF2*. Cancer Res, 2014. **74**(24): p. 7430-41.
30. Huang, L., et al., *KRAS mutation: from undruggable to druggable in cancer*. Signal Transduct Target Ther, 2021. **6**(1): p. 386.
31. Guan, J.L., et al., *KRAS mutation in patients with lung cancer: a predictor for poor prognosis but not for EGFR-TKIs or chemotherapy*. Ann Surg Oncol, 2013. **20**(4): p. 1381-8.
32. Yang, H., et al., *New Horizons in KRAS-Mutant Lung Cancer: Dawn After Darkness*. Front Oncol, 2019. **9**: p. 953.
33. Simanshu, D.K., D.V. Nissley, and F. McCormick, *RAS Proteins and Their Regulators in Human Disease*. Cell, 2017. **170**(1): p. 17-33.
34. Hunter, J.C., et al., *Biochemical and Structural Analysis of Common Cancer-Associated KRAS Mutations*. Mol Cancer Res, 2015. **13**(9): p. 1325-35.
35. Veluswamy, R., et al., *KRAS G12C-Mutant Non-Small Cell Lung Cancer: Biology, Developmental Therapeutics, and Molecular Testing*. J Mol Diagn, 2021. **23**(5): p. 507-520.
36. Pereira, F., et al., *KRAS as a Modulator of the Inflammatory Tumor Microenvironment: Therapeutic Implications*. Cells, 2022. **11**(3).
37. Negri, F., et al., *KRAS: A Druggable Target in Colon Cancer Patients*. Int J Mol Sci, 2022. **23**(8).
38. The Lancet, O., *Undruggable KRAS-time to rebrand?* Lancet Oncol, 2021. **22**(3): p. 289.
39. Ryan, M.B. and R.B. Corcoran, *Therapeutic strategies to target RAS-mutant cancers*. Nat Rev Clin Oncol, 2018. **15**(11): p. 709-720.
40. Ostrem, J.M., et al., *K-Ras(G12C) inhibitors allosterically control GTP affinity and effector interactions*. Nature, 2013. **503**(7477): p. 548-51.
41. Patricelli, M.P., et al., *Selective Inhibition of Oncogenic KRAS Output with Small Molecules Targeting the Inactive State*. Cancer Discov, 2016. **6**(3): p. 316-29.
42. Janes, M.R., et al., *Targeting KRAS Mutant Cancers with a Covalent G12C-Specific Inhibitor*. Cell, 2018. **172**(3): p. 578-589 e17.
43. Goebel, L., et al., *KRAS G12C inhibitors in clinical trials: a short historical perspective*. RSC Med Chem, 2020. **11**(7): p. 760-770.
44. Canon, J., et al., *The clinical KRAS(G12C) inhibitor AMG 510 drives anti-tumour immunity*. Nature, 2019. **575**(7781): p. 217-223.
45. Kwan, A.K., et al., *The path to the clinic: a comprehensive review on direct KRAS(G12C) inhibitors*. J Exp Clin Cancer Res, 2022. **41**(1): p. 27.

46. Awad, M.M., et al., *Acquired Resistance to KRAS(G12C) Inhibition in Cancer*. N Engl J Med, 2021. **384**(25): p. 2382-2393.
47. Desage, A.L., et al., *Targeting KRAS Mutant in Non-Small Cell Lung Cancer: Novel Insights Into Therapeutic Strategies*. Front Oncol, 2022. **12**: p. 796832.
48. Kalluri, R. and R.A. Weinberg, *The basics of epithelial-mesenchymal transition*. J Clin Invest, 2009. **119**(6): p. 1420-8.
49. Haensel, D. and X. Dai, *Epithelial-to-mesenchymal transition in cutaneous wound healing: Where we are and where we are heading*. Dev Dyn, 2018. **247**(3): p. 473-480.
50. Saitoh, M., *Involvement of partial EMT in cancer progression*. J Biochem, 2018. **164**(4): p. 257-264.
51. Guaita, S., et al., *Snail induction of epithelial to mesenchymal transition in tumor cells is accompanied by MUC1 repression and ZEB1 expression*. J Biol Chem, 2002. **277**(42): p. 39209-16.
52. Serrano-Gomez, S.J., M. Maziveyi, and S.K. Alahari, *Regulation of epithelial-mesenchymal transition through epigenetic and post-translational modifications*. Mol Cancer, 2016. **15**: p. 18.
53. Singh, A., et al., *A gene expression signature associated with "K-Ras addiction" reveals regulators of EMT and tumor cell survival*. Cancer Cell, 2009. **15**(6): p. 489-500.
54. Adachi, Y., et al., *Epithelial-to-Mesenchymal Transition is a Cause of Both Intrinsic and Acquired Resistance to KRAS G12C Inhibitor in KRAS G12C-Mutant Non-Small Cell Lung Cancer*. Clin Cancer Res, 2020. **26**(22): p. 5962-5973.
55. Tsai, Y.S., et al., *Rapid idiosyncratic mechanisms of clinical resistance to KRAS G12C inhibition*. J Clin Invest, 2022. **132**(4).
56. Jonckheere, S., et al., *Epithelial-Mesenchymal Transition (EMT) as a Therapeutic Target*. Cells Tissues Organs, 2022. **211**(2): p. 157-182.
57. Kelley, R.K., et al., *A Phase 2 Study of Galunisertib (TGF-beta1 Receptor Type I Inhibitor) and Sorafenib in Patients With Advanced Hepatocellular Carcinoma*. Clin Transl Gastroenterol, 2019. **10**(7): p. e00056.
58. Young, K.H., et al., *A phase II trial of TGFβ type I receptor inhibitor, galunisertib, plus neoadjuvant chemoradiation in patients with locally advanced rectal cancer*. Journal of Clinical Oncology, 2022. **40**(16\_suppl): p. 3617-3617.
59. Schmid, S., et al., *Clinical Outcome of ALK-Positive Non-Small Cell Lung Cancer (NSCLC) Patients with De Novo EGFR or KRAS Co-Mutations Receiving Tyrosine Kinase Inhibitors (TKIs)*. J Thorac Oncol, 2017. **12**(4): p. 681-688.
60. Lou, K., et al., *KRAS(G12C) inhibition produces a driver-limited state revealing collateral dependencies*. Sci Signal, 2019. **12**(583).
61. Ryan, M.B., et al., *Vertical Pathway Inhibition Overcomes Adaptive Feedback Resistance to KRAS(G12C) Inhibition*. Clin Cancer Res, 2020. **26**(7): p. 1633-1643.
62. ClinicalTrials.gov. *Tarlox and Sotorasib in Patients With KRAS G12C Mutations NCT05313009*. 2022 04.11.2022 [cited 2022 03.12.2022]; Available from: <https://clinicaltrials.gov/ct2/show/NCT05313009>.
63. ClinicalTrials.gov. *Phase 3 Study of MRTX849 With Cetuximab vs Chemotherapy in Patients With Advanced Colorectal Cancer With KRAS G12C Mutation (KRYSTAL-10) NCT04793958*. 2021 01.12.2022 [cited 2022 03.12.2022]; Available from: <https://clinicaltrials.gov/ct2/show/NCT04793958>.
64. Skoulidis, F., et al., *Co-occurring genomic alterations define major subsets of KRAS-mutant lung adenocarcinoma with distinct biology, immune profiles, and therapeutic vulnerabilities*. Cancer Discov, 2015. **5**(8): p. 860-77.
65. Aubrey, B.J., A. Strasser, and G.L. Kelly, *Tumor-Suppressor Functions of the TP53 Pathway*. Cold Spring Harb Perspect Med, 2016. **6**(5).
66. Bungaro, M., S. Novello, and F. Passiglia, *Targeting KRASp.G12C Mutation in Advanced Non-Small Cell Lung Cancer: a New Era Has Begun*. Curr Treat Options Oncol, 2022.

67. Taguchi, K. and M. Yamamoto, *The KEAP1-NRF2 System in Cancer*. Front Oncol, 2017. **7**: p. 85.
68. Ricciuti, B., et al., *Diminished Efficacy of Programmed Death-(Ligand)1 Inhibition in STK11- and KEAP1-Mutant Lung Adenocarcinoma Is Affected by KRAS Mutation Status*. J Thorac Oncol, 2022. **17**(3): p. 399-410.
69. Skoulidis, F., et al., *Sotorasib for Lung Cancers with KRAS p.G12C Mutation*. N Engl J Med, 2021. **384**(25): p. 2371-2381.
70. Poulaki, V., et al., *The Antidiabetic Biguanide Metformin Induces Growth Arrest in Retinoblastoma Cells in vitro*. Investigative Ophthalmology & Visual Science, 2009. **50**(13): p. 1699-1699.
71. Shackelford, D.B., et al., *LKB1 inactivation dictates therapeutic response of non-small cell lung cancer to the metabolism drug phenformin*. Cancer Cell, 2013. **23**(2): p. 143-58.
72. Mahauad-Fernandez, W.D. and D.W. Felsher, *The Myc and Ras Partnership in Cancer: Indistinguishable Alliance or Contextual Relationship?* Cancer Res, 2020. **80**(18): p. 3799-3802.
73. Kortlever, R.M., et al., *Myc Cooperates with Ras by Programming Inflammation and Immune Suppression*. Cell, 2017. **171**(6): p. 1301-1315 e14.
74. Hall, Z., et al., *Myc linked to dysregulation of cholesterol transport and storage in nonsmall cell lung cancer*. J Lipid Res, 2020. **61**(11): p. 1390-1399.
75. Mugarza, E., et al., *Therapeutic KRAS(G12C) inhibition drives effective interferon-mediated antitumor immunity in immunogenic lung cancers*. Sci Adv, 2022. **8**(29): p. eabm8780.
76. Madden, S.K., et al., *Taking the Myc out of cancer: toward therapeutic strategies to directly inhibit c-Myc*. Mol Cancer, 2021. **20**(1): p. 3.
77. Posternak, V. and M.D. Cole, *Strategically targeting MYC in cancer*. F1000Res, 2016. **5**.
78. Rodrigues, J., et al., *3D In Vitro Model (R)evolution: Unveiling Tumor-Stroma Interactions*. Trends Cancer, 2021. **7**(3): p. 249-264.
79. Wong, C.H., K.W. Siah, and A.W. Lo, *Estimation of clinical trial success rates and related parameters*. Biostatistics, 2019. **20**(2): p. 273-286.
80. Pape, J., M. Emberton, and U. Cheema, *3D Cancer Models: The Need for a Complex Stroma, Compartmentalization and Stiffness*. Front Bioeng Biotechnol, 2021. **9**: p. 660502.
81. Denys, H., et al., *The extracellular matrix regulates cancer progression and therapy response: implications for prognosis and treatment*. Curr Pharm Des, 2009. **15**(12): p. 1373-84.
82. Klemm, F. and J.A. Joyce, *Microenvironmental regulation of therapeutic response in cancer*. Trends Cell Biol, 2015. **25**(4): p. 198-213.
83. Sant, S. and P.A. Johnston, *The production of 3D tumor spheroids for cancer drug discovery*. Drug Discov Today Technol, 2017. **23**: p. 27-36.
84. Langhans, S.A., *Three-Dimensional in Vitro Cell Culture Models in Drug Discovery and Drug Repositioning*. Front Pharmacol, 2018. **9**: p. 6.
85. Vinci, M., et al., *Advances in establishment and analysis of three-dimensional tumor spheroid-based functional assays for target validation and drug evaluation*. BMC Biol, 2012. **10**: p. 29.
86. Schmidt, M., et al., *Spheroid-based 3-dimensional culture models: Gene expression and functionality in head and neck cancer*. Oncol Rep, 2016. **35**(4): p. 2431-40.
87. Pomo, J.M., R.M. Taylor, and R.R. Gullapalli, *Influence of TP53 and CDH1 genes in hepatocellular cancer spheroid formation and culture: a model system to understand cancer cell growth mechanics*. Cancer Cell Int, 2016. **16**: p. 44.
88. Lin, R.Z., et al., *Dynamic analysis of hepatoma spheroid formation: roles of E-cadherin and beta1-integrin*. Cell Tissue Res, 2006. **324**(3): p. 411-22.
89. Nunes, A.S., et al., *3D tumor spheroids as in vitro models to mimic in vivo human solid tumors resistance to therapeutic drugs*. Biotechnol Bioeng, 2019. **116**(1): p. 206-226.

90. Meier-Hubberten, J.C. and M.P. Sanderson, *Establishment and Analysis of a 3D Co-Culture Spheroid Model of Pancreatic Adenocarcinoma for Application in Drug Discovery*. *Methods Mol Biol*, 2019. **1953**: p. 163-179.
91. Yakavets, I., et al., *Stroma-Rich Co-Culture Multicellular Tumor Spheroids as a Tool for Photoactive Drugs Screening*. *J Clin Med*, 2019. **8**(10).
92. Courau, T., et al., *Cocultures of human colorectal tumor spheroids with immune cells reveal the therapeutic potential of MICA/B and NKG2A targeting for cancer treatment*. *J Immunother Cancer*, 2019. **7**(1): p. 74.
93. Melissaridou, S., et al., *The effect of 2D and 3D cell cultures on treatment response, EMT profile and stem cell features in head and neck cancer*. *Cancer Cell Int*, 2019. **19**: p. 16.
94. Imamura, Y., et al., *Comparison of 2D- and 3D-culture models as drug-testing platforms in breast cancer*. *Oncol Rep*, 2015. **33**(4): p. 1837-43.
95. Cui, X., Y. Hartanto, and H. Zhang, *Advances in multicellular spheroids formation*. *J R Soc Interface*, 2017. **14**(127).
96. Zhang, X., et al., *Decellularized extracellular matrix scaffolds: Recent trends and emerging strategies in tissue engineering*. *Bioact Mater*, 2022. **10**: p. 15-31.
97. Unnikrishnan, K., L.V. Thomas, and R.M. Ram Kumar, *Advancement of Scaffold-Based 3D Cellular Models in Cancer Tissue Engineering: An Update*. *Front Oncol*, 2021. **11**: p. 733652.
98. Gilbert, T.W., T.L. Sellaro, and S.F. Badylak, *Decellularization of tissues and organs*. *Biomaterials*, 2006. **27**(19): p. 3675-83.
99. Holle, A.W., J.L. Young, and J.P. Spatz, *In vitro cancer cell-ECM interactions inform in vivo cancer treatment*. *Adv Drug Deliv Rev*, 2016. **97**: p. 270-9.
100. Gentilin, E., et al., *Decellularized normal and cancer tissues as tools for cancer research*. *Cancer Gene Ther*, 2022. **29**(7): p. 879-888.
101. Wu, C., *Focal adhesion: a focal point in current cell biology and molecular medicine*. *Cell Adh Migr*, 2007. **1**(1): p. 13-8.
102. van Dijk, M., S.A. Goransson, and S. Stromblad, *Cell to extracellular matrix interactions and their reciprocal nature in cancer*. *Exp Cell Res*, 2013. **319**(11): p. 1663-70.
103. Stratmann, A.T., et al., *Establishment of a human 3D lung cancer model based on a biological tissue matrix combined with a Boolean in silico model*. *Mol Oncol*, 2014. **8**(2): p. 351-65.
104. Nietzer, S., et al., *Mimicking Metastases Including Tumor Stroma: A New Technique to Generate a Three-Dimensional Colorectal Cancer Model Based on a Biological Decellularized Intestinal Scaffold*. *Tissue Eng Part C Methods*, 2016. **22**(7): p. 621-35.
105. Wallstabe, L., et al., *ROR1-CAR T cells are effective against lung and breast cancer in advanced microphysiologic 3D tumor models*. *JCI Insight*, 2019. **4**(18).
106. Kuhnemundt, J., et al., *Modular micro-physiological human tumor/tissue models based on decellularized tissue for improved preclinical testing*. *ALTEX*, 2020. **38**(2): p. 289-306.
107. Baur, F., et al., *Connecting Cancer Pathways to Tumor Engines: A Stratification Tool for Colorectal Cancer Combining Human In Vitro Tissue Models with Boolean In Silico Models*. *Cancers (Basel)*, 2019. **12**(1).
108. Pelner, L., G.A. Fowler, and H.C. Nauts, *Effects of concurrent infections and their toxins on the course of leukemia*. *Acta Medica Scandinavica. Supplementum*, 1958. **338**: p. 1-47.
109. Cao, G.D., et al., *The Oncolytic Virus in Cancer Diagnosis and Treatment*. *Front Oncol*, 2020. **10**: p. 1786.
110. Santos Apolonio, J., et al., *Oncolytic virus therapy in cancer: A current review*. *World J Virol*, 2021. **10**(5): p. 229-255.
111. Lawler, S.E., et al., *Oncolytic Viruses in Cancer Treatment: A Review*. *JAMA Oncol*, 2017. **3**(6): p. 841-849.

112. Kaufman, H.L., S.Z. Shalhout, and G. Iodice, *Talimogene Laherparepvec: Moving From First-In-Class to Best-In-Class*. *Front Mol Biosci*, 2022. **9**: p. 834841.
113. Koch, M.S., S.E. Lawler, and E.A. Chiocca, *HSV-1 Oncolytic Viruses from Bench to Bedside: An Overview of Current Clinical Trials*. *Cancers (Basel)*, 2020. **12**(12).
114. Farooq, A.V., T. Valyi-Nagy, and D. Shukla, *Mediators and mechanisms of herpes simplex virus entry into ocular cells*. *Curr Eye Res*, 2010. **35**(6): p. 445-50.
115. Verzosa, A.L., et al., *Herpes Simplex Virus 1 Infection of Neuronal and Non-Neuronal Cells Elicits Specific Innate Immune Responses and Immune Evasion Mechanisms*. *Front Immunol*, 2021. **12**: p. 644664.
116. Wojton, J. and B. Kaur, *Impact of tumor microenvironment on oncolytic viral therapy*. *Cytokine Growth Factor Rev*, 2010. **21**(2-3): p. 127-34.
117. Berkey, S.E., S.H. Thorne, and D.L. Bartlett, *Oncolytic Virotherapy and the Tumor Microenvironment*. *Adv Exp Med Biol*, 2017. **1036**: p. 157-172.
118. NCIDictionaries. *Oncolytic Virus*. [cited 2022 05.12.]; Available from: <https://www.cancer.gov/publications/dictionaries/cancer-terms/def/oncolytic-virus>.
119. Marcocci, M.E., et al., *Herpes Simplex Virus-1 in the Brain: The Dark Side of a Sneaky Infection*. *Trends Microbiol*, 2020. **28**(10): p. 808-820.
120. Bairoch, A., *The Cellosaurus, a Cell-Line Knowledge Resource*. *J Biomol Tech*, 2018. **29**(2): p. 25-38.
121. Scholtalbers, J., et al., *TCLP: an online cancer cell line catalogue integrating HLA type, predicted neo-epitopes, virus and gene expression*. *Genome Med*, 2015. **7**: p. 118.
122. CharlesRiver. *Tumor Model Compendium*. [Database] [cited 2022 22.12.2022]; Available from: <https://compendium.criver.com/compendium2/search?query.key=3aacc76889d8e75ba02134675d0640a1>.
123. Gerhard Keller, A.-L.P., Jutta Fehr, Hagen Klett, Armin Meier, Markus Posch, Thomas Metz. *Characterisation of a panel of 79 PDX-derived cell lines with a focus on the EGFR exon 20 insertion mutation-driven NSCLC model LXFE2478*. International Conference on Molecular Targets and Cancer Therapeutics 2019; Available from: <https://www.criver.com/sites/default/files/resource-files/SP-EORTC-19-characterization-of-a-panel-of-79-PDX-derived-cell-lines-with-a-focus-on-the-EGFR-exon-20-insertion-mutation.pdf>.
124. Mu, X., et al., *Ubiquitin ligase Cbl-b is involved in icotinib (BPI-2009H)-induced apoptosis and G1 phase arrest of EGFR mutation-positive non-small-cell lung cancer*. *Biomed Res Int*, 2013. **2013**: p. 726375.
125. Todo, T., et al., *Oncolytic herpes simplex virus vector with enhanced MHC class I presentation and tumor cell killing*. *Proc Natl Acad Sci U S A*, 2001. **98**(11): p. 6396-401.
126. Pfaffl, M.W., *A new mathematical model for relative quantification in real-time RT-PCR*. *Nucleic Acids Res*, 2001. **29**(9): p. e45.
127. Stael, S., et al., *Detection of Damage-Activated Metacaspase Activity by Western Blot in Plants*. *Methods Mol Biol*, 2022. **2447**: p. 127-137.
128. Peindl, M., et al., *EMT, Stemness, and Drug Resistance in Biological Context: A 3D Tumor Tissue/In Silico Platform for Analysis of Combinatorial Treatment in NSCLC with Aggressive KRAS-Biomarker Signatures*. *Cancers (Basel)*, 2022. **14**(9).
129. Gyorffy, B., *Survival analysis across the entire transcriptome identifies biomarkers with the highest prognostic power in breast cancer*. *Comput Struct Biotechnol J*, 2021. **19**: p. 4101-4109.
130. Shah, P.P., et al., *Common cytotoxic chemotherapeutics induce epithelial-mesenchymal transition (EMT) downstream of ER stress*. *Oncotarget*, 2017. **8**(14): p. 22625-22639.
131. Martin, J., et al., *Role of the epithelial-mesenchymal transition-related circular RNA, circ-10720, in non-small-cell lung cancer*. *Transl Lung Cancer Res*, 2021. **10**(4): p. 1804-1818.

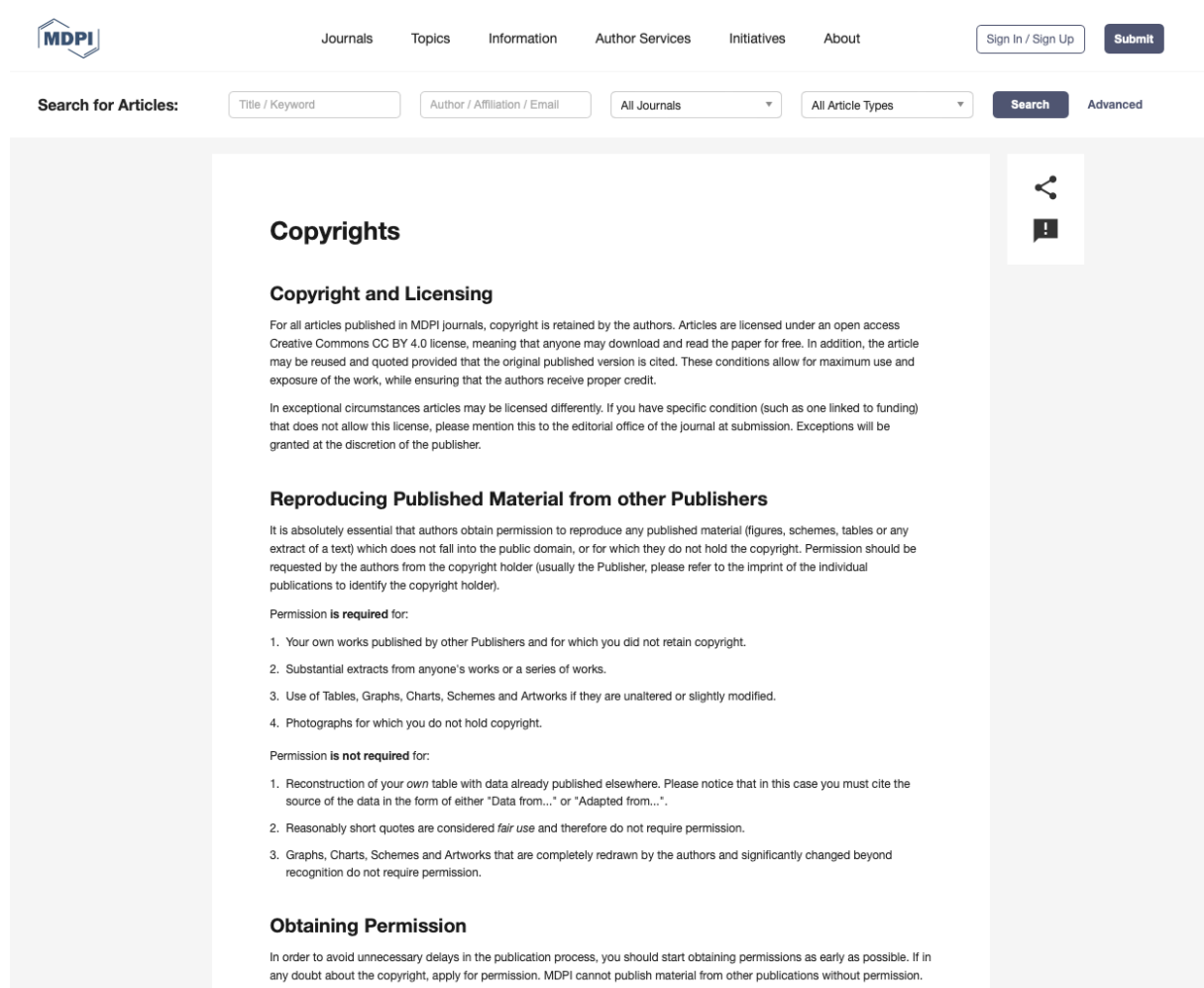
132. Cook, D.P. and B.C. Vanderhyden, *Context specificity of the EMT transcriptional response*. Nat Commun, 2020. **11**(1): p. 2142.
133. Thapa, R. and G.D. Wilson, *The Importance of CD44 as a Stem Cell Biomarker and Therapeutic Target in Cancer*. Stem Cells Int, 2016. **2016**: p. 2087204.
134. Weidenfeld, K. and D. Barkan, *EMT and Stemness in Tumor Dormancy and Outgrowth: Are They Intertwined Processes?* Front Oncol, 2018. **8**: p. 381.
135. Wilson, M.M., et al., *Emerging Mechanisms by which EMT Programs Control Stemness*. Trends Cancer, 2020. **6**(9): p. 775-780.
136. Souza, A.G., et al., *Comparative Assay of 2D and 3D Cell Culture Models: Proliferation, Gene Expression and Anticancer Drug Response*. Curr Pharm Des, 2018. **24**(15): p. 1689-1694.
137. Jensen, C. and Y. Teng, *Is It Time to Start Transitioning From 2D to 3D Cell Culture?* Front Mol Biosci, 2020. **7**: p. 33.
138. Warth, A., et al., *Tumour cell proliferation (Ki-67) in non-small cell lung cancer: a critical reappraisal of its prognostic role*. Br J Cancer, 2014. **111**(6): p. 1222-9.
139. Blanco, R., et al., *A gene-alteration profile of human lung cancer cell lines*. Hum Mutat, 2009. **30**(8): p. 1199-206.
140. Elkin, S.R., et al., *A systematic analysis reveals heterogeneous changes in the endocytic activities of cancer cells*. Cancer Res, 2015. **75**(21): p. 4640-50.
141. Cho, K.B., et al., *Overexpression of c-myc induces epithelial mesenchymal transition in mammary epithelial cells*. Cancer Lett, 2010. **293**(2): p. 230-9.
142. Yin, S., et al., *Myc mediates cancer stem-like cells and EMT changes in triple negative breast cancers cells*. PLoS One, 2017. **12**(8): p. e0183578.
143. Lai, X., et al., *Epithelial-Mesenchymal Transition and Metabolic Switching in Cancer: Lessons From Somatic Cell Reprogramming*. Front Cell Dev Biol, 2020. **8**: p. 760.
144. Goldstein, L.D., et al., *Recurrent Loss of NFE2L2 Exon 2 Is a Mechanism for Nrf2 Pathway Activation in Human Cancers*. Cell Rep, 2016. **16**(10): p. 2605-2617.
145. *Probing Mutant KRAS, STK11, KEAP1 in NSCLC*. Cancer Discov, 2022. **12**(10): p. 2226.
146. Zhang, J. and N. Veeramachaneni, *Targeting interleukin-1beta and inflammation in lung cancer*. Biomark Res, 2022. **10**(1): p. 5.
147. Shang, G.S., L. Liu, and Y.W. Qin, *IL-6 and TNF-alpha promote metastasis of lung cancer by inducing epithelial-mesenchymal transition*. Oncol Lett, 2017. **13**(6): p. 4657-4660.
148. Tokunaga, R., et al., *CXCL9, CXCL10, CXCL11/CXCR3 axis for immune activation - A target for novel cancer therapy*. Cancer Treat Rev, 2018. **63**: p. 40-47.
149. Yu, R., B. Zhu, and D. Chen, *Type I interferon-mediated tumor immunity and its role in immunotherapy*. Cell Mol Life Sci, 2022. **79**(3): p. 191.
150. Nagarsheth, N., M.S. Wicha, and W. Zou, *Chemokines in the cancer microenvironment and their relevance in cancer immunotherapy*. Nat Rev Immunol, 2017. **17**(9): p. 559-572.
151. Du, J., et al., *Murine chronic graft-versus-host disease proteome profiling discovers CCL15 as a novel biomarker in patients*. Blood, 2018. **131**(15): p. 1743-1754.
152. Misale, S., et al., *KRAS G12C NSCLC Models Are Sensitive to Direct Targeting of KRAS in Combination with PI3K Inhibition*. Clin Cancer Res, 2019. **25**(2): p. 796-807.
153. Kim, D., J.Y. Xue, and P. Lito, *Targeting KRAS(G12C): From Inhibitory Mechanism to Modulation of Antitumor Effects in Patients*. Cell, 2020. **183**(4): p. 850-859.
154. Addeo, A., G.L. Banna, and A. Friedlaender, *KRAS G12C Mutations in NSCLC: From Target to Resistance*. Cancers (Basel), 2021. **13**(11).
155. Chun, S.Y., et al., *Oncogenic KRAS modulates mitochondrial metabolism in human colon cancer cells by inducing HIF-1alpha and HIF-2alpha target genes*. Mol Cancer, 2010. **9**: p. 293.
156. Pupo, E., et al., *KRAS-Driven Metabolic Rewiring Reveals Novel Actionable Targets in Cancer*. Front Oncol, 2019. **9**: p. 848.
157. Wei, L., et al., *Lysyl oxidase may play a critical role in hypoxia-induced NSCLC cells invasion and migration*. Cancer Biother Radiopharm, 2012. **27**(10): p. 672-7.



158. Li, C., et al., *Dusp6 (Mkp3) is a negative feedback regulator of FGF-stimulated ERK signaling during mouse development*. *Development*, 2007. **134**(1): p. 167-76.
159. Xiao, X., et al., *TMPRSS2 Serves as a Prognostic Biomarker and Correlated With Immune Infiltrates in Breast Invasive Cancer and Lung Adenocarcinoma*. *Front Mol Biosci*, 2022. **9**: p. 647826.
160. Zhang, J., et al., *The Functional Effects of Key Driver KRAS Mutations on Gene Expression in Lung Cancer*. *Front Genet*, 2020. **11**: p. 17.
161. Ding, X., et al., *EIF3C Promotes Lung Cancer Tumorigenesis by Regulating the APP/HSPA1A/LMNB1 Axis*. *Dis Markers*, 2022. **2022**: p. 9464094.
162. Ning, W., et al., *Non-genetic adaptive resistance to KRAS(G12C) inhibition: EMT is not the only culprit*. *Front Oncol*, 2022. **12**: p. 1004669.
163. Wilson, C., et al., *Overcoming EMT-associated resistance to anti-cancer drugs via Src/FAK pathway inhibition*. *Oncotarget*, 2014. **5**(17): p. 7328-41.
164. Hill, C. and Y. Wang, *The importance of epithelial-mesenchymal transition and autophagy in cancer drug resistance*. *Cancer Drug Resist*, 2020. **3**(1): p. 38-47.
165. Pan, X.N., et al., *Inhibition of c-Myc overcomes cytotoxic drug resistance in acute myeloid leukemia cells by promoting differentiation*. *PLoS One*, 2014. **9**(8): p. e105381.
166. Zhu, Y., et al., *The potential role of c-MYC and polyamine metabolism in multiple drug resistance in bladder cancer investigated by metabolomics*. *Genomics*, 2022. **114**(1): p. 125-137.
167. Zhang, Y., et al., *Sp1 and c-Myc modulate drug resistance of leukemia stem cells by regulating survivin expression through the ERK-MSK MAPK signaling pathway*. *Mol Cancer*, 2015. **14**: p. 56.
168. Soucek, L., et al., *Inhibition of Myc family proteins eradicates KRas-driven lung cancer in mice*. *Genes Dev*, 2013. **27**(5): p. 504-13.
169. Zhao, Y., et al., *Diverse alterations associated with resistance to KRAS(G12C) inhibition*. *Nature*, 2021. **599**(7886): p. 679-683.
170. van Meerloo, J., G.J. Kaspers, and J. Cloos, *Cell sensitivity assays: the MTT assay*. *Methods Mol Biol*, 2011. **731**: p. 237-45.
171. Stepanenko, A.A. and V.V. Dmitrenko, *Pitfalls of the MTT assay: Direct and off-target effects of inhibitors can result in over/underestimation of cell viability*. *Gene*, 2015. **574**(2): p. 193-203.
172. Herzig, S. and R.J. Shaw, *AMPK: guardian of metabolism and mitochondrial homeostasis*. *Nat Rev Mol Cell Biol*, 2018. **19**(2): p. 121-135.
173. Nwizu, T., et al., *Crizotinib (PF02341066) as a ALK /MET inhibitor- Special Emphasis as a Therapeutic Drug Against Lung Cancer*. *Drugs Future*, 2011. **36**(2): p. 91-99.
174. Nikonova, A.S., et al., *Aurora A kinase (AURKA) in normal and pathological cell division*. *Cell Mol Life Sci*, 2013. **70**(4): p. 661-87.
175. Tang, A., et al., *Aurora kinases: novel therapy targets in cancers*. *Oncotarget*, 2017. **8**(14): p. 23937-23954.
176. Xue, J.Y., et al., *Rapid non-uniform adaptation to conformation-specific KRAS(G12C) inhibition*. *Nature*, 2020. **577**(7790): p. 421-425.
177. Burtneess, J.W.L.S.K.C.Y.B., *Abstract P078: Aurora A kinase inhibition with VIC-1911 overcomes intrinsic and acquired resistance to KRASG12C inhibition in KRAS(G12C)-mutated lung cancer*. *Molecular Cancer Therapeutics*, 2021. **Mol Cancer Ther (2021) 20 (12\_Supplement): P078**.
178. Lu, H., et al., *Compensatory induction of MYC expression by sustained CDK9 inhibition via a BRD4-dependent mechanism*. *Elife*, 2015. **4**: p. e06535.
179. ClinicalTrials.gov, *VIC-1911 Monotherapy in Combination With Sotorasib for the Treatment of KRAS G12C-Mutant Non-Small Cell Lung Cancer (NCT05374538)*. U.S. National Library of Medicine, 2022.
180. Garcia-Carbonero, R., et al., *Phase 1 study of intravenous administration of the chimeric adenovirus enadenotucirev in patients undergoing primary tumor resection*. *J Immunother Cancer*, 2017. **5**(1): p. 71.

181. Jahan, N., et al., *In Situ Cancer Vaccination and Immunovirotherapy Using Oncolytic HSV*. *Viruses*, 2021. **13**(9).
182. Longo, V., et al., *Strategies to Improve Cancer Immune Checkpoint Inhibitors Efficacy, Other Than Abscopal Effect: A Systematic Review*. *Cancers (Basel)*, 2019. **11**(4).
183. Li, Z., et al., *Lung cancer and oncolytic virotherapy--enemy's enemy*. *Transl Oncol*, 2022. **27**: p. 101563.
184. Kemp, V., et al., *Developing oncolytic viruses for clinical use: A consortium approach*. *Cytokine Growth Factor Rev*, 2020. **56**: p. 133-140.
185. Dautzenberg, I.J., et al., *Mammalian orthoreovirus T3D infects U-118 MG cell spheroids independent of junction adhesion molecule-A*. *Gene Ther*, 2014. **21**(6): p. 609-17.
186. Tong, J.G., et al., *Evidence for differential viral oncolytic efficacy in an in vitro model of epithelial ovarian cancer metastasis*. *Mol Ther Oncolytics*, 2015. **2**: p. 15013.
187. McKenna, M.K., A. Rosewell-Shaw, and M. Suzuki, *Modeling the Efficacy of Oncolytic Adenoviruses In Vitro and In Vivo: Current and Future Perspectives*. *Cancers (Basel)*, 2020. **12**(3).
188. Colao, I., et al., *The ERK-1 function is required for HSV-1-mediated G1/S progression in HEP-2 cells and contributes to virus growth*. *Sci Rep*, 2017. **7**(1): p. 9176.
189. Wirtz, L., et al., *Susceptibility of Human and Murine Dermal Fibroblasts to Herpes Simplex Virus 1 in the Absence and Presence of Extracellular Matrix*. *J Virol*, 2022. **96**(4): p. e0206821.
190. Davido, D.J., et al., *Attenuated Herpes Simplex Virus 1 (HSV-1) Expressing a Mutant Form of ICP6 Stimulates a Strong Immune Response That Protects Mice against HSV-1-Induced Corneal Disease*. *J Virol*, 2018. **92**(17).
191. Zhao, J., et al., *Herpes Simplex Virus and Pattern Recognition Receptors: An Arms Race*. *Front Immunol*, 2020. **11**: p. 613799.
192. Ebrahimi, S., et al., *Developing oncolytic Herpes simplex virus type 1 through UL39 knockout by CRISPR-Cas9*. *Iran J Basic Med Sci*, 2020. **23**(7): p. 937-944.
193. Peters, C. and S.D. Rabkin, *Designing Herpes Viruses as Oncolytics*. *Mol Ther Oncolytics*, 2015. **2**: p. 15010-.
194. Acosta, M.F., et al., *In Vitro Pulmonary Cell Culture in Pharmaceutical Inhalation Aerosol Delivery: 2-D, 3-D, and In Situ Bioimpactor Models*. *Curr Pharm Des*, 2016. **22**(17): p. 2522-31.
195. Bartling, B., et al., *Prognostic potential and tumor growth-inhibiting effect of plasma advanced glycation end products in non-small cell lung carcinoma*. *Mol Med*, 2011. **17**(9-10): p. 980-9.
196. Ekert, J.E., et al., *Three-dimensional lung tumor microenvironment modulates therapeutic compound responsiveness in vitro--implication for drug development*. *PLoS One*, 2014. **9**(3): p. e92248.
197. Kaur, G., J.H. Doroshov, and B.A. Teicher, *Format (2D vs 3D) and media effect target expression and response of patient-derived and standard NSCLC lines to EGFR inhibitors*. *Cancer Treat Res Commun*, 2021. **29**: p. 100463.
198. Van Der Steen, N., et al., *Crizotinib sensitizes the erlotinib resistant HCC827GR5 cell line by influencing lysosomal function*. *J Cell Physiol*, 2020. **235**(11): p. 8085-8097.
199. Smyrek, I., et al., *E-cadherin, actin, microtubules and FAK dominate different spheroid formation phases and important elements of tissue integrity*. *Biol Open*, 2019. **8**(1).
200. Friedrich, J., et al., *Spheroid-based drug screen: considerations and practical approach*. *Nat Protoc*, 2009. **4**(3): p. 309-24.
201. Mittler, F., et al., *High-Content Monitoring of Drug Effects in a 3D Spheroid Model*. *Front Oncol*, 2017. **7**: p. 293.
202. Zhu, X., et al., *Fabrication of Size-Controllable and Arrangement-Orderly HepG2 Spheroids for Drug Screening via Decellularized Liver Matrix-Derived Micropattern Array Chips*. *ACS Omega*, 2022. **7**(2): p. 2364-2376.

- 203. Zhang, Z., et al., *Establishment of patient-derived tumor spheroids for non-small cell lung cancer*. PLoS One, 2018. **13**(3): p. e0194016.
- 204. Hofmann, S., et al., *Patient-derived tumor spheroid cultures as a promising tool to assist personalized therapeutic decisions in breast cancer*. Transl Cancer Res, 2022. **11**(1): p. 134-147.



Screenshot of the MDPI publisher webpage taken on the 25.01.2023, showing that the copyright of the corresponding published articles is retained by the authors.

---

### List of Abbreviations

ALK	Anaplastic lymphoma kinase
AMP	Adenosine monophosphate
AMPK	AMP-activated protein kinase
APC	Antigen-presenting cells
ASC	Adipose derived stem cells
AURKA	Aurora kinase A
AURKB	Aurora kinase B
AXL	AXL tyrosine kinase
BRAF	Serine/threonine-protein kinase B-Raf
C-MET	Hepatocyte growth factor receptor
CDH1	E-cadherin
CDH2	N-cadherin
CK	Cytokeratin
CT	Computer tomography
CXCL	Cys-X-Cys Chemokines
DEG	Differentially expressed gene
DOC	Deoxycolate
Dpi	Days post infection
EC <sub>50</sub>	Excitatory concentration 50
ECM	Extracellular matrix
EGFR	Epidermal growth factor receptor
EMT	Epithelial-mesenchymal transition
HER2	Human epidermal growth factor receptor 2
ERK	Extracellular signal regulated kinase
FDA	Food and Drug Administration
FGFR	Fibroblast growth factor receptor
GAP	GTPase activating proteins
GDP	Guanine diphosphate
GEF	Guanosine exchange factor
GFR	Growth factor receptor
GM-CSF	Granulocyte-macrophage colony-stimulating factor
GRB2	Growth factor receptor bound protein 2
GSEA	Gene set enrichment analysis
GTP	Guanine triphosphate
HGF	Hepatocyte growth factor
hLF	Human lung fibroblasts

---

HSV-1	Herpes simplex virus 1
HTS	High throughput screening
IC <sub>50</sub>	Inhibitory concentration 50
ICI	immune checkpoint inhibitor
ICP	Infected cell protein
IFN	Interferon
IGF1R	Insulin like growth factor 1 receptor
IL	Interleukin
IRF	Interferon regulatory factor
KEAP	Kelch-like ECH-associated protein
KRAS	Kirsten rat sarcoma
LOX	Lysyl oxidase
MAPK	Mitogen-activated proteinkinase
MET	Mesenchymal-epithelial transition
MLV	Moloney's leukemogenic virus
MMP	Matrix-metallo proteinase
MOI	Multiplicity of infection
mTOR	Mammalian target of rapamycin
MUC-1	Mucin 1
N	Technical replicate
n	Biological replicate
NCCN	National Comprehensive Cancer Network
NF-κB	Nuclear factor kappa light chain enhancer of activated B cell:
NK	Natural killer
NRF2	NF-E2-related factor 2
NSCLC	Non-small cell lung cancer
NTRK	Neurotrophic tyrosine receptor kinase
ORR	Overall response rate
OV	Oncolytic virus
PCK	Pan-cytokeratin
PD-L1	Programmed cell death 1 ligand
PDX	Patient-derived xenograft
PFS	Progression-free survival
PI	Propidium iodide
PI3K	Phosphatidylinositol 3-kinase
RAF	Rapidly accelerated fibrosarcoma
RAL	Ras-like GTPase

---

RET	Ret proto-oncogene
ROS1	Ros proto-oncogene 1
RTK	Receptor tyrosine kinase
S-IIP	Switch-II pocket
SCC	Squamous cell carcinoma
SCLC	Small-cell lung cancer
SHP2	Src homology region 2 domain-containing phosphatase-2
SNAI	Snail family zinc finger
SOS	Son of sevenless
STAT2	Signal transducer and activator of transcription 2
STK11	Serine/threonine kinase 11
T-VEC	Talimogene laherparepvec
TGF- $\beta$	Transforming growth factor $\beta$
TKI	Tyrosine kinase inhibitor
TME	Tumor microenvironment
TNF	Tumor necrosis factor
TP53	Tumor protein 53
T $\beta$ RI	TGF- $\beta$ receptor I
ULA	Ultra low attachment
VIM	Vimentin
ZEB	Zinc finger E-box-binding homeobox

## **Acknowledgments**

First and foremost, I thank Dr. Gudrun Dandekar and Dr. Sarah Nietzer for giving me the opportunity to do my doctoral thesis in their group and for their constant supervision of the work. Thank you for your support, advice, and helping me out whenever I asked. You always kept me motivated, opened many doors and, in my eyes, you are role models for other group leaders in science. Both of you are responsible for the perfect working atmosphere that we have in our group, and I wish you and the “tumor group” all the best for the future. Please stay as you are and thank you for your support!

Secondly, I want to strongly emphasize my gratitude for Heide Häfner. We both know that you at the end of the day deserve a shared first authorship for this thesis, as without your constant help in the lab I would have lost track from the first day on. You never got tired of answering my (repetitive) questions, taught me several methods, supported me in dozens of experiments and always had an overview about everything! I will not miss doing Western Blots in the protein chemistry lab, but I will definitely miss working together with you! Thank you, Heide!!! Enjoy your well-deserved retirement.

I furthermore thank Prof. Thomas Dandekar and the Chair of Bioinformatics in Würzburg for the supervision of my thesis and the collaboration in the Remis3R project, respectively. I always enjoyed your enthusiasm for science, your reliability and your personal support, Prof. Dandekar. Here, I also want to thank Aylin Caliskan, Samantha Crouch, Dr. Chunguang Liang and Weimeng Yu from the Chair of Bioinformatics especially for the great cooperation in this project and the evaluation of the RNAseq data! It was an honor to work with you and benefit from your expertise!

I also want to thank Prof. Christian Stigloher for being the third supervisor of my thesis. I already enjoyed your practical courses and lectures during the master studies, and you always had a close look at my data during the progress reports, giving great suggestions and advice from a more “external” and objective point of view. Thank you for always taking your time and all your help!

Also, I say thanks to Lukas Königer and Dalia Mahdy from the Fraunhofer ISC in Würzburg for the cooperation in the FORTiTher project. I was always impressed by your skills regarding interdisciplinary work. It seems like you understood what I was talking about tumor biology, while I must admit I did not understand a single word when you were talking about coding and programming. I enjoyed working with you in a team but please finally give that robot a name!!!

Furthermore, I want to thank Dr. Susanne Bailer and Dr. Christina Funk from the Fraunhofer IGB (Stuttgart), Dr. Christian Werno and Catherine Botteron from Fraunhofer ITEM (Regensburg), Dr. Thomas Grunwald and Dr. Nadja Uhlig from the Fraunhofer IZI (Leipzig), for the nice cooperation during the TheraVision joint project. It was a great experience!

Many students helped to advance in the patient stratification for KRAS<sup>G12C</sup>-mutated tumors during their master thesis or in an internship. Tamara Lüttgens, Pia Wittmann, Celina May and Frederik Fabian Feigl did an outstanding job during their work, and I thank all of you for your contribution and effort (and cake).

Of course, I want to thank all members of the Chair of Tissue Engineering and Regenerative Medicine (TERM). Here, I want to especially mention my former and current colleagues from the “tumor group” who helped me along the way: Dr. Florentin Bauer, Dr. Johanna Kühnemundt and Jesús Nieves. I also thank Dr. Christina Fey, Dr. Constantin Berger and Thomas Däullary for their advice in scientific questions. Sanjana Mathew-Schmitt and Spyridon Damigos I want to not only thank for the productive scientific discussions we had in the office but also for the conversations about extraterrestrial life forms and conspiracy theories. Alevtina Cubukova and Sebastian Häusner I want to thank for the nice talks about hunting and wish you “Waidmannsheil”!

Last but not least, my biggest thanks go however to my wife Laura, my parents Josef and Ursula, my brothers Franz-Xaver (“Deine Hobbies miassn de aafhaxen!”) and Josef (“Revertigo”). This would not have been possible without you!



## Appendix

### List of Publications

#### Publications directly related with the doctoral *thesis*:

Peindl M\*, Göttlich C\*, Crouch S, Hoff N, Lüttgens T, Schmitt F, Pereira JGN, May C, Schliermann A, Kronenthaler C, Cheufou D, Reu-Hofer S, Rosenwald A, Weigl E, Walles T, Schüler J, Dandekar T, Nietzer S, Dandekar G. EMT, Stemness, and Drug Resistance in Biological Context: A 3D Tumor Tissue/In Silico Platform for Analysis of Combinatorial Treatment in NSCLC with Aggressive KRAS-Biomarker Signatures.

Cancers. 2022; 14(9):2176. doi: 10.3390/cancers14092176 (\*shared first authorship)

*Submitted (Molecular Therapy)*: Christina Funk, Nadja Uhlig, Zsolt Ruzsics, Florentin Baur, Matthias Peindl, Sarah Nietzer, Gudrun Dandekar, Catherine Botteron, Christian Werno, Thomas Grunwald, Susanne M. Bailer: TheraVision - Platform Technology for the Development of Oncolytic Viruses based on Herpes Simplex Virus Type 1.

#### Publications without direct relation to the doctoral *thesis*:

Shirley AJ, Schweeberg S, Waag T, Peindl M, Dandekar G, Walles H, Jakob F, Krueger A, Ebert R. The influence of differently functionalized nanodiamonds on proliferation, apoptosis and EMT/MET phenomena in 2D and 3D tumor cell cultures. J Mater Chem B. 2021 Nov 24;9(45):9395-9405. doi: 10.1039/d1tb01739j. PMID: 34734960.

Kühnemundt J, Leifeld H, Scherg F, Schmitt M, Nelke LC, Schmitt T, Baur F, Göttlich C, Fuchs M, Kunz M, Peindl M, Brähler C, Kronenthaler C, Wischhusen J, Prelog M, Walles H, Dandekar T, Dandekar G, Nietzer SL. Modular micro-physiological human tumor/tissue models based on decellularized tissue for improved preclinical testing. ALTEX. 2020 Dec 11;38(2):289-306. doi: 10.14573/altex.2008141. Epub ahead of print. PMID: 33313956.

Feigl, F.F.; Stahringer, A.; Peindl, M.; Dandekar, G.; Koehl, U.; Fricke, S.; Schmiedel, D. Efficient Redirection of NK Cells by Genetic Modification with Chemokine Receptors CCR4 and CCR2B. *Int. J. Mol. Sci.* 2023, 24, 3129. doi: 10.3390/ijms24043129

## Curriculum Vitae

### Berufserfahrung:

- **Universitätsklinikum, Würzburg** (10/2019 – aktuell)  
**Wissenschaftlicher Mitarbeiter, Doktorand** am Lehrstuhl für Tissue Engineering und Regenerative Medizin (TERM, Dr. Dandekar / Dr. Nietzer) zur Promotion mit dem Titel „Refinement of 3D lung cancer models for automation and patient stratification“
- **Universitätsklinikum, Würzburg** (03/2019 – 09/2019)  
**Masterand** am Lehrstuhl für Tissue Engineering und Regenerative Medizin (TERM, Dr. Dandekar / Dr. Nietzer) zur Erlangung des M.Sc. mit dem Titel „Investigation on 3D tumor models with stromal components and the impact of biomarker mutations on tissue generation“
- **Universität Würzburg** (04/2017 – 08/2017)  
**Bachelorand** am Lehrstuhl für Biochemie (Prof. Schulze) zur Erlangung des B.Sc. mit dem Titel „Metabolic characterization of 4T1 cells in a newly formulated mouse plasma-like medium“
- **Prienamed, München** (2012 - 2014)  
**Physiotherapeut** in der Praxis „exaktaktiv“ im Ärztehaus Prienamed

### Bildungsweg:

- **JMU, Würzburg** (10/2017 – 09/2019)  
Master of Science Biomedizin
- **JMU, Würzburg** (10/2014 – 08/2017)  
Bachelor of Science Biomedizin
- **Berufsfachschule für Physiotherapie, Freyung** (10/2009 – 09/2012)  
Staatsexamen
- **Landgraf-Leuchtenberg-Gymnasium** (bis 2008)  
Allgemeine Hochschulreife

### Zusatzqualifikationen:

- FELASA B
- Fortbildung Gentechnik und biologische Sicherheit
- Gefahrgutschulung IATA-DGR

### Sprachkenntnisse:

- Deutsch, fließend
- Englisch, fließend
- Französisch, Grundkenntnisse

**Eidesstattliche Erklärungen  
nach §7 Abs. 2 Satz 3, 4, 5 der Promotionsordnung der Fakultät für Biologie**

**Eidesstattliche Erklärung**

Hiermit erkläre ich an Eides statt, die Dissertation: „**Weiterentwicklung von 3D Lungentumormodellen zur Automatisierung und Patienten-Stratifizierung mit Untersuchungen zur Wirkungsweise**“, eigenständig, d. h. insbesondere selbständig und ohne Hilfe eines kommerziellen Promotionsberaters, angefertigt und keine anderen, als die von mir angegebenen Quellen und Hilfsmittel verwendet zu haben.

Ich erkläre außerdem, dass die Dissertation weder in gleicher noch in ähnlicher Form bereits in einem anderen Prüfungsverfahren vorgelegen hat.

Weiterhin erkläre ich, dass bei allen Abbildungen und Texten bei denen die Verwertungsrechte (Copyright) nicht bei mir liegen, diese von den Rechtsinhabern eingeholt wurden und die Textstellen bzw. Abbildungen entsprechend den rechtlichen Vorgaben gekennzeichnet sind sowie bei Abbildungen, die dem Internet entnommen wurden, der entsprechende Hypertextlink angegeben wurde.

**Affidavit**

I hereby declare that my thesis entitled: „ **Refinement of 3D lung cancer models for automation and patient stratification with mode-of-action studies**” is the result of my own work. I did not receive any help or support from commercial consultants. All sources and / or materials applied are listed and specified in the thesis.

Furthermore I verify that the thesis has not been submitted as part of another examination process neither in identical nor in similar form.

Besides I declare that if I do not hold the copyright for figures and paragraphs, I obtained it from the rights holder and that paragraphs and figures have been marked according to law or for figures taken from the internet the hyperlink has been added accordingly.

Würzburg, den \_\_\_\_\_

\_\_\_\_\_  
Signature PhD-student